Structural and Dynamic Investigations of Graphite Based Materials

Alice May Bailey

Materials and Physics Research Centre
School of Computing, Science and Engineering
University of Salford, Salford, UK

Submitted in partial fulfilment of the requirements of
the degree of Doctor of Philosophy

2014

Contents

List of Figures

List of Tables

I would like to thank the students and lecturers I have known at Salford. I have made friends for life and been inspired to do more physics than I ever imagined.

I must also thank my family and friends for all the support both physical and emotional given through my undergraduate and postgraduate degrees. You have made it possible for me to achieve this.

My thanks to Dr. Simon Keens for creating the samples and providing data and information. Also all who helped with measurements at Helmholtz Centrum Berlin.

My final and most significant thanks must go to Dr. Daniel Roach and Prof. Keith Ross. They envisaged this project before I was even aware of neutron scattering and supported me as I learned more about their pet fields of expertise, and through all the changes that were made to well laid plans. Thank you for all the information and feedback you have given me, I will leave with skills I didn't know I could obtain.

Abstract

Graphite based materials are of particular interest as energy materials. Graphite is used as a moderator in nuclear reactors and there have been investigations into the ability of modified graphites, such as expanded or intercalated graphite, to store hydrogen. Poly-crystalline coherent inelastic neutron scattering (poly-CINS) is used to give information on the dynamic properties of materials. Typically poly-CINS produces large and difficult to interpret data sets. Neutronplot, a novel analysis software suite described in this work, is used in conjunction with predicted dynamic information to analyse poly-CINS data. X-ray diffraction measurements taken by Keens[1] were used to investigate the bulk structural properties of several natural graphites, one of which was chosen for poly-CINS analysis using IN5 experimental data, simulated data and Neutronplot. These investigations were also replicated with an exfoliated graphite sample. Both x-ray and neutron diffraction were used to investigate the structure of a C60 intercalated graphite sample derived from the exfoliated graphite and a Poly-CINS experiment was conducted using the NEAT spectrometer.

We have found that the current IUPAC lattice values for rhombohedral stacking in graphite do not fit with experimental measurements. Also the interlayer spacing of rhombohedrally stacked graphite in natural graphite samples tends to be larger than that of hexagonal graphite. The investigations of exfoliated graphite show how interactions other than the graphene interlayer begin to dominate as disorder is added into the system. Successful C60 intercalation in graphite layers is confirmed by neutron diffraction.

Measurements of the elastic constant C_{33} for natural and exfoliated graphite show good agreement with other graphite measurements. The intercalate poly-CINS measurement suffered from low statistics and shows how Neutronplot can be used for less than ideal data sets. The data shows diffuse C60 in the graphite matrix, this result is reflected in the diffraction measurements.

Chapter 1

Introduction

1.1 Motivation

Graphite is a material of both economical and scientific interest and despite much historical investigation, there is still much that is not understood about the graphite structure. The anisotropy and weak interlayer bonding of graphite make modelling difficult and it is also prone to defects in both natural and manufactured forms. It is still a matter of debate how defects in the material contribute to its behaviour in bulk, particularly in its use as a graphite moderator, now that graphite moderated reactors are coming to the end of their lives. This application and investigations into hydrogen storage mean it is particularly of interest as an energy material. In this work we will investigate the structure and dynamics of natural and expanded graphite samples to further knowledge of defected graphite crystals.

Investigations of graphite as a potential hydrogen storage material, have led to the hypothesis that its capacity to store hydrogen increases when the planes of graphite are expanded[2]. To investigate this phenomenon a C60 Graphite intercalate (C60 GIC) sample was created by Keens[1]. This is a novel material and although it was tested for hydrogen storage potential by Keens the

material was never fully characterised and its dynamic properties were not investigated. It was unknown whether the sample did indeed contain intercalate rather than just a mixture of graphite and C60, a matter which is settled in this work.

Thermal neutrons provide an ideal probe of the dynamics of matter, due to their wavelength relative to interatomic spacing and energy, compared with lattice vibrations. Full dispersion curves of materials can be directly traced using a triple axis spectrometer containing a single crystal sample of coherently scattering elements. However this method is unusable when a large area of space needs to be explored using detector banks covering large solid angles or when the sample is poly-crystalline. The majority of dynamical analysis on poly-crystalline samples is performed using incoherent, inelastic, neutron scattering. Incoherent scattering gives density of state information on phonon modes. However information on the spatial displacements involved in particular phonon modes are often useful and this requires coherent, inelastic, neutron scattering (poly-CINS) measurements which result in large complicated data sets.

Due to the difficulties associated with interpreting poly-CINS measurements, currently available neutron scattering visualisation packages are designed primarily for the analysis of incoherent scattering data. These packages have typically been created independently at several experimental centres, thus there is no industry standard for the visualisation of inelastic neutron scattering data, and neutron scatterers must learn to use several different programs each with their own strengths and weaknesses. Some advances in the interpretation of poly-CINS data have been made recently with the advent of the Scatter code by Roach[3]. Scatter uses lattice dynamics data, calculated by GULP (General Utility Lattice Program) to create theoretical poly-CINS data. This code is still in development but a working version is available to members of the group.

This project will utilise Scatter data and due to the difficulty of comparing experimental and theoretical data from different sources a program has been created by the author to enable the easy viewing and analysis of poly-CINS data. This program will be of use primarily in this project, and could also be of benefit to the wider scattering community.

Carbon based structures are ideally suited to poly-CINS analysis, as many of these materials are created in powder form, and others such as graphite are easily ground into powder samples. Carbon also has an almost completely coherent cross section, the only incoherent contribution would come from the presence of the C^{13} isotope, which is sufficiently rare as to be unnoticeable in scattering measurements.

1.2 Experimental Methods of Materials Characterisation

The suitability of a particle as a probe of materials depends on several important properties. An ideal probe would be easy to produce and detect, have a tuneable wavelength and have the ability to differentiate clearly between different species in a sample. The energy of the probe should also be around the same magnitude as the vibrations in the lattice in order to measure these with inelastic scattering.

1.2.1 X-Rays

X-rays at certain energies have wavelengths roughly equal to the atomic spacing in materials. Historically they were the most important probe of matter for diffraction studies, as x-rays suitable for diffraction are relatively easy to detect

and produce. X-rays suitable for dynamics research are generally produced in synchrotrons as these provide a much more powerful source of x-rays than a standard x-ray tube. X-rays can be used to study both single crystals and powder samples. X-rays interact with the electrons in the system. This means that the intensity of the diffraction increases as electron number per atom increases and has no dependence on isotope. Thus x-rays detect large atoms more strongly than light atoms so these can be 'lost' in systems containing large atoms. These attributes make x-rays a poor tool for use in studies such as hydrogen diffusion experiments. As detection of isotopes is not possible, x-rays cannot be used to study the isotopes in a material, for example what their ratios are, or if there is any difference in the behaviour of the isotopes.

1.2.2 Raman and Infrared Spectroscopy

Raman spectroscopy involves shining monochromatic light on a sample. Although most of the light will scatter elastically some of the light will undergo inelastic collisions with polarisable molecules. If the polarisability of the molecule changes its value in a given vibration mode, Raman spectra are observed. The absorption of Infrared Radiation (IR) at wavelengths above one micro-meter distorts dipoles in molecules thus molecules with symmetrical bonds are not excited unless they can be induced by the IR to undergo bending or rocking motions.

As Raman and IR have different selection rules these techniques are used in a complementary fashion. They are used mostly in the field of molecular characterisation. Raman and IR instruments are relatively small and are present in a typical materials analysis lab. For this reason they are the first option for dynamic analysis. A disadvantage of infrared spectroscopy and Raman is that it is not guaranteed that all modes will be activated. The frequency range of

Raman is typically confined to zero momentum transfer. Also some materials, such as metals, do not have a Raman signature.

1.2.3 Electron Diffraction and Microscopy

Electrons[4] readily lead themselves to be used as a probe of matter due to their wavelengths and ease of detection. Electron microscopes are common in scientific environments. Electrons can be used in both diffraction and imaging applications. Electrons interact with the electrons in the material, so again different isotopes can not be detected. The suitability of electrons as a probe depends on the material in question. Electrons react strongly with material and so can only pass through thin slices of material. The beams are also highly focused, thus electrons can often tell you more about surface and local effects, and are often not suitable for researching the bulk properties of a material. Not all materials can be formed into specimens suitable for electron microscopy. For energetic studies Electron Energy Loss Spectroscopy (EELS) is used, typically for finding the chemical composition and types of chemical bonds in the material. The effectiveness of EELS depends upon the elements in use, it is particularly suited for the elements ranging from carbon to the 3d transition metals.

1.2.4 Neutron Scattering

Neutrons[5] are not easy to produce at the flux necessary for materials study, A high flux reactor such as the ILL creates 1.5×10^{15} neutrons per cm^2 sec this flux is then moderated and spilt between several experiments. In comparison an electron microscope produces 4×10^{16} electrons per second per cm^2 as a minimum, however this flux is attenuated quickly by a sample. Neutrons

are also relatively difficult to detect, due to the lack of electron interactions, so neutron experiments are performed at large centralised facilities. As the neutron's main interaction is with the nucleus of an atom they can be used to detect different isotopes of an element. The interaction between a neutron and the nucleus does not depend on atom size so small atoms are equally easy to detect. The neutron also has a magnetic dipole which reacts with the unpaired electrons in the system so the neutron is well suited to magnetic studies.

1.3 Current Neutron Data Analysis Programs

The two main programs for looking at neutron scattering data are LAMP (Large Array Manipulation Program)[6] developed at the Institut Laue-Langevin (ILL) in Grenoble and Mslice[7] developed in the ISIS facility in Oxfordshire. Both have issues related to usability and functionality. Neither has been designed specifically with coherent inelastic neutron scattering in mind.

1.3.1 LAMP

LAMP was developed initially for treating the output from scattering experiments at the ILL. LAMP is based on the IDL language and its functionality is in the form of macros. In its data analysis processes LAMP takes into account the experiment used. This is a very powerful feature of LAMP as idiosyncrasies in the instrument can be taken into account, for example malfunctioning detectors or instrument setup. To perform any sort of evaluation on the data, the user has to take the original data then type into the analysis area which functions the user wants to apply to the data and the parameters they want this analysis to be performed under. This is not a very user friendly way of manipulating data. An advantage of LAMP is that one can write their own

macros and thus extend the functionality for their own needs, however this requires knowledge of the programming language and some knowledge of how LAMP works as a whole.

1.3.2 Mslice

Mslice is a scattering visualisation program based on the MATLAB programming language. The ISIS team uses a family of data analysis programs, written in different languages, to analyse their data. Their data analysis needs range from processing the raw output from the detectors, to various fitting tools. Mslice was designed to read data files produced from Homer[8]. Homer is a data transformation routine involved in further processing of raw data.

1.3.3 Introduction to Neutronplot

Neutronplot was developed for this project and aims to have the useful functionally of both LAMP and Mslice without the drawbacks. Neutronplot should be user friendly, and it will aim to appeal to all members of the neutron scattering community. It can been seen as a useful addition to GULP and the Scatter code and hopefully an independent tool in its own right for use by both experimental and theoretical neutron scatterers. It has been developed using MATLAB[9] and has a Graphical User Interface (GUI). Most operations are performed at the click of a button to enable ease of use. However simplicity and an easy learning curve can lead to a lack of flexibility, functionality and difficulty in code analysis for users. Hopefully a good compromise can be found. Neutronplot has been written so that each operation that can be performed is a separate MATLAB function. This should make it easy to add new functionality and update the existing code.

1.4 Graphitic Structures

The main materials focus of this project is the study of the structure and dynamic of graphite based materials. The hexagonal form is the most common form of graphite, and differs from the rhombohedral form only in its stacking. Hexagonal graphite stacks in an ABAB pattern, whereas rhombohedral graphite stacks in an ABCABC pattern. Other possible types of graphite include pyrolytic graphite where the graphene layers are bound by a high number of crystallographic defects and turbostratic graphite where the layers of graphene are rotated with respect to each other. It was shown that in graphitic carbons, the fraction of correctly orientated graphitic layers, p, was related to both the interlayer spacing and the intensity of diffraction peaks[10]. Turbostratic graphite was first discovered in carbon fibres by Johnson & Watt[11].

Figure 1.1: C60 intercalated graphite model created in Materials Studio

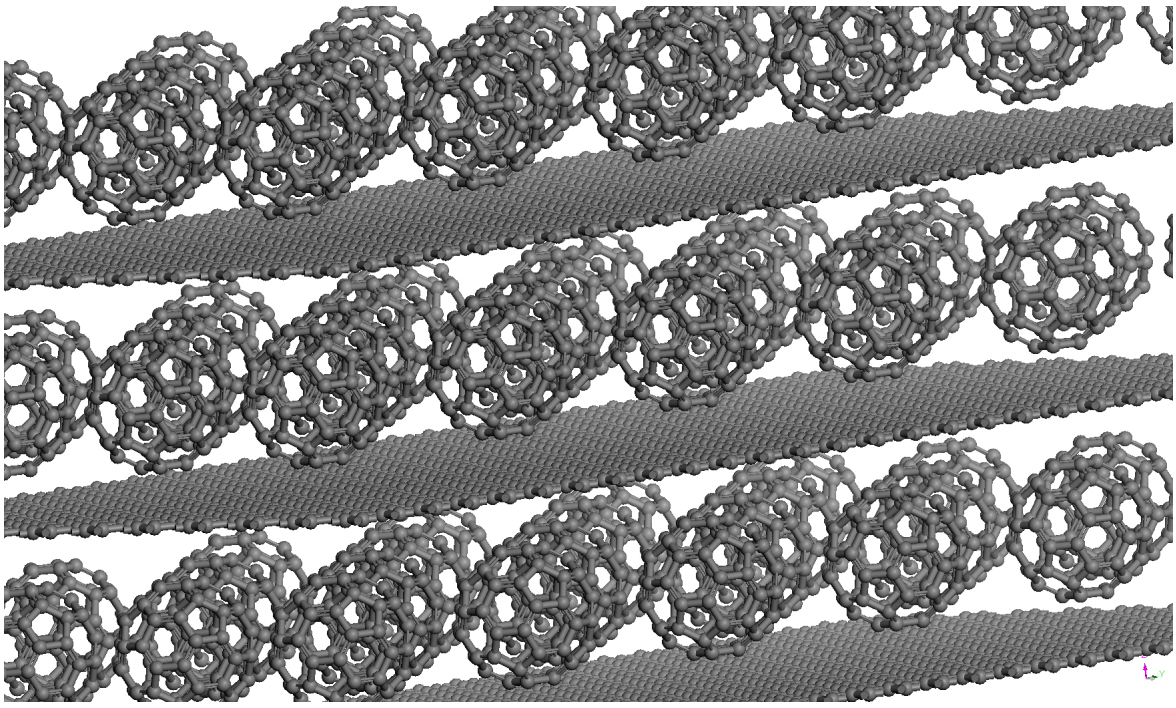

The model in figure (1.1) is based on the dimensions stated in Gupta *et al.*[12]

Other important graphitic structures are graphite intercalated compounds (GICs).

These compounds are currently being studied by many groups as they may have applications in hydrogen storage. It has been proposed by Kuc *et al.*[2] that the capability of a graphitic material to store hydrogen molecules is determined by the graphite interlayer distance. Therefore a method of changing the interlayer distance, such as by the introduction of C60, is desirable. C60 GIC can be modelled as layers of graphene with C60 between the layers. A sample of C60 GIC was created by Keens[1] to investigate the hydrogen storage properties of the material. This sample was used in the C60 GIC poly-CINS analysis in later chapters.

A study of C60 GIC using neutron scattering has not been previously performed, thus the information gained by these investigations is unique and should prove very useful in understanding the dynamics of C60 GIC.

Chapter 2

Background and Theory

Both x-rays and neutrons were used for materials investigation in this work. To aid understanding of the results shown and the reasons behind the design of Neutronplot, a background of the physics of these probes is provided. This chapter covers both elastic and inelastic neutron scattering as well as information about the instruments used to analyse samples. In this work x-rays are only used to produce powder diffraction patterns so the description of x-ray scattering will be limited to elastic scattering.

The crystal lattice and lattice vibrations are also described as these concepts are essential to understanding the dynamics of solid materials.

2.1 Neutron and X-Ray Spectrometry

The neutron has several properties which make it a useful probe of matter. Firstly it has no detectable electrical charge or electrical dipole moment. Hence the neutron can penetrate deeply into the material giving nucleus positions rather than electron cloud positions. For low energy neutrons the wavelength of the neutron is comparable to the typical spacing of nuclei in materials, giving good diffraction patterns from the atoms in a crystal. These neutrons are

known as thermal neutrons as they have the energies they would possess at room temperature which is around 0.025 eV. The energy of thermal neutrons is also comparable to that of phonons in a material so interactions between the neutron and the lattice vibrations can be measured. Experimental neutron scattering consists of a variety of techniques which use neutron radiation as a probe of materials.

X-rays are commonly used as a probe of the structure of crystallographic materials. They can be created with wavelengths of the order of the spacing between atoms in a material and are easier to create than neutrons in the intensities necessary to penetrate samples. Laboratories typically contain an x-ray diffractometer, leading to XRD being one of the first lines of investigation for material samples. X-rays react with the electrons around the atom in a material and so do not differentiate between different isotopes but between different elements. They also attenuate relatively quickly in a sample. X-rays can be used as a probe of the dynamics of a material, but this requires a synchrotron source, which removes the advantage of convenience that x-rays have over neutrons.

Neutrons for materials investigation are created either in a nuclear or spallation source. In the case of spallation accelerated protons hit a heavy element such as tungsten and neutrons are released. In a nuclear reactor neutrons are released from the nucleus of radioactive material in the fission process. In both cases neutrons are moderated after release to ensure that the majority are at the energies required for neutron scattering. Neutrons are typically detected using tubes filled with ^{3}He which absorbs the neutron and then decays to ^{1}H and ^{3}H which can be detected easily. Scintillating detectors are becoming more commonly used and are based on the absorption of the neutron by ^{6}Li giving ^{3}H and a helium nucleus.

X-rays in a diffractometer are created by electrons from a cathode hitting a charged metal surface, known as the source, which is typically copper. When hit the electrons in the metal are excited and release radiation in the form of x-rays. The x-rays are then usually monochromated and collimated by a series of mirrors. Samples are rotated in the beam to cover the different crystallographic directions in the material. X-rays can be detected by anything capable of reacting to electromagnetic radiation, historically photographic film was used but this has largely been replaced by CCDs.

The scattering of a neutron by a nucleon is typically described in terms of a scattering cross-section. This cross-section is the equivalent to the effective area presented by the nucleus to the passing neutron, this area is measured in barns ($10^{-28}m^2$). The cross-section is an experimentally derived quantity which varies from element to element and from isotope to isotope. As the scattering cross-section varies from isotope to isotope, different isotopes can be used in a sample to create the best conditions for the type of neutron scattering being undertaken.

As x-rays interact with the electron cloud the scattering cross-section of x-rays is proportional to the size of the atom. Thus heavy elements interact more strongly with x-rays than light elements.

This relationship is represented in figure (2.1), demonstrating the increase in cross-section with increased electrons for x-rays and the lack of correlation for neutrons.

Neutrons are scattered both elastically and inelastically. Elastic neutron scattering is used in neutron diffraction. Neutron diffraction assumes no movement on the part of the nucleons and no energy gain or loss for the neutrons interacting with the nucleons. This gives a diffraction pattern which contains structural information about the sample. Elastic neutron scattering can also

Figure 2.1: A comparison of scattering cross-sections of neutrons and x-rays for some elements and isotopes[13]

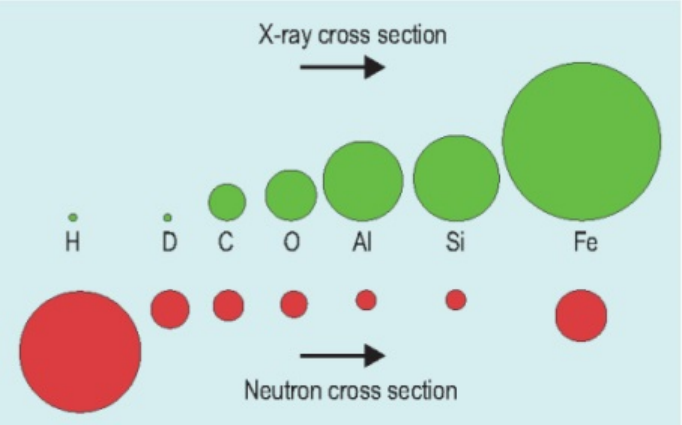

be used to measure fluctuations in the neutron scattering density function in the range of 10-1000 Å using small angle neutron scattering. Depth profiles can also be measured using reflectometry. Inelastic neutron scattering gives information about the thermal properties of a material, its phonon properties. This in turn gives information on the inter-atomic forces in the system.

2.2 Introduction to Scattering

This treatment broadly follows that of Squires[14], with a particular focus on coherent inelastic scattering and some important physical results. Vectors are indicated by a ***bold*** typeface. The scattering of neutrons and x-rays shares basic similarities as both involve particles scattering from an atom leading to a change in the momentum of the scattered particle.

The change in momentum $\boldsymbol{P}$ of the scattered particle is represented as,

$$\boldsymbol{P} = \hbar\boldsymbol{k} - \hbar\boldsymbol{k}' = \hbar\boldsymbol{Q} \tag{2.1}$$

$\boldsymbol{k}$ and $\boldsymbol{k}'$ denote the initial and final wavevectors of the scattering particle, the

magnitude of $\boldsymbol{k}$ is $|\boldsymbol{k}| = \frac{2\pi}{\lambda}$, λ is the wavelength of the scattering particle. $\boldsymbol{Q}$ is the scattering vector.

$$\boldsymbol{Q} = \boldsymbol{k} - \boldsymbol{k}' \tag{2.2}$$

This scattering vector allows analysis of scattering independent of experimental conditions, such as incident angle, as different $\boldsymbol{k}$ and $\boldsymbol{k}'$ can give the same momentum change and thus the same $\boldsymbol{Q}$ value.

The particle also has an energy E which is related to the angular frequency of the particle.

$$E = \hbar\omega \tag{2.3}$$

where $\omega = 2\pi v$ and v is the speed of the scattering particle.

$$dE = \hbar\omega - \hbar\omega' \tag{2.4}$$

gives the change in energy of the scattered particle.

For elastic scattering there is no energy transfer thus the wavelength of the scattered particle is unchanged. Only the direction of the particle is affected.

For elastic scattering

$$|\boldsymbol{k}| = |\boldsymbol{k}'| = \frac{2\pi}{\lambda} \tag{2.5}$$

In two dimensions $\boldsymbol{Q}$ can be found as

$$\boldsymbol{Q} = \frac{4\pi \sin\theta}{\lambda} \tag{2.6}$$

and in three

$$\boldsymbol{Q} = \frac{4\pi \sin\theta}{\lambda}(-\cos\theta\cos\phi, -\cos\theta\sin\phi, \sin\theta) \tag{2.7}$$

in the polar co-ordinate system.

2.2.1 The Neutron Scattering Cross-Section

We now concentrate on the case of neutron scattering specifically.

Figure 2.2: A scattering system[14]

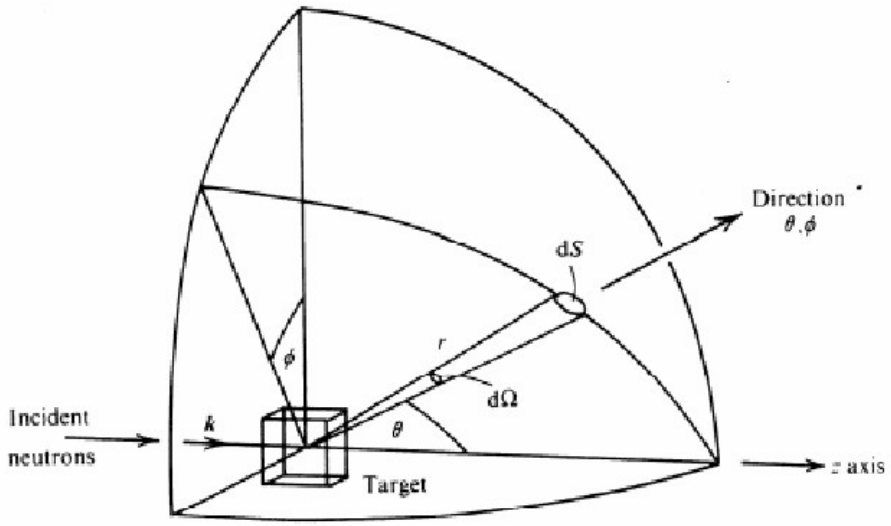

Above we see a representation of a neutron scattering experiment where a beam of neutrons with the same incident energy E are shone on a target. The measurements made on the scattered neutrons can be expressed in terms of a cross-section. The distance between the detector and the sample is assumed to be large so the solid angle $d\Omega$ is well defined. The co-ordinate system chosen is polar so the direction of the neutrons is ϕ, θ.

The measured quantity in a scattering experiment is the double differential

cross-section.

$$\frac{\partial^2\sigma}{\partial\Omega\partial E'} \tag{2.8}$$

It is defined to be "number of neutrons scattered per second into a small solid angle $d\Omega$ in the direction θ,ϕ with final energy between E' and $E' + dE'$, divided by Φ the flux of incident neutrons $d\Omega dE$"[14]

If the energy of the neutrons is not analysed we can obtain the differential cross-section, by integration over E'. The differential cross-section is therefore defined as

$$\frac{d\sigma}{d\Omega} = (\text{number of neutrons scattered per second into } d\Omega \text{ in the direction } \phi, \theta)/\Phi\ d\Omega \tag{2.9}$$

The total scattering cross-section, obtained by integrating over Ω is defined by the equation

$$\sigma_{tot} = (\text{number of neutrons scattered per second})/\Phi \tag{2.10}$$

The scattering cross-section is equivalent to the effective area presented to the neutron by the nucleus. Neutron scattering theory is based on attempting to find theoretical expression for the cross-sections. Experimental cross-sections are quoted per atom or per molecule i.e. the cross-sections defined above are divided by the number of atoms or molecules present in the scattering system.

2.2.2 Scattering of Neutrons by a Single Fixed Nucleus

We take the origin to be at the position of the nucleus and the z axis to be along the direction of $\boldsymbol{k}$, the wavevector of the incident neutrons (see fig 2.2). So the wavefunction of incident neutron is a plane wave of the form.

$$\Psi_{\boldsymbol{k}} = e^{i\boldsymbol{k}\bullet z} \tag{2.11}$$

When a plane wave is scattered from a point it gives a spherical wavefunction of the form

$$\Psi_{\boldsymbol{k}'} = -\frac{b}{r} e^{i\boldsymbol{k}'\bullet r} \tag{2.12}$$

where b is a constant normally independent of the angles ϕ, θ.

In the spherical wavefunction the minus sign is used to give a positive value of b for the majority of materials. This is explored further in the section concerning coherence. The b value is called the 'scattering length' and depends upon the interaction with the nucleus of the particle and the combined spin of the neutron nucleus system. For low neutron energies, as explored in this work, it is independent of the energy of the neutron. As we do not have a full theory of nuclear forces the scattering length cannot be calculated theoretically. This means that b is a parameter which has to be found experimentally. The scattering lengths do not correlate directly with any property such as nucleus size and they vary between elements and isotopes.

Using the expressions (2.11) and (2.12) it is possible to calculate the cross-section $d\phi/d\Omega$ for scattering from a single fixed nucleus.

For elastic collisions v the velocity of the neutrons will be the same before and after scattering. The number of neutrons passing through the area dS per

second is

$$v\ dS|\Psi_{k'}|^2 = v\ dS\frac{b^2}{r^2} = vb^2\ d\Omega \tag{2.13}$$

The flux of incident neutrons will be

$$\Phi = v|\Psi_{\boldsymbol{k}}|^2 = v \tag{2.14}$$

From the definition of the cross-section

$$\frac{d\sigma}{d\Omega} = \frac{vb^2 d\Omega}{\Phi d\Omega} = b^2 \tag{2.15}$$

So in this case the total cross-section is

$$\sigma_{tot} = 4\pi b^2 \tag{2.16}$$

2.2.3 Fermi's Golden Rule

Looking at a general system of particles we need to find an expression for the double differential cross-section for a specific transition of the scattering system from one quantum state to another.

Starting with equation (2.9), the definition of the differential cross-section, we will denote the state of the scattering system with μ and the wavefunction of the scattering system with χ_μ. The wavevector of the incident neutron is $\boldsymbol{k}$ and the wavefunction of the neutron is $\Psi_{\boldsymbol{k}}$. We assume a co-ordinate system where $\boldsymbol{R}_j$ is the position vector of the jth nucleus and $\boldsymbol{r}$ is the position vector of the neutron. In this situation $(j = 1, ...N)$ where N is the number of nuclei in the scattering system.

We now sum over all changes μ to μ' and from $\boldsymbol{k}$ to $\boldsymbol{k}'$ over all values of $\boldsymbol{k}'$ that lie in the solid angle $d\Omega$ in the direction ϕ, θ. These conditions give

$$\frac{d\sigma}{d\Omega}_{\mu\to\mu'} = \frac{1}{\Phi}\frac{1}{d\Omega}\sum_{\boldsymbol{k}'} \quad W_{\boldsymbol{k},\mu\to\boldsymbol{k}'\mu'} \tag{2.17}$$

where $W_{\boldsymbol{k},\mu\to\boldsymbol{k}'\mu'}$ is the number of transitions from the state $\boldsymbol{k}, \mu$ to the state $\boldsymbol{k}', \mu'$, and Φ is the flux of incident neutrons. To evaluate the expression on the right hand side we use a fundamental result in quantum mechanics known as Fermi's golden rule. (This result can be found in most quantum mechanics textbooks for example see Merzbacher chapter 18[15]).

$$\sum_{k'} \quad W_{\boldsymbol{k},\mu\to\boldsymbol{k}'\mu'} = \frac{2\pi}{\hbar}\rho_{\boldsymbol{k}'}|\langle \boldsymbol{k}'\mu'|V|\boldsymbol{k}\mu\rangle|^2 \tag{2.18}$$

In this result V is the interaction potential and $\rho_{\boldsymbol{k}'}$ is the number of momentum states in $d\Omega$ per unit energy range for neutrons in the state $\boldsymbol{k}'$. For the equation (2.18) the matrix element can be expressed in standard notation as

$$\langle \boldsymbol{k}'\mu'|V|\boldsymbol{k}\mu\rangle = \int \Psi^*_{\boldsymbol{k}'}\chi^*_{\mu'}V\Psi_{\boldsymbol{k}}\chi_{\mu}\, d\boldsymbol{R}\, d\boldsymbol{r} \tag{2.19}$$

where

$$d\boldsymbol{R} = d\boldsymbol{R}_1 d\boldsymbol{R}_2 ... d\boldsymbol{R}_N \tag{2.20}$$

We can now perform a standard procedure known as box normalisation. This is a quantum mechanical device where one imagines the neutron and scattering systems are within a large box. This enables the calculation of $\rho_{\boldsymbol{k}'}$ and fixes the normalisation constant of the neutron wave functions. The full derivation of this is included in appendix A.

The result of this operation is

$$\left(\frac{d\sigma}{d\Omega}\right)_{\mu\to\mu'} = \frac{\boldsymbol{k}'}{\boldsymbol{k}}\left(\frac{m}{2\pi\hbar^2}\right)^2 |\langle \boldsymbol{k}'\mu'|V|\boldsymbol{k}\mu\rangle|^2 \tag{2.21}$$

Differentiation by E' reintroduces the energy terms and gives

$$\left(\frac{d^2\sigma}{d\Omega\, dE'}\right)_{\mu\to\mu'} = \frac{\boldsymbol{k}'}{\boldsymbol{k}}\left(\frac{m}{2\pi\hbar^2}\right)^2 |\langle \boldsymbol{k}'\mu'|V|\boldsymbol{k}\mu\rangle|^2 \delta(E_\mu - E_{\mu'} + E - E') \tag{2.22}$$

We need a form of this equation which is closer to that measured in scattering experiments. This requires expanding the terms in the equation above and expressing it terms which can be measured by neutron scattering. $\boldsymbol{Q}, \boldsymbol{R}, \boldsymbol{k}$ and ω. Taking the Hamiltonian of the scattering system into account gives us functions with these terms with the addition of some other considerations.

The energy function on the left hand size of (2.22) is an energy δ function which can be expressed as an integral over time

$$\delta(E_\mu - E_{\mu'} + E - E') = \frac{1}{2\pi\hbar}\int_{-\infty}^{\infty} \exp\{i(E_\mu - E_{\mu'})t/\hbar\}\exp(i\omega t)dt \tag{2.23}$$

V is found to be

$$V(\boldsymbol{Q}) = \frac{2\pi\hbar^2}{m} b_j \tag{2.24}$$

by considering the effect of an unbound nucleus on scattering length.

These factors lead to a form of the double differential cross-section which will be used in the rest of this work

$$\frac{d^2\sigma}{d\Omega\, dE'} = \frac{\boldsymbol{k}'}{\boldsymbol{k}} \frac{1}{2\pi\hbar} \sum_{jj'} b_{j'} b_j \int \langle exp\{-i\boldsymbol{Q}.\boldsymbol{R}'_j(0)\} exp\{i\boldsymbol{Q}.\boldsymbol{R}_j(t)\}\rangle \times exp(-i\omega t) dt \tag{2.25}$$

2.2.4 Coherent and Incoherent Scattering Systems

Given a system with one element where the scattering length b varies from one nucleus to another owing to nuclear spin or to the presence of isotopes or both. If the value b_i occurs with relative frequency f such that

$$\sum_i f_i = 1 \tag{2.26}$$

The average b value is

$$\bar{b} = \sum_i f_i b_i \tag{2.27}$$

and the average value of b^2 is

$$\bar{b^2} = \sum_i f_i {b_i}^2 \tag{2.28}$$

The cross-section in this case will be

$$\frac{d^2\sigma}{d\Omega\, dE'} = \frac{\boldsymbol{k}'}{\boldsymbol{k}} \frac{1}{2\pi\hbar} \sum_{jj'} \overline{b_{j'} b_j} \int \langle j', j\rangle exp(-i\omega t) dt \tag{2.29}$$

where

$$\langle j', j\rangle = \langle exp\{-i\boldsymbol{Q}.\boldsymbol{R}'_j(0)\} exp\{i\boldsymbol{Q}.\boldsymbol{R}_j(t)\}\rangle \tag{2.30}$$

Assuming no correlation between the scattering lengths b of different nuclei.

$$\overline{b_{j'}b_j} = (\bar{b})^2, \qquad j' \neq j$$
$$\overline{b_{j'}b_j} = \bar{b^2}, \qquad j' = j. \tag{2.31}$$

So for a sum excluding $j = j'$

$$\begin{aligned}\frac{d^2\sigma}{d\Omega\, dE'} =& \frac{\boldsymbol{k}'}{\boldsymbol{k}}\frac{1}{2\pi\hbar}(\bar{b})^2 \sum_{jj'} \int \langle j', j\rangle exp(-i\omega t)dt \\ &+ \frac{\boldsymbol{k}'}{\boldsymbol{k}}\frac{1}{2\pi\hbar}\bar{b^2} \sum_{j} \int \langle j, j\rangle exp(-i\omega t)dt\end{aligned} \tag{2.32}$$

$$= \frac{\boldsymbol{k}'}{\boldsymbol{k}}\frac{1}{2\pi\hbar}(\bar{b})^2 \sum_{jj'} \int \langle j', j\rangle exp(-i\omega t)dt + \frac{\boldsymbol{k}'}{\boldsymbol{k}}\frac{1}{2\pi\hbar}\{\bar{b^2} - (\bar{b})^2\} \sum_{j} \int \langle j, j\rangle exp(-i\omega t)dt \tag{2.33}$$

The first term in equation (2.33) is known as the *coherent* scattering term. The second term in the equation is the *incoherent* scattering term. Splitting these terms gives

$$\left(\frac{d^2\sigma}{d\Omega\, dE'}\right)_{coh} = \frac{\sigma_{coh}}{4\pi}\frac{\boldsymbol{k}'}{\boldsymbol{k}}\frac{1}{2\pi\hbar} \sum_{jj'} \int_{-\infty}^{\infty} \langle exp(-i\boldsymbol{Q}.\boldsymbol{R}_{j'}(0)) exp(i\boldsymbol{Q}.\boldsymbol{R}_j(t))\rangle \times exp(-i\omega t)dt \tag{2.34}$$

$$\left(\frac{d^2\sigma}{d\Omega\, dE'}\right)_{inc} = \frac{\sigma_{inc}}{4\pi}\frac{\boldsymbol{k}'}{\boldsymbol{k}}\frac{1}{2\pi\hbar} \sum_{j} \int_{-\infty}^{\infty} \langle exp(-i\boldsymbol{Q}.\boldsymbol{R}_{j}(0)) exp(i\boldsymbol{Q}.\boldsymbol{R}_j(t))\rangle \times exp(-i\omega t)dt \tag{2.35}$$

where

$$\sigma_{coh} = 4\pi(\bar{b})^2, \qquad \sigma_{inc} = 4\pi\{\bar{b^2} - (\bar{b})^2\} \tag{2.36}$$

For coherent inelastic scattering, the interference between waves produced by the scattering of a single neutron from all the nuclei in a sample is described. The intensity of scattering for coherent scattering depends strongly on scattering angle. Incoherent scattering assumes that scattered waves from different nuclei sum to zero so that the observed scattering is all self scattering. The lack of interference from different nuclei makes incoherent scattering a good tool for studying the motions of atomic tracer diffusion, averaged over the system. Elastic incoherent scattering is isotropic, so the scattering angle does not affect the intensity. This makes the coherent scattering component easy to separate from the incoherent.

As mentioned after equation (2.12) the choice of a negative sign in the spherical wavefunction results from the normal situation with hard sphere scattering, that is a repulsive potential which gives rise to a phase change. Some isotopes such as ^{1}H have an attractive potential resulting in a negative scattering length.

2.3 Crystal Structure and Lattices

This project is focused on materials properties and characterisation. It is helpful therefore to give an explanation of the conventions for describing the structure of a crystalline material. To this end, a short background on crystallography is provided. For a more in-depth introduction see Dove[16].

2.3.1 The Lattice and Atomic Basis

Crystalline materials are periodic in nature and contain symmetries in the arrangement of atoms in the material. This allows for clearly defined diffraction patterns. The structure of crystalline materials can be explained in terms of a lattice. Lattices are constructed of a series of points which are periodic and can cover all space without gaps. They should be described completely by three basis vectors, here known as $\boldsymbol{a}, \boldsymbol{b}$ and $\boldsymbol{c}$, which allow a linear combination of the basis vectors to describe the vector between any two points on the lattice, such that

$$\boldsymbol{t}_{UVW} = h\boldsymbol{a} + k\boldsymbol{b} + l\boldsymbol{c} \tag{2.37}$$

where *h,k,l* are integers. The vector $\boldsymbol{t}_{hkl}$ can be represented by the short hand *hkl* such that a direction through a symmetric lattice can be defined. For example the 100 plane in a cubic lattice which is normal to the 100 direction.

Figure 2.3: 100 plane of a cubic lattice[17]

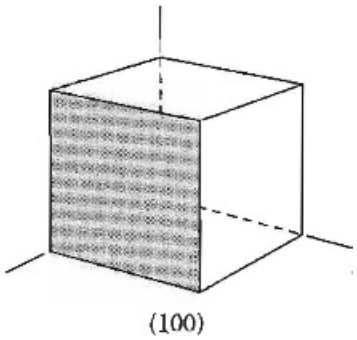

Crystalline materials are defined by their lattice and the basis of atoms in that lattice. For example NaCl has a simple cubic lattice with Na and Cl atom basis arranged alternately on the corners of the lattice.

2.3.2 Lattice Geometry

Following from symmetry concerns fourteen Bravais lattices are defined. The Bravais lattices are generally defined in terms of their lattice parameters, but symmetry must also be taken into account when fully explaining the origin of Bravais lattices. Lattices are also defined in terms of space groups of which there are 230 derived from the 14 Bravais lattices, again they arise from symmetries and require group theory to fully explain. Space groups are labelled either by number or by systems such as Hermann-Mauguin notation otherwise known as international notation which is used to describe the lattice structures in this work.

Bravais lattices can be described by the centreing of their lattice points. For example primitive cells only have lattice points on the corners of the cell whereas face centred lattices have an additional point in the centre of the face of cell. In the table below P is the primitive lattice, I is a body centred lattice with a point at the centre of the lattice cell, F is the face centred lattice and base centred lattices have points at alternate ends of the lattice cell and are denoted by B.

Figure 2.4: Examples of lattice centreing in cubic lattices[17]

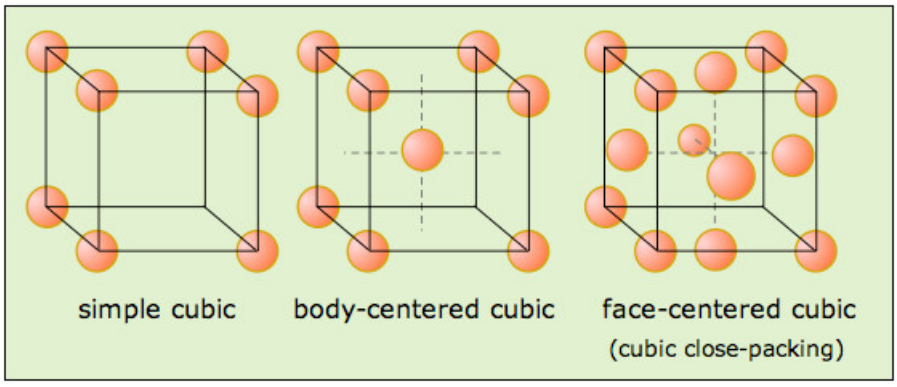

The structure of the materials in the following chapters will be described in terms of Hermann-Mauguin notation. This notation first describes the centreing of the Bravais lattice. For example the hexagonal lattice present in graphite

Table 2.1: The Fourteen Bravais lattices and associated space groups

Name	Types	Geometry	Space Groups
Triclinic	P	$a \neq b \neq c; \alpha \neq \beta \neq \gamma$	1-2
Monoclinic	P, B	$a \neq b \neq c; \alpha = \gamma = 90 \neq \beta$	3-15
Orthorhombic	P, B, I, F	$a \neq b \neq c; \alpha = \beta = \gamma = 90$	16-74
Tetragonal	P, I	$a = b \neq c; \alpha = \beta = \gamma = 90$	75-142
Rhombohedral	P	$a = b = c; \alpha = \beta = \gamma \neq 90$	143-167
Hexagonal	P	$a = b \neq c; \alpha = \beta = 90, \gamma = 120$	168-194
Cubic	P, I, F	$a = b = c; \alpha = \beta = \gamma = 90$	195-230

is P 6_3/mmc. Thus P represents a primitive lattice, the rest of the notation describes the symmetry elements of the lattice. The symmetry elements can be separated such that 6_3/m, m and c represent different symmetry planes in the lattice. 6_3/m is a 6_3/ screw axis with a perpendicular mirror plane and the letters m and c describe other mirror and glide planes in the lattice.

2.3.3 Identifying Crystals

The structure of a crystalline material can be explored using a diffraction pattern. The diffraction pattern of a purely crystalline material will be in the form of a series of points, in the case of a 2D diffraction pattern or peaks in the case of a diffraction spectrum. As the particles diffracted by the material interact with planes of atoms rather than individual atoms, these peaks are related to the planes in the lattice. Relating the planes in the lattice to the points in a diffraction measurement leads to the concept of a reciprocal lattice, using the diffraction peaks as a basis to discover the structure of the reciprocal lattice. This gives a mathematical representation of the planes of atoms in a real lattice. Therefore the reciprocal lattice aids interpretation of diffraction data. It also simplifies calculations involving planes or surfaces and is necessary for describing the waves and vibrations within the material.

Mathematically the reciprocal lattice is defined as

$$e^{i\boldsymbol{G}\cdot\boldsymbol{R}} = 1 \tag{2.38}$$

where $e^{i\boldsymbol{G}\cdot\boldsymbol{R}}$ is a wave with the same periodicity of vector points depicted by $\boldsymbol{R}$ of the Bravais lattice, and $\boldsymbol{G}$ is the reciprocal lattice which arises from a set of vectors which satisfy equation (2.38). The reciprocal lattice will be a Bravais lattice. Taking the reciprocal of a reciprocal lattice gives the original lattice.

The three basis vectors of the reciprocal lattice are mathematically determined from the basis vectors $\boldsymbol{a}, \boldsymbol{b}$ and $\boldsymbol{c}$.

$$\boldsymbol{a}^* = 2\pi \frac{\boldsymbol{b} \times \boldsymbol{c}}{\boldsymbol{a} \cdot \boldsymbol{b} \times \boldsymbol{c}} \tag{2.39}$$

$$\boldsymbol{b}^* = 2\pi \frac{\boldsymbol{a} \times \boldsymbol{c}}{\boldsymbol{a} \cdot \boldsymbol{b} \times \boldsymbol{c}} \tag{2.40}$$

$$\boldsymbol{c}^* = 2\pi \frac{\boldsymbol{a} \times \boldsymbol{b}}{\boldsymbol{a} \cdot \boldsymbol{b} \times \boldsymbol{c}} \tag{2.41}$$

Where $\boldsymbol{a} \cdot \boldsymbol{b} \times \boldsymbol{c}$ is the volume of the unit cell. The factor 2π is not always included by crystallographers.

2.3.4 Powder Diffraction

The interaction of waves with planes in the lattice is known as Bragg's law and is described thus

$$N\lambda = 2d \sin\theta \tag{2.42}$$

Where N is an integer specifying the number of the wavelength λ, d is the distance between planes and θ is the direction of the scattering vector $\boldsymbol{Q}$. The conditions of Bragg's law must be met for diffraction peaks to be observed.

Figure 2.5: Bragg's law for planes of atoms in a lattice[17]

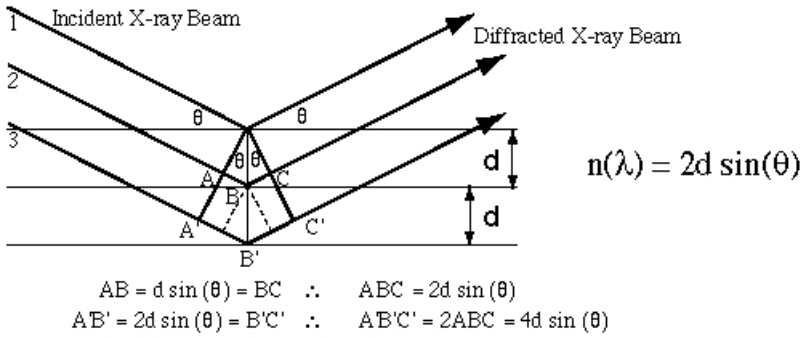

Historically samples for X-ray diffraction were in the form of large single crystals, often grown specifically for structural analysis. It is not always possible to create these samples but fine powders can be manufactured for most materials. In this case powder diffraction can be used, this form of diffraction has several factors which should be taken into account when interpreting powder diffraction data.

In the case of single crystals the orientation of the crystal in relation to the incoming beam dictates which planes are scattered from. In the case of powder samples the crystal directions are averaged over all directions. Thus rather than a set of diffraction points, cones of scattering are created known as Debye-Scherrer Cones. These lead to circles of scattering intensities when viewed perpendicular to the direction of scattering.

In theory powder samples should lead to a complete insensitivity to the orientation of the sample with respect to the incoming beam, however the shape of the powder particles can lead to preferred orientation of the crystal so this must be kept in mind, especially when interpreting the intensities of diffrac-

Figure 2.6: Debye-Scherrer cones from a randomly orientated powder sample[18]

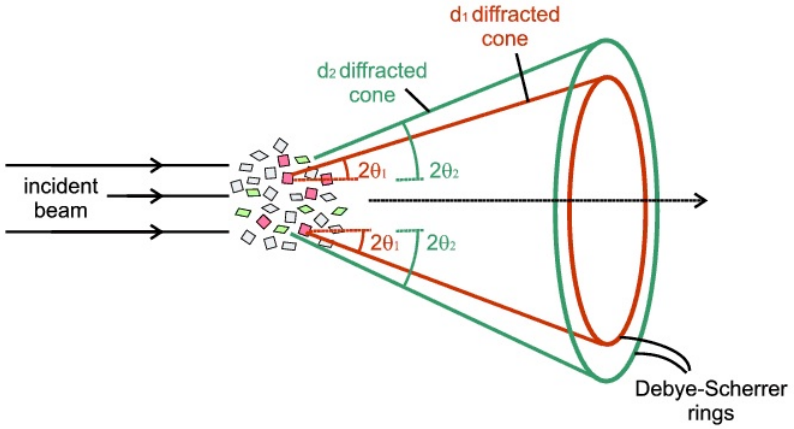

tion peaks. XRD machines can be set up in transmission or reflection modes, in Bragg-Brentano geometry, which is typical, lattice planes are measured parallel to the sample surface. Neutron diffraction is more commonly performed in transmission.

The width of diffraction peaks can be affected by the range of widths of planes in the material, and thus the inhomogeneous strain in the material which will lead to differing plane widths. The peak width is also affected by crystallite size. Relationships between the Bragg angle θ and broadening allow us to investigate these two contributions. Ignoring strain gives the Scherrer formula for crystallite size

$$\beta_\tau = \frac{K\lambda}{\tau \cos\theta} \tag{2.43}$$

where τ is average crystallite size, K is a factor related to crystallite shape, usually a value of 0.9 is used, λ is the incident wavelength, β_τ is the peak broadening at full width half maximum and θ is the Bragg angle.

It is also possible to consider only the broadening due to strain β_ε, which is

given by the Stokes and Wilson equation

$$\beta_\varepsilon = C\varepsilon \tan\theta \tag{2.44}$$

where C is a constant related to the nature of the strain and is usually around 4 or 5, ε is the inhomogeneous strain in the sample, θ is again the Bragg angle.

Given these two equations for broadening caused by strain and crystallite size we can combine them to get an expression for total broadening.

$$\beta_{tot} = C_\varepsilon \tan\theta + \frac{K\lambda}{\tau \cos\theta} \tag{2.45}$$

A line graph of the form $y = mx + c$ can be created by multiplication of $\cos\theta$

$$\beta_{tot} \cos\theta = C_\varepsilon \tan\theta + \frac{K\lambda}{\tau} \tag{2.46}$$

This method of broadening analysis is known as the Williamson Hall method and the line graph described is a Williamson Hall plot.

2.4 Phonons

The primitive cell of a reciprocal lattice is know as the Brillouin zone. It can be found by taking surfaces at the same distance from one element of the reciprocal lattice and its neighbours. The volume included is the first Brillouin zone. The primitive cell of a real lattice can also be found in the same way, in this case it is know as the Wigner-Seitz cell.

The Brillouin zone aids understanding of crystallography and simplifies concepts in phonon physics.

Figure 2.7: First Brillouin zone of a 2D lattice[17]

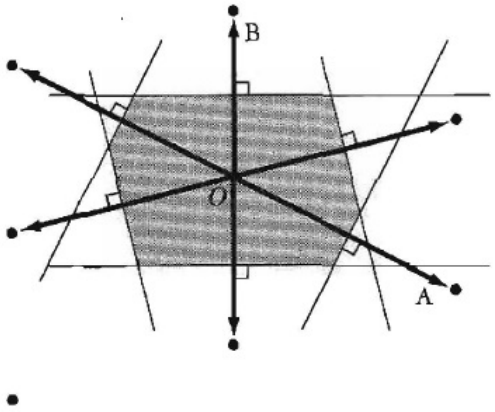

The atoms in real materials undergo constant vibrations. These vibrations are linked to the other atoms in the lattice and so the movements can be interpreted in terms of lattice vibrations. In the simplest possible system of linked atoms, a 1-D chain of atoms with a spring like force between them, the displacement of each atom is u_l. The force on the atom at origin F_{0l} due to the lth atom will be proportional to $u_l - u_0$

thus

$$F_{0l} = \gamma_l(u_l - u_0) \tag{2.47}$$

where γ_l is a force constant between the atoms 0 and l.

So the total force acting on atom 0 is

$$F_0 = \sum F_{0l} = \sum_{l \neq 0} \gamma_l(u_l - u_0) \tag{2.48}$$

and the equation of motion for atom 0 is

$$m\frac{\delta^2 u_n}{\delta t^2} = F_0 = \sum F_{0l} = \sum_{l \neq 0} \gamma_l(u_l - u_0) \tag{2.49}$$

As each vibration of an atom will affect the others, a representation for the collective oscillations of the atoms must be found. The most simple representation assumes these are normal modes and that they take the form of waves such that

$$u(x) = Ae^{i(\omega t - \boldsymbol{q}x)} \tag{2.50}$$

where $\boldsymbol{q} = \frac{2\pi}{\lambda}$ and ω is the frequency of the wave.

As this is a quantum mechanical system the amplitude A is quantised.

So for the lth atom $u(x)$ becomes

$$u(l) = Ae^{i(\omega t - \boldsymbol{q}la)} \tag{2.51}$$

where a is the distance between atoms.

Substitution of this condition into the equation of motion for atom 0 confirms that the waves are normal modes. Thus the frequencies of the modes can be found.

$$-Am\omega^2 e^{i\omega t} = \sum_{l \neq 0} \gamma_l A(e^{i(\omega t - \boldsymbol{q}la)} - e^{i\omega t}) \tag{2.52}$$

removing $Ae^{i\omega t}$ from both sides gives

$$-m\omega^2 = \sum_{l \neq 0} \gamma_l (e^{i\boldsymbol{q}la} - 1) \tag{2.53}$$

As all the atoms are identical $\gamma_l = \gamma_{-l}$, meaning that positive and negative powers of e can be combined in pairs of terms with positive and negative l.

$$e^{ix} + e^{-ix} = 2\cos x \tag{2.54}$$

The summation thus becomes one over $l > 0$, when adding together the pair terms.

$$-m\omega^2 = \sum_{l>0} \gamma_l (2\cos \boldsymbol{q} la - 2) \tag{2.55}$$

Dividing through by 2 and m gives the equation in terms of ω.

$$\omega^2 = \frac{2}{m} \sum_{l>0} \gamma_l (1 - \cos \boldsymbol{q} la) \tag{2.56}$$

If we only consider nearest neighbour forces $\gamma_1 = \gamma$, $\gamma_2 = \gamma_3 = ... = 0$. This reduces the summation for ω^2 to a single term

$$\omega^2 = \frac{2\gamma}{m} (1 - \cos \boldsymbol{q} a) \tag{2.57}$$

Using the double angle expansion $\cos 2x = 1 - 2\sin^2 x$ and treating $\boldsymbol{q}a$ as a double angle gives

$$\omega^2 = \frac{2\gamma}{m} . 2\sin^2 \frac{1}{2} \boldsymbol{q} a \tag{2.58}$$

thus

$$\omega = 2\sqrt{\frac{\gamma}{m}} \left| \sin \frac{1}{2} \boldsymbol{q} a \right| \tag{2.59}$$

Lattice vibrations with a quantised frequency are known as phonons. They have a wavevector $\boldsymbol{q}$ and an angular frequency ω. The graph of frequency ω verses wavevector $\boldsymbol{q}$ is known as a dispersion curve. These curves are related

to the graphs obtained from a poly-CINS experiment. In a periodic lattice, two waves with wavevectors q and q' that differ only by a reciprocal lattice vector have the same properties. They will produce identical displacements at each lattice position. Thus only wavevectors that differ within a reciprocal lattice vector contain unique information. This property is equivalent to the Brillouin zone of a lattice, thus dispersion curves can be represented in terms of Brillouin zone boundaries. All vibrations can be seen as equivalent to a vibration in the Brillouin zone.

Atoms move in different ways depending on the forces acting on them. They can move in the direction of wave propagation, known as *longitudinal* motion. Movement at right angles to the wave is known as *transverse* motion. If the material contains more than one kind of atom they may react in different ways to the propagation of the waves. If the motion of the different types of atom are in phase, at long wavelength, this is known as an *acoustic* mode. If the different atoms are in anti-phase this is known as an *optic* mode. Below is a theoretical phonon dispersion curve which represents the motion of a line of atoms, where alternate atoms differ in mass. We can see that two forms of motion, or modes, are possible in this case.

Figure 2.8: Simple dispersion curves[17]

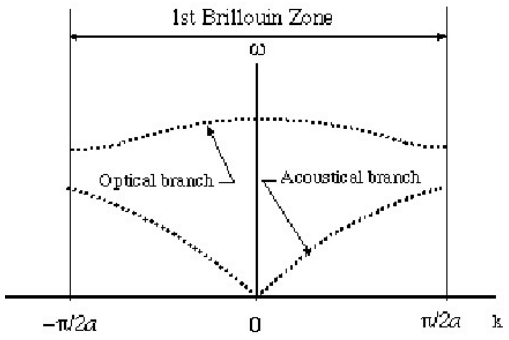

For real structures the dispersion curves become much more complicated. In figure (2.9) experimental dispersion data for silicon is shown and the modes

are labelled. For example LO is a Longitudinal Optic mode.

Figure 2.9: Experimentally determined dispersion curves of crystalline silicon[19]

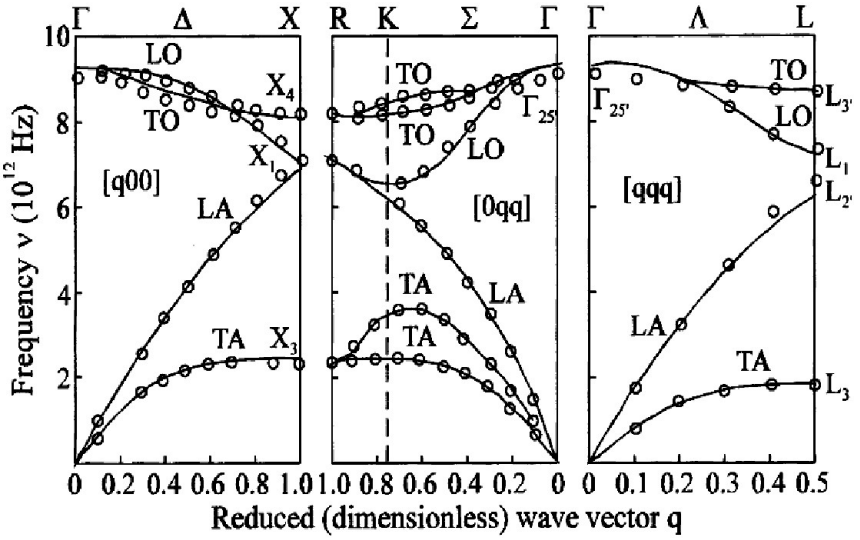

When interpreting data the labelling of modes is not a trivial task. The use of models and theoretical dispersion curves becomes very important.

The calculation of dispersion curves is dependent on accurate models for the forces in a system. Forces are typically modelled as a system of force constants describing the relationship between any atom in the system and its near neighbours. These force constants can be derived from density functional code, thus giving unbiased non-empirical data for the system, or from lattice dynamics calculations using force constant models derived from the observed interactions between atoms. Both of these approaches have their disadvantages. In general performing DFT calculations is time consuming and behaviours which occur above the ground state energy can be poorly modelled, as can weak forces such as the bonding between graphite layers. Lattice dynamics calculations using force constant models are typically much faster to perform, but are much more reliant on the accuracy of the model they are based on.

2.4.1 The Debye Waller Factor

If we treat the scattering system as a crystal phonon interactions are introduced. This leads to the inclusion of the phonon terms due to normal modes such as $\boldsymbol{q}$ the wavevector of the mode. We will also define ω_p as the angular frequency of the phonon mode, $\boldsymbol{e}_p$ its polarisation vector, $\boldsymbol{l}$ is a lattice vector and $\boldsymbol{u}_l$ is the displacement of the atom from its equilibrium position.

Functions V and U are defined to be

$$V = i\boldsymbol{Q}.\boldsymbol{u}_l(t) = i\sum_p h_p a_p + h_p^* a_s^+ \tag{2.60}$$

$$U = -i\boldsymbol{Q}.\boldsymbol{u}_0(0) = -i\sum_p g_p a_p + g_p^* a_s^+ \tag{2.61}$$

where

$$h_p = \left(\frac{\hbar}{2NM}\right)^{1/2} \frac{\boldsymbol{Q}.\boldsymbol{e}_p}{\sqrt{\omega_p}} exp\{i(\boldsymbol{q}.\boldsymbol{l} - \omega_s t)\} \tag{2.62}$$

$$g_s = \left(\frac{\hbar}{2NM}\right)^{1/2} \frac{\boldsymbol{Q}.\boldsymbol{e}_p}{\sqrt{\omega_p}} \tag{2.63}$$

The UV notation is related to photon creation and annihilation operators.

From the phonon interactions we can obtain an important result.

Here we show equations of coherent and incoherent scattering when in a crystal system in terms of U and V. In these equations N is the number of nuclei in the crystal.

$$\left(\frac{d^2\sigma}{d\Omega\, dE'}\right)_{coh} = \frac{\boldsymbol{k}'}{\boldsymbol{k}} \frac{1}{2\pi\hbar} \sum_l (\bar{b})^2 N exp\langle U^2\rangle \sum_l exp(i\boldsymbol{Q}.l) \int_{-\infty}^{\infty} exp(UV) exp(-i\omega t) dt \tag{2.64}$$

The term U^2 is known as the Debye Waller factor and is typically represented as

$$2W = -\langle U^2 \rangle = \frac{\hbar}{2MN} \sum_s \frac{(\boldsymbol{Q}.e_s)^2)}{\omega_s} \langle 2n_s + 1 \rangle \tag{2.65}$$

Where $\langle U^2 \rangle$ is the mean square displacement of the atom from the centre of its motion. A standard result for the expansion of the $\langle 2n_s + 1 \rangle$ term for an isotropic oscillator is

$$\langle 2n_s + 1 \rangle = \coth\left(\frac{1}{2}\hbar\omega_s\beta\right) \tag{2.66}$$

this gives the Debye Waller factor as

$$2W = \frac{\hbar}{2MN} \sum_s \frac{(\boldsymbol{Q}.e_s)^2}{\omega_s} \coth\left(\frac{1}{2}\hbar\omega_s\beta\right) \tag{2.67}$$

The Debye Waller factor is an important effect in both coherent neutron scattering and x-ray scattering. Physically it takes into account the thermal motion of atoms, leading to a suppression of intensity in scattering peaks with increasing $\boldsymbol{Q}$.

2.5 Inelastic Neutron Scattering

2.5.1 $S(\boldsymbol{Q}, \omega)$

An important quantity in neutron scattering experiments is the scattering function $S(\boldsymbol{Q}, \omega)$. This quantity comes from using Van Hove[20] correlation functions in terms of scattering cross-sections. Converting experimental results to $S(\boldsymbol{Q}, \omega)$ data allows more direct comparison with phonon dispersion curves

and more importantly allows comparison between experiments as it removes experiment dependent factors such as the angular range or initial energy of the instrument.

Starting with an expression for the coherent double differential cross-section

$$\left(\frac{d^2\sigma}{d\Omega dE'}\right)_{coh} = \frac{\sigma_{coh}}{4\pi}\frac{\boldsymbol{k}'}{\boldsymbol{k}}\frac{1}{2\pi\hbar}\int\sum_{jj'}\langle exp\{-i\boldsymbol{Q}.\boldsymbol{R}_{j'}(0)\}exp\{i\boldsymbol{Q}.\boldsymbol{R}_j(t)\}\rangle \times exp(-i\omega t)dt \tag{2.68}$$

we take a function I to be

$$I(\boldsymbol{Q},t) = \frac{1}{N}\sum_{jj'}\langle exp\{-i\boldsymbol{Q}.\boldsymbol{R}_{j'}(0)\}exp\{i\boldsymbol{Q}.\boldsymbol{R}_j(t)\}\rangle \tag{2.69}$$

we then define a function G as

$$G(\boldsymbol{r},t) = \frac{1}{(2\pi)^3}\int I(\boldsymbol{Q},t)exp(-i\boldsymbol{Q}.\boldsymbol{r})dk \tag{2.70}$$

and a function S as

$$S(\boldsymbol{Q},\omega) = \frac{1}{2\pi\hbar}\int I(\boldsymbol{Q},t)exp(i\omega t)dt \tag{2.71}$$

We can obtain the inverse relations for the equations using Fourier transforms

$$I(\boldsymbol{Q},t) = \int G(\boldsymbol{r},t)exp(-i\boldsymbol{Q}.\boldsymbol{r})dr \tag{2.72}$$

$$I(\boldsymbol{Q},t) = \hbar\int S(\boldsymbol{Q},\omega)exp(i\omega t)d\omega \tag{2.73}$$

this gives us relationships between G and S.

$$G(\boldsymbol{r},t) = \frac{1}{(2\pi)^3}\int S(\boldsymbol{Q},\omega)exp\{-i(\boldsymbol{Q}.\boldsymbol{r}-\omega t)\}d\boldsymbol{Q}\;d\omega \tag{2.74}$$

$$S(\boldsymbol{Q},\omega) = \frac{1}{2\pi\hbar}\int G(\boldsymbol{r},t)exp(-i(\boldsymbol{Q}.\boldsymbol{r}-\omega t))d\boldsymbol{r}\;dt \tag{2.75}$$

We now define a quantity called the self intermediate function by

$$I_s(\boldsymbol{Q},t) = \frac{1}{N}\sum_j \langle exp\{-i\boldsymbol{Q}.\boldsymbol{R}_j(0)\}exp\{i\boldsymbol{Q}.\boldsymbol{R}_j(t)\}\rangle \tag{2.76}$$

Using the relationship between S and I gives

$$S_i(\boldsymbol{Q},\omega) = \frac{1}{2\pi\hbar}\int I_s(\boldsymbol{Q},t)exp(-i\omega t))dt \tag{2.77}$$

This now allows us to substitute $S(\boldsymbol{Q},\omega)$ into cross-section expressions

$$\left(\frac{d^2\sigma}{d\Omega\,dE'}\right)_{coh} = \frac{\boldsymbol{k}'}{\boldsymbol{k}}\frac{(\bar{b})^2}{2\pi\hbar}NS(\boldsymbol{Q},\omega) \tag{2.78}$$

$$\left(\frac{d^2\sigma}{d\Omega\,dE'}\right)_{inc} = \frac{\boldsymbol{k}'}{\boldsymbol{k}}\frac{(\bar{b^2}-(\bar{b})^2)}{2\pi\hbar}NS_i(\boldsymbol{Q},\omega) \tag{2.79}$$

We can now see that the function $S(\boldsymbol{Q},\omega)$ and $S_i(\boldsymbol{Q},\omega)$ are closely related to the coherent and incoherent scattering cross-sections. Plotting neutron scattering experiments in terms of $S(\boldsymbol{Q},\omega)$ gives a plot which shows phonon curves and more importantly removes instrument and experiment based factors allowing direct comparison between experiments taken at different locations and under different conditions.

2.5.2 The Principle of Detailed Balance

Using an expression for the scattering cross-section with explicit energy terms leads to an important result in scattering physics

$$\left(\frac{d^2\sigma}{d\Omega dE'}\right)_{coh} = \frac{\sigma_{coh}}{4\pi}\frac{\boldsymbol{k}'}{\boldsymbol{k}}\sum_{\mu} p_\mu \sum_{\mu'} |\sum_j \langle \mu' | exp(i\boldsymbol{Q}.\boldsymbol{R}_j)|\mu\rangle|^2 \partial(E_\mu - E_{\mu'} + \hbar\omega) \quad (2.80)$$

thus $S(\boldsymbol{Q},\omega)$ becomes

$$S(\boldsymbol{Q},\omega) = \frac{1}{NZ}\sum_{\mu'\mu} exp(-E_\mu\beta)|\sum_j \langle \mu' | exp(i\boldsymbol{Q}.\boldsymbol{R}_j)|\mu\rangle|^2 \partial(E_\mu - E_{\mu'} + \hbar\omega) \quad (2.81)$$

substituting $S(\boldsymbol{Q},\omega)$ with $S(-\boldsymbol{Q},-\omega)$ gives

$$\begin{aligned} S(-\boldsymbol{Q},-\omega) &= \frac{1}{NZ}\sum_{\mu'\mu} exp(-E_{\mu'}\beta)|\sum_j \langle \mu' | exp(-i\boldsymbol{Q}.\boldsymbol{R}_j)|\mu'\rangle|^2 \partial(E_\mu - E_{\mu'} - \hbar\omega) \\ &= exp\{-(E_{\mu'} - E_\mu)\beta\}\frac{1}{NZ}\sum_{\mu\mu'} exp(-E_\mu\beta)|\sum_j \langle \mu' | exp(i\boldsymbol{Q}.\boldsymbol{R}_j)|\mu\rangle|^2 \\ &\times \delta(E_\mu - E_{\mu'} + \hbar\omega) \\ &= exp(-\hbar\omega\beta)S(\boldsymbol{Q},\omega) \end{aligned} \quad (2.82)$$

$$S(-\boldsymbol{Q},-\omega) = exp(-\hbar\omega\beta)S(\boldsymbol{Q},\omega) \quad (2.83)$$

Equation (2.83) tells us the relationship for the cross-section, between the en-

ergy lost and the energy gained by the neutron in inelastic scattering. It shows that the chance of a neutron gaining energy from the lattice is lower than the chance of the neutron losing energy to the lattice, by a factor of $exp(-\hbar\omega\beta)$. Physically this can be taken as a consequence of the fact that, regardless of the energy of the lattice it can always gain energy but it needs to have certain minimum energy to be able to impart some to a scattered neutron.

2.6 Neutron Scattering Instruments

Neutron scattering experiments give information about scattering cross-sections, scattering lengths and can be used to provide $S(\boldsymbol{Q}, \omega)$ plots.

There are two ways of producing neutrons with high enough flux for scattering experiments. The first is to use a High Flux Beam Reactor, these reactors are specifically designed to produce a high flux beam of neutrons at useful energies for neutron scattering experiments. The alternative to using a nuclear reactor is to use a particle accelerator in combination with a suitable material to create a spallation source.

In both cases neutrons are typically created at higher energies than are useful for materials research so the energy of the neutrons is reduced by the use of neutron moderators. The thermal neutrons suitable for lattice dynamic and lattice structure investigations require different moderators to those for neutrons needed at higher and lower energies, known as hot ($\approx$ 2000 K) and cold neutrons ($\approx$ 20 K), the different neutron energies give different wavelengths and are therefore useful for probing different scales. In the case of the ILL, a reactor source, liquid D_2 is used as a moderator to produce cold neutrons, liquid D_2O for thermal neutrons and graphite for hot neutrons. Spallation sources produce higher energy neutrons and typically use solid methane, solid hydro-

gen or a combination for moderation. Moderation produces neutrons with a range of energies similar to a Maxwell Boltzmann distribution.

Some experiments use this white beam of neutrons but monochromation is also often used after moderation to select neutrons with a specific energy. Monochromation techniques are discussed later in the chapter.

Inelastic neutron scattering can be measured by using a triple axis spectrometer (TAS) or a time of flight (TOF) technique. Triple axis spectrometers are best used when information on excitations in single crystals is sought, at well defined points or along a given direction in $\boldsymbol{Q}$ space. In a triple axis spectrometer the experiment is set up such that one energy transfer is chosen by varying the initial wavevector of the neutron whilst keeping $\boldsymbol{Q}$ constant[21], giving measurements of ω peaks. This method gives a high flux but is relatively inflexible and time consuming if many different $\boldsymbol{Q}$ values are needed.

Figure 2.10: A diagram of triple axis spectrometer[22]

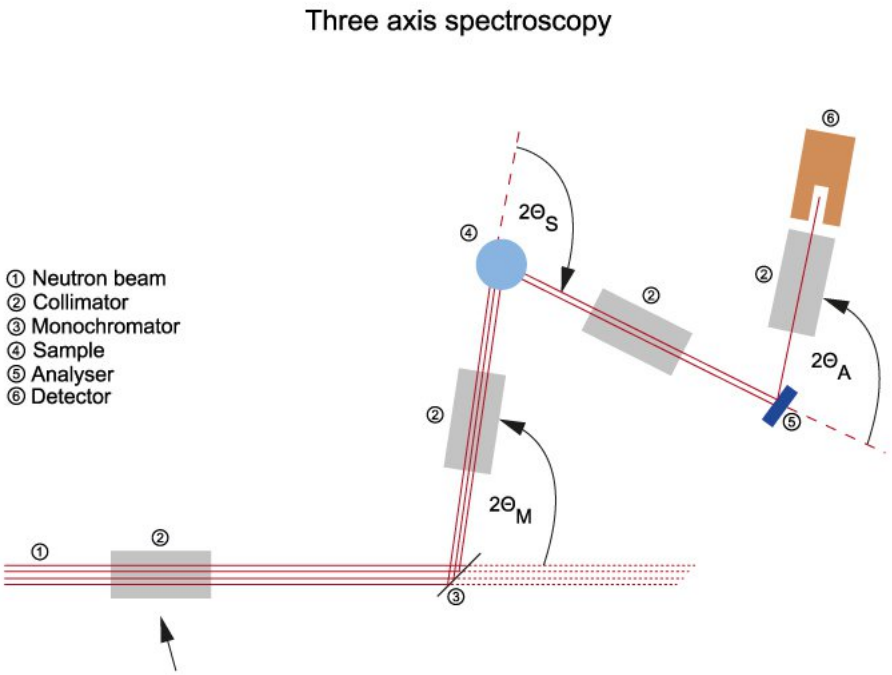

Time of flight techniques give a global overview of excitations in a broad Q, ω range and are suitable for analysing powder samples. All pulsed spallation sources use time of flight techniques to measure material properties. The experiments in the later chapters were performed using TOF spectrometers due to the powdered nature of the sample and the need for an broad overview of excitations, we will therefore discuss TOF spectroscopy and instruments in more detail.

2.6.1 Time of Flight Spectroscopy

A time of flight spectrometer can be described as either direct or indirect.

Figure 2.11: A diagram of direct geometry and indirect geometry spectrometers[23]

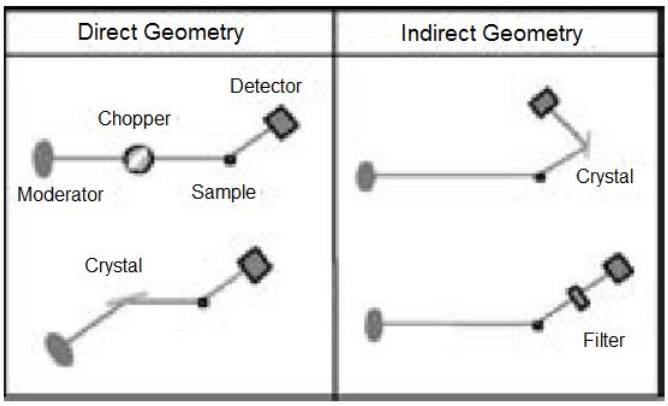

A direct geometry spectrometer defines the incident energy of the neutron by the use of synchronised choppers or a crystal and the final energy is determined by time of flight. An indirect geometry spectrometer illuminates the sample with a white pulse of neutrons. The final energy is defined by a crystal or filter, the initial energy is found from the time of flight of the neutron from source to sample.

Choppers are a mechanical means of selecting energies in a neutron beam. Unlike other methods such as monochromating crystals, choppers can be tuned

by varying their speed to select a range of energies. There are two main forms of choppers, Fermi choppers and disk choppers.

Figure 2.12: Diagrams of neutron choppers

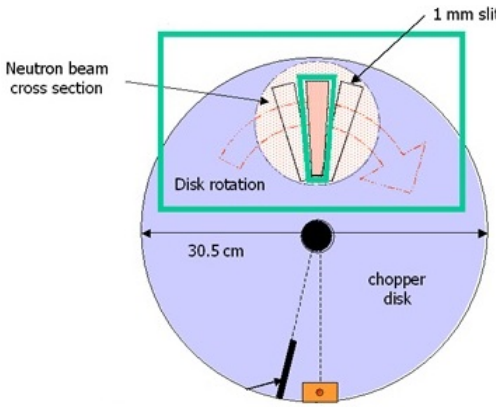

(a) Diagram of a disc chopper. The neutron beam is perpendicular to the surface of the disk[24]

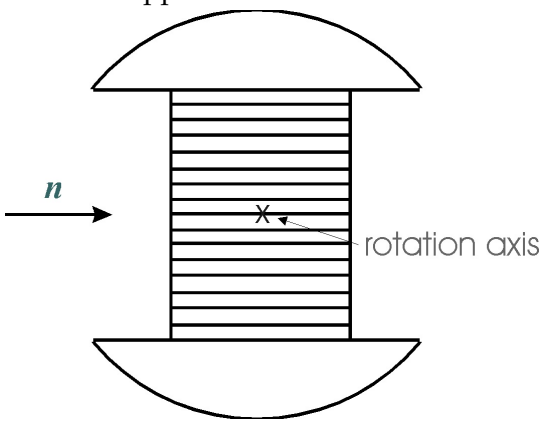

(b) Diagram of a Fermi chopper, the direction of the neutron beam is shown by n[25]

Fermi choppers are rotating drums with a hole along the diameter. The hole is filled with layers of alternating absorbing and transmitting material. Pulses are produced when the axis of the slit is parallel to the incident neutron direction. The chopper is arranged with an axis of spin normal to the incident neutron direction. Disk choppers are simply rotating disks with holes at or near the circumference to allow the transmission of some neutrons. Disk choppers and Fermi choppers are equally flexible in selection of E. Both Fermi and disc choppers are subject to a maximum rotational speed determined by the mechanical strength of the structure, this effect is typically more of a problem for disk choppers. An advantage of disk choppers is that they will transmit any neutron velocity, Fermi choppers will not transmit slow neutrons because the slit closes while the neutron is inside it, unless the slits are curved.

The parameters of interest for inelastic neutron scattering are energy and momentum transfer $\hbar\omega$ and $\hbar\boldsymbol{Q}$ respectively. Not all regions of $\boldsymbol{Q}, \omega$ space are accessible to neutron detectors. The scattering triangles below demonstrate

the trajectories of Q, ω .

Figure 2.13: Scattering triangles for a direct geometry and indirect geometry spectrometer[23]

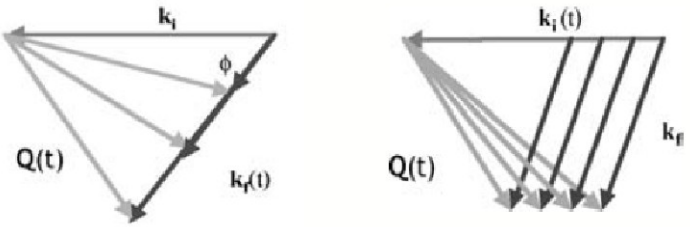

The cosine rule is then applied to find Q

$$Q^2 = k^2 + k'^2 - 2kk' \cos\phi \tag{2.84}$$

Remembering that $Q = k - k'$ and $\hbar\omega = E - E'$. This equation can be converted to energy by substituting in the expression for k

$$\frac{\hbar^2 Q^2}{2m} = E + E' - 2(EE')^{1/2} \cos\phi \tag{2.85}$$

for direct geometry E' can be eliminated giving

$$\frac{\hbar^2 Q^2}{2m} = 2E - \hbar\omega - 2\cos\phi(E(E - \hbar\omega))^{1/2} \tag{2.86}$$

for indirect geometry E can be eliminated leaving

$$\frac{\hbar^2 Q^2}{2m} = 2E' + \hbar\omega - 2\cos\phi(E'(E' + \hbar\omega))^{1/2} \tag{2.87}$$

Thus each detector has a parabolic trajectory through Q, ω space. For direct geometry spectrometers large arrays of detectors are used to show large areas of Q ω space. For indirect geometry spectrometers the parabola are inverted

Figure 2.14: Parabola of direct and indirect geometries

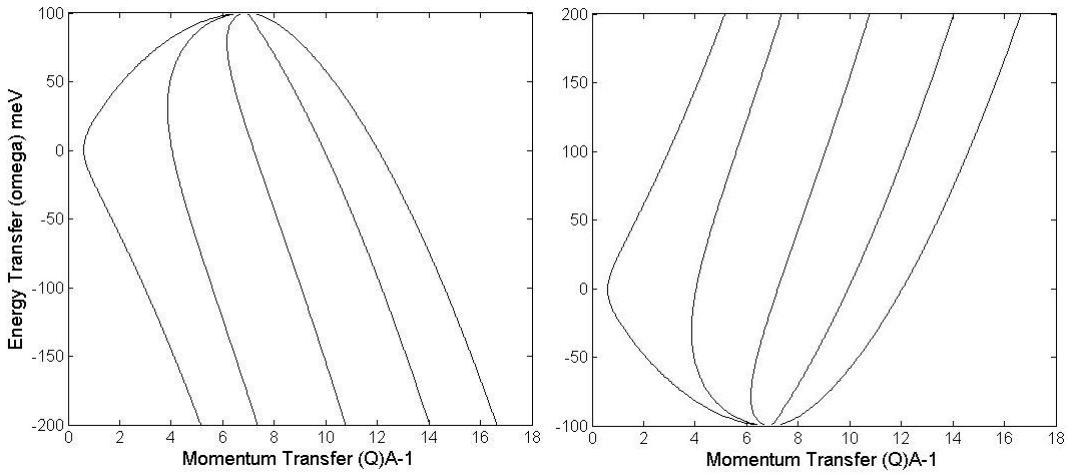

so they show a wide range of energy transfers from the energy loss side of the spectrum. The maximum energy transfer for neutron energy loss is E, the initial energy of the neutrons. This comes at $\boldsymbol{Q} = \boldsymbol{k}$, and for large neutron energy gain $\boldsymbol{Q}$ tends to $\boldsymbol{k}'$.

2.6.2 Instrument Details

Here we can see the layout of a typical neutron scattering centre. The neutrons in this case are produced in a reactor, beams of neutrons are then split and sent to various experiments.

When deciding which experiment would be most suitable for the study of a sample there are several factors which need to be taken into account. For poly-CINS measurements it is necessary to use an experiment which has been designed for measuring inelastic scattering. The angular range of detectors affects how much of $\boldsymbol{Q}, \omega$ space is visible. Detectors also vary in their resolution. Neutron flux varies slightly from experiment to experiment but mainly from centre to centre. Reactors produce a constant beam of relatively low flux, whereas the flux from spallation sources is relatively high in the pulse but can

Figure 2.15: Floor plan of HZB[26]

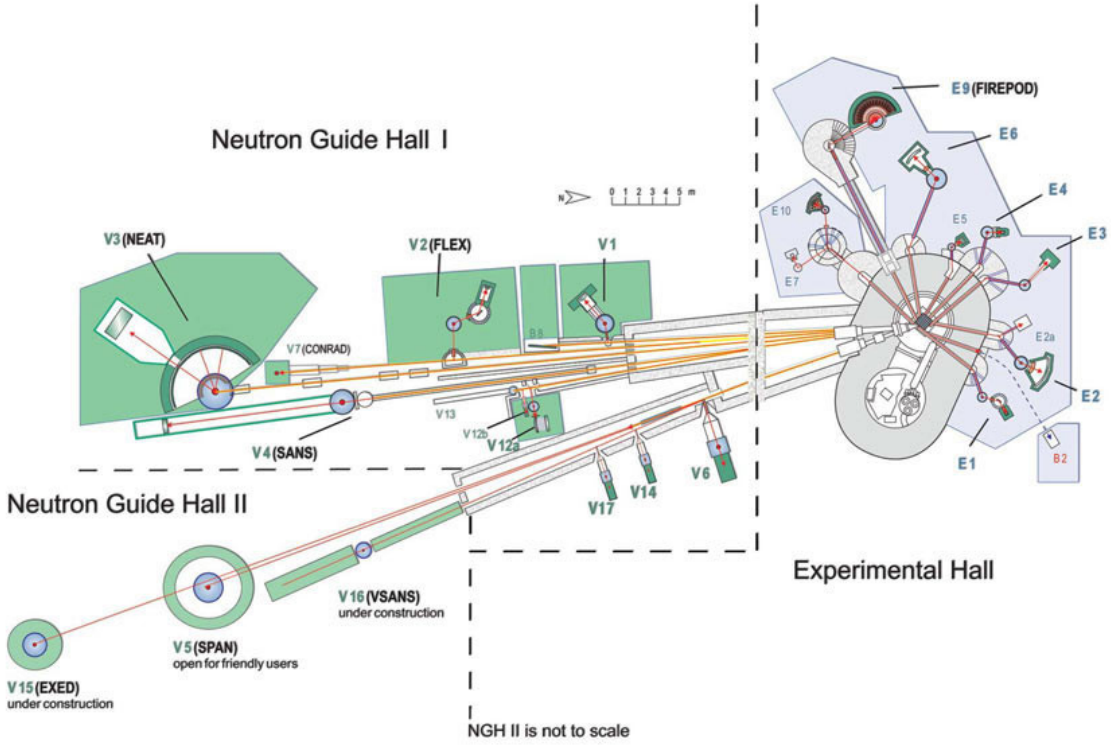

be low when averaged over time. Flux affects how long it takes to obtain results, and thus the quality of scattering obtained. The flux at the sample also depends on the energy of neutrons required for the experiment.

Instrument types can be roughly defined in terms of the neutron source, and whether the instrument is direct or indirect geometry. Two important spallation sources are ISIS[27] in Oxfordshire and SNS[28] in OakRidge USA. An example of an indirect geometry machine that can be used for coherent inelastic scattering is TOSCA at ISIS. Tosca can measure both forward and back scattering with a resolution around 1%. Other experiments useful for coherent inelastic scattering at ISIS are direct geometry machines such as; MARI, MERLIN, MAPS and LET. The neutron flux at ISIS varies from 2 to 5×10^4 n/cm^{2}s in the pulse depending on the instrument in question. SNS has been designed

to produce very high fluxes. The useful instruments for Poly-CINS at SNS are the direct geometry machines ARC and SEQUOIA. The neutron flux at SNS is greater than $5 \times 10^5 n/cm^2s$ at the sample position.

Two reactor centres are at the ILL[29] in France and Helmholtz Zentrum Berlin (HZB)[26]. At the ILL the instruments that are useful for coherent inelastic scattering are IN4 and IN5. These are both direct geometry chopper instruments. IN4 uses both a monochromating crystal and a system of choppers to achieve desired energies. IN5 uses a system of six choppers to achieve the desired energy, the neutron flux at sample at the ILL is typically around 5×10^5 n/cm^2s.

At HZB the most useful instrument for poly-CINS is V3 (NEAT). V3 is a multi-chopper spectrometer which uses a primary and a secondary detector. The flux at sample is around 2×10^4 n/cm^2s and so is substantially lower than the ILL.

The incident energy effect governs which half of the neutron spectrum will contain the most information. So for the IN5, which depends on cadmium absorption, incident energies are low, therefore only a small amount of energy loss can be measured. Other instruments such as MERLIN are mainly used for energy loss spectra as they have high incident energies.

During an experiment it is also important to have the ability to produce different temperatures and pressures. This can then allow you to study different attributes of your system and reduce the Debye Waller effect. These abilities are generally dependent on the sample holder used, a wide range of sample environments can be provided at most modern experiments.

Chapter 3

Neutronplot

This chapter describes the Neutronplot program which was developed by the author to improve poly-CINS analysis tools. We will start with a discussion of the equations which underpin the Neutronplot program. The architecture and development of the program will be described to demonstrate how the program could be modified in the future and to show the philosophies and decisions behind its development. A guide to using Neutronplot is also included.

3.1 Background

Neutronplot was originally conceived as a visualisation program for Scatter output as using Excel or other commercially available graphing software was time consuming and not designed for the analysis of neutron scattering data. It was also necessary to be able to compare Scatter data with experimental data. Current visualisation software varies from centre to centre and in some cases between instruments.

There is currently an attempt to create a more universal software for neutron scattering in the form of the Mantid[30] project, however this has not yet been

completed. Current analysis software was not created with Poly-CINS as a priority and so is missing functionality which is useful to Poly-CINS analysts. It was therefore decided that a more user friendly and flexible viewing software should be created.

MATLAB was chosen for this purpose due to its native sophisticated graph creation capabilities and the ease of matrix manipulation. MATLAB also features a Graphical User Interface (GUI) editor GUIDE. GUIs are visual interfaces which allow functions created by the programmer to be accessed by the user without using a command line or requiring hard coding.

3.2 Fundamentals

The principal function of Neutronplot is to create $S(\boldsymbol{Q}, \omega)$ graphs. For experimental data this will mean some level of conversion from the data as received. This is necessary as at the instrument data is collected in terms of time and angle, the time of flight will obviously vary from instrument to instrument and depends on initial energy. The angular range of instruments and experimental conditions also vary and so to compare data from different sites the data needs to be converted to terms of energy and momentum transfer which will be universal.

The equations governing the relationships between time, energy and momentum for neutron scattering were presented in the theory and are repeated below.

$$E = \frac{m_n v^2}{2} \tag{3.1}$$

Where E is the energy of the neutron, m_n is the mass of the neutron, and v is

the speed of the neutron. As $v = distance/time$ the equation above shows the relationship between time and energy for the neutron.

$$Q^2 = k^2 + k'^2 - 2kk' \cos\phi \tag{3.2}$$

Where Q is momentum transfer of the neutron, k is the initial wavevector, k' is the final and ϕ is the scattering angle.

At some sites, such as ISIS, the experimental data is given to the user with the conversion from time to energy already performed, but this is not always the case, the example below shows the conversion for ILL data. The code is from a routine for reading in IN5 data in Neutronplot, and is a modified version of a section of the 't2e' routine in LAMP.

```
const1 = 5.22697;  % E(meV)=const1*V(m/ms)^2 for neutron
const2 = 2.07193571; % E(meV)=const2*k(A^-1)^2 for neutron
ei   = const2/lambda^2; % Initial energy
Vi   = sqrt(ei/const1);% Speed
Tel  = Distance/Vi;
time = chan_width*(Xaxis - elastic_chan) + Tel;
ef   = const1*((Distance./time).^2);% Final energy array
energies  = ei - ef;% Energy transfer
```

The initial energy is found from the initial wavelength of the neutrons (lambda), and the array of final energies is found from the time associated with each channel. The energy transfer is then calculated allowing the data to be presented in terms of neutron energy loss and gain.

All instrument data requires conversion from scattering angle and energy to $S(\boldsymbol{Q}, \omega)$. This conversion is a coordinate transfer and is governed by the equation (3.2).

Neutronplot implements this conversion by splitting the data into energy loss and gain and finding the Q loci for each side.

```
for i = 1:ndets %Loop over scattering angles
    current_theta = angles(i);
    for j = 1:loss_chans(2)% Loop over energy
       current_energy = Etrans_loss(i,j);
       Ef  = Einit + current_energy; % Final energy
       kf2 = Ef/16.7;% Final wavevector
       kf  = sqrt(kf2);% Square of final wavevector
       Qloc_loss(i,j) = sqrt(kinit2+kf2-2*kinit*kf*cos(current_theta));
      % creating Q loci array
    end;
end;
```

In the code above an array of Q values is created by selecting an angle then looping over all energy values to find all the Q values for that angle, the next angle value is then selected and the process repeats until Q values have been found for every energy and angle value in the data.

The Q array creation also underpins many of the analysis functions of Neutronplot such as comparing experimental and theoretical data and showing the loci of neutron scattering instruments. These functions are detailed later in the chapter.

3.3 Architecture

Neutronplot is comprised of several interacting GUIs which are underpinned with visualisation and analysis functionality. MATLAB GUIs consist of a related .m and .fig file which must have the same name. Elements of the GUI

such as buttons and text boxes are shown in the .fig file and are linked to functions in the .m file known as 'Callbacks' which are triggered by the user interacting with the element.

Typical features of a MATLAB GUI are text boxes, both for the user to enter information and to inform the user. There are also push buttons, tick boxes, sliders, drop down menus and radio buttons. It is also possible to embed graphs and tables into MATLAB GUIs. Using a GUI gives easy access to functions and saves data within the program so it only has to be loaded once when running the program. GUIs are designed using GUIDE then responses to the users actions are programmed. For example when the user pushes the Contour Graph button this calls a function which calls other functions to select the correct data set, and plot the requested graph.

Neutronplot as a whole consists of around 75 separate .m files, most of which would cover more than two pages of A4 in standard format. The .m files which control GUIs are around 18 pages long, the bulk of which is created automatically in the form of the callbacks, which then need to be individually edited and expanded to give the desired functionality.

Named functions within Neutronplot shall be referred to in italics to avoid confusion as, for example, there is a function named *neutronplot* within the Neutronplot program.

There are two main functions in Neutronplot, *neutronplot* which is the user interface for reading in an working with time of flight data and *Contour_plots* which contains analysis and visualisation tools for $S(\boldsymbol{Q}, \omega)$ data.

3.3.1 The *neutronplot* function

The Neutronplot program is started by running the *neutronplot* function which brings up a GUI. The *neutronplot* GUI links to several other functions related to data input, it also contains tools for data correction and experiment planning. Typically the user starts by reading in the data to be analysed which can be in the formats given by Scatter, LAMP, mSlice or NEAT. This data can be time of flight or $S(\boldsymbol{Q},\omega)$ depending on the format specified. The user specifies the data type to be read in and can browse for the path to the file.

Figure 3.1: Loading data in Neutronplot

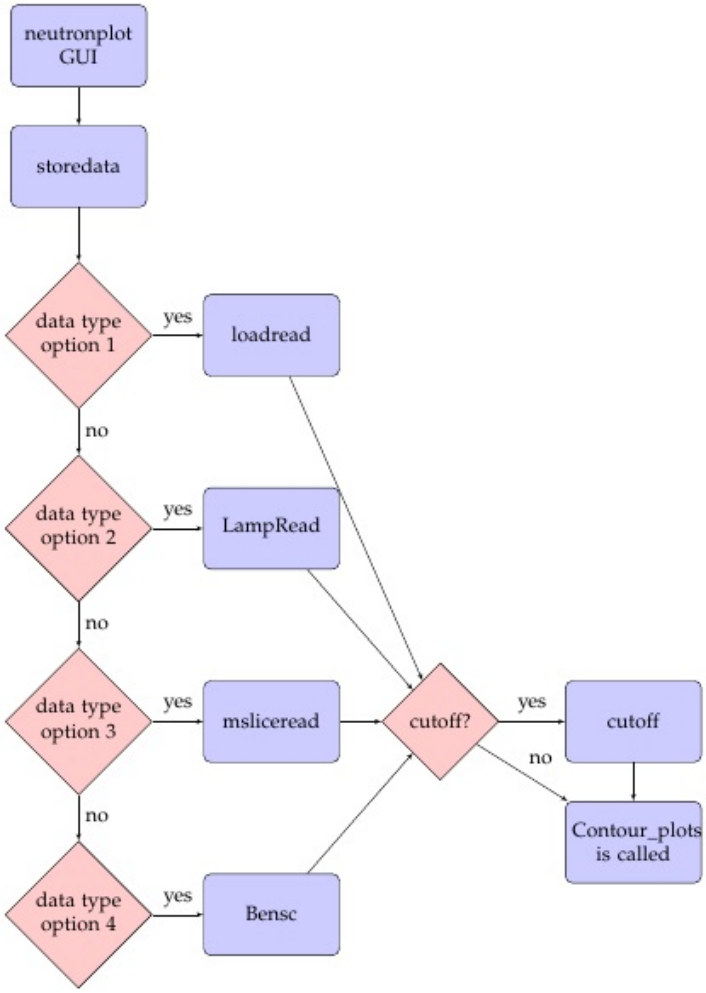

Neutronplot is designed to create an easy to view useful plot of the data as

soon as the data is loaded. Therefore on loading the data various default actions are performed to give an easily interpretable spectra to the user. All original data is stored so that any changes that need to be made by the user can be easily executed.

Data is stored in the form of global variables to enable easy access of data for each function. Figure (3.1) demonstrates how reading in data is handled in Neutronplot. The *neutronplot* function passes the name, location and type of the text file to *storedata*, which then chooses the correct data loading function and passes the file information to this function. The data loading function will read the data, transform it if necessary and then call the *cutoff* function which removes higher intensity data for easy viewing of low intensity data. Cutoffs can be easily changed in the Contour Plots window.

3.3.2 The *Contour_ Plots* Function

The *Contour_ Plots* GUI is the primary tool for analysis of Poly-CINS data. It contains links to other analysis tools as well as functionality to show full spectra and refine the viewing of the spectra.

Contour_ Plots is linked to several different types of function. These functions can be characterised as separate groups. First are those which create new GUIs these contain links to many other functions and require the user to give further information about the analysis they require. Secondly there are internal functions which are coded only in the larger *Contour_ Plots* function. An example is changing the azimuth and elevation of graphs, the internal functions do not call any functions other than the standard functions. The 'standard' functions are called by all internal, external and GUI functions connected to *Contour_ Plots*. One such function is the data section function *DataSetSelect* which is called every time a new data set needs to be accessed and *graphcreation* which

Figure 3.2: Function links in *Contour_ Plots*

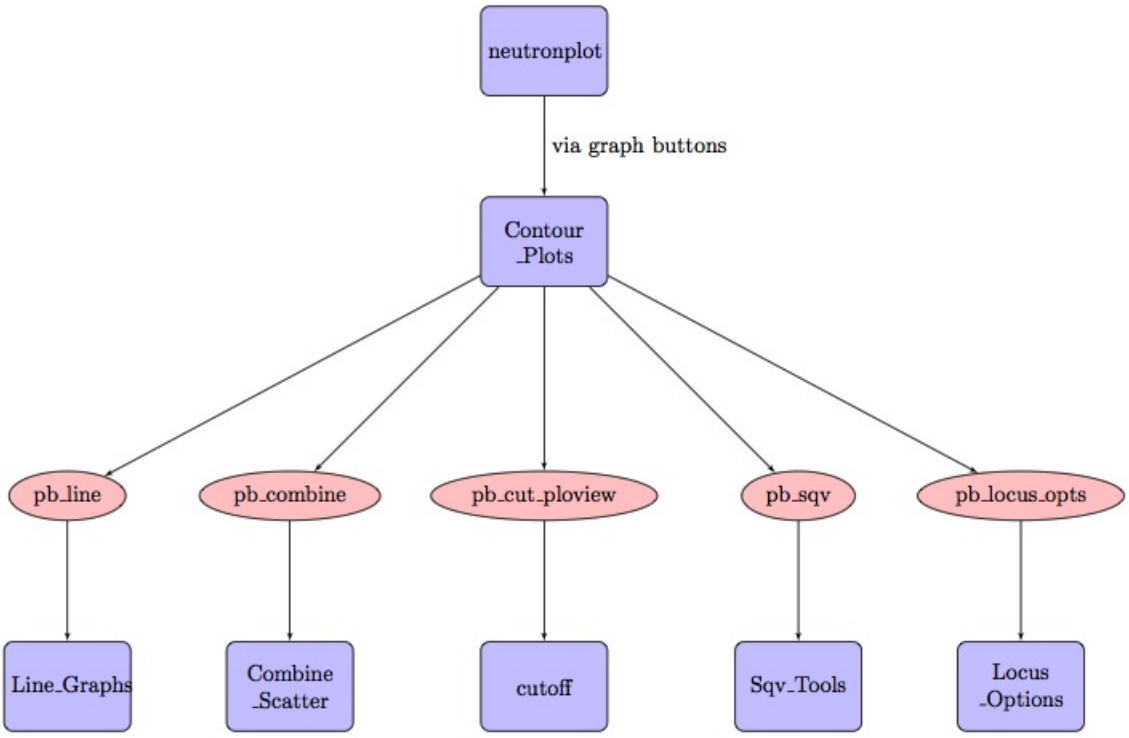

is called every time a graph is changed. External functions do not create a GUI and are not performed within *Contour_ Plots* the standard functions are of this type.

3.4 Development

Neutronplot started life as single page program which was used to load Scatter data and output it as a 3D graph or as line graph cuts through the data. The data could also be smoothed using a broadening routine and cut offs could be applied. Locus cuts through the data could also be shown. This functionality remains in the current Neutronplot code. When operating the original program the data had to be read in every time an option was changed or if the user wanted to look at a different type of graph. It was designed only to

read in Scatter code output and any changes to the file name or size had to be hard-coded into the program.

Figure 3.3: First version of Neutronplot

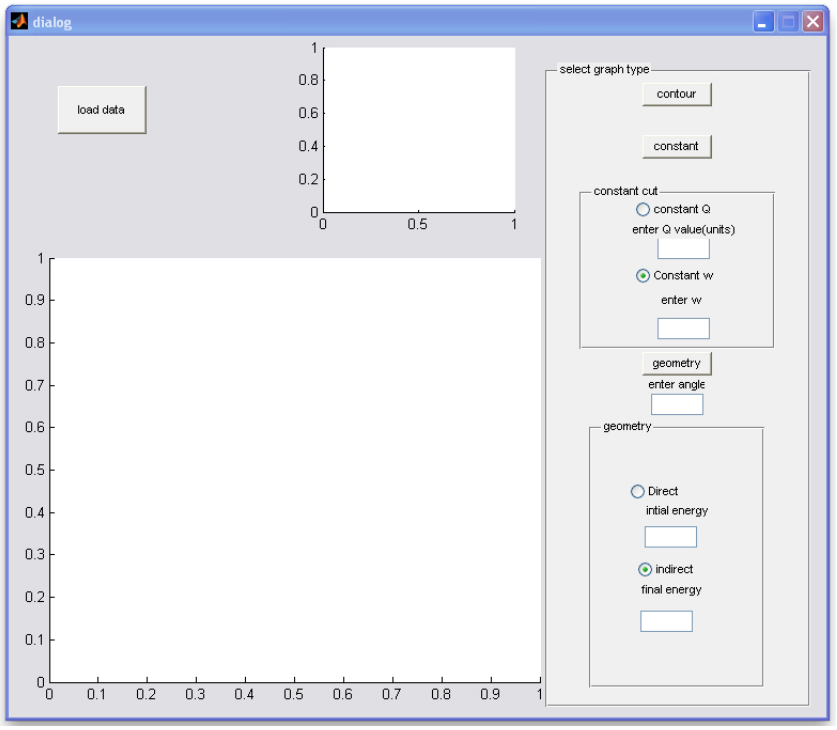

The first step was to make a GUI which would allow the creation of the different graph types by pressing a button and allow the user to define the values used in the cuts. In the example shown, the name of the data file used still has to be hard coded and the ability to look at two different graphs at the same time is possible. When the data set is loaded the user can then choose whether to look at a contour plot or constant cuts. It is possible to specify whether the instrument is direct or indirect for the locus cuts. This version of Neutronplot used the original program as a function and very few variables were passed between functions.

The loading and viewing parts of the program were then separated and the ability to add masks to the data was added. In this version the file path and name are added by the user. The user also had to know the size of the file

in advance and enter this information into the set-up options panel. Most of the graph options, such as cutoffs, have to be selected before loading the data and the amount that can be done afterwards by the user was limited. Graph options such as plotting a contour graph or a cut were selected on the Neutronplot bar. In the code new functions were written to perform each action. This meant that many variables had to be passed from one function to another. This led to the use of global variables so that each variable could be stored in memory and accessed at will.

Figure 3.4: Second version of Neutronplot

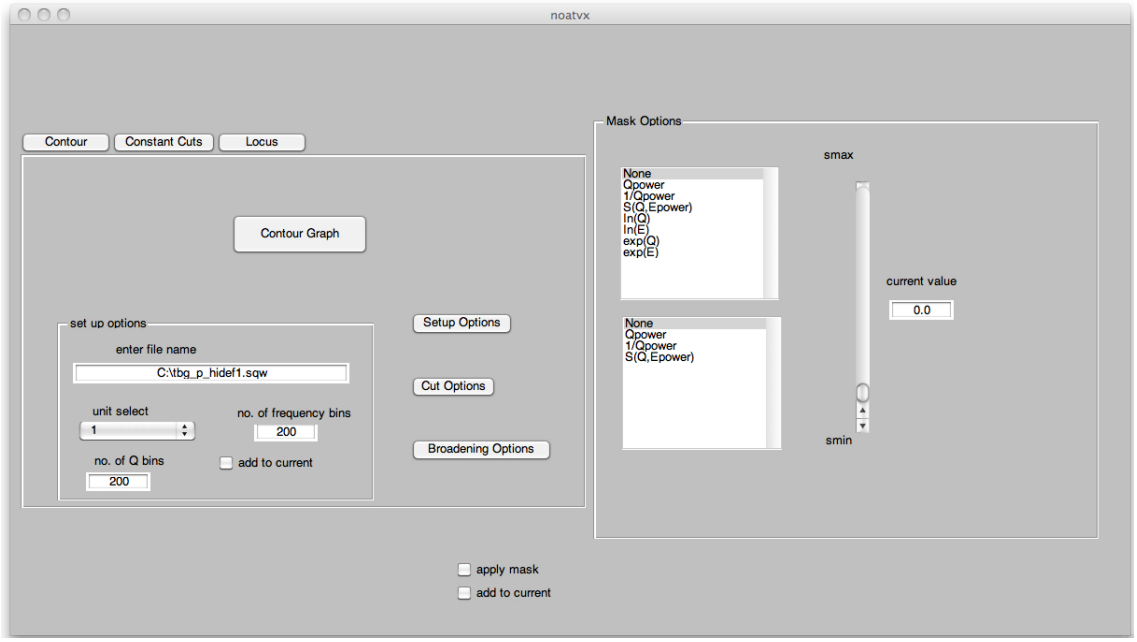

The next stage was to improve the layout of the Neutronplot interface. The tabs were removed and the options boxes condensed. It was also important to add a progress box as reading in the files could be time consuming, over 15 seconds for some LAMP files. The graph GUI remained the same and the file name and path still had to be added manually.

The next step was to add different types of data so the ability to read in LAMP and Mslice data was added, as was a file browser. The new file types were

Figure 3.5: First version of Plotview

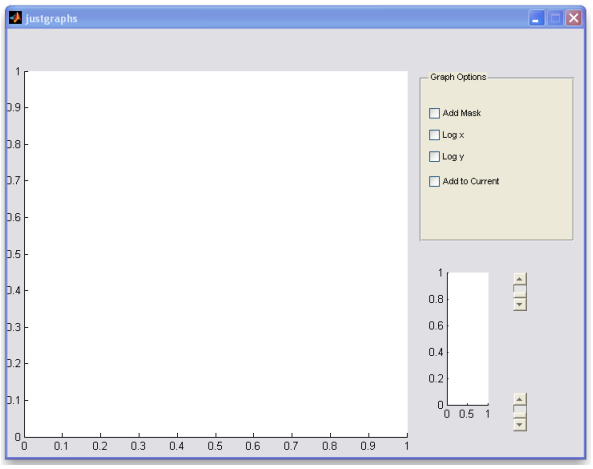

Figure 3.6: Third version of Neutronplot

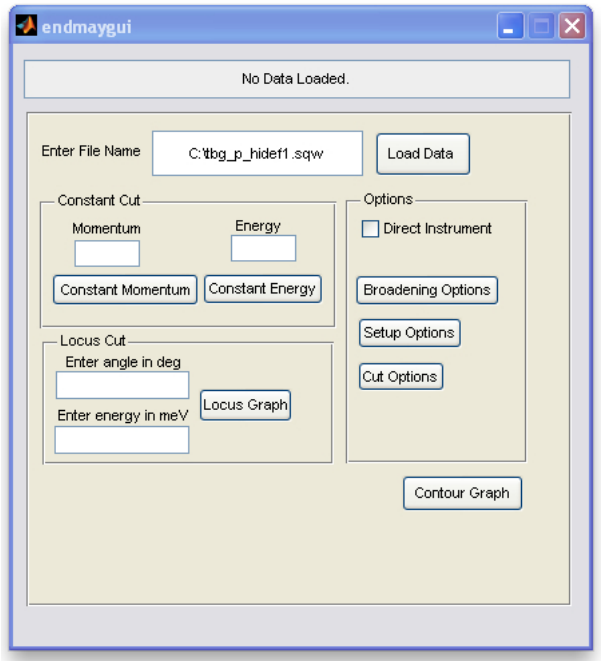

accompanied by the addition of several functions to the graph GUI. As the LAMP and Mslice data were experimental the separation of the energy gain and energy loss halves of the spectrum became beneficial. The user could also select where constant cuts were taken by using a data point on the 3D graph to specify the exact co-ordinates of a feature. Neutronplot changed to being purely a loading and set-up options GUI as more options involving the graphs

were moved to the graph GUI throughout the process of development. This change meant that more options could be changed by the user on the fly rather than being set at the start. Creating a flexible cut-off was very important and removed the need for a colour bar. A structural variable was added to store all the data, meaning that only one global variable needed to be used and all the data could be accessed by using that variable.

Figure 3.7: Graphing GUIs

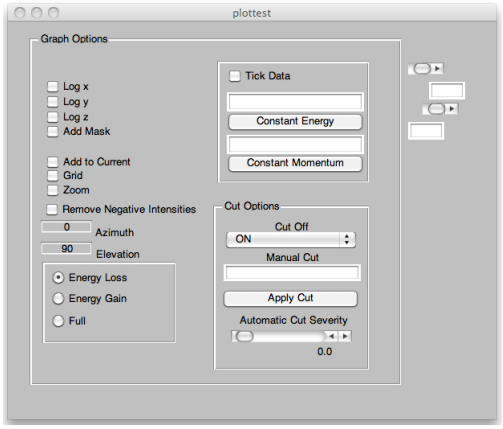

(a) First attempt at new Graph GUI

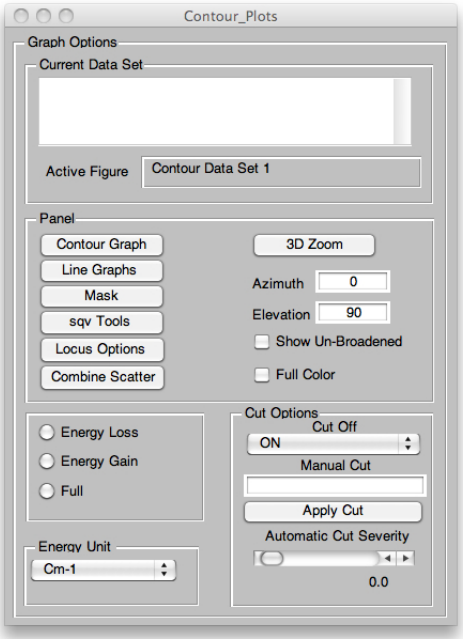

(b) Final version of graph GUI, now known as Contour Plots

It was then decided to decouple the graph from the graph GUI in order to take advantage of the capabilities of the MATLAB graph viewer and to allow the user to view multiple graphs at once.

The capabilities of the current version of Neutronplot will be described in detail below. The major addition to functionality at this point was the ability to load multiple data sets, this enabled easy comparison of different data sets.

The original code was continually updated as the original was written without

awareness of the full capabilities of MATLAB. MATLAB was created for use with matrices and thus many lines of code which would be necessary in a language such as C or FORTRAN can be removed or changed. For example the full routine for looping over the matrix and applying the cut-off.

```
for i = 1:mcut
  for j = 1:ncut
    if (zcut(i,j)> cutoff)
        zcut(i,j) = cutoff;
    end
  end %for loop over j - energy transfer
 end% for loop over i - momentum transfer
```

could be replaced with this line:-

```
 zcut(zcut>cutoff)=cutoff;
```

Data files were also originally read in line by line in a loop which then allocated data to different matrices, this process took several seconds depending on the size of the file. MATLAB is capable of reading in all of the data in a document as a single matrix, if the format of the file is known. This is much quicker and matrix elements such as columns can then be assigned as different collections of data such as energy or angle. This reduced the time to load data from LAMP files from fifteen seconds to under two.

3.5 Using Neutronplot

Neutronplot is started by running the neutronplot.m file, this brings up a window for loading data.

Figure 3.8: The loading window of Neutronplot

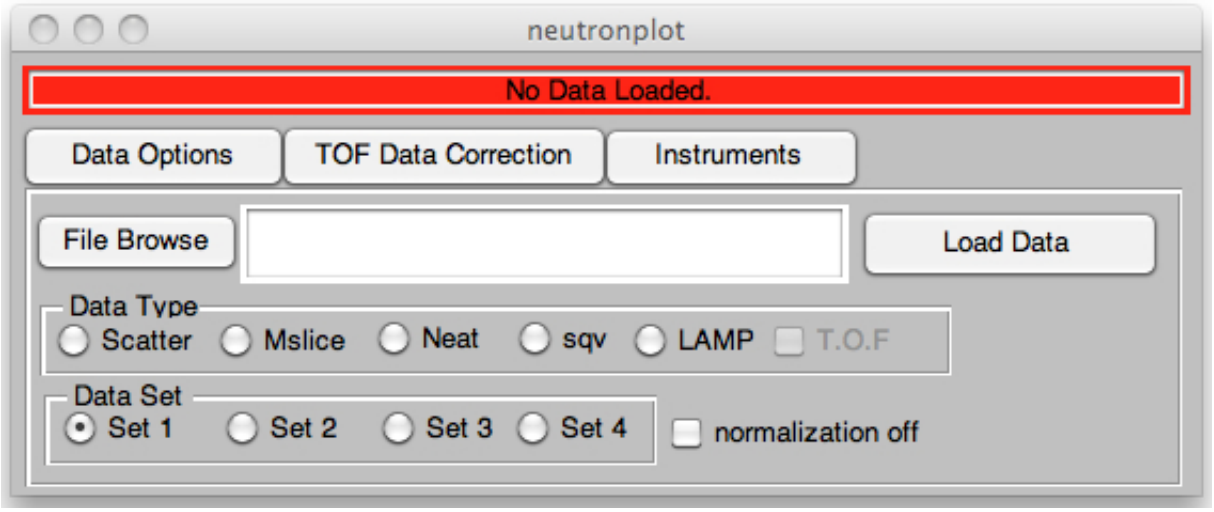

The user chooses the data type by clicking on the radio buttons. Four data sets can be used in Neutronplot at any one time. These are numbered and the set number can be chosen by the user or Neutronplot will automatically move to the next set when one is loaded. After browsing for a data file and pressing the Load Data button the Contour Plots window opens if the data has loaded successfully. The location of the last file loaded is saved so that the browser will open in that folder when the user next looks for a data file.

3.5.1 Contour Graphs

Typically the first action performed by the user is the creation of a graph, the Contour Graph button (2) gives the poly-CINS data set with the parameters set by Neutronplot. These can then be changed with the use of the functions on the Contour Plots window.

The Current Data Set box (1) is used to choose which data set you are working on at any particular time. The sets are named after the file which contained the initial data. Selecting a data set means that any options chosen on the

Figure 3.9: The *Contour_Plot* GUI with areas numbered

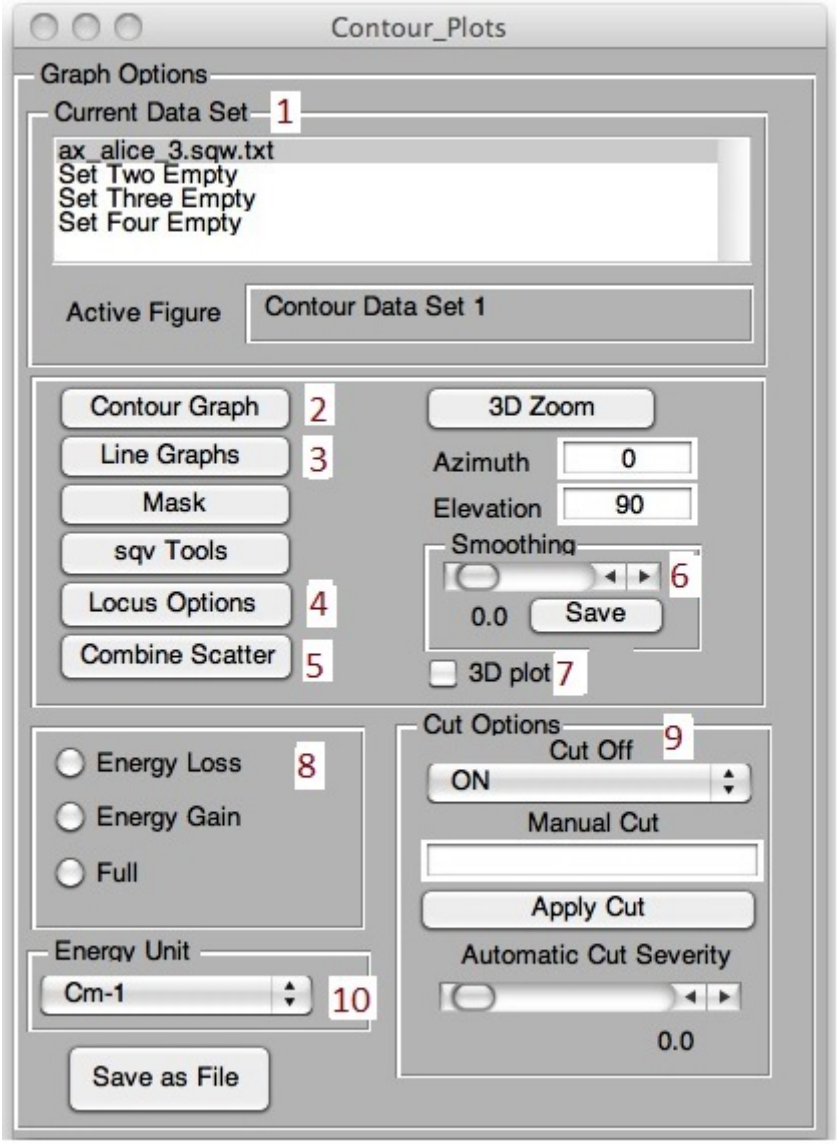

Contour Plot window will be applied to that data set only. Graphs containing information from other sets remain open and are unaltered. The Active Figure box informs the user which one of any open graphs will be altered.

The energy units preferred can be selected with the Energy Unit drop down list (10), this immediately changes the energy axis of the active figure and remains selected when new graphs are created. Old graphs remain unchanged.

The 3D plot box (7) allows the user to user to toggle between 3D surface and

Figure 3.10: 3D plot options

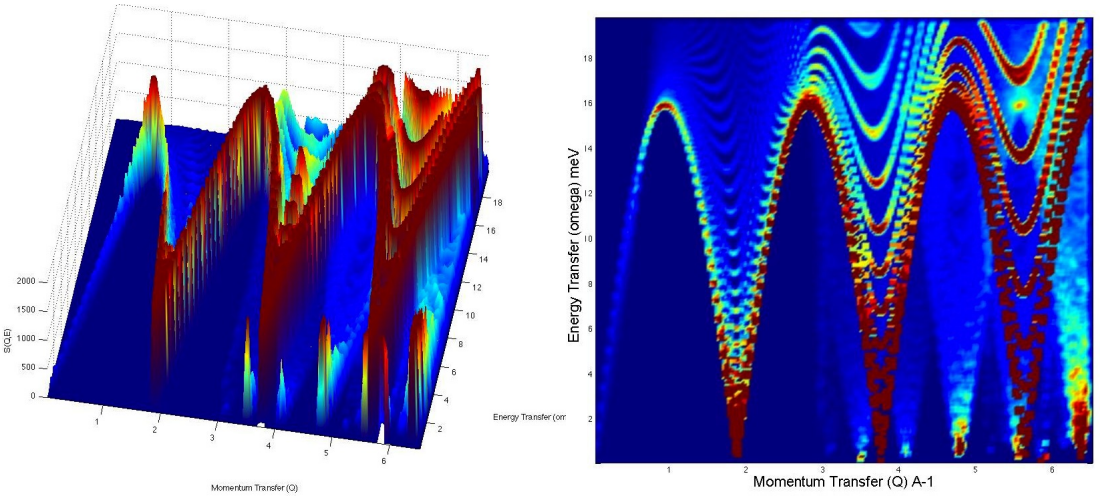

(a) Surf plot of theoretical graphite data **(b)** Pcolor plot of theoretical graphite data

flat color plots. One of the difficulties with interpreting poly-CINS data is that the data sets are 3D so, unlike a line graph, features can be far from obvious. Neutronplot has two possible viewing methods for viewing a 3D data set. These use the pcolor and surf commands. Surf allows you to see and rotate a 3D plot of the data, looking at the data in this way can be very useful for picking more subtle features. However it can also make the more obvious features seem more subtle.

This is where pcolor comes in as this gives a better overview of the data and makes zooming more useful. It also allows the overlay of 2d data sets. In figure (3.10) the peaks at high $\boldsymbol{Q}$ and low ω are more obvious in the surf graph. Pcolor shows them in relation to the rest of the data.

For the surface graph it is possible to specify the exact azimuth and elevation you wish to see the data from by typing in the relevant boxes. This is particularly useful for flipping the data by 180°.

Changes to intensity data can be saved in the form of text files. These are saved in the same format as the original data.

3.5.2 Cut-Offs and Smoothing

In experimental data the highest intensities are found at the elastic line. This tends to mask the lower intensity dynamic data removing the high intensity data allows the dynamic data to be viewed.

Figure 3.11: Demonstration of cutoffs on surface plots

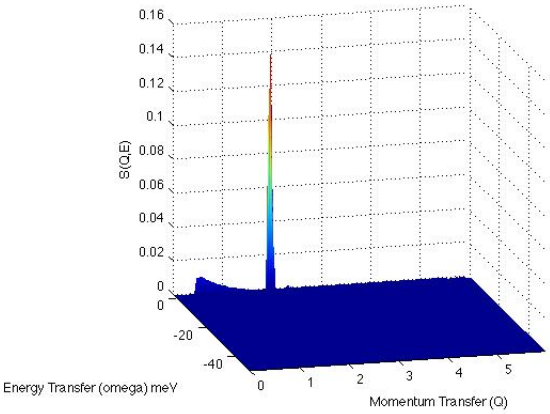

(a) The full intensity spectrum of graphite, taken at IN5

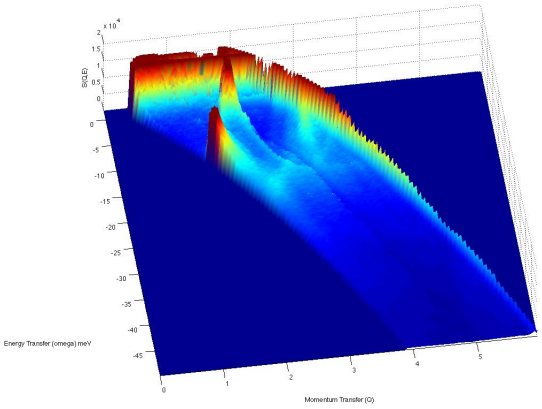

(b) The IN5 graphite spectrum with high intensities removed, showing dispersion curve detail

Figure 3.12: Demonstration of cutoffs on colour 3D plots

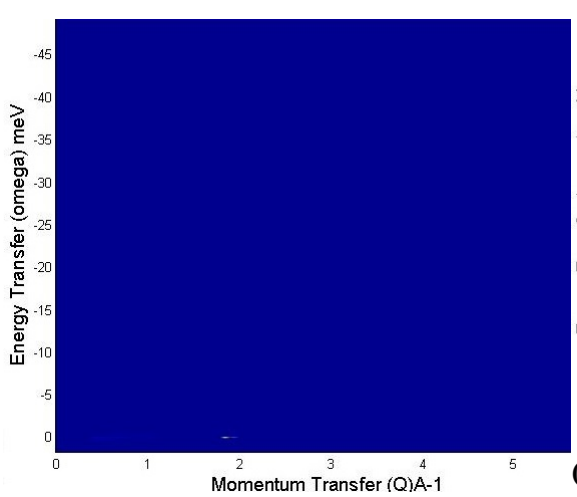

(a) The full intensity spectrum of graphite, taken at IN5

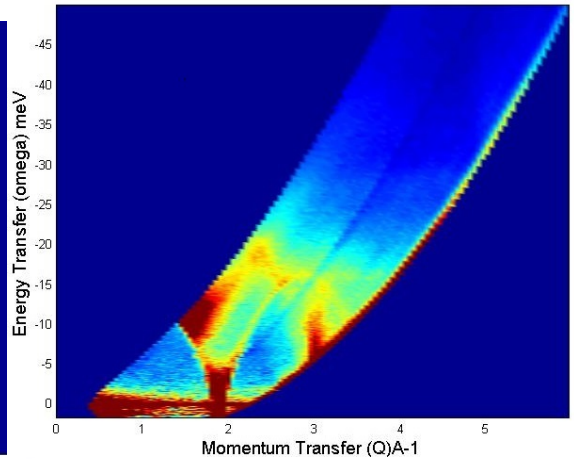

(b) The IN5 graphite spectrum with high intensities removed, showing dispersion curve detail

The figures (6.30) and (6.31) demonstrate the use of the cut-off feature.

Figure 3.13: Demonstration of smoothing on model graphite data

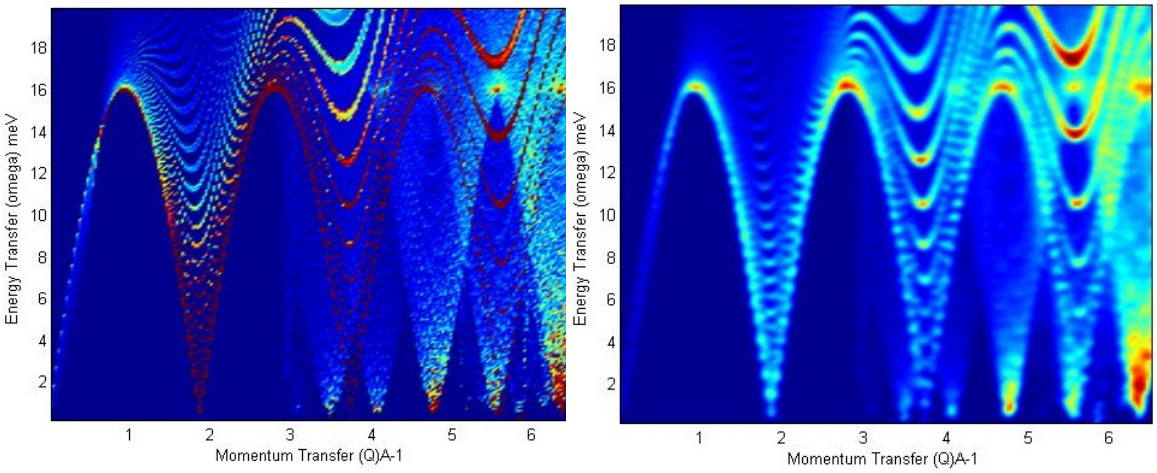

(a) Graphite Scatter data as given **(b)** Graphite Scatter data smoothed

Poly-CINS data is often saved in quite a rough form either due to the discrete channels in an instrument or due to the sampling used in calculations of modelled data. This does not give an accurate representation of the vibrations in the material and thus smoothing can be used to give a more accurate view of how data would look if all neutrons were captured or modelled. The Smoothing slider (6) allows the user to select the degree of smoothing desired. Pressing Save allows the user to work with this smoothed data for the rest of the analysis.

3.5.3 TOF Data Correction

Raw data is taken in the form of angle verses channel number and can have detector faults as well as other issues which make interpretation difficult. For this reason the TOF Data Correction panel was created.

T.O.F data loaded into Neutronplot is automatically converted into $S(\boldsymbol{Q}, E)$ data, but the original data is stored in case any corrections need to be made.

Figure 3.14: The TOF data correction panel of the neutronplot GUI

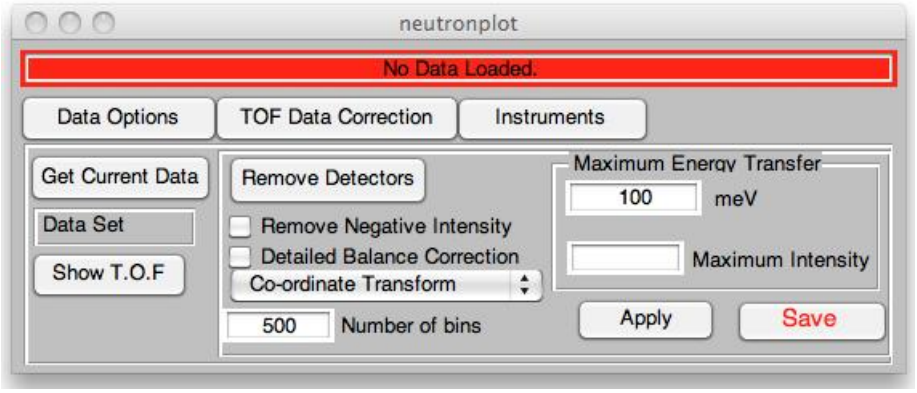

Raw data does not show phonon features clearly, and needs to be converted to Q and E. This conversion uses equation (3.2) to perform a co-ordinate transform of the data. The intensity data is reassigned to new array elements depending on the Q loci information.

Figure 3.15: Conversion from TOF to S(Q,E)

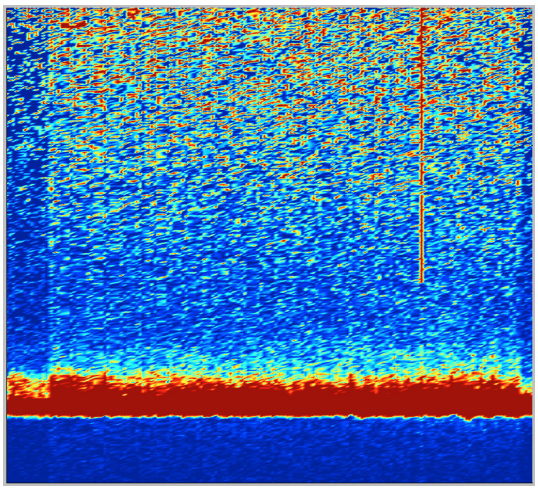

(a) Raw data. y axis is angle, x axis is channel

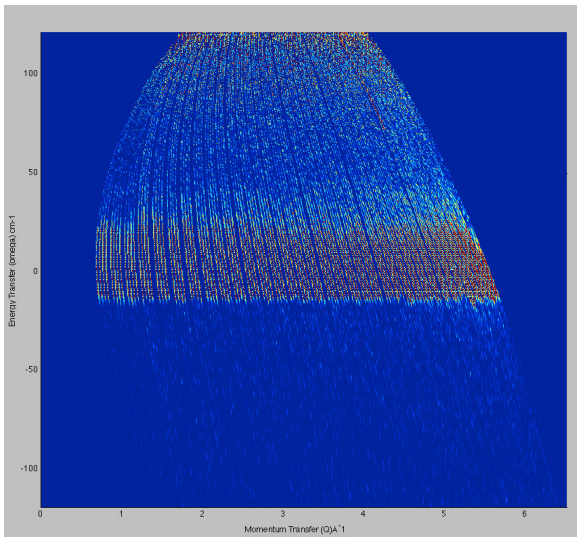

(b) $S(\boldsymbol{Q}, E)$ data

The data in figure (3.15) shows a detector fault at 1.9 Å^{-1}. This defect can be removed to make real features clearer.

This is especially useful for cuts through the data as it can be impossible to distinguish detector faults from real features. To remove detectors the user

Figure 3.16: Detector removal interface

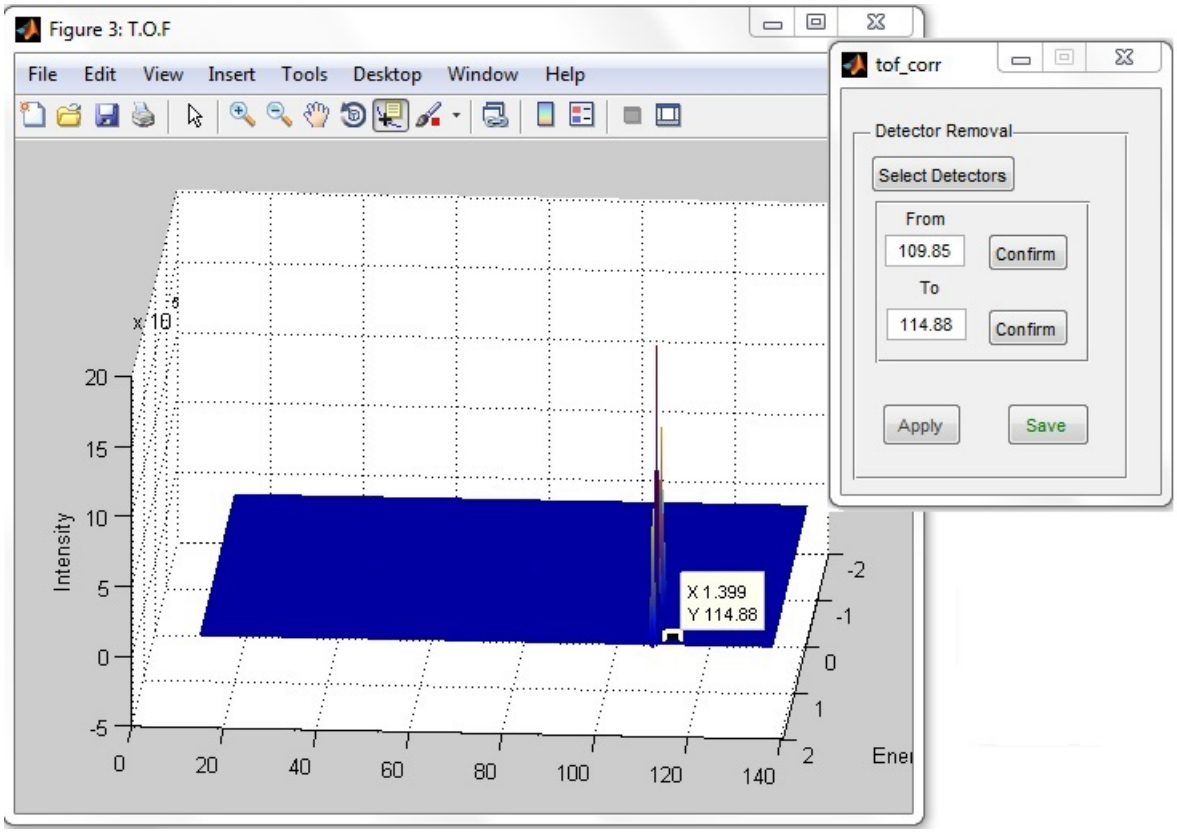

goes to the TOF Data Correction tab and presses Get Current Data. Neutron-plot then shows the data set selected in Contour Plots if there is time-of-flight data present for the data set. Pressing Show T.O.F gives a surface graph of the data in terms of energy verses angle. The user then presses Remove Detectors which brings up a window tof_corr. Pressing Select Detectors in the Detector Removal window gives a data point cursor which fills in the first text box when a point is selected. Pressing Confirm moves a cursor to the next text box which is filled in when another point is selected. Pressing the second confirm button then allows you to Apply the removal, which gives the user a graph of the T.O.F data with the detectors removed. Pressing Save then saves this change for the $S(\boldsymbol{Q}, E)$ data which can be viewed with the Contour Plot Window.

Figure (3.17) shows a data set with a detector fault before and after the removal

Figure 3.17: Detector fault removal

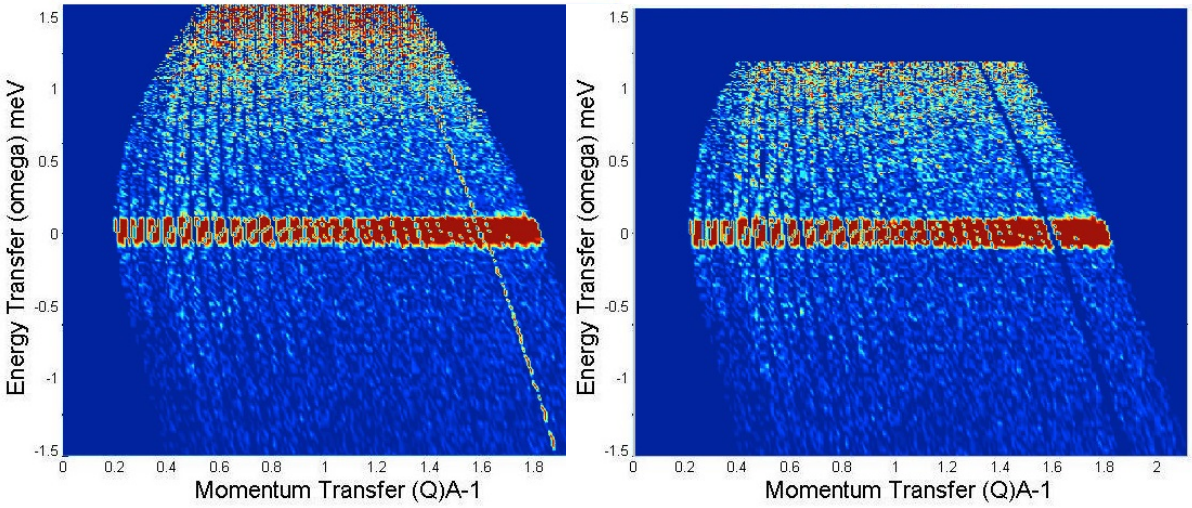

(a) Unaltered scan **(b)** Corrected scan

of the fault.

3.5.4 Instruments

Figure 3.18: The Instruments panel on the Neutronplot GUI

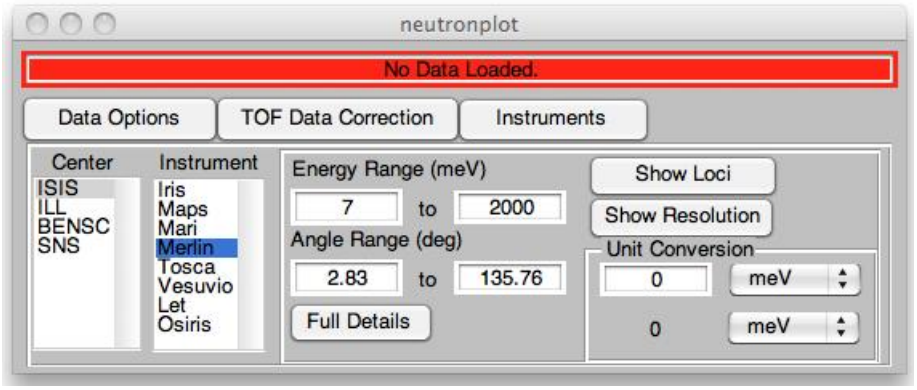

Also on the neutronplot window is the Instruments panel. Neutronplot contains a database of the angular range and energy range of all the relevant Poly-CINS instruments, and thus can produce loci for all Poly-CINS capable instruments. Figure (3.19) shows the area covered by the NEAT spectrometer

in Berlin, given an initial energy of 5 meV.

Figure 3.19: Loci of the NEAT spectrometer for an initial energy of 5 meV

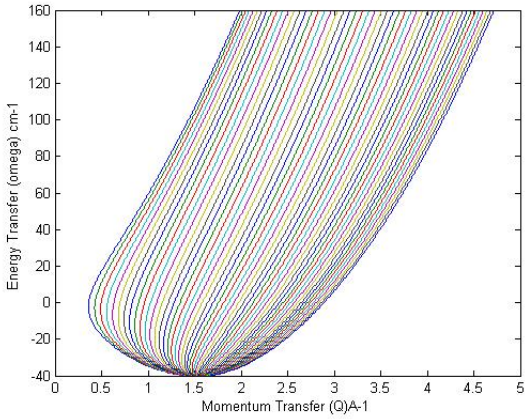

This graph is created using equation (3.2) together with the data saved in Neutronplot. Pressing the Show Loci button gives the user a window to enter an initial energy, the maximum energy transfer they are interested in and choose the units they are using.

3.5.5 The Neutronplot Suite

Figure (3.20) shows the full layout of the Neutronplot suite as set out by default when the individual windows are called. In this figure A is the neutronplot GUI, which as well as the data saving functions detailed above also contains functionality on different tabs for correcting time-of-flight data and information on neutron scattering instruments.

Window B is an example of a line graph produced by Neutronplot, C is an example of a poly-CINS data plot, D controls the creation of graphs based on Q loci and E allows the combination of data sets.

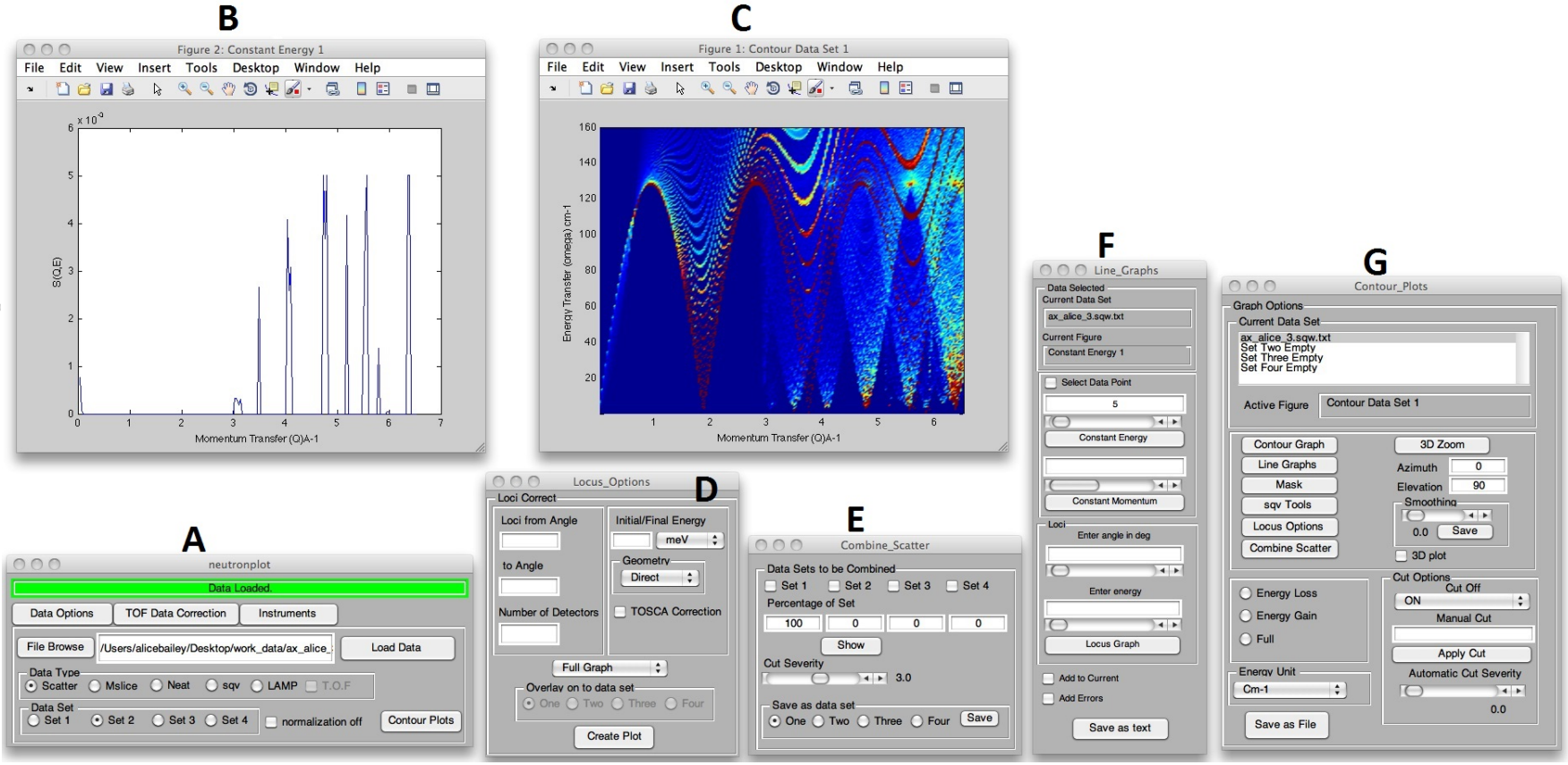

Figure 3.20: Neutronplot Suite

F is the Line Graph creation window and G is the Contour Plots window as described above. We will now give a full description of the use of the functionality of these other windows.

3.5.6 Line Graphs

Figure 3.21: Pcolor graphite data with constant cuts taken from the data point

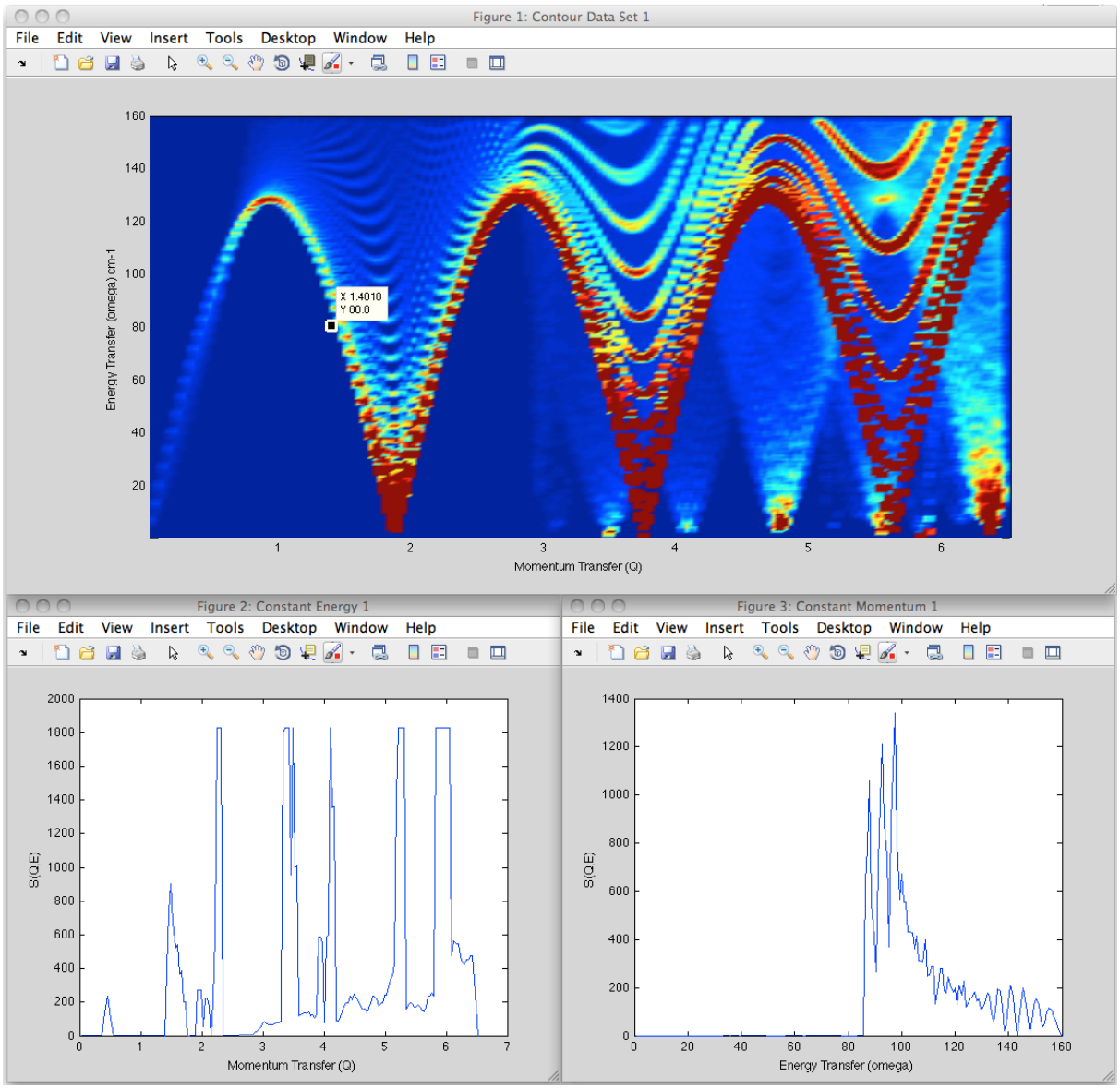

Neutronplot can be used to create several types of 2D line graphs from the scattering data. These are, a cut at constant Q, a cut at constant E and a cut

along a locus. These graphs help to identify and quantify features in the full poly-CINS plot.

To create a line graph the user presses the Line Graphs button on the Contour Plots window. This brings up a new window with options for the creation of line graphs, this is shown in figure (3.20) as window F. The window gives information on which data set is currently selected and the user can either type in a value for a constant energy or momentum value through the data, or an angle and energy for a locus through the data. In the case of constant values a point can be chosen by clicking on the poly-CINS graph after checking the Select Data Point box. This is demonstrated in figure (3.21).

The data point shown is chosen by the user clicking on a point in the graph, this action shows the axis points this point corresponds to, and these values are also sent to the boxes in the line graphs window. The lines through the data at these points are created as graphs when the user clicks on the Constant Energy or Constant Momentum buttons on the line graphs window.

The first graph below the poly-CINS plot shows a line though the data at an energy of 80 cm^{-1}, the second graph a cut at constant momentum of 1.4018 $Å^{-1}$. The peaks and edges from the poly-CINS data can be seen clearly.

Figure (3.22) shows a locus cut through the data at an angle of 40° with an initial energy of 10 meV.

It is also possible to plot several lines on the same graph, allowing the user to see the evolution of a feature over $S(\boldsymbol{Q},\omega)$ space. On the Line Graphs window there is a tick box called Add to Current, this box will allow the addition of more line graph data to graphs of the same type and data set as demonstrated in figure (3.23).

Figure 3.22: Cut along a locus

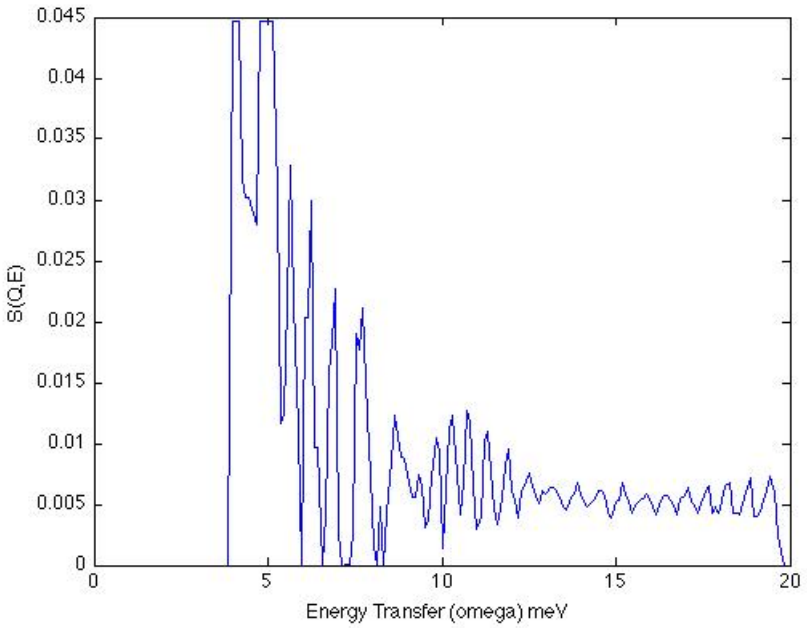

Figure 3.23: Several cuts at different energy values

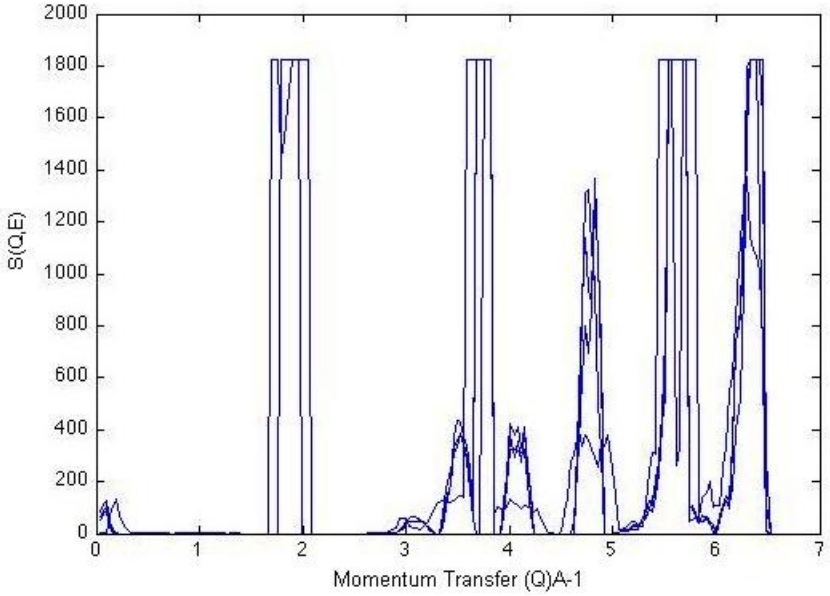

3.5.7 Combine Scatter

Scatter data can also be combined. This helps to show if experimental data has contributions from different force constants or elements. Figure (3.24) shows individual Scatter data for magnesium deuteride and for graphite.

Figure 3.24: Scatter data sets for different materals

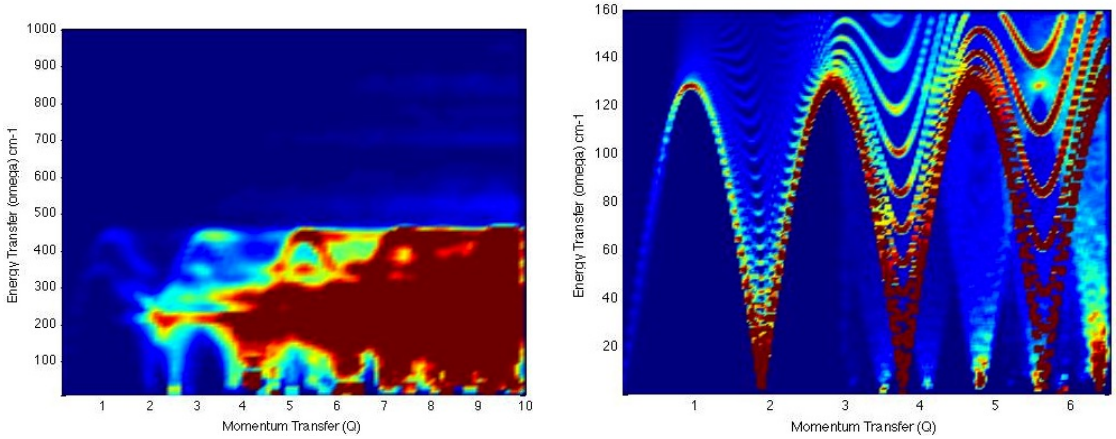

(a) Scatter data for a MgD2 crystal

(b) Scatter data for graphite

Figure 3.25: Combination of Scatter data

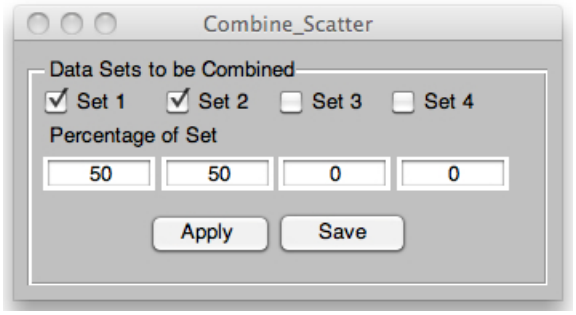

(a) The combine scatter GUI

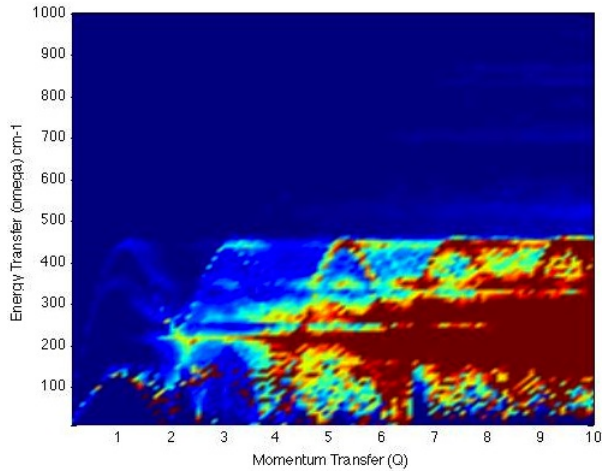

(b) An equal ratio combination of MgD2 and graphite Scatter data

The window which controls the combination of data is shown in figure (3.20) as window E and also in figure (3.25a). The window is shown when the user presses the Combine Scatter button which is button (5) in the Contour Plots figure (3.9). The user chooses which data sets are to be combined and at what ratios. Applying this combination shows the user a plot of the combined sets. The Save button saves this combination as a data set which can then be worked with.

Figure (3.25b) shows a model graphite data set combined with a model magnetism deuteride for demonstration.

3.5.8 Locus Options

As covered previously the loci an instrument covers can be easily found given details such as angular range and initial energy.

Figure 3.26: Creating experimental loci

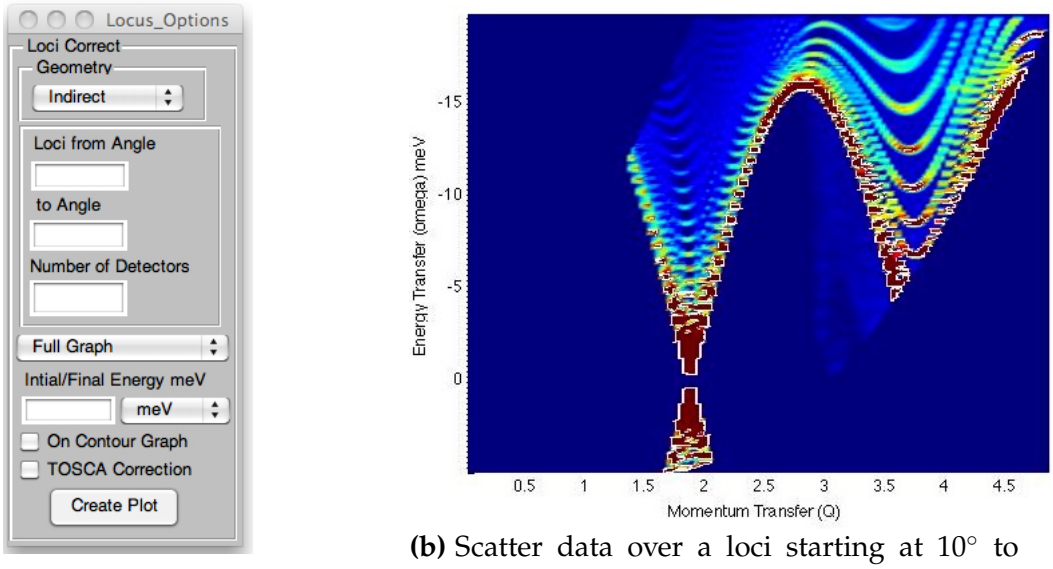

(a) The locus options GUI

(b) Scatter data over a loci starting at 10° to 160° with an initial energy of 5meV

Using the Locus Options window, which is shown to the user by Contour Button (4), instrument loci can be applied to Scatter data. This is useful for

planning experiments as the user can check if features predicted by Scatter are covered. It is also useful in interpreting experimental data, this functionally is highlighted in the Graphite chapter.

The loci are found using equation (3.2) once again and the user then has the option of showing just the loci as demonstrated in the Instruments section, the loci applied to Scatter data as demonstrated in figure (3.26b) or Scatter data overlayed on experimental as demonstrated in figure (3.27).

Figure 3.27: Contours of Scatter data, over graphite IN5 measurement

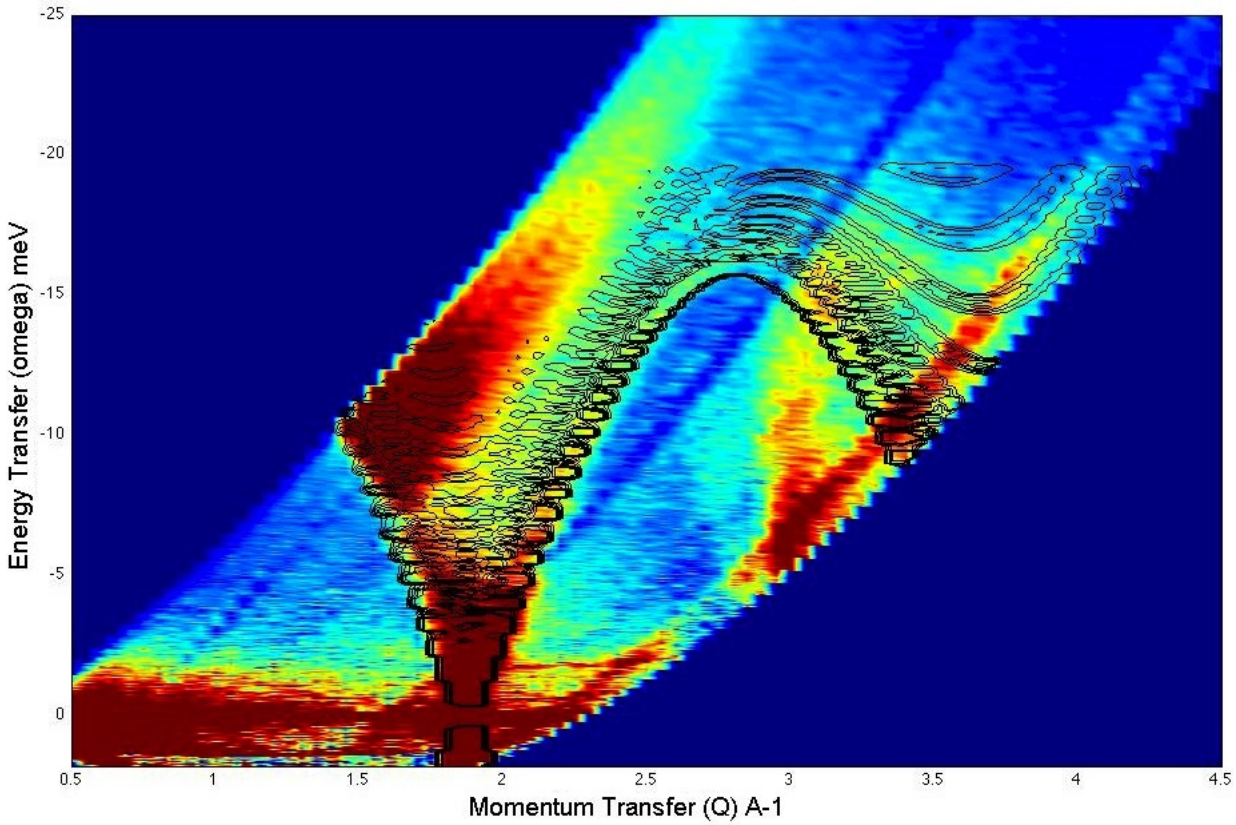

The application of Neutronplot to the analysis of poly-CINS data is shown in chapters 4 and 5.

Chapter 4

Structure of Graphite Based Materials

4.1 Graphite Background

In this chapter we will investigate the structure of several natural graphite powder samples. Historically the study of the structure and dynamics of graphite focused on the perfect crystal, this was followed by studies of various artificial graphitic materials such as those suitable for use as neutron moderators. The natural graphite samples allow us to investigate the defects in graphite. We will particularly focus on stacking faults such as the rhombohedral and turbostratic structures present in these samples. We will also investigate how the structure of an expanded graphite derived from natural graphite is changed by the processes it has undergone.

Graphite was amongst the earliest materials studied using x-ray diffraction with measurements taken by both Bragg[31] and Ewald[32] in 1914. The structure of graphite was confirmed in 1924 by Bernal[33]. Investigations into the behaviour and structure of graphites continued, peaking during the creation of graphite moderated reactors. The study of graphite then waned but was

recently revived with the discovery of fullerenes and the need to investigate the end of life of nuclear reactors.

Figure 4.1: The structure of hexagonal graphite created in Materials Studio

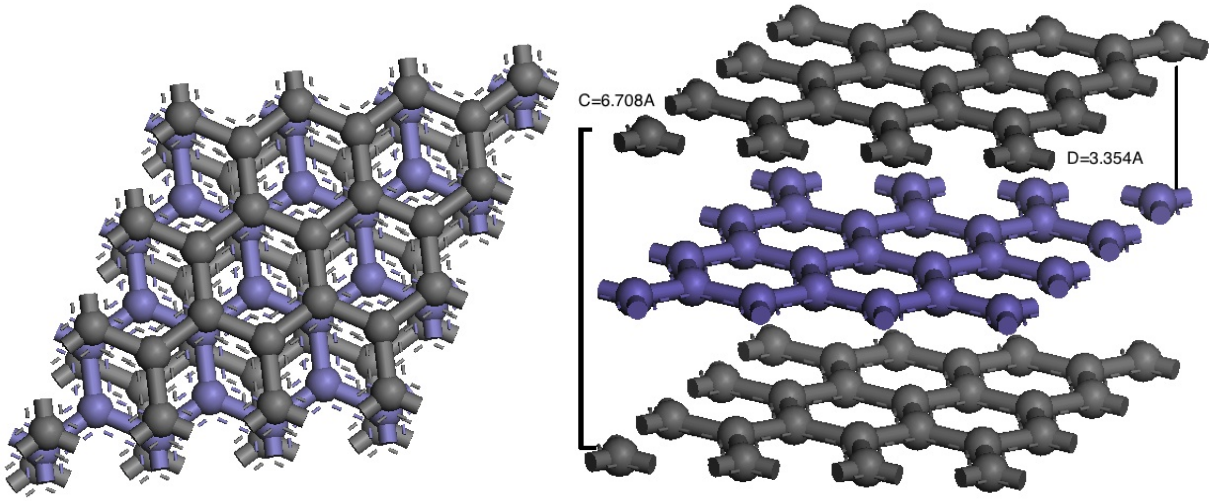

(a) Hexagonal graphite structure viewed perpendicular to graphene planes

(b) Hexagonal graphite structure showing layered structure and stacking

Perfect crystalline graphite is comprised of carbon atoms in a hexagonal lattice structure. It has the space group $P6_3/mmc$ and lattice parameters of a=2.461 Å and c=6.708 Å giving a plane to plane distance of 3.354 Å.

Atoms are arranged in sheets with strong sp^2 covalent bonding between the atoms in the layer, leaving free electrons in the material allowing graphite to act as a conductor. Layers are weakly bound to each other by Van der Waals interactions. The high anisotropy in graphite means that its properties vary depending on the orientation of the sample with phonons travelling quickly in the layers but slowly between. Graphite has a high melting point and a low thermal conductivity perpendicular to the plane. Its electrical properties lead to its use as an electrode and in batteries. It has a low neutron absorption cross-section and is therefore used as a moderator.

Natural graphite is formed by the reduction of carbon deposits during metamorphosis. Under high temperatures hexagonal graphite will form together

with possible non-carbon impurities. Graphite can experience mechanical forces in the earth creating areas of rhombohedral and turbostratic graphites. These can be annealed fully or partially due to heating of the material far underground. Geologists study the structure of natural graphite to discover the geological history of the areas in which it is found[34]. As natural graphite samples can contain elements of different graphite structures, we will investigate the structure of Highly Ordered Pyrolytic Graphite (HOPG), rhombohedrally stacked graphite and turbostratic graphite, to aid understanding of the full structure of natural graphite.

Figure 4.2: Two of the 00*l* planes in the hexagonal lattice shown in the graphite structure

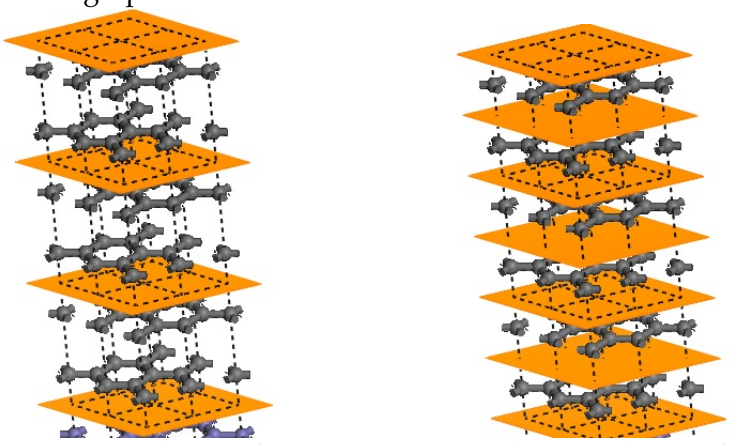

(a) The 001 planes of the hexagonal lattice

(b) The 002 planes of the hexagonal lattice

There are several important planes of atoms present in the graphite lattice which give rise to peaks in the graphite XRD pattern. The 00*l* planes are parallel to the layers of carbon atoms in graphite. Odd 00*l* directions do not correspond with layers of atoms and so give no peaks in a diffraction measurement. Even 00*l* reflections do correspond with atomic planes and the 002 plane gives the most intense diffraction peak of these reflections and generally the whole XRD measurement, depending on orientation and the disorder in the sample. The 00*l* peaks give information about the spacing of graphene layers

in graphite. The broadness and position of the peaks can give information on the range of interlayer widths which is related to the level of disorder in the material.

Figure 4.3: *hkl* planes of the hexagonal lattice shown in graphite

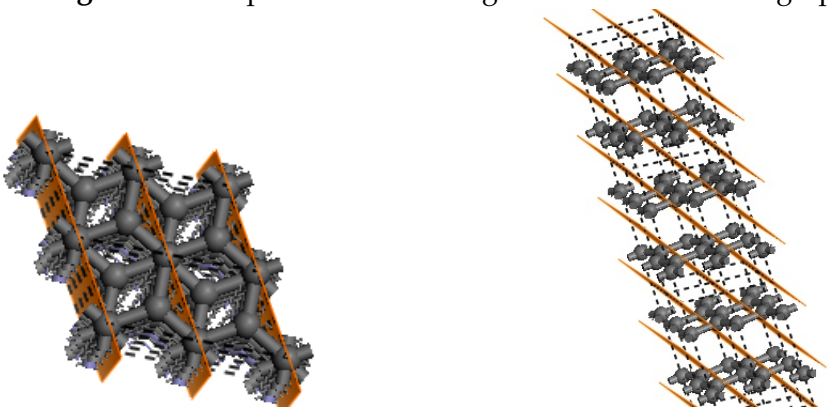

(a) The 100 planes of the hexagonal lattice

(b) The 102 planes of the hexagonal lattice

Other planes in the hexagonal lattice are the *hk*0 planes such as 110, 100 and 010. These directions are equivalent and are perpendicular to the 00*l* reflections. The *hk*0 planes give information about the distance between atoms within the graphene plane.

Other planes cover directions both in and perpendicular to the graphite plane such as the 101 102 and 212 directions. Peaks arising from these planes will be seen in following diffraction measurements.

As our measurements are on powder samples, as discussed in the theory chapter, this should mean the effects of orientation are removed as all planes are distributed equally. However in practice the shape of the powder particles affects how the planes are orientated with respect to the diffraction surface. Natural graphite shows substantial peak broadening particularly on the 00*l* peaks as graphite is particularly susceptible to changes of graphene interlayer distance due to the weak bonding between these layers.

4.1.1 HOPG

HOPG (Highly Ordered Pyrolytic Graphite) is an artificial form of graphite. It is produced by applying high temperatures and pressures to pyrocarbons. HOPG has an almost perfect structure in reference to the layered structure in graphite. The process of creating HOPG results in pinning between the layers giving highly defined layers of graphite with very little difference in the distance between layers and in the orientation of the layers. Single crystal samples of graphite consist of small blocks of crystal known as 'mosaic blocks', the average angular spread of orientation of these blocks is known as 'mosaic spread'. A high mosaic spread affects diffraction patterns and results in peak broadening. HOPG is defined by having a mosaic spread of less than 1%.

Figure 4.4: XRD measurements of HOPG compared to natural graphite[35]

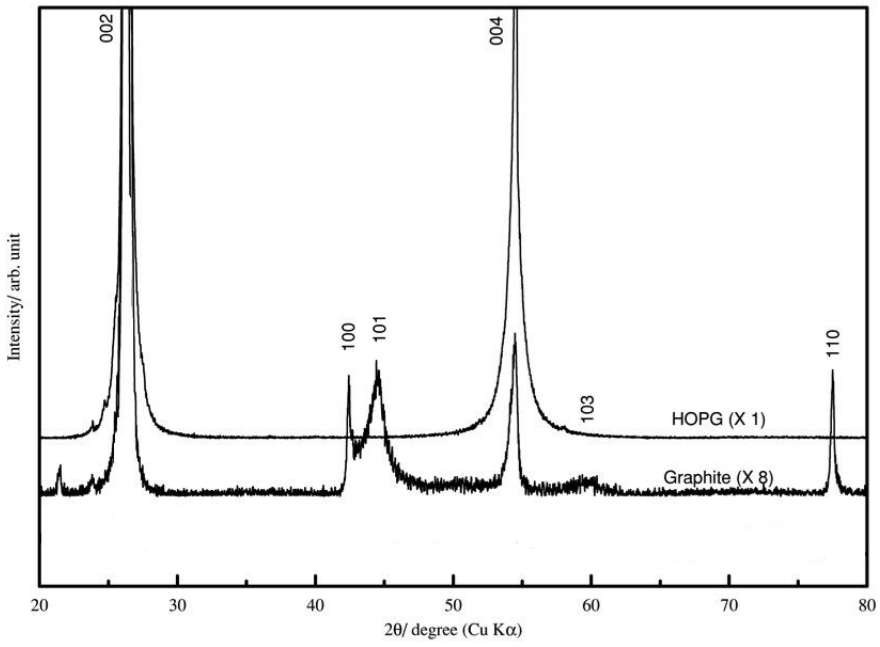

Stacking faults leading to features such as turbostratic and rhombohedral graphite, as described below, are deliberately minimised. It is used as a model material for calibrating microscopes and a basis of comparison to other graphitic materials. Due to its use as a reference material XRD measurements of HOPG

occur frequently in literature. Figure (4.4) shows work by Endo *et al.*[35]with XRD measurements of HOPG compared to a coke derived graphite.

Taken on a Rigaku RINT 2100 powder diffractometer it clearly highlights the difference between the graphite and HOPG XRD measurements, with the graphite having much lower intensity 00*l* peaks, thus highlighting the other reflections in the material. The graphite also shows peaks at a lower angle than the 002 indicating the presence of impurities in the material.

This figure demonstrates that pure HOPG gives very high intensity narrow width peaks in the 00*l* reflections with minimal other reflections visible. The lack of other visible reflections could be due to the way the planes are bonded with interstitial atoms, thus removing the planes of atoms for other reflections. Alternatively the relative peak intensity of the 002 peak could be so high that the other reflections cannot be seen in the intensities shown. In contrast the natural graphite has wider 00*l* peaks due to the range of plane spacing and orientation and at least the 100, 101 and 110 peaks are clearly present.

4.1.2 Turbostratic

Turbostratic graphite is defined as having layers which are randomly rotated and translated with respect each other. This means that the stacking patterns, such as ABAB, are lost. This affects the interlayer spacing and the intensity of diffraction peaks[10] depending on the fraction of correctly orientated graphite layers.

As previously stated the interlayer spacing in perfect hexagonal graphite is 3.35 Å, this can increase to a maximum of 3.44 Å[36]. Natural graphite is likely to have interlayer values somewhere between these figures depending on the degree of disorder in the material.

Figure 4.5: Turbostratic graphite. This view is perpendicular to the graphite layers which are rotated with respect to each other

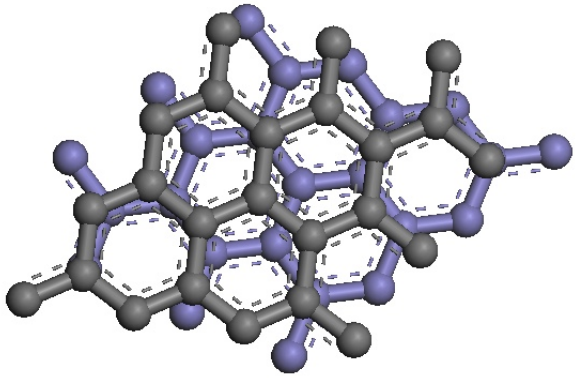

Figure (4.6) shows XRD patterns obtained from graphite after milling and annealing[37]. It demonstrates how graphite becomes more turbostratic in nature after undergoing mechanical pressure.

Figure 4.6: XRD patterns of different graphite powders. (a) As-received, (b) Ball-milled for 20 h,(c) Ball-milled for 20 h and then annealed at 1700C for 9h[37]

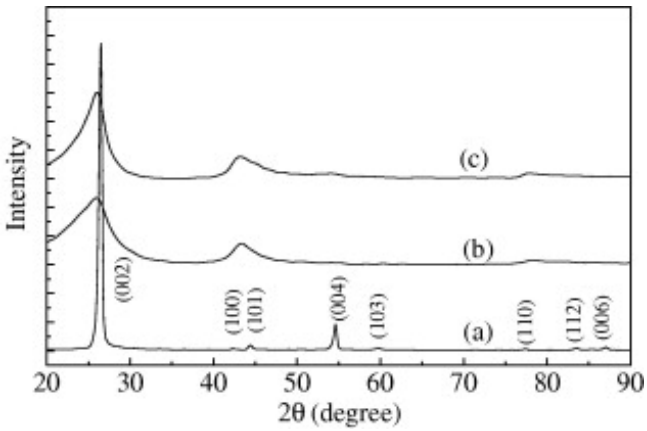

This figure demonstrates the reduction in peak height and increased broadening of the 00*l* peaks in graphite when the material becomes more disordered. As they are before and after measurements of the same material these changes can be directly compared. In the samples analysed in this work such direct comparisons to a perfectly ordered graphite cannot be made, but a measure-

ment of the turbostratic nature of a graphite sample is possible.

As shown in figure (4.6) turbostratic layers result in a shift in the 002 peak to the left as wider layers are present. The peak position can be converted to a measurement of layer spacing and the fraction of turbostratic graphite found.

Given the relative interlayer spacings for hexagonal and turbostratic graphite a measure of the turbostratic nature of a graphite sample can be found. This measure is known as the p value of the graphite, it is defined as "the proportion of disorientated layers"[10] and was originally proposed by Franklin[38].

From Franklin we have

$$d(002) = \frac{c}{2} = 3.354 - 0.086(1 - p^2) \tag{4.1}$$

where 3.354 is the value in angstroms for the interlayer spacing of hexagonal graphite. The average interlayer spacing of the sample $d(002)$ is found from the XRD peak position.

This can be re-arranged to give the p value of the sample.

$$p = \sqrt{\frac{\frac{c}{2} - 3.354}{0.086}} \tag{4.2}$$

This equation gives perfect graphite a p value of 0 and fully turbostratic graphite a p value of 1, HOPG would have a p value of 0.

It is possible that turbostratic stacking could lead to areas of rhombohedral graphite.

4.1.3 Rhombohedral Graphite

Rhombohedral graphite has an ABCABC stacking structure and is formed by slipping of layers by mechanical deformation. It has a $D_{3d^5} - R\bar{3}m$ lattice structure with unit cell constants of a = 2.566 Å and c = 10.062 Å as described by IUPAC.

Figure 4.7: Rhombohedral graphite lattice structure. The c lattice parameter labelled is in Angstroms

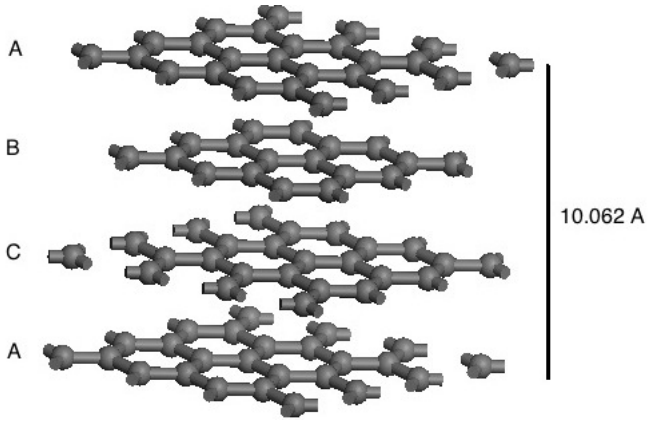

These dimensions give a plane to plane distance S of 3.354 Å, matching that of hexagonal graphite. Rhombohedrally stacked graphite is generally found in small fractions in natural graphite and converts to hexagonal graphite on annealing.

The structure of rhombohedral graphite is often described in terms of a rhombohedral lattice structure, where the dimensions are described in terms of an angle α and distance a where all angles and dimensions of the cell are equal $a = b = c$, $\alpha = \beta = \gamma$. Hexagonal cells have parameters of $a = b \neq c$, $\alpha = \beta = 90$ $\gamma = 120$. These crystal structures are equivalent as shown in figure (4.8) which shows the rhombohedral cell within the hexagonal.

XRD measurements of natural graphite in literature typically highlight the presence of rhombohedral graphite. For example figure (4.9) from Parthasarathy

Figure 4.8: Rhombohedral graphite lattice structure. The *c* lattice parameter labelled is in Angstroms

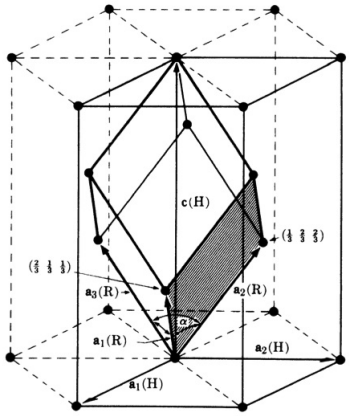

et al.[39] shows XRD patterns of natural graphite containing rhombohedral layers, compared to a sample without the presence of rhombohedral graphite. The rhombohedral peaks are labelled with R.

Figure 4.9: Comparison of graphite samples with and without rhombohedral stacking

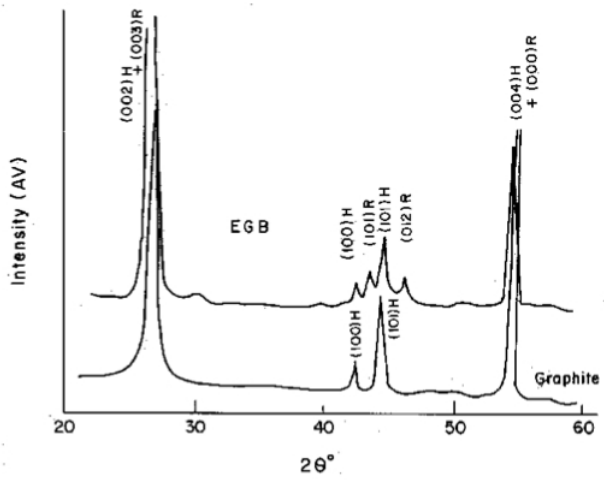

Figure (4.10) is an XRD measurement of natural graphite taken by Ong and Yang[40] which also labels rhombohedral peaks.

Both of these figures show the R101 and R012 peaks at approximately 43° and 46° which are common to all samples containing a detectable fraction of

Figure 4.10: A natural graphite sample containing rhombohedral stacking[40]

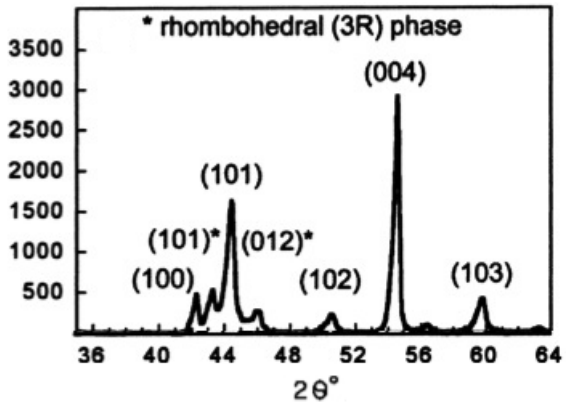

rhombohedral graphite. Other peaks of rhombohedral graphite such as the 00l reflections are so close to hexagonal graphite reflections that these hexagonal peaks dominate. Parthasarathy *et al.* estimated the proportion of rhombohedral graphite in their sample to be 20-25%, by comparison of the intensity ratios for the 101 peaks of both forms.

The distance between planes in a material d can be calculated if the lattice parameters, which can be found from XRD measurements, are known. The d equation for the hexagonal cell is

$$d_{hkl} = \frac{1}{\sqrt{\frac{4}{3}a^2(h^2+k^2+hk)+\frac{l^2}{c^2}}} \tag{4.3}$$

where a and c are lattice parameters, h, k and l are set to the relevant index to find the distances required. The d spacing for rhombohedral cells can also be found. The following equation is taken from Klug[41].

$$d_{hkl} = \frac{a}{\sqrt{\frac{(h^2+k^2+l^2)\sin^2\alpha+2(hk+hl+kl)(\cos^2\alpha+\cos\alpha)}{1+2cos^3\alpha-3\cos^2\alpha}}} \tag{4.4}$$

Hexagonal lattice parameters can be converted to rhombohedral using the fol-

lowing equations[41].

$$a_R = \frac{1}{3}\sqrt{3a_H^2 + c^2} \tag{4.5}$$

$$\sin\frac{\alpha}{2} = \frac{3}{2\sqrt{3 + (c/a_H)^2}} \tag{4.6}$$

4.2 Analysis of Natural Graphite

Figure 4.11: Low intensity detail of XRD patterns from untreated Branwell graphites, as received, taken with D-5000 diffractometer, CuKa radiation. Data has been normalised to the (002) reflections

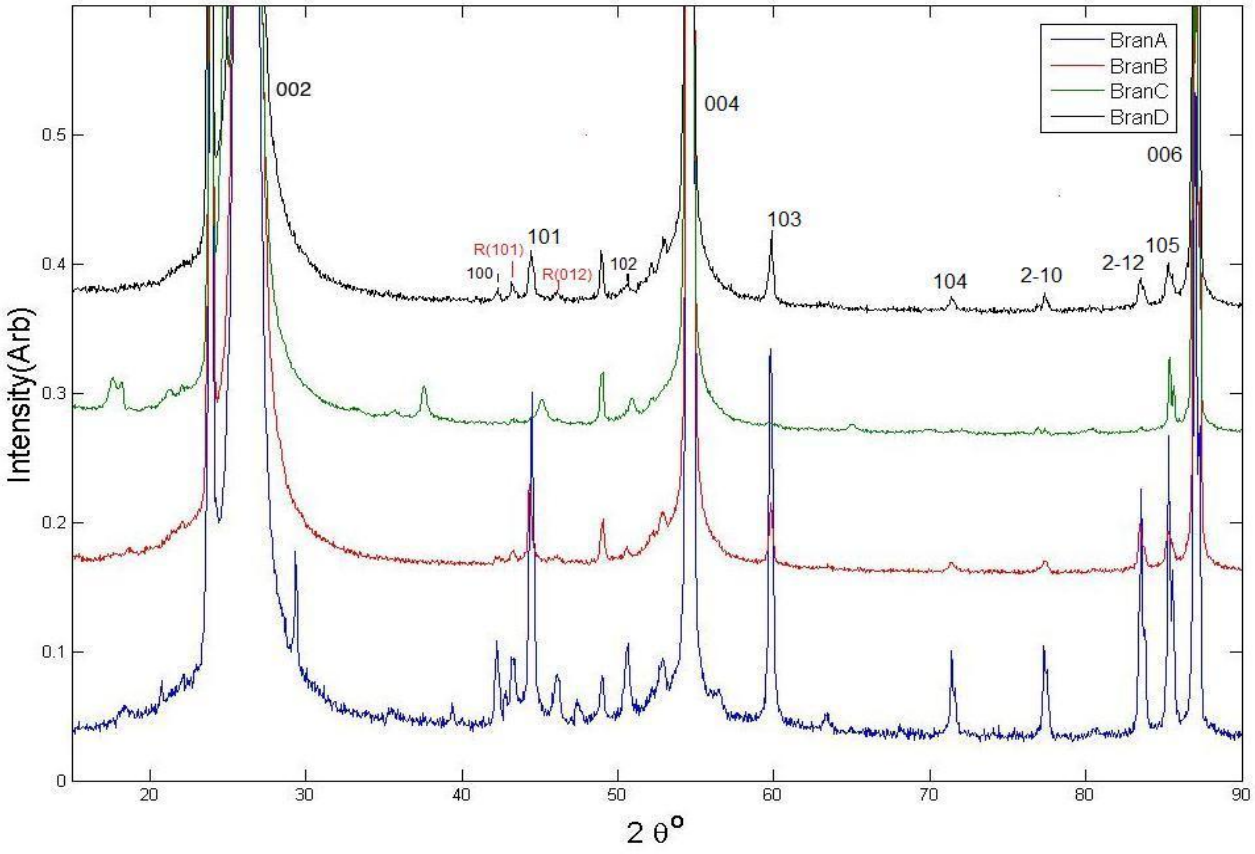

Natural graphite typically contains examples of different types of graphite structures. Four natural graphite samples were provided by Branwell Graphite

which were labelled A, B, C and D. For analysis of the graphite samples graphs will be presented in terms of 2θ for ease of comparison with other examples. All of the structural data for the Branwell graphites was taken with a CuKa radiation powder XRD diffractometer.

In figure (4.11) all of the peaks which fit hexagonal or rhombohedral graphite are indexed. The peaks without indices do not fit any known graphite structures. The peaks in Branwell A and Branwell C at 18° are likely to be defects with long range order rather than impurities, as typical impurities such as metals have smaller lattice parameters than graphite. Rhombohedral peaks are visible in all the samples other than Branwell C, and a large peak attached to the left of 002 peak is present in all of the samples. They were analysed by Keens[1] for the likelihood of successful C60 intercalation.

4.2.1 Previous Analysis

The structure of the Branwell Graphites was analysed by Keens[1], who wanted to ascertain which specimen would be most suitable for C60 intercalation. It was decided that purity and disorder were the most important characteristics, with high purity and high disorder being desirable. The samples were analysed using electron microscopy to check the visual structure at nanometer scale and with XRD to check the bulk structure.

The interlayer spacing of the graphites was found from equation (4.3) In the cases of Branwell B and Branwell D the distance between layers was found to be 3.3645 Å and 3.3595 Å respectively by Keens, these slight increases on the standard interlayer value suggesting some turbostratic nature to the samples with Branwell B showing this more. The p values of the Branwell graphites was then calculated from these values.

Below we have a comparison of the interlayer spacing and p value of the

graphite samples analysed by Keens values quoted above.

Table 4.1: Interlayer distances and p values for Branwell graphites found by Keens[1].

Graphite	Interlayer Distance (Å)	p value
Branwell A	3.3695	0.425
Branwell B	3.3636	0.349
Branwell C	3.3645	0.349
Branwell D	3.3693	0.253

Branwell A has high disorder but also has high quantities of impurities as shown by the unindexed peaks in the XRD data making it unsuitable for intercalation. Branwell C has an average level of disorder for the samples and also has impurities shown in the XRD data and so was deemed unsuitable. Branwell D has a low level of impurities but also a low level of disorder, thus Branwell B was chosen for intercalation as it best matched the criteria of low levels of impurities and high disorder needed.

4.2.2 New Analysis

In this analysis we will mainly focus on the Branwell B and D samples for similar reasons to those given above. Branwell D graphite was chosen as a candidate for study as a good example of natural graphite due to the low levels of impurities in the material and the presence of rhombohedral graphite. It also has a similar structure to Branwell B and so provides a good comparison for further studies to the altered materials which arise from Branwell B.

Branwell B was sourced in China and is 98% carbon. Branwell D was found in Zimbabwe and is more than 99% carbon. The XRD data gathered by Keens was analysed further as it was to be used as supporting information for the neutron scattering data analysed later in this work. The rhombohedral and unexplained XRD peaks were of particular interest in this analysis, as well as changes in peak intensity due to disorder.

Figure 4.12: Comparison of the XRD patterns of Branwell D and B graphite

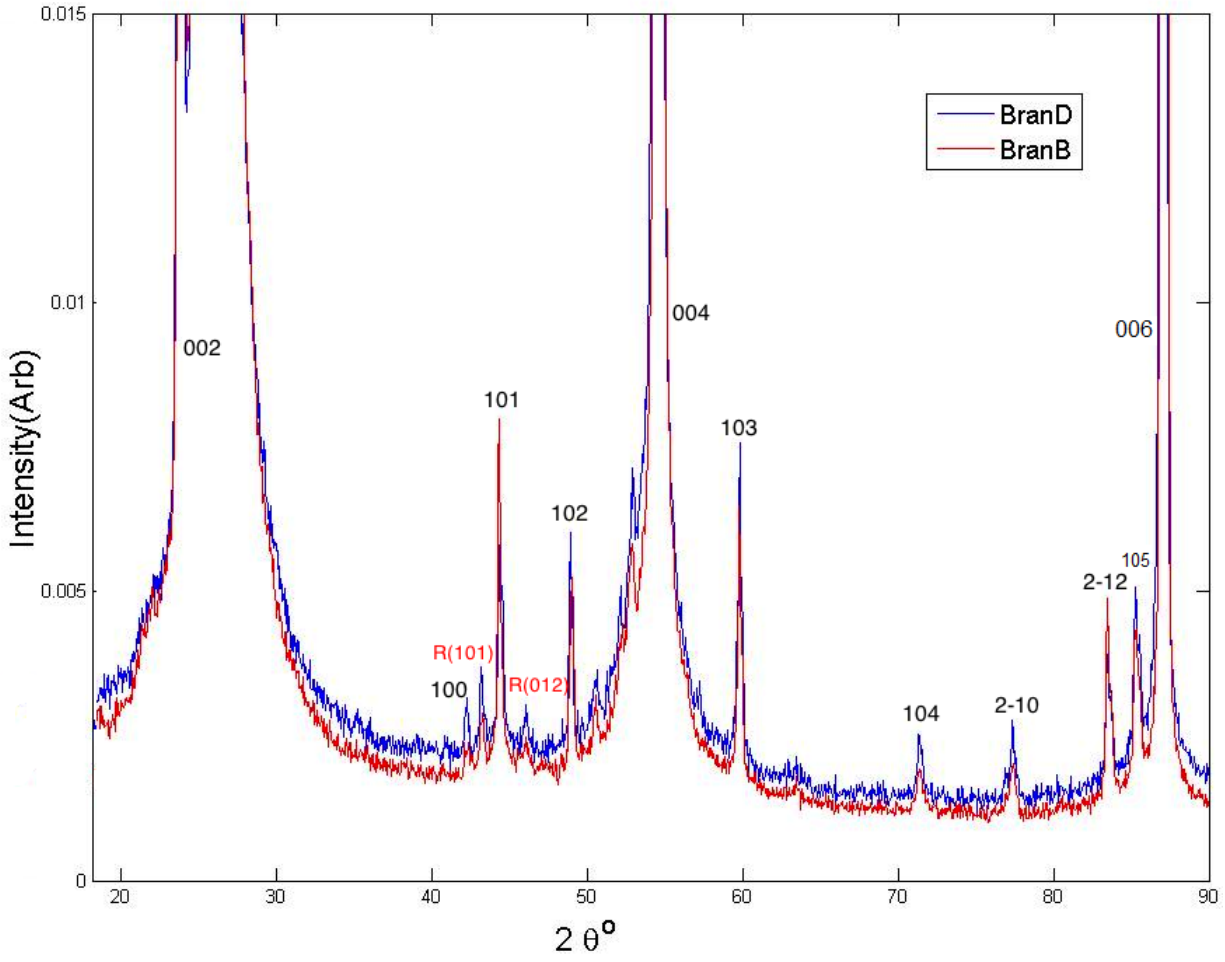

Figure 4.12 shows a direct comparison of the XRD patterns of Branwell D and Branwell B graphite. Visually these patterns seem very similar, with a deviation at around 58° where Branwell D shows a small peak that is not present in the Branwell B graph, probably due to impurities in the material. The indexing clarifies the existence of rhombohedral graphite in the sample and highlights the presence of impurities in the material.

Table (4.2) shows a comparison of the interlayer spacing and p value of the graphite samples analysed. These values have been recalculated and thus differ slightly from the Keens values quoted above.

The peak measurements for Branwell B and D graphite give increases in the

Table 4.2: Interlayer distances and p values for different graphites

Graphite	Interlayer Distance (Å)	p value
Hexagonal	3.354	0
Rhombohedral	3.354	0
Branwell B	3.3613	0.29
Branwell D	3.367	0.39
Expanded Graphite	3.3818	0.57

interlayer distance of perfect graphite of 0.0073 Å and 0.013 Å respectively.

4.2.3 Rhombohedral Lattice Parameters

Rhombohedral graphite was first reported by Lipson and Stokes[42] who described a R-3mr symmetry with a=3.635 Å and $\alpha = 39.49°$. This is equal to a hexagonal structure where a=2.456 Å and c=10.044 Å. This gives an interlayer distance S of 3.348 Å which is slightly smaller than the current accepted value of 3.354 Å. The graphite studied was described as artificial but they mentioned that the rhombohedral structure seems to be present in natural graphite in the same proportions as their sample, which they give as 14% rhombohedral, 6% disordered and 80% hexagonal.

As previously mentioned the currently accepted lattice parameters are a $D_{3d^5} - R\bar{3}m$ structure with a=2.566 Å and c=10.062 Å as found in the IUPAC Compendium of Chemical Terminology (1997) giving a interlayer value of 3.354 Å matching that of hexagonal graphite.

The XRD simulation routine Reflex in Materials Studio was used in conjugation with the equation

$$d_{hkl} = \frac{1}{\sqrt{\frac{4}{3}a^2(h^2 + k^2 + hk) + \frac{l^2}{c^2}}} \tag{4.7}$$

to analyse the rhombohedral content of the Branwell graphites.

The Branwell graphite samples which contain detectable rhombohedral peaks show them at around 43.3°, 46.1° and 63.2° for the 101, 102 and 105 reflections respectively. Models were created in Materials Studio to check the fit of the rhombohedral peaks with those predicted by IUPAC. The models had atomic bases at $\pm(u,u,u)$ where u is $\frac{1}{6}$ for the rhombohedral lattice as suggested by Lipson and Stokes[42] and the Naval Research Laboratory Crystal Lattice Structure database.

Figure 4.13: Rhombohedral graphite structure created with IUPAC dimensions for the creation of XRD simulations.

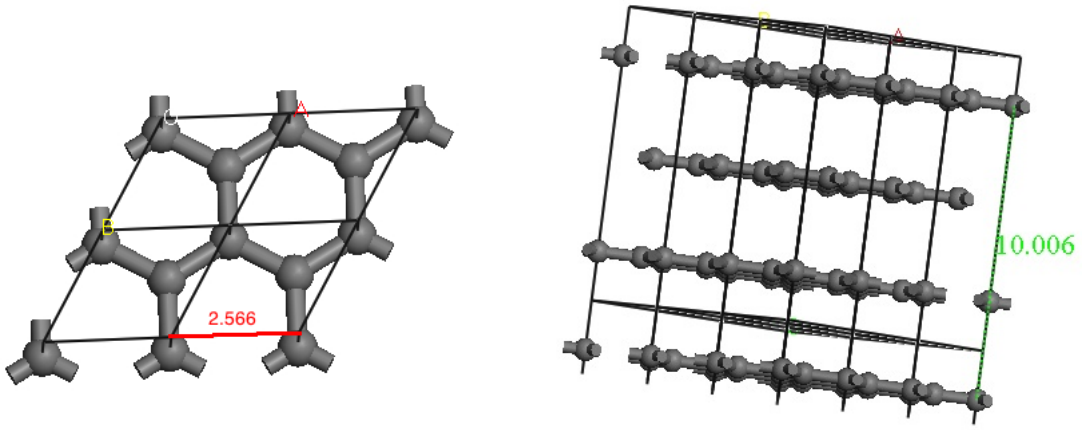

(a) Rhombohedral graphite model viewed normal to the graphite planes with the *a* lattice parameter shown in red

(b) Rhombohedral graphite model viewed parallel to the graphite planes with the *c* lattice parameter shown in green.

Using the IUPAC values for rhombohedral graphite peaks would be expected at 41.6° for 101 and 44.6° for 102 reflections. As the peaks did not fit well with the indices predicted by IUPAC, being around 1.5° larger which corresponds to a 10% change in *c* dimension, a literature search was performed to see if the peaks found by others matched or disagreed with the Branwell peaks.

Five papers with graphite XRD patterns containing rhombohedral peaks were chosen for comparison. These were: Soneda *et al.*[43] shown in figure (4.14a). Kohs *et al.*[44] shown in figure (4.14b, Parthasarathy *et al.*[39] shown in figure (4.14c), Touzain *et al.*[34] shown in figure (4.14d) and Matuyama *et al.*[45]shown

in figure (4.15). These papers include both natural and manufactured graphite samples.

Figure 4.14: XRD peaks of graphite samples containing rhombohedral stacking in terms of 2θ.

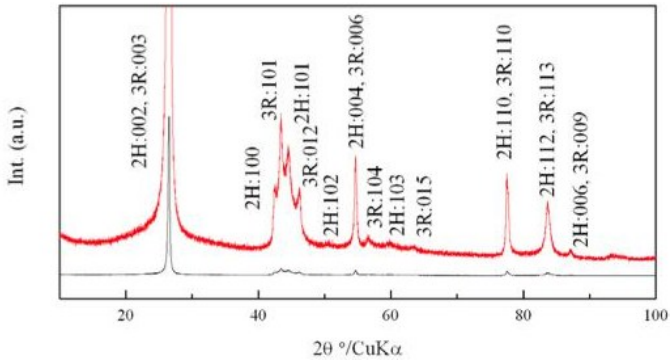

(a) Graphite nanofibers containing rhombohedral stacking

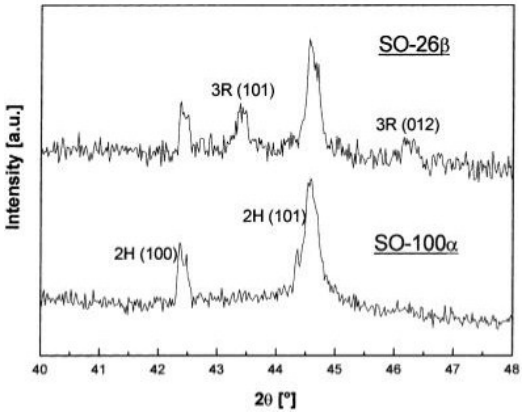

(b) Comparison of graphite anodes containing and not containing rhombohedral stacking

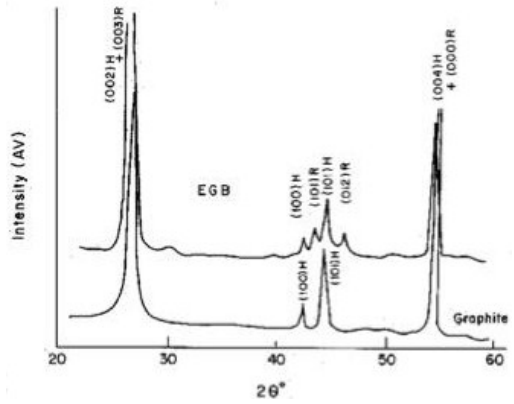

(c) Natural graphite containing rhombohedral stacking compared to graphite without

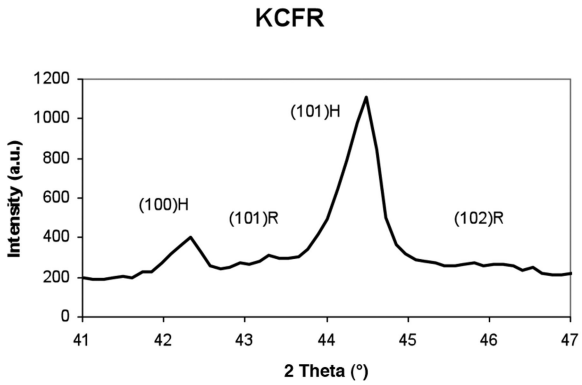

(d) Natural graphite containing rhombohedral stacking

None of the papers suggested a difference in interlayer distance from hexagonal graphite and several mentioned that rhombohedral graphite has the same interlayer spacing as hexagonal.

All of the figures from literature show rhombohedral peaks within 0.5° of the Branwell peaks, and thus show disagreement of around 1.5° of the predicted IUPAC values.

Figure 4.15: XRD peaks of a graphite sample containing rhombohedral stacking 1/d

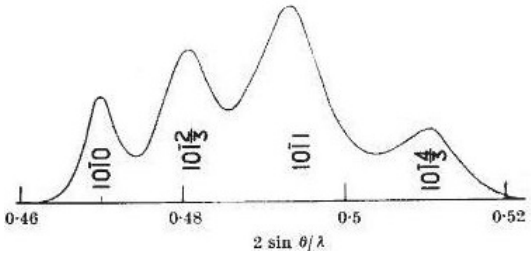

An estimate of interlayer spacing for the rhombohedral structures in these graphites can be made. However as the peak positions are taken from the figures these values will not be highly accurate but will give enough information for comparison with the Branwell graphites. The results of S spacing calculations using d_{khl} values derived from the peak positions in the XRD patterns is shown below. The error in the estimates from literature is around $\pm$ 0.5 Å.

Table 4.3: S parameters from XRD peaks with *a* set to 2.566 Å

hkl	Branwell Mean	Soneda	Kohs	Parthasatly	Touzain	Matuyama	Average
101 S	2.10 Å	2.05 Å	2.01 Å	2.19 Å	2.22 Å	1.99 Å	2.10 Å
102 S	2.81 Å	2.86 Å	2.83 Å	2.86 Å	2.91 Å	2.65 Å	2.82 Å
105 S	3.25 Å	3.286 Å	N/A	N/A	N/A	N/A	3.266 Å

For the first calculation the *a* parameter used was the IUPAC value as it was assumed that the *a* lattice value for rhombohedral graphite would remain fixed as this bond is much stronger than that between the layers and any change in dimension would be confined to the *c* direction.

It is obvious that these values are drastically smaller than the 3.354 Å value expected, with the calculated distance increasing at higher reflections. As these values were so far from those expected the calculations were repeated using the hexagonal *a* lattice parameter. As the *a* value only applies to atoms within the layer there seems to be no reason why it would differ from hexagonal to rhombohedral stacking. The IUPAC value also gives a nearest neighbour distance of 1.482 Å, when the hexagonal graphite value is 1.420 Å. The Lipson

and Stokes *a* parameter gives a nearest neighbour distance much closer to that of hexagonal graphite. The increase in nearest neighbour distance for rhombohedral graphite given by IUPAC is likely to be unphysical as the graphite structure is very stable in the plane.

Repeating the calculation with the hexagonal graphite parameter of a=2.461 Å gave results much closer to the expected value.

Table 4.4: S parameters from XRD peaks with a set to 2.461 Å

hkl	Branwell Mean	Soneda	Kohs	Parthasatly	Touzain	Matuyama	Average
101 S	3.75 Å	4.14 Å	3.53 Å	4.32 Å	4.76 Å	3.27 Å	3.87 Å
102 S	3.39 Å	3.48 Å	3.43 Å	3.48 Å	3.57 Å	3.12 Å	3.41 Å
105 S	3.37 Å	3.41 Å	N/A	N/A	N/A	N/A	3.38 Å

This demonstrates that the IUPAC a value is incorrect if using an atomic basis of $\pm(\frac{1}{6}, \frac{1}{6}, \frac{1}{6})$ and that the standard hexagonal a value can be used to analyse the structure of rhombohedral graphite in the Branwell samples. Thus we will continue our analysis using this value.

Figure 4.16: Comparison of the area containing rhombohedral peaks in exfoliated and natural Branwell B graphite XRD

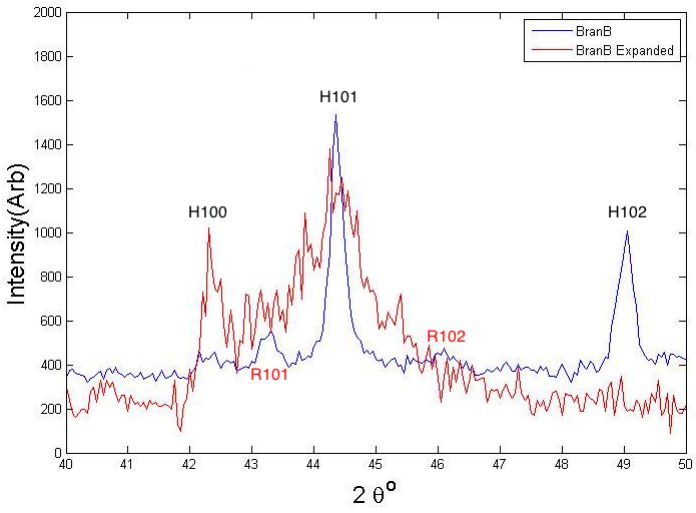

Lattice parameters for rhombohedral graphite were found by Keens in the exfoliated graphite using GSAS profile refinement. For Branwell B exfoliated

α was found to be 39.1468° and a=3.8069 Å, giving hexagonal parameters of a= 2.5507 Å and c= 10.5316 Å and thus an interlayer spacing of 3.5105 Å, this fits well with the values found for the rhombohedral peaks in Branwell B. However the evidence for rhombohedral peaks in the exfoliated sample is unconvincing as shown in the figure (4.16).

The first attempt at finding the dimensions of rhombohedral graphite in the Branwell samples used the peak positions for different indices along with the d_{hkl} equation. This equation is very sensitive to small changes in peak position, a 1% change in peak position translates to a 10% change in the S value calculated hence the errors in the individual S values are quite large. The peaks also vary in their sharpness making it difficult to obtain accurate values for peak position. Plotting the S values found with both a parameters shows how the calculated parameter is affected by index and a parameter.

Figure 4.17: S values calculated from Branwell graphite and literature rhombohedral peaks. Points were calculated using the hexagonal a parameter

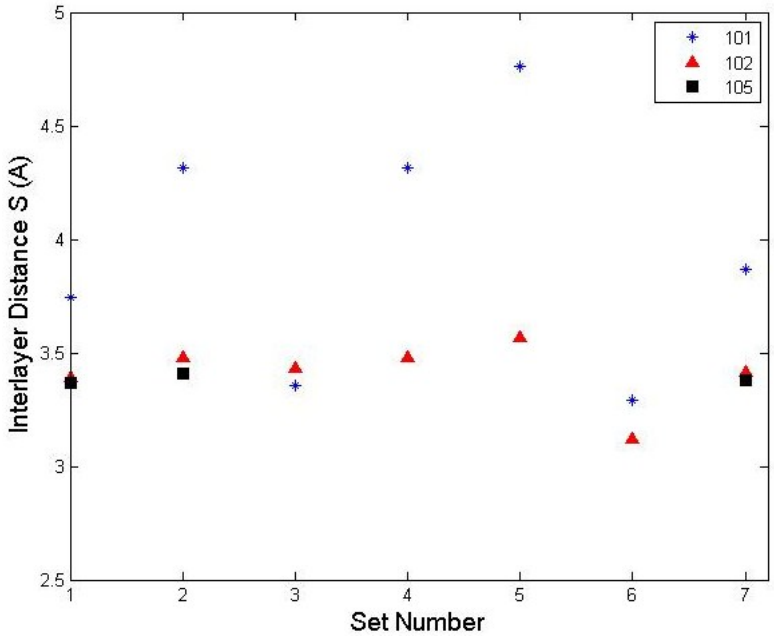

For figure (4.17) set 1 is the average Branwell graphite peak, sets 2 to 7 are the

literature values in the order of the tables above thus set 4 is Soneda and so on. The graph shows that the majority of the measurements using the hexagonal *a* parameter give an S value between 3 Å and 5 Å.

From this analysis it seems that the interlayer spacing of rhombohedral graphite is larger than that of hexagonal, however the estimated literature values can not be relied upon as the errors will be too large. We need to find a value for the interlayer spacing in the Branwell graphites as we have the raw diffraction data for these samples.

Figure 4.18: Interlayer spacing calculated for the Branwell graphites with error bars

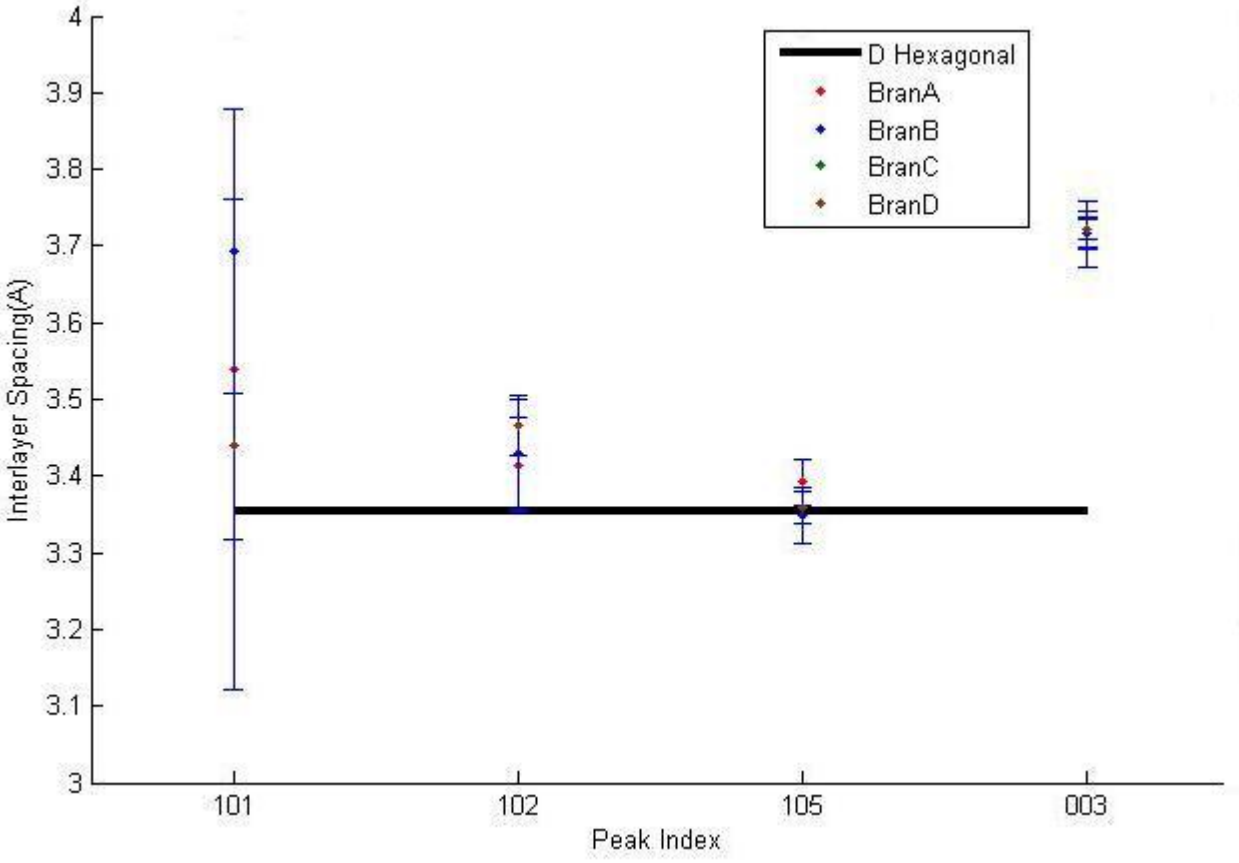

Figure (4.18) shows the interlayer spacing calculated from each sample's rhombohedral peaks. The 101 peak gives a much larger error in the interlayer spacing value although, as shown below, errors in the peak position are similar for

all the indices. Figure (4.19) shows the d values of the peaks taken directly from the XRD measurements.

Figure 4.19: Peak positions of rhombohedral planes with error bars

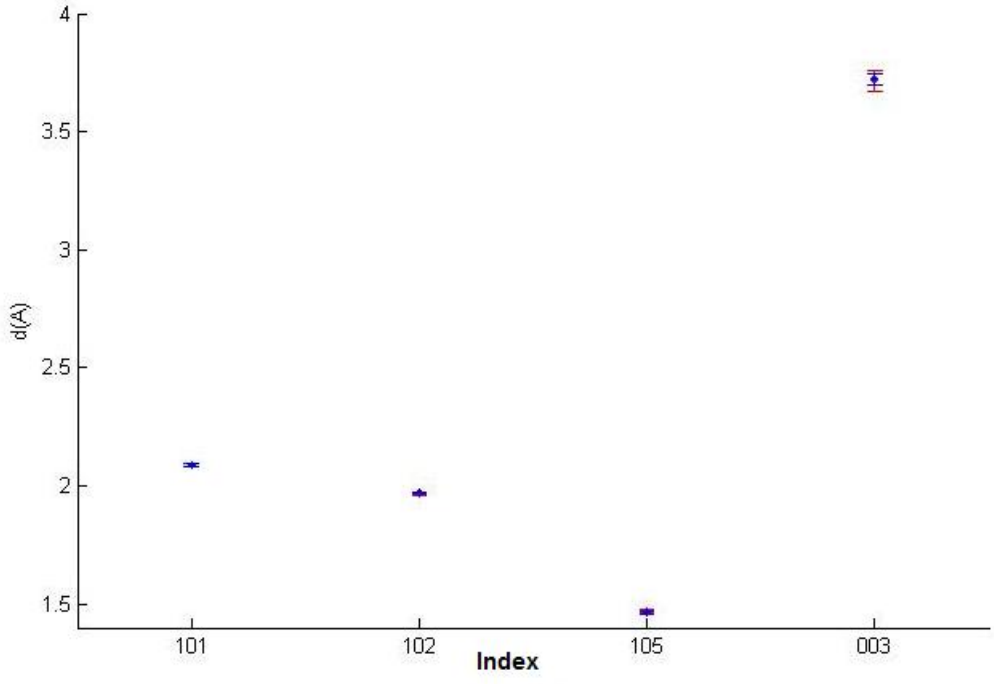

Table 4.5: c values derived from rhombohedral peaks

hkl	Branwell B (Å)	Branwell D (Å)
101	3.503	3.760
102	3.428	3.616
105	3.366	3.361

We have several candidates therefore when defining the rhombohedral c lattice parameter in the Branwell graphites. The average from the values of Branwell B and D give an interlayer value of 3.529 Å, which is greater than that of turbostratic graphite. The values from Branwell B have the highest agreement between themselves and give an average interlayer of 3.442 Å which is similar to the turbostratic value. The lowest possible estimate comes from the Branwell D 105 value which gives an interlayer value of 3.361 Å, which is again higher than the standard hexagonal graphite value but fits within turbostractic bounds.

Due to the variance in values obtained looking at individual peaks GSAS was used to perform a Rietveld refinement on the A B and D samples.

The results of this analysis gave interlayer values of 3.396 Å, 3.397 Å and 3.375 Å for A,B and D respectively. The full values obtained are shown in table 4.6.

Comparison of calculated and measured peak positions show some disagreement however, as shown in figure (4.20).

Table 4.6: Lattice Parameter *a*, interlayer distance S and *p* value of rhombohedral graphite in the Branwell samples calculated with GSAS

Sample	*a* (Å)	S (Å)	*p*
Ideal	2.461	3.354	0
Branwell A	2.464	3.396	0.6988
Branwell B	2.460	3.397	0.7071
Branwell D	2.464	3.375	0.4942

Figure 4.20: GSAS matches to Branwell graphite peaks

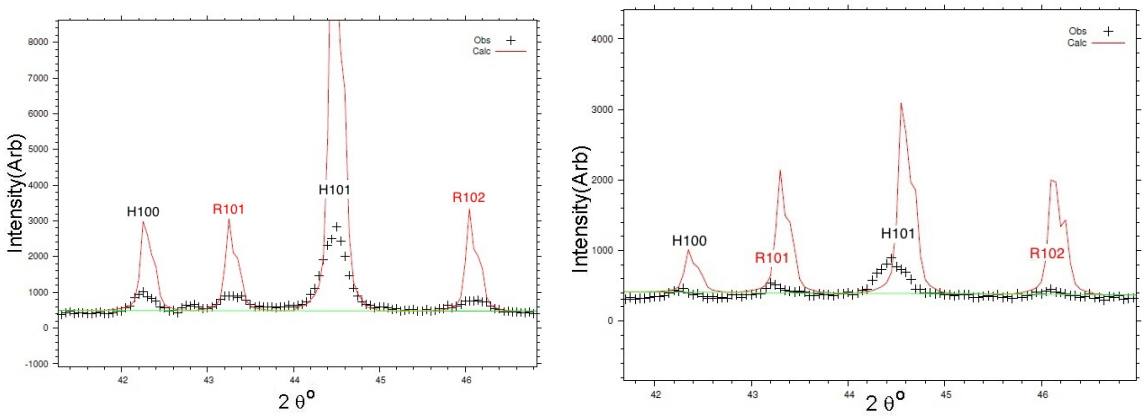

(a) GSAS fits to Branwell A graphite peaks **(b)** GSAS fits to Branwell D graphite peaks

These fits show that although the 002 hexagonal peak in the Branwell graphites is well defined the 101 peaks of both the hexagonal and rhombohedral stacking are broad and tend towards high interlayer spacing, assuming that the *a* parameter is unaffected. As discussed in the later Interlayer Distance Analysis section, the proof for a larger *a* parameter is not present.

Due to an issue with the validity of some peaks before the hexagonal 002, new XRD measurements of the Branwell D graphite were taken. The details

of these experiments are given in a later section. In these measurements the rhombohedral peaks of the Branwell D are shown to resolve into two peaks.

Figure 4.21: XRD of Branwell D showing the results of new measurements

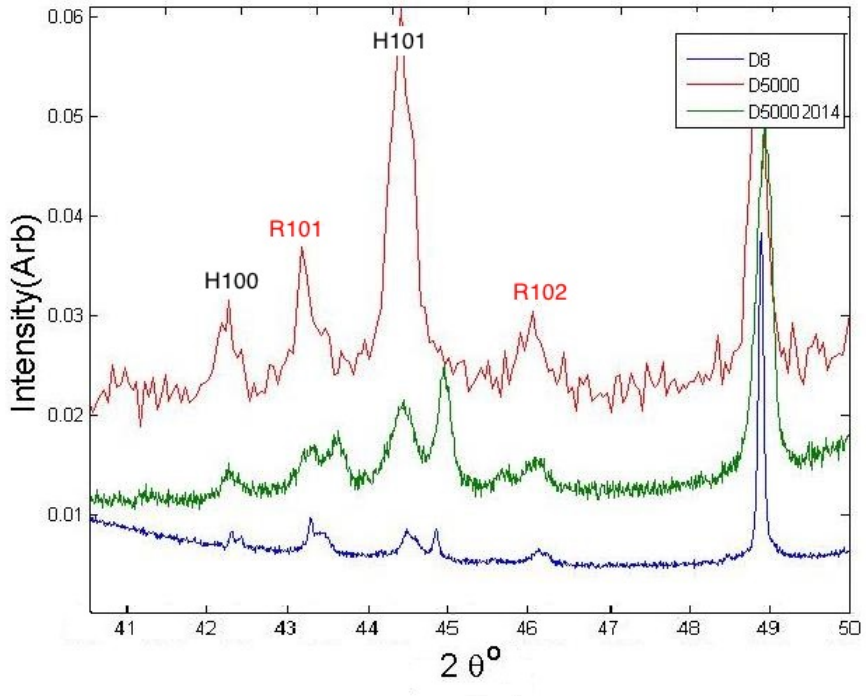

This suggests that there is more than one phase of rhombohedral graphite in the sample. The two peaks are shown in measurements from two separate instruments and fit the ranges shown by the original measurements. If these separate peaks were also present in the other Branwell samples this would explain the errors and range in the rhombohedral interlayer values present in the samples. This also explains the difficulty with obtaining good GSAS fits.

Bringing this information together therefore points to two possible solutions for the rhombohedral parameters found in the Branwell graphites. The large interlayer distances could be due to a mixture of high disorder and different phases of graphite together with errors due to the lack of an 00X peak for the rhombohedral graphite. It is also possible that Rhombohedral graphites tend to have larger interlayer spacing than hexagonal. Some evidence of this can be

found in (4.22) by Wang *et al.*[46].

Figure 4.22: XRD measurements of graphite at different pressures

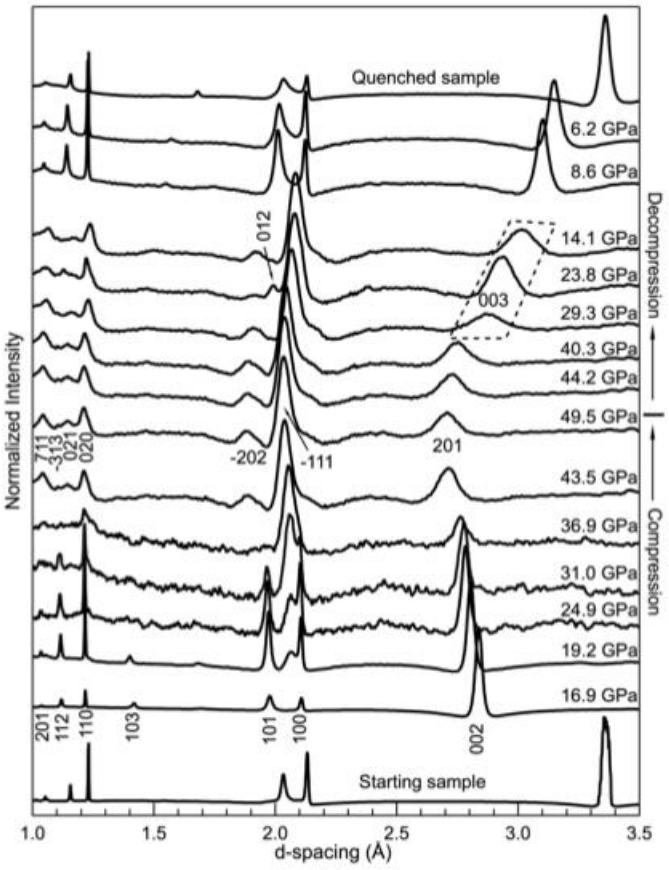

In figure (4.22) 002 is the hexagonal graphite *d* spacing, the peaks enclosed by the dashed 003 area are interpreted as rhombohedral peaks. For this experiment a graphite sample was put under pressure and a synchrotron XRD measurement was taken at different points of compression and decompression. The figure shows the 003 *d* spacing as larger than the 002 *d* spacing at similar pressures. Nuske *et al.*[47] also has rhombohedral peaks which suggest an interlayer spacing of between 3.4 and 3.5 Å.

Whether deliberately formed or naturally occurring, rhombohedral layers will form in the most disordered or stressed areas of the graphite. Due to this it would follow that in the majority of cases rhombohedral graphite has a larger

interlayer spacing than hexagonal graphite. More work specifically on rhombohedral graphites would have to be undertaken to see if this is the case for all rhombohedral graphites. Finding lattice parameters is especially difficult as rhombohedral graphite lacks the visible 00X peaks of the hexagonal graphite which allow the interlayer spacing for the bulk of the material to be measured, without being affected by the *a* parameter. In the case of the Branwell graphites the calculated interlayer spacing for rhombohedral stacking is around 0.03 Å higher than the standard value.

4.2.4 Interlayer Distance Analysis

All of the Branwell samples contain a peak at around 23.9° including the Branwell C sample which shows no rhombohedral peaks. We shall refer to this peak as '23'. It comes before the hexagonal 002 peak and corresponds to a *d* spacing of 3.723 Å. This is substantially larger than the interlayer spacing in graphite and does not match any typical impurities found in graphite such as transition metals. We will therefore need to investigate possible origins of this peak.

One possibility is that this is the 003 peak of the rhombohedral graphite in the samples. The peak does give a similar interlayer spacing value to that given by the rhombohedral 101 peak but there are several issues with this assumption. Firstly this peak is also present in the Branwell C sample which shows no other signs of rhombohedral graphite. In the samples which do show rhombohedral stacking the 101 spacing values have large error bounds making it difficult to trust the figures given by the 101 peak.

The possible 003 peak also underestimates the quantity of rhombohedral graphite in the sample. Typically the proportion of rhombohedral graphite in a sample is taken from the ratio between the rhombohedral and hexagonal 101 peaks.

Figure 4.23: Peak before 002 in Branwell graphite samples

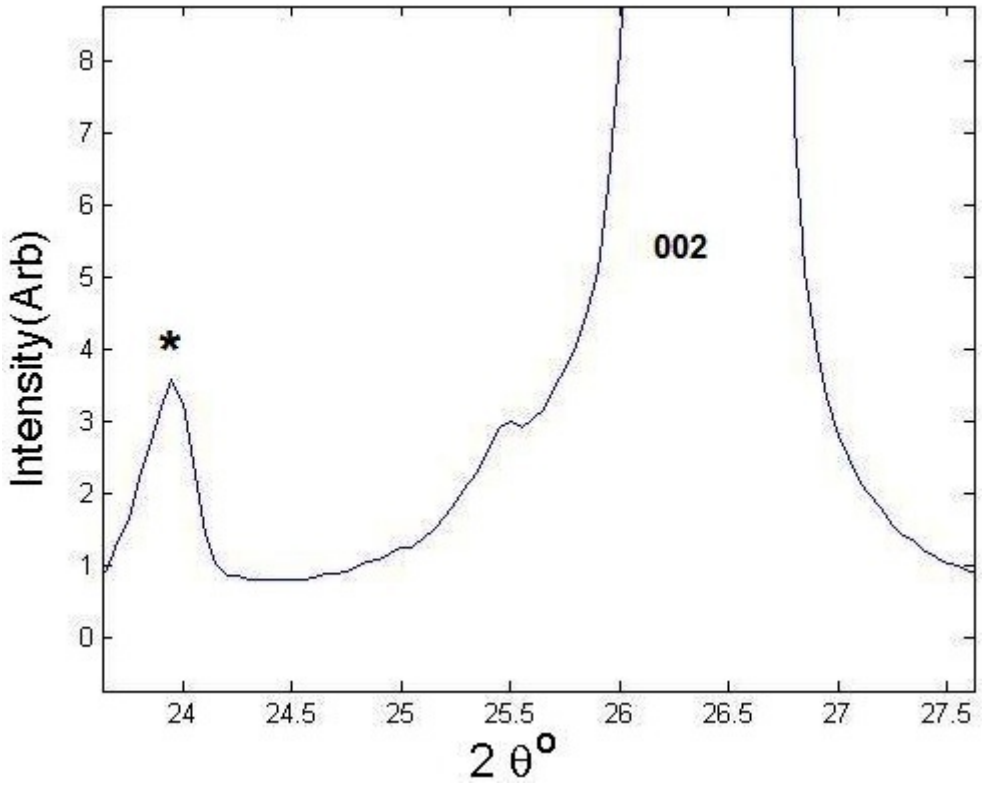

In the case of Branwell D the hexagonal 101 peak is 2.7 times higher than the rhombohedral peak, however the 002 peak is 129 times higher than this possible 003 peak indicating that this peak is either unrelated to rhombohedral graphite or only represents a small proportion of it.

The samples show a high level of agreement of intensity and position of this peak, with a difference of only 0.05° between samples. In contrast the 101 peaks of the samples show more variance on intensity and position. This suggests that the 23 peak is a 00X peak of graphite as it does not match the pattern shown by the 101 intensities for the samples. The 23 peak does not fit well with the intensities given by the 004 peaks for each sample but does correlate well with the pattern of positions shown.

Table 4.7: Comparison of peak position and intensity for Branwell graphites, where intensity is relative to the 002 peak.

	Branwell A	Branwell B	Branwell C	Branwell D
23 position	23.95°	23.95°	23.9°	23.9°
101 position	44.50°	44.35°	n/a	44.50°
004 position	54.65°	54.56°	54.55°	54.55°
23 intensity	0.89	0.77	0.86	0.72
101 intensity	0.30	0.08	n/a	0.06
004 intensity	4.70	5.58	5.70	7.14

Figure 4.24: XRD of all the Branwell samples highlighting the peak at 23.9°

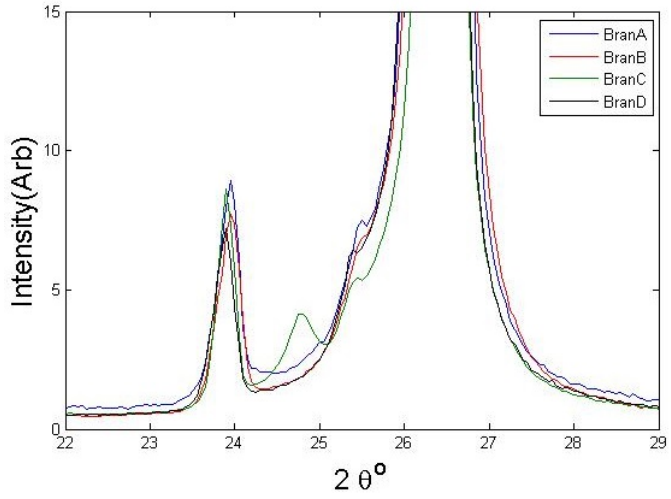

Figure 4.25: 101 peaks of the Branwell samples

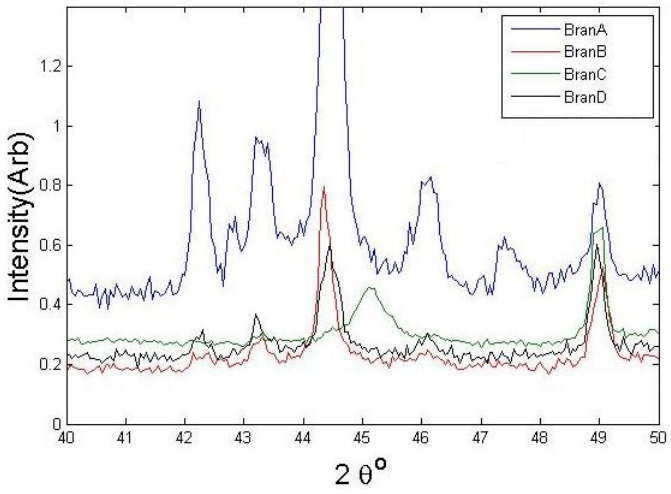

Due to the unusual agreement of position and intensity given by peak 23 in

samples which do not otherwise have much in common an investigation of whether this peak was an artifact was undertaken.

Data from the elastic line of a Poly CINS measurement of Branwell D did not show this peak, however spectrometers are poor diffractometers and cannot be relied upon to show fine detail.

Figure 4.26: Comparison of elastic line of poly-CINS measurement to XRD

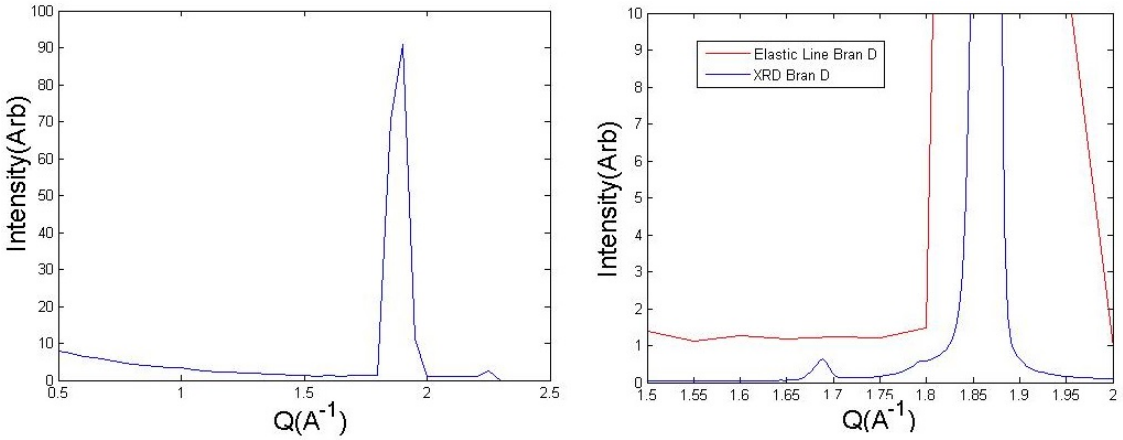

(a) IN5 poly-CINS elastic line measurement of Branwell D

(b) Elastic line measurement of Branwell D compared with XRD of Branwell D

An exfoliated sample of the Branwell B was measured on the same instrument under the same conditions as the Branwell samples.

Figure 4.27: 002 peak of exfoliated graphite

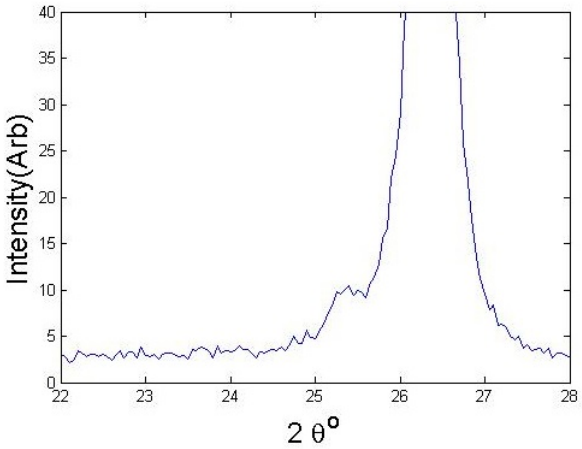

The exfoliated sample does not show the 23 peak, this suggests the peak is not

an artifact and could be annealed out, though this is not fully clear as the noise of the sample also removes fine detail of the peaks in the sample.

A measurement of Branwell D graphite was retaken for this work, three years after the original measurement on a more modern Siemens D5000 diffractometer and on a Bruker AXS D8 to ensure the feature was not due to an instrument artifact. Only the Branwell D was remeasured as unfortunately this was the only sample still available.

Figure 4.28: New measurements of Branwell D XRD

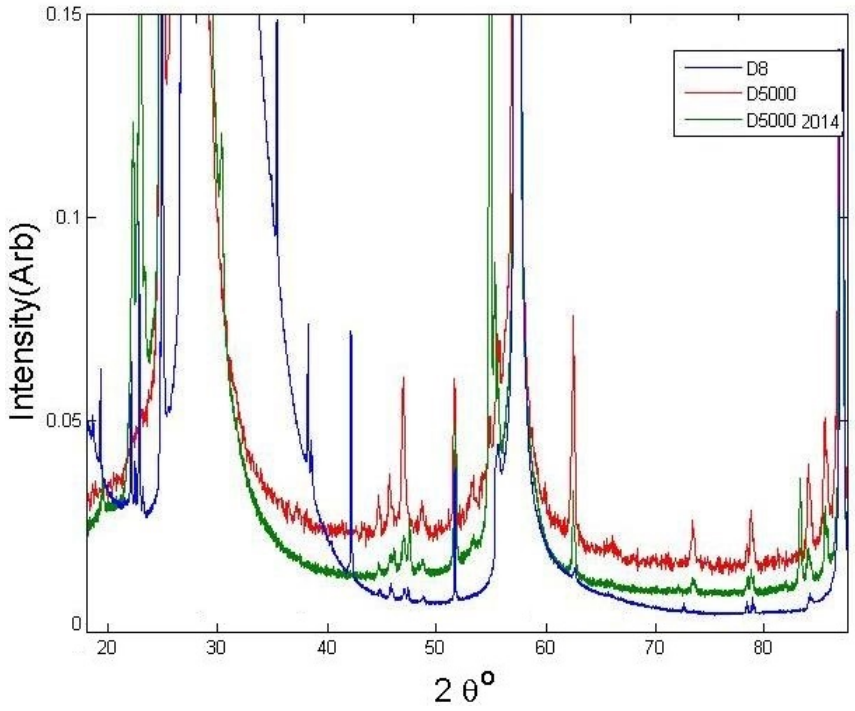

The D5000 measurements were taken by running the sample from 10 2θ to 90 2θ with a step size of 0.01 and step time of 25 seconds. The sample was prepared by packing directly into a standard holder. The D8 measurements were taken under the same criteria but silicon grease was used to secure the powder sample in this diffractometer. The D5000 has better optics than the D8 and thus gives a better peak shape, but the D8 has a better peak detection system.

Figure 4.29: Low 2θ new XRD data

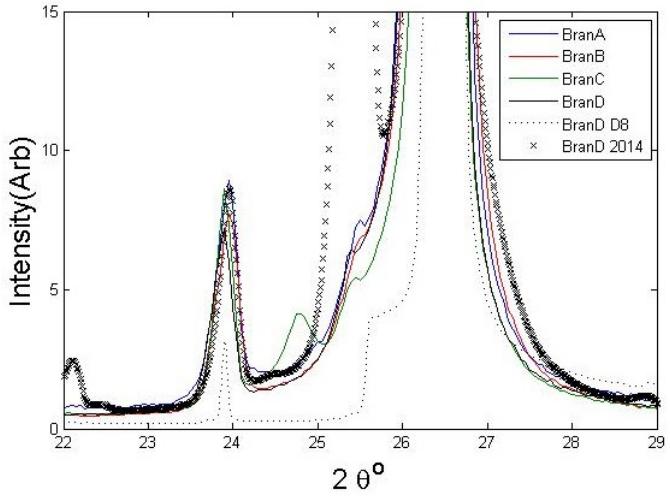

These measurements give a range of interlayer values for Branwell D, the original D5000 gave a value of 3.366 Å, the D8 gave 3.356 Å and the 2014 D5000 gave 3.361 Å. It can be assumed the 2014 value is the most accurate due to the superior optics. All the measurements still show the 23 peak indicating that it is not an instrument artifact. They also show additional peaks to the original measurement, for example the new D5000 highlights a peak at 25.4° which corresponds to a distance of 3.5039 Å. This peak is also present in the exfoliated sample.

Figure 4.30: Peak at 25.4° in exfoliated and Branwell B graphite

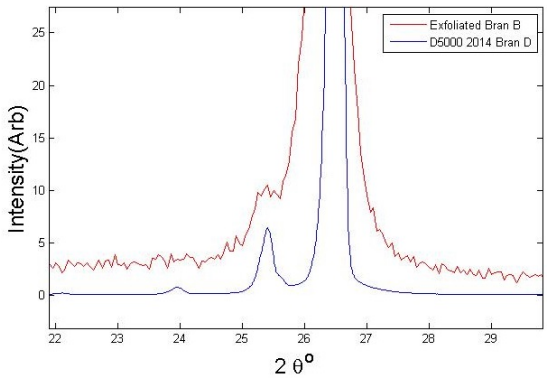

A peak is also shown before the 004 peak which would correspond to an inter-

Figure 4.31: 004 peaks of new XRD measurements

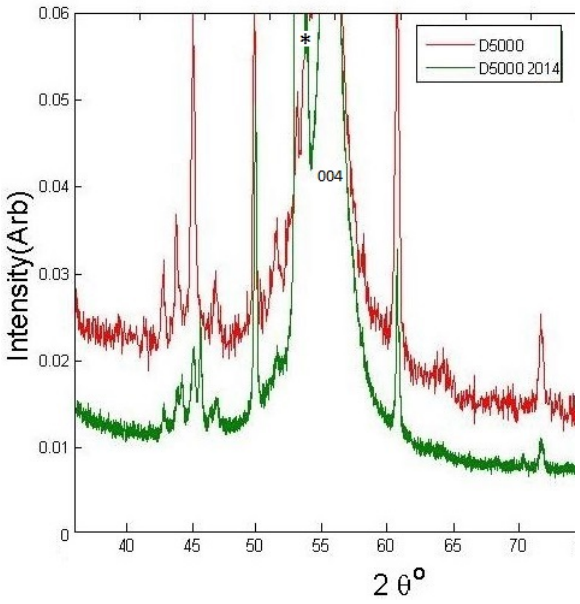

layer spacing of 3.512 Å. The 101 peaks of both hexagonal and rhombohederal graphite are resolved into two peaks in both the new measurements.

Figure 4.32: Peaks around 101 in new XRD measurements

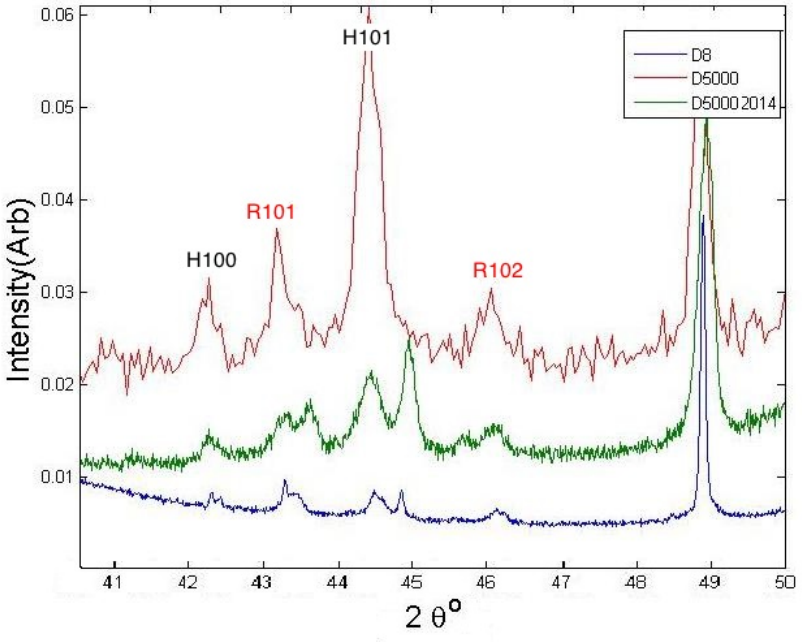

The splitting is most obvious in the hexagonal 101 peak but is not shown in

the 10X peaks from 102 to 105. Splitting is shown strongly in the hexagonal 2-12 peak and the rhombohedral 101, it is subtle in the rhombohedral 102.

The new XRD data shows there is a range of interlayer spacings in the hexagonal and rhombohedral stacking in Branwell D graphite. All the hexagonal 00X peaks show adjacent lower intensity peaks suggesting several areas of the graphite with a wider interlayer spacing than the bulk.

This also shows an effect in other peaks, but does not seem to affect those from in plane peaks such as the 100. Though it is possible there is a range of a parameters, they do not drastically affect the peaks shown. It is not possible to match any particular auxiliary peak to just the hexagonal or rhombohedral stacking as both show the same splitting of the 101 peaks. If we assume the other Branwell samples would show similar features to the Branwell D this range of interlayer spacings would explain the issues with finding good interlayer values from 101 peaks as well as the problems of characterising the rhombohedral stacking in the graphites.

4.2.5 Exfoliated Graphite

Branwell B was exfoliated by Keens[1] using an an acid mixture followed by thermal shock, resulting in a visible expansion of the material of around 30 times original size. X-ray analysis was performed under the same conditions of the previous experiments. This treatment has had several effects on the XRD pattern of the material.

The most obvious difference is the relative peak intensities, in figure (4.33) the diffraction patterns have been normalised to the 002 peak which highlights the increase in relative intensity of the non 00l peaks. In the case of the Branwell B graphite the 002 peak is 786 times higher than the 101 peak, whereas for the exfoliated graphite this is decreased to a difference of just 14 times.

Figure 4.33: XRD pattern of expanded Branwell B graphite, compared with the original sample, data normalised to the 002 peak

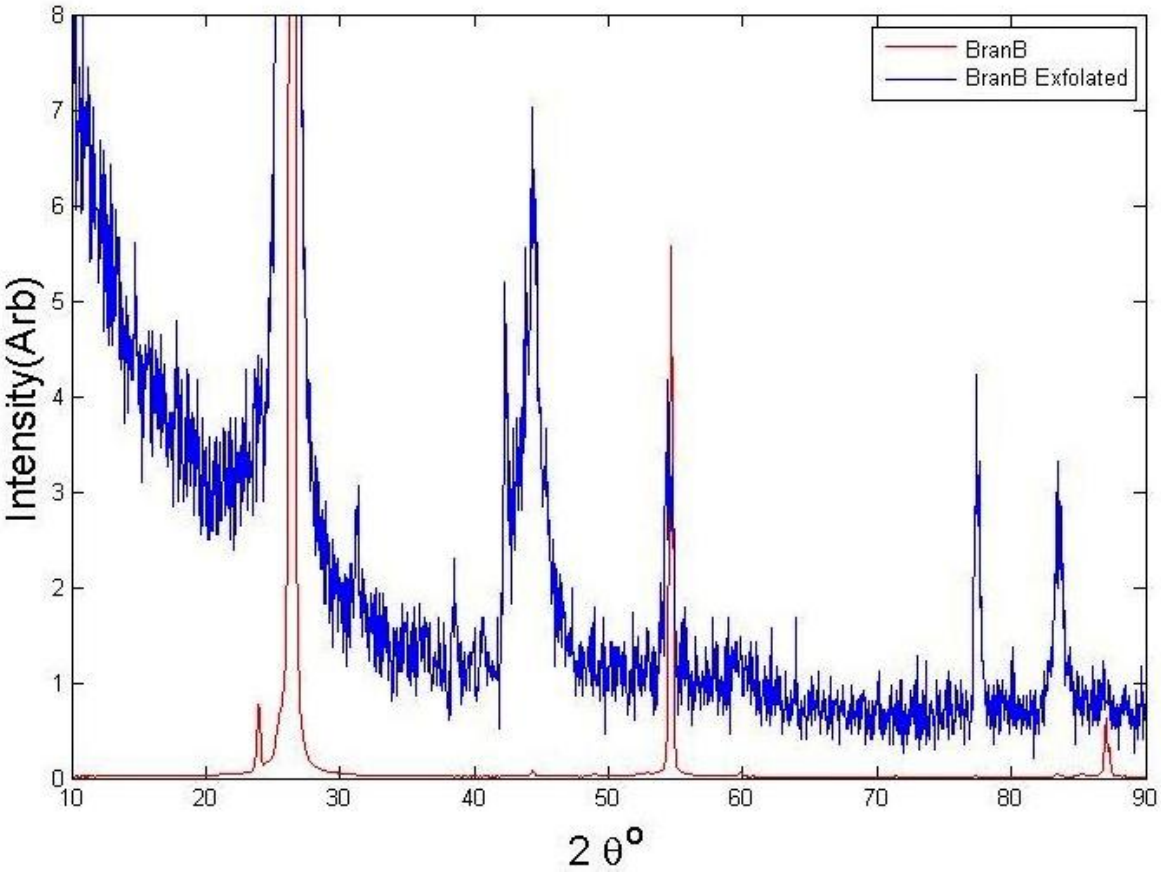

The difference in area between the 002 and 101 peaks for the exfoliated and Branwell B has also been calculated by multiplying the peak height with the width at half maximum. For Branwell B graphite the 002 peak is 340 ± 5 times the area of the 101. For exfoliated graphite the difference in peak areas is 18 ± 2 thus the intensity of the 002 peak has been reduced by an order of magnitude, or 19 times after exfoliation.

If we plot the expanded graphite with Branwell B at 50 times normal intensity we can see the effect exfoliation has had on the rest of the XRD pattern. The 100 and 101 peaks of the exfoliated sample are much less well defined and several peaks are missing entirely. The peaks have broadened indicating a much wider range of layer spacing in the material. The rhombohedral peaks are no

Figure 4.34: XRD pattern of exfoliated Branwell B graphite, compared with the original sample at fifty times the original intensity

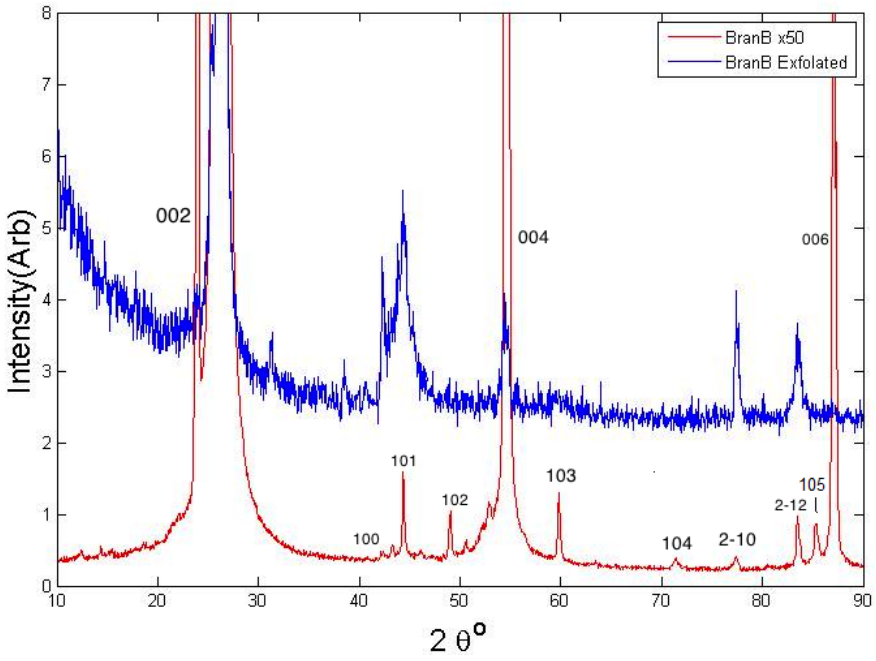

longer present, this could be due to the process changing the stacking of the rhombohedral areas or to the broadening of other peaks overlapping the rhomboheral peaks. In any case the sample no longer has detectable rhombohederal stacking.

The loss of 002 intensity could be attributed to a change in orientation of the sample compared to the Branwell sample, as the two samples had different particle shapes which would lead to different packing in the sample holder. However it is much more likely that the exfoliation process itself, with the weakening of the bonds between the layer, would give rise to fewer layers with the same distance between them, thus a reduction of intensity. This is also shown in the evolution of the change in peak intensity as the material moves further from the HOPG structure, with HOPG XRD showing 00*l* peaks almost to the exclusion of all others and other peaks becoming more prominent as the layers become less defined and well ordered.

We would like to determine if there is any evidence that the change in peak intensity is due to a change in the material rather than an orientation issue. As shown in table 4.1 above, the p value of exfoliated graphite is increased substantially. Given intensity data for the graphite samples we can check if p value has an effect on the relative intensity the 002 and 101 peaks. To do this we have set the intensity of the 002 peak to equal 100 for each sample, we can then compare p value to the intensity of the 101 peak.

Table 4.8: A comparison of 101 intensity to the p value of the material

Graphite	101 intensity	p value
Branwell A	0.312	0.425
Branwell B	0.07986	0.349
Branwell D	0.06076	0.253
Expanded Graphite	7.034	0.5686

Figure 4.35: Intensity of 101 Branwell graphite peaks vs p value

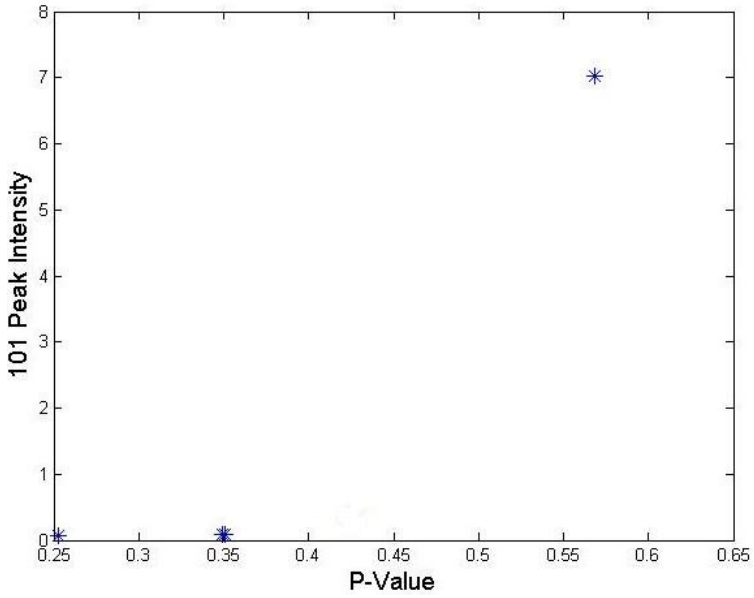

Figure 4.35 shows the relationship between p value and relative 101 intensity. The relationship seems to be exponential but more samples would be needed to prove this.

4.2.6 Summary of Branwell Graphite Structure Investigation

The investigation of the natural graphite samples has raised several important areas for discussion. The investigation started with information on previous analysis of the Branwell graphites and what was missed in this analysis. Some analysis was then repeated, during this problems were found with some assumptions such as the rhombohedral interlayer distance and unexplained peaks. The investigation of the rhombohedral stacking showed that the a lattice parameter given by IUPAC is incorrect assuming an atomic basis of $\pm(\frac{1}{6}, \frac{1}{6}, \frac{1}{6})$ and that the a parameter of hexagonal graphite also fits that of rhombohedral.

New measurements of Branwell D graphite showed that there are several areas in the natural graphite samples with larger than expected interlayer distances, some even exceeding those of turbostratic graphite. These also give almost complete splits of the 101 hexagonal and rhombohedral peaks, thus explaining the issues with getting good values from these peaks and showing that the different interlayer spacings are not confined to one type of stacking. The exfoliated sample shows that many of the distinct interlayer peaks are removed by exfoliation but not all. This sample also demonstrated the link between relative peak intensity and disorder.

The Branwell D and exfoliated graphite samples have been further analysed using inelastic neutron scattering as detailed in the Graphite poly-CINS chapter.

Chapter 5

Structure of C60 Graphite Intercalate

5.1 Background

Carbon can bond with up to four other atoms allowing a great flexibility in carbon based structures. Allotropes of carbon other than diamond and graphite had been proposed since the 1970s but were not discovered until the deliberate synthesis of C60 by Kroto *et al.*[48] in 1985. C60 is also known as Buckminsterfullerene, other spherical forms of carbon are known as fullerenes. Carbon molecules can also take on hollow tube forms known as carbon nanotubes. Fullerenes and nanotubes occur in nature and are stable, C60 is the most well known as it was the first to be synthesised and is the most common fullerene. Fullerenes are one of the products of soot[49] and evidence of C60 molecules has recently been found in space[50].

Solid C60 has a face centred cubic lattice structure in the space group Fm-3m with a lattice constant a of 14.154 Å at room temperature. Below 249 K this structure changes to a simple cubic lattice. This is discussed in detail in Heiney *et al.*[51]. Molecular C60 binds strongly with hydrogen if its structure

Figure 5.1: A single Buckminsterfullerene C60 molecule

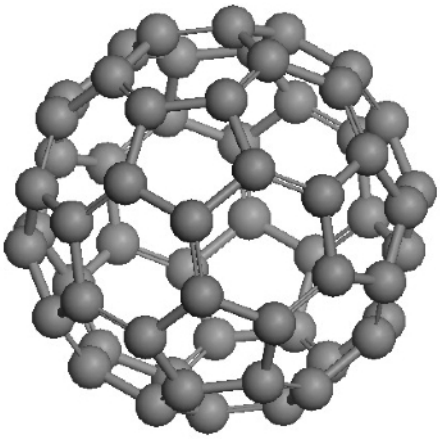

is modified such as by doping with transition metals[52].

The structure of graphite lends itself to the addition of molecules between the layers, providing natural pores for other materials to bind to. The addition of material within layers of graphite is known as intercalation. Graphite intercalation is typically used to improve the electronic properties of graphite, it is used in lithium ion batteries in the form of carbon monoflouride and in potassium ion batteries. Graphite also has a long history of investigation as a hydrogen storage medium due to its low weight, cost and toxicity. However in its pure state it is a poor hydrogen storage medium, its capacity is improved by increasing the interlayer distance[2] and thus creating more porosity in the material. This can be achieved with the addition of a relatively large molecule such as C60.

C60 graphite intercalate (C60 GIC) was first synthesised by Gupta *et al.*[12] in 2004, similar materials had been proposed by Saito and Oshiyama[53] previously. The sample of C60 GIC analysed in this work was created by Keens[1]. The methods followed in the production of the intercalate by Gupta and Keens were similar.

The first process in intercalation was to apply acid to a graphite sample. Keens

Figure 5.2: A simple model of C60 graphite intercalate

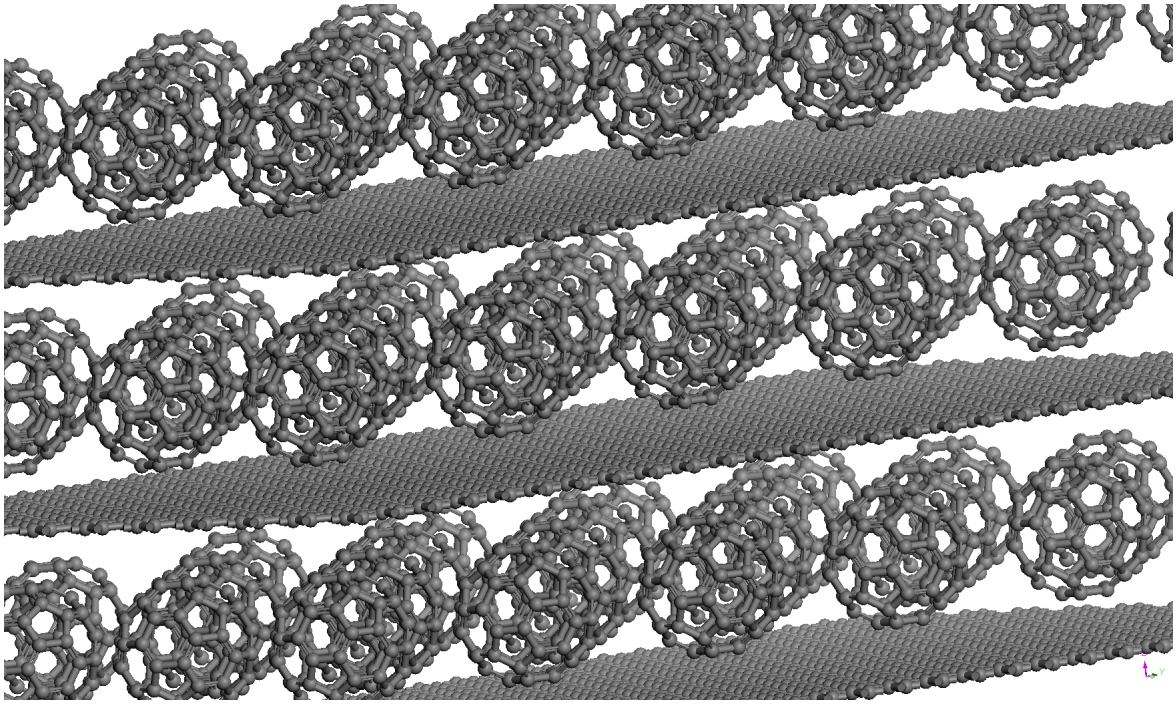

added both sulphuric and nitric acid which intercalate in the graphite over time. The mixture is then heated rapidly to 1173 K releasing a gas of the acid molecules, forcing apart the layers of graphite. This led to the exfoliated graphite, for C60 intercalation the now exfoliated graphite and powdered C60 were added to a vessel which was then evacuated and sealed. This vessel was heated at 883 K, the sublimation temperature of C60, for several weeks. When the mixture was removed from the vessel and washed very little free C60 was present. This sample was then tested for its hydrogen retaining properties by Keens, but its structure was not fully analysed and the presence of intercalate was not definitively proved. We therefore present a full analysis of the structure below.

5.2 Diffraction of C60 GIC

It is assumed that the C60 GIC will retain some of the characteristics of pure graphite and pure C60. Therefore these peaks must be identified before planes associated with the intercalation of C60 and graphite can be determined. The structural analysis of the C60 GIC will be presented with graphs in terms of Q to allow comparison between neutron diffraction, x-ray diffraction and literature.

Figure 5.3: X-ray diffraction measurement of C60 GIC with graphite 002 peak indexed

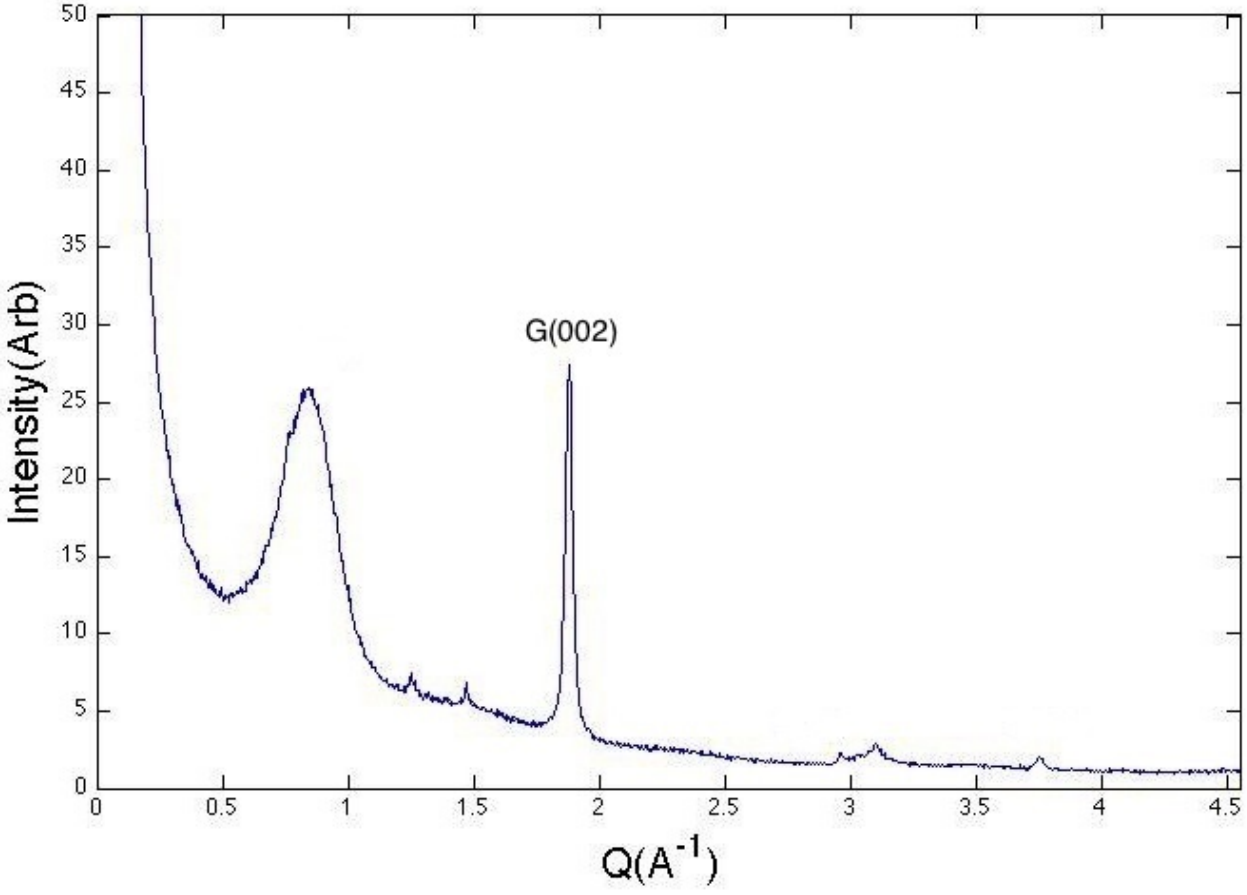

X-ray diffraction data of the C60 GIC sample was taken by Keens[1]. This was taken with a D-5000 diffractometer at room temperature using CuKa radiation giving a wavelength of 1.5418 Å.

Figure 5.4: Neutron diffraction of C60 GIC with C60 peaks indicated

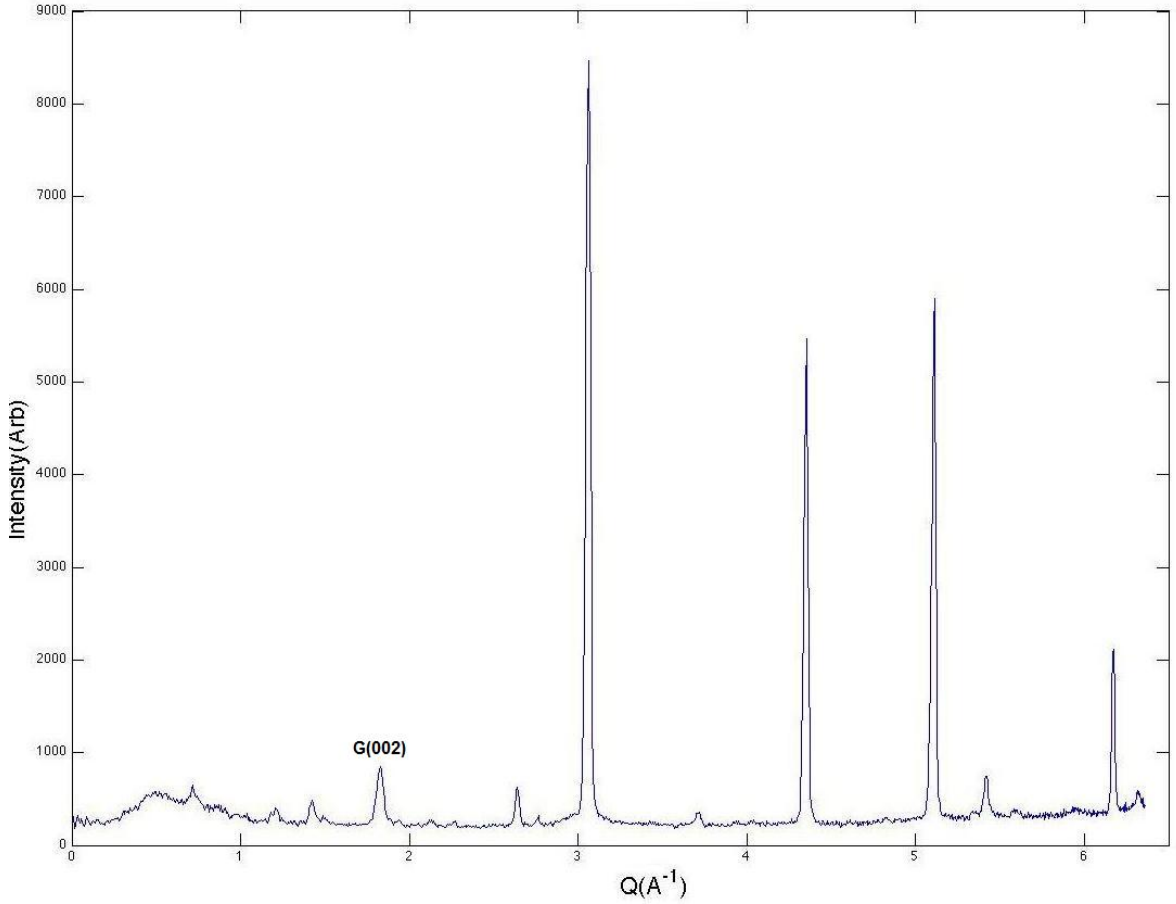

A neutron diffraction measurement of the intercalate was also taken, at the E9 spectrometer at Helmholts Zentrum Berlin by Dr P. Henry, Dr D.Roach and the author. This measurement was taken at a wavelength of 1.8 Å at room temperature. This measurement was the first neutron diffraction experiment performed on a C60 GIC sample and shows additional detail to the XRD data.

5.2.1 Graphite Content

The analysis of the graphite content presumes a hexagonal structure for graphite with a plane to plane distance of 3.354 Å.

In general for the diffraction measurements the peaks beyond the 002 graphite

peak in Q are assumed to belong to graphite. Those below 002 will involve C60 as the 002 peak has the lowest Q value in graphite as it is the widest distance structure. The XRD measurement shows a C60 peak at a similar intensity to the 002 graphite peak suggesting that the two materials are represented in similar proportions in the intercalate.

Figure 5.5: X-ray diffraction measurement of C60 GIC with graphite 002 peak indexed

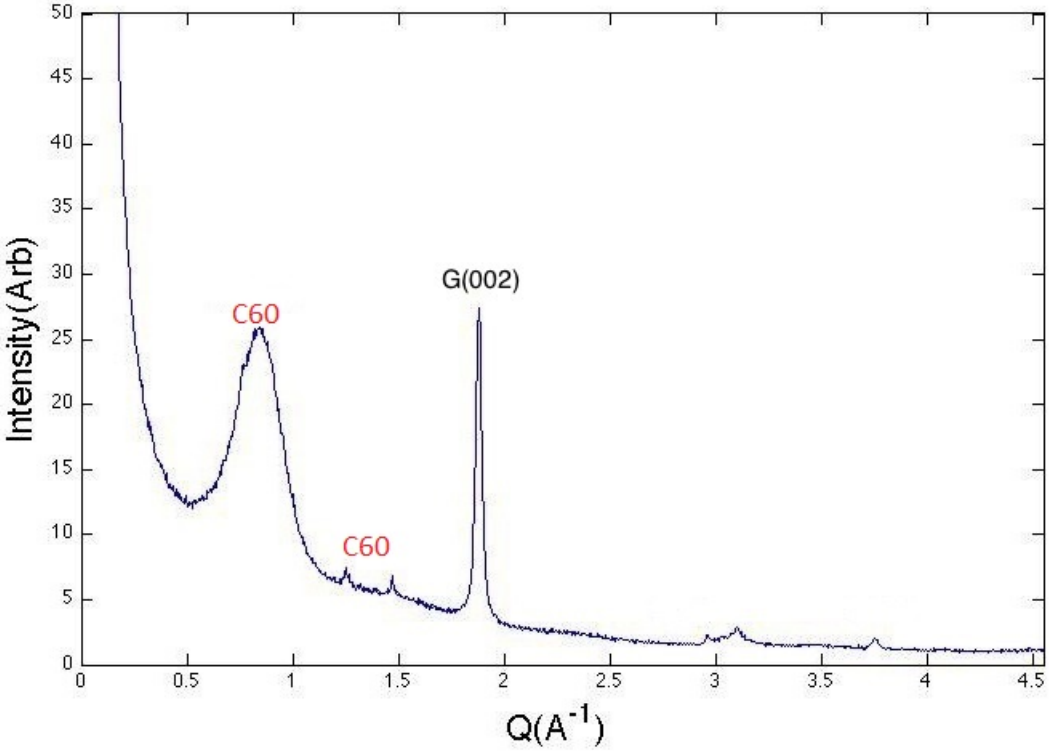

The neutron diffraction measurement however shows several graphite peaks at a much higher intensity than the C60 peaks. The Q values of the intercalate were compared to those expected from pure graphite. The calculated values were generated using the software CaRIne Crystallography[54], using a basic pure hexagonal graphite model. Table (5.1) shows those peaks which are altered by changes in graphite interlayer spacing.

For the C60 GIC sample it would be expected that the peaks which contain a contribution from the interlayer spacing would have a smaller Q value than

Table 5.1: A comparison of predicted and found Q values, for the C60 GIC at different reflections

hkl	Calculated Q $^{-1}$	Neutron Q Å^{-1}	Exfoliated Q $^{-1}$	XRD Q Å^{-1}
002	1.8722	1.828	1.854	1.892
101	3.0891	3.036	3.07	3.116
004	3.7444	3.717	3.729	3.757
103	4.0694	4.041		
104	4.7636	4.846		
2-10	5.1000	5.111		
2-12	5.4306	5.415		
006	5.6150	5.580		

that of standard graphite as this corresponds to a larger lattice parameter. This decrease in Q is shown in the exfoliated XRD and neutron diffraction but the C60 GIC XRD has higher Q peaks suggesting a smaller lattice parameter than that of graphite.

Direct comparison of the XRD data of exfoliated graphite sample and the intercalate highlights the peak shift.

Figure 5.6: X-ray diffraction of exfoliated graphite and C60 GIC, with peaks identified

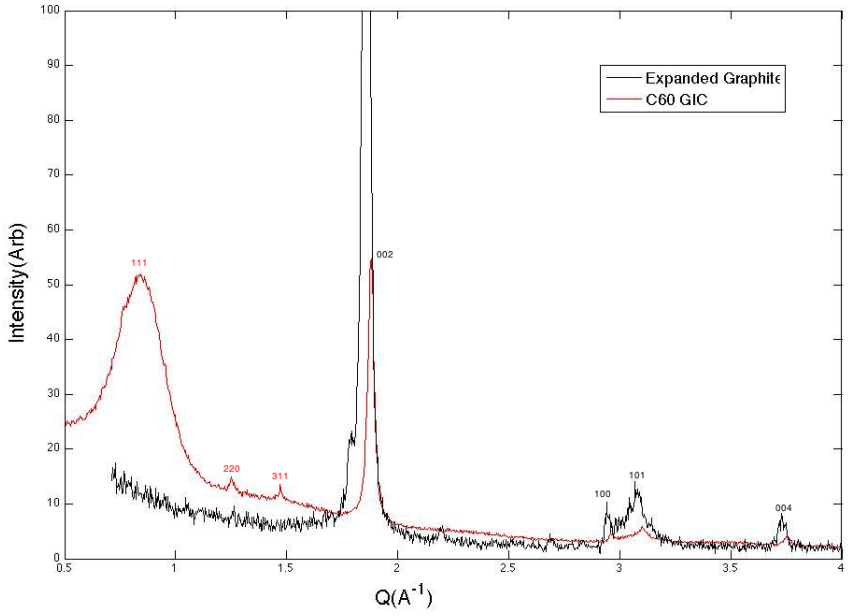

The reasons for this shift are not clear especially as the C60 GIC material was

created using the exfoliated graphite and there is no reason why the spacing should have decreased, the neutron diffraction of the same material also does not show this behaviour, suggesting some form of error in the GIC XRD.

Figure 5.7: Comparison of intensities predicted by CaRIne to those measured

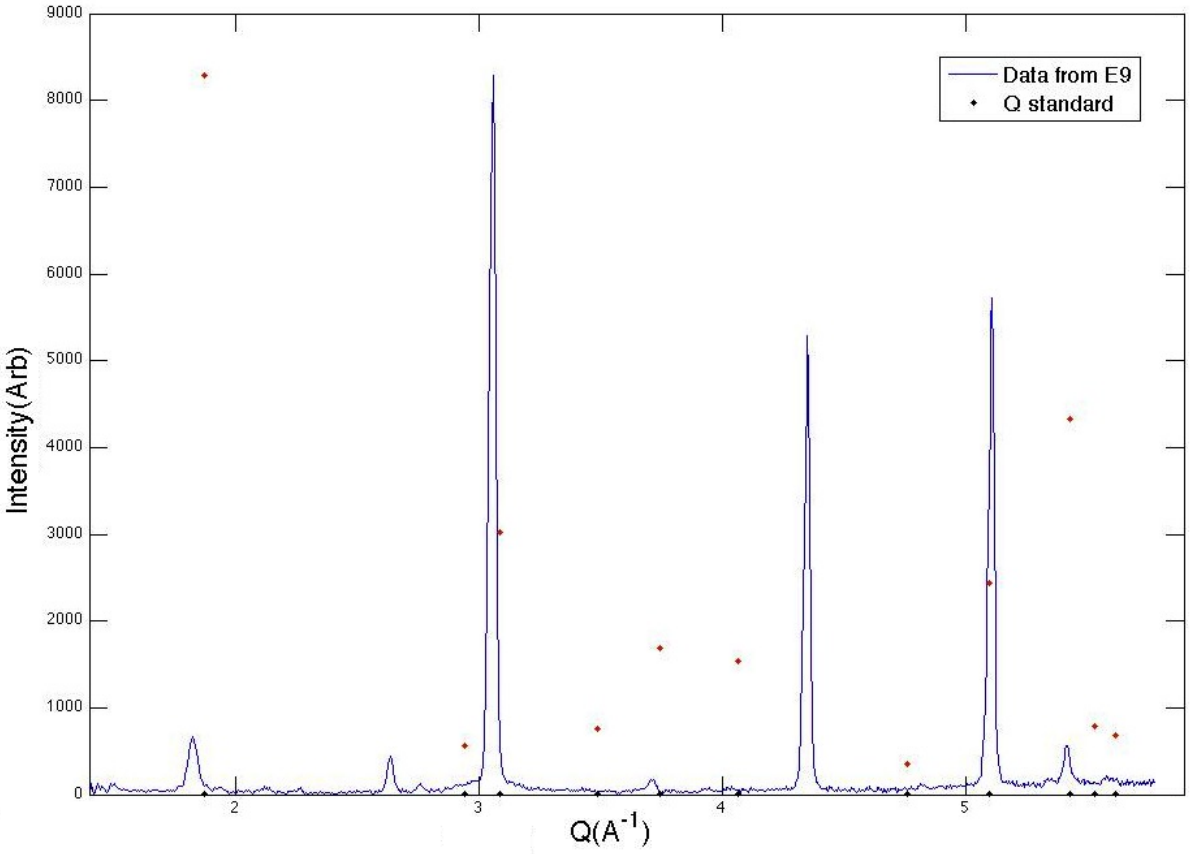

In the case of the neutron diffraction it is believed that the differences in Q from the hexagonal graphite values are accounted for by an increase in the graphite plane to plane distance. This increase could be due to the intercalate or to an increase in the possible turbostratic nature of the graphite.

For the neutron diffraction data the indexed peaks in figure (5.8) were identified as belonging to graphite. Using the relationship

$\frac{1}{d^2} = \frac{4}{3}(\frac{[h^2+k^2+hk]}{a^2}) + (\frac{l^2}{c^2})$, as well as $d = \frac{\lambda}{\sin\theta}$ and $Q = \frac{2\pi}{d}$.

An increase of around 0.5 Å is found in c. From the CaRIne model expected

Figure 5.8: Graphite peaks in neutron diffraction of C60 GIC

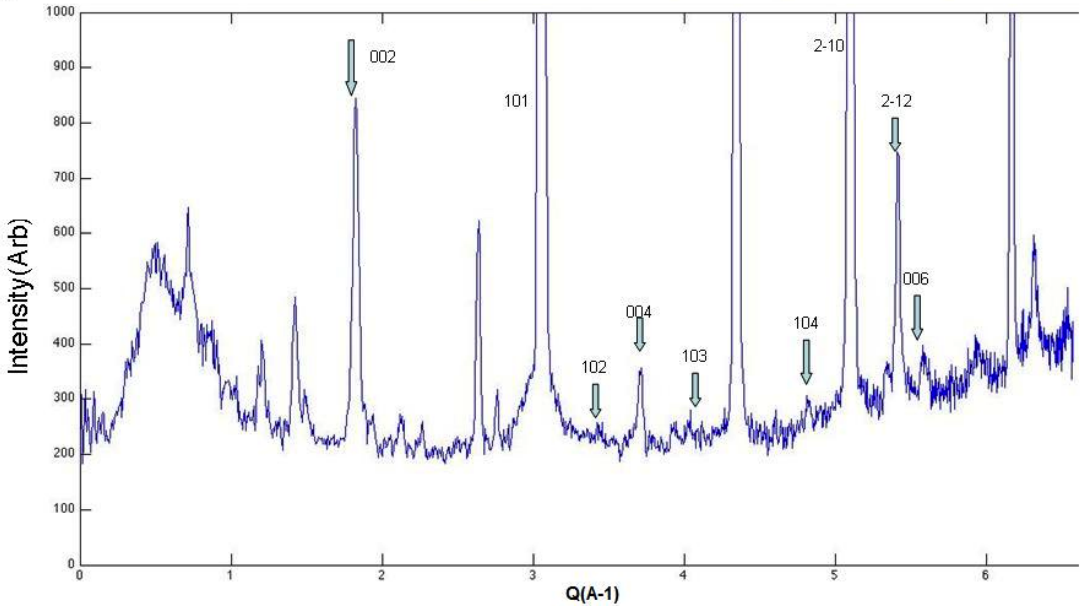

intensities can also be found. Comparing these and the expected Q values shows some discrepancies. Clearly the 002 and 2-12 reflections are of a much lower intensity than expected, and those at 101 and 2-10 are much higher than expected. This demonstrates how preferred orientation can affect powder samples, the neutron diffraction measurements are taken in transmission geometry rather than reflection as for the XRD. The sample holders are also different shapes which could affect how the C60 powder orientates. However the peak positions are not affected and the increase in interlayer spacing from the exfoliated graphite is still clear.

5.2.2 C60 Content

Figure (5.9) shows x-ray diffraction data of a pure C60 powder sample at two different temperatures, these results were presented by Heiney *et al.*[51]. This data demonstrates the change from FCC to simple cubic lattice structure at low temperatures. As both our diffraction data sets were taken at room tem-

perature we assume C60 is present only in FCC form.

Figure 5.9: X-ray diffraction of pure C60 at two temperatures, in terms of Q and intensity

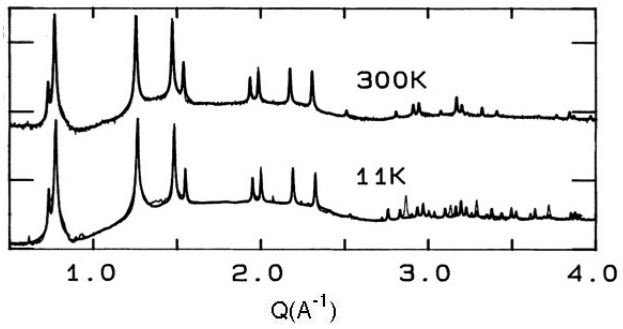

Expected Q peaks for a cubic structure can be calculated using the equation

$$d = \frac{a}{\sqrt{h^2 + k^2 + l^2}} \tag{5.1}$$

hkl	Calculated Q^{-1}	Heiney Q^{-1} [51]
111	0.76	0.75
220	1.25	1.25
311	1.47	1.47
222	1.53	1.53
330	1.88	1.93

Together with the relationships for d and Q above. Comparing the peaks with calculated values gives a very good agreement with an FCC lattice. Peaks which fit those found in FCC C60 can be seen in the x-ray diffraction data of the C60 GIC sample.

The C60 peaks shown by XRD are present at the positions expected for the C60 lattice but with a large hump around the 111 peak suggesting a range of lattice parameters. These peaks are also present in the neutron diffraction measurement, this measurement covers a lower Q range and shows the 111 peak as slightly more defined. It also shows peaks which are not present in the C60 lattice most prominently the hump at 0.5 $Å^{-1}$.

Figure 5.10: X-ray diffraction of C60 GIC, with peaks identified

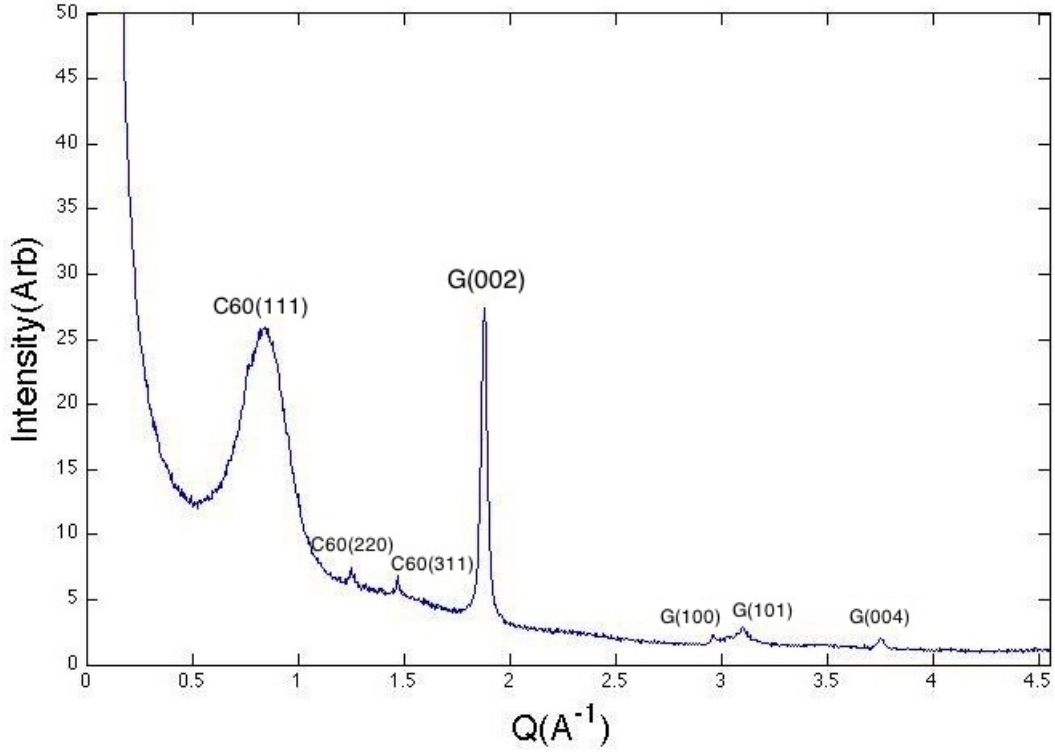

Figure 5.11: Neutron diffraction of C60 GIC showing C60 FCC peaks

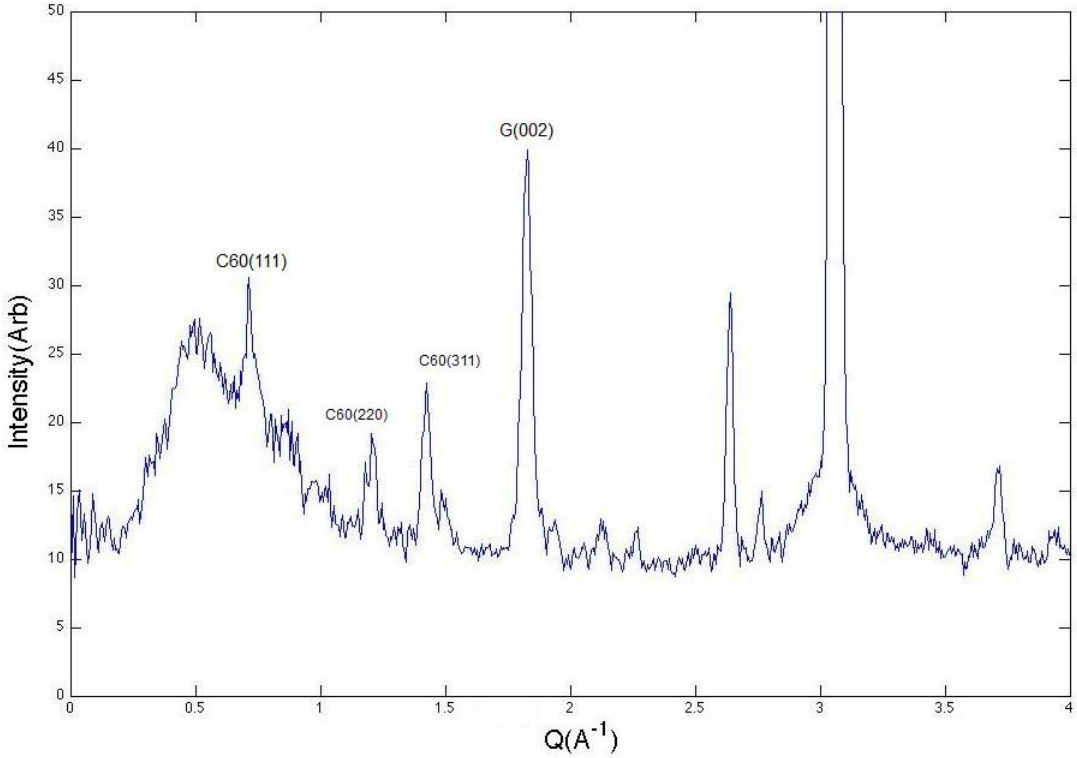

A calculation of the peaks in a pure C60 lattice has been made using the diffraction simulation package in Materials Studio. This can be compared with diffraction peaks to show any changes from the standard lattice clearly.

Figure (5.12a) shows a good match with the 220 and 311 C60 peaks with the 111 peak shifted to the right and broadened. This suggests the lattice has been compressed in this direction, showing the reduction in lattice parameter also predicted by the XRD graphite peaks. This reduction is likely to be unphysical and could result from an error in the measurement shifting all the peaks to the right. The presence of C60 in the sample is clear but there is no indication of intercalation.

The calculated peaks can also be compared to the neutron diffraction measurement as shown in figure (5.12b). As mentioned before all the peaks measured by E9 show a shift to the left indicating a larger lattice parameters. The low Q measurement also show peaks which could not be detected with the XRD measurements. Centred around 0.5 Å^{-1} is an amorphous hump and peaks around 1 Å^{-1} are unexplained by the presence of C60.

The 1/d values for the three C60 FCC peaks in the sample can be compared. The calculated values assume a lattice parameter a=14.2 Å.

Table 5.2: Comparison C60 FCC peaks shown by diffraction

hkl	Calculated 1/d $^{-1}$	XRD1/d Å^{-1}	E9 data 1/d Å^{-1}
111	0.1220	0.1220	0.1139
220	0.1992	0.200	0.1916
311	0.2336	0.2340	0.2268

For both measurements C60 lattice peaks with Q values higher than 1.9 Å^{-1} are lost in the graphite diffraction peaks. The peaks in the neutron diffraction data which do not fit C60 must be explained.

Figure 5.12: Comparison of calculated C60 peaks with diffraction

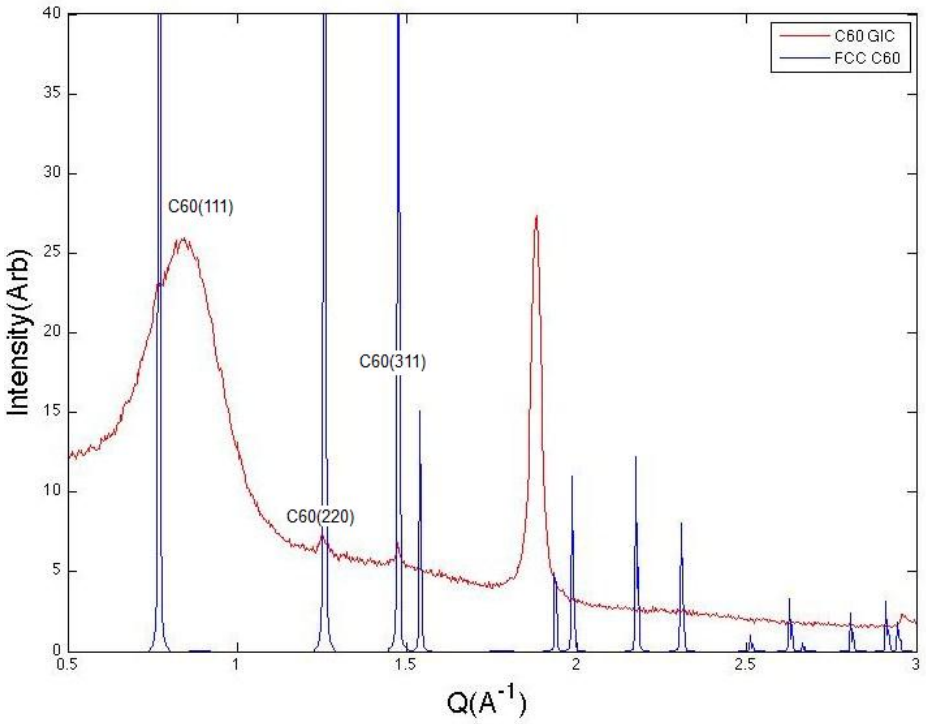

(a) Comparison of calculated C60 XRD with the C60 GIC XRD

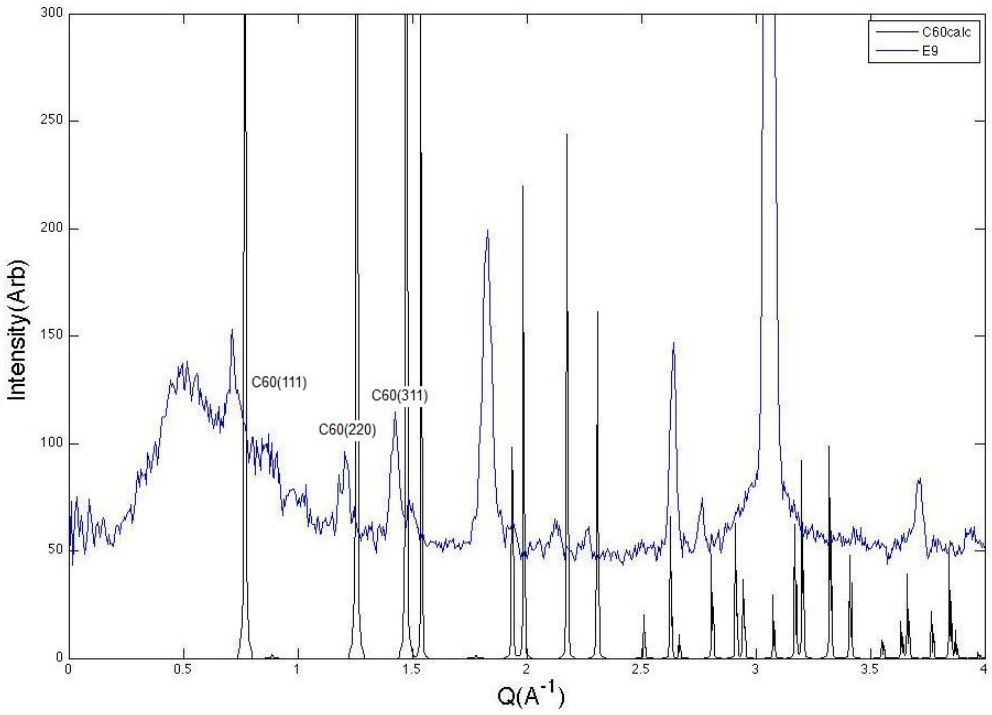

(b) Comparison of calculated C60 XRD with GIC E9 data

5.2.3 Calculated Intercalate XRD

A simple lattice model of C60 GIC based on the lattice parameters given by Gupta *et al.* was created using Materials Studio which was then used to create an XRD simulation as above. This model has a C60-C60 centre distance of 12.9 Å and will not capture the large amounts of pure graphite and C60 that are expected to remain in the material.

Figure 5.13: GIC model with parameters

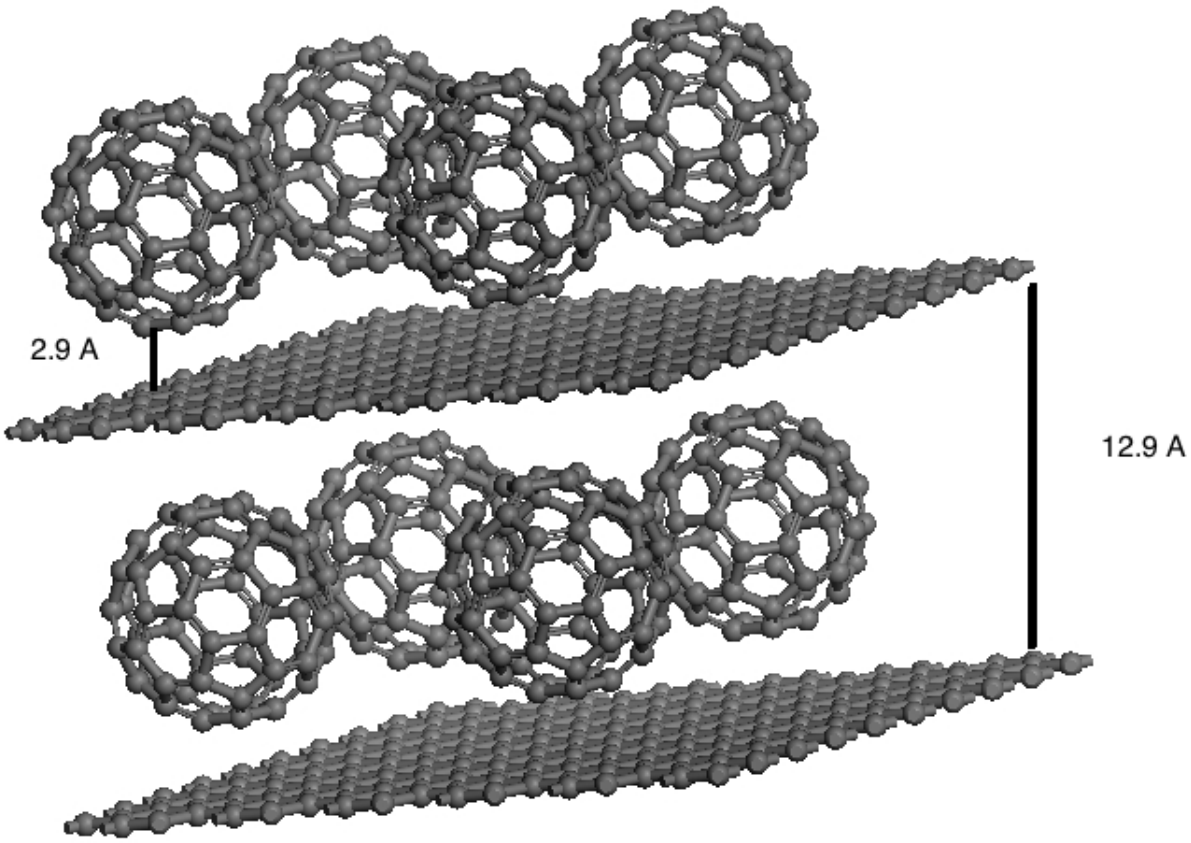

The model was created as a triclinic lattice, the key peaks in the XRD above are the 00X peaks, which correspond to the layers of graphene with a distance of 12.9 Å. The other peaks include the 101 and 111 directions which are illustrated in figure (5.15).

The simulated XRD pattern was first compared with the C60 GIC XRD mea-

Figure 5.14: Calculated XRD pattern of the C60 GIC model with key peaks indexed

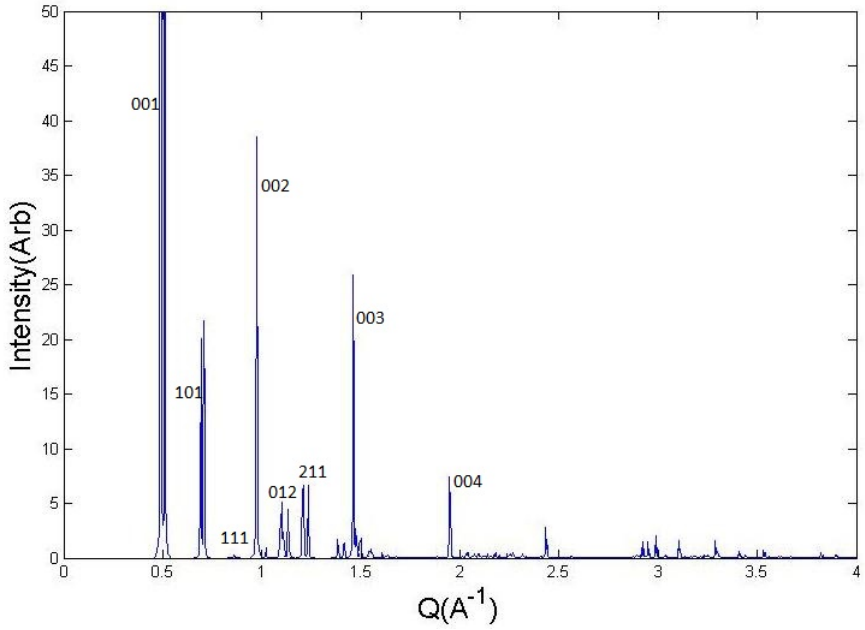

Figure 5.15: Planes in C60 GIC model

(a) 101 planes of the C60 GIC model **(b)** 111 planes of the C60 GIC model

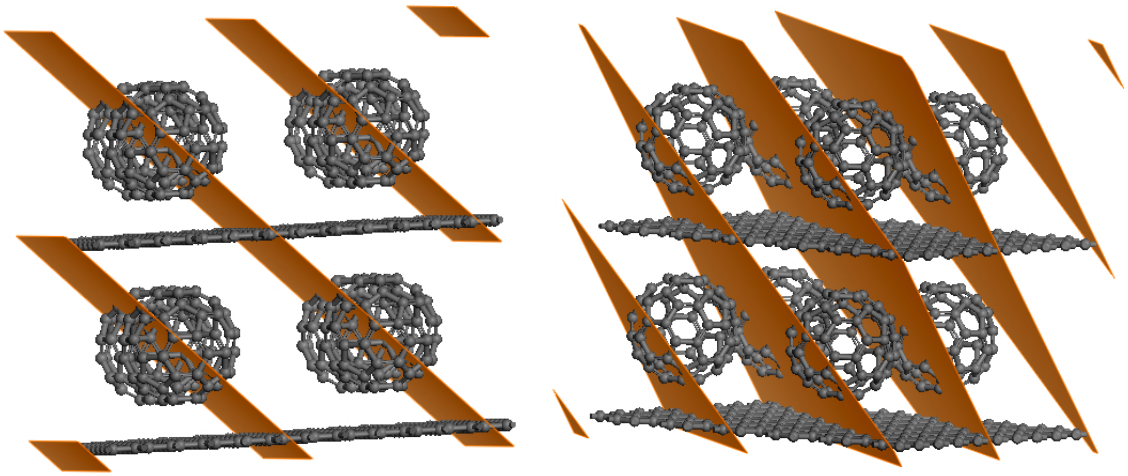

surement.

Figure (5.16) shows that the C60 111 peak falls between two peaks of the GIC lattice possibly explaining the broadening of this peak. The peak at 0.5 $Å^{-1}$ could not have been captured by this XRD measurement.

Figure 5.16: Comparison of calculated GIC XRD with the C60 GIC XRD

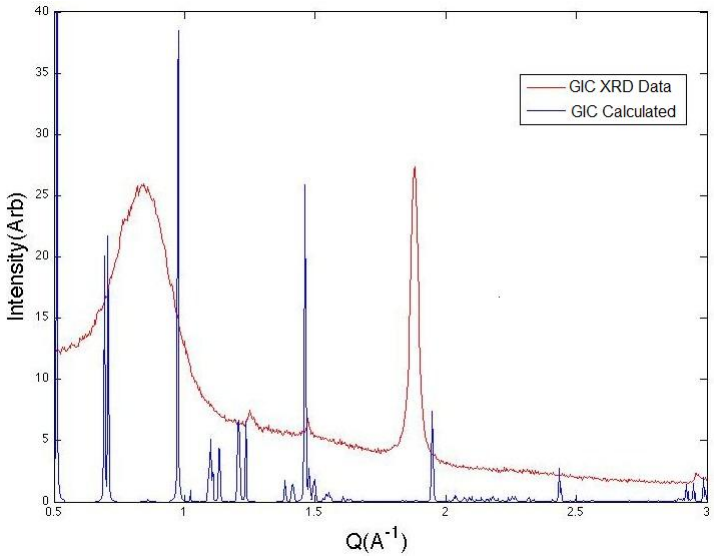

Figure 5.17: Comparison of calculated GIC XRD with the C60 GIC E9 data

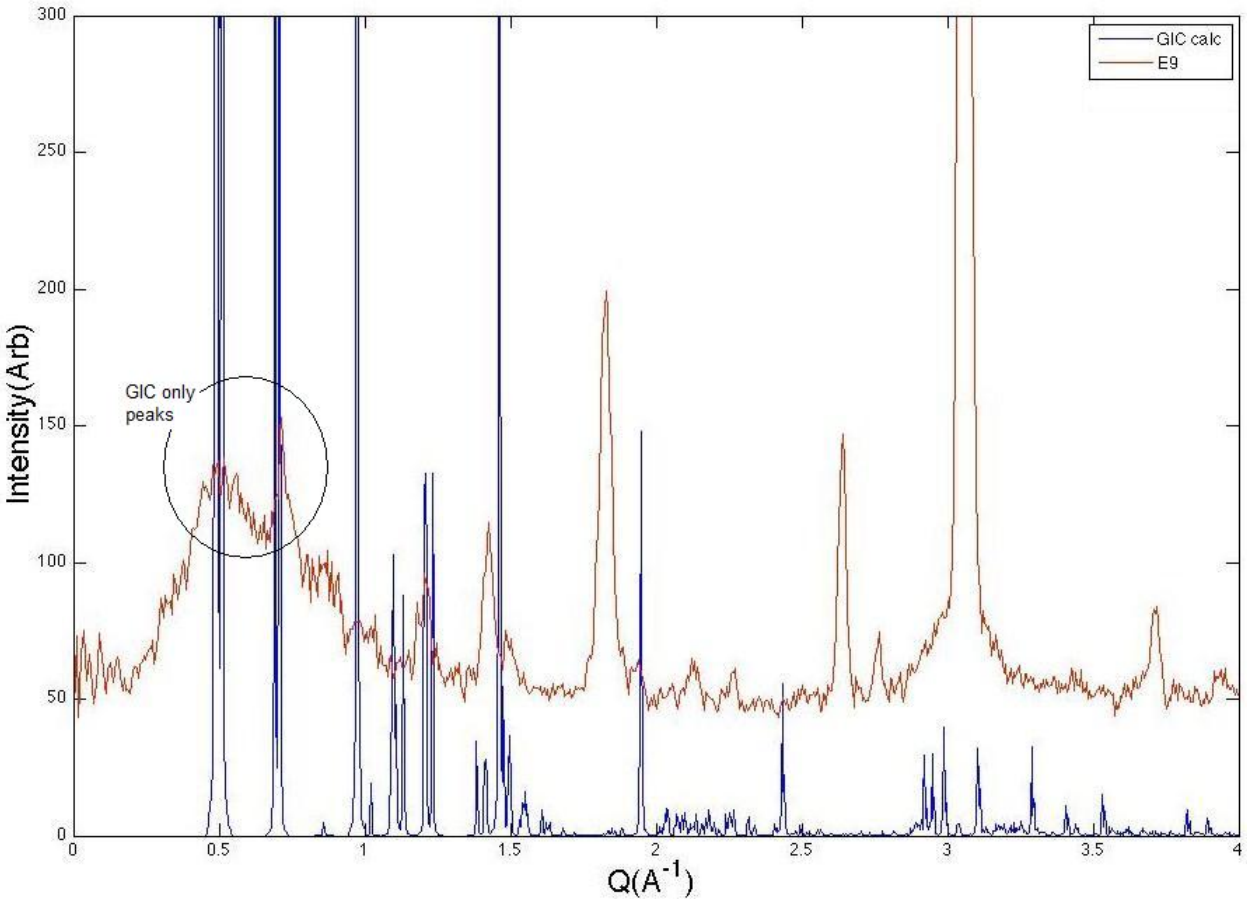

Comparison with the neutron diffraction data shows that the unexplained peaks at 0.5 and 1 $Å^{-1}$ are present in the model.

This confirms the presence of C60 intercalate in the material as there are features in the diffraction pattern which can only be explained by lattice planes which match those of C60 GIC. The GIC clearly has a large range of plane distances which would be expected due to the nature of the C60 in the sample. It shows features found in disordered C60. This information allows us to index almost all the peaks in the diffraction pattern.

Figure 5.18: C60 GIC E9 data indexed

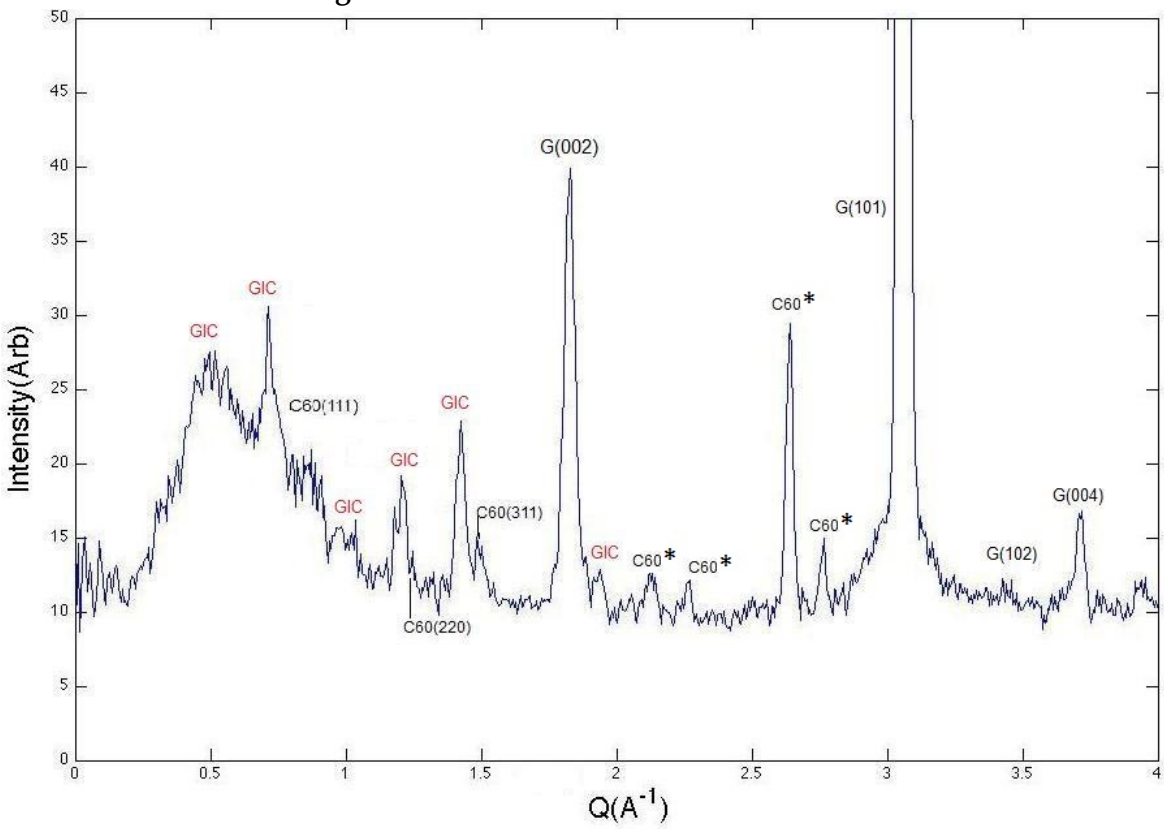

Figure (5.18) shows the culmination of the analysis. We can be confident that the first two GIC indexes are so far from anything expected in graphite or C60 alone that they must be the product of an intercalate structure. They also fit well with predictions given by other groups. This is the first analysis of its type, no neutron scattering and very few other diffraction measurements

have been performed on this material. The neutron diffraction shows a clear advantage, giving good results at low Q values. In the case of this sample the humps around the GIC peaks suggest that there is a range of interlayer spacing for the intercalate. It is less obvious whether the last four GIC peaks are more connected to the C60 lattice or the intercalate as there is overlap in this area. Some C60 peaks are starred as although they match well with some predicted C60 peaks and do not fit with graphite or the GIC model, it is possible they are connected to the GIC as the model is not exhaustive.

Chapter 6

Dynamic Analysis of Graphite

6.1 Background

Graphite is a historically important material in neutron scattering studies due to its low neutron absorption which makes it suitable for use as a moderator for nuclear reactors. It has a very small incoherent scattering cross-section and so is well suited to coherent scattering analysis. The dynamics of graphite can be challenging to study. Its extreme asymmetry makes creating simple force constant models difficult. In the case of experiments producing large, single crystal, defect free samples is rarely possible. The difficulty of obtaining single crystal samples of graphite means that powder analysis is generally necessary.

Measurements of the density of states of graphite were performed in the late sixties by several groups using the incoherent approximation. The phonon dispersion curve measurements were taken on single crystal samples, particularly focusing on the vibrations between the 00l planes at relatively low energies, by groups including Ross[55]. Nicklow *et al.*[56] and others also calculated elastic constants under different conditions.

Some recent work has shed light on the high energy optical modes which have been badly modelled historically. Using x-ray techniques Maultzsch *et al.*[57]

shows these modes are important in the free carrier dynamics and electronic transport. However this work will focus on the low energy acoustic modes as we are more interested in the thermal properties of the material and expanding the knowledge of perfect hexagonal graphite to studies of natural graphites.

6.1.1 Force Constant Models

There are two graphite force constant models used in this thesis to replicate poly-CINS experimental results. One is a bond bending, bond stretching model (BBS) the form of which was described by Young and Koppel[58], building on work by Yoshimori and Kitano[59]. This model is comprised of four interaction types between nearest neighbour atoms. Bond stretching in the plane, bond bending in the plane, bond stretching between the plane and bond bending between atoms in the same plane in the c axis direction. This model emphasises the covalent bonds in the material, fitting well with the structure of the material. However issues arise as the third nearest neighbour interaction is not present and the fourth nearest neighbour interaction is only partial. Also the C_{44} elastic constant is calculated to be zero in this form, due to matrix elements being set to zero. The dispersion curves predicted by this model are shown in figure (6.1a) below.

The axially symmetric model as described by Nicklow *et al.*[56] depends on interactions between pairs of atoms. The forces between these are assumed to be harmonic and depend only on the distance between the atoms. This model is more general, with less of the restrictions which give rise to the unphysical results of the (BBS) model. However the interactions between the atoms is over simplified which leads to zone boundary effects. The dispersion curves predicted by this model are shown in figure (6.1b) below.

Phonon dispersion curves for both of the models were created using GULP.

Figure 6.1: Phonon dispersion curves predicted by Young and Kopple and axially symmetrical models

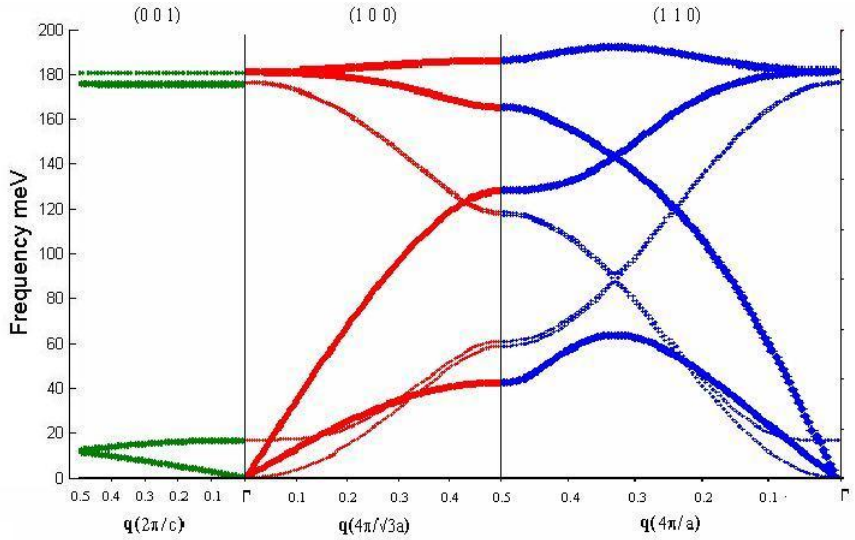

(a) Young and Kopple model 100(red) 110(blue) 001(green)[3]

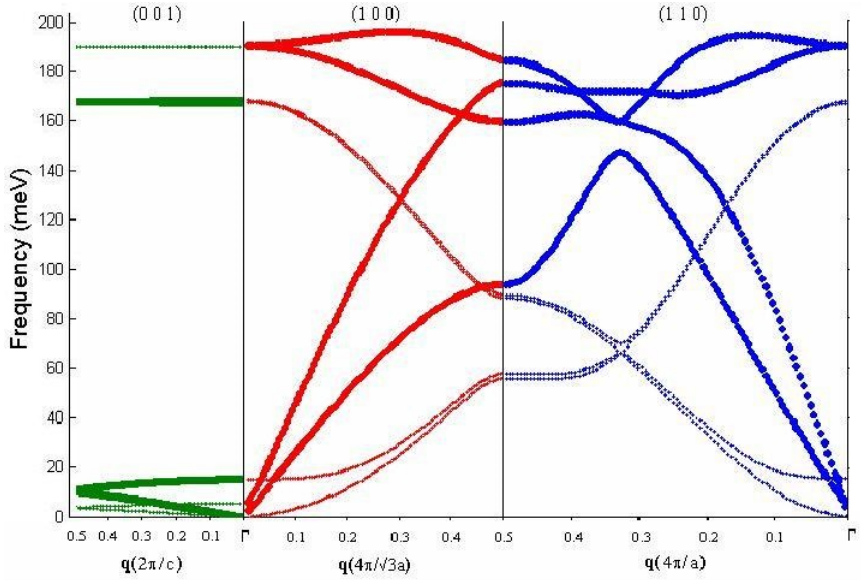

(b) Axially symmetrical model 100(red) 110(blue) 001(green)[3]

They are represented in terms of scans through the atomic planes of graphite, these planes were illustrated in the Structure chapter of this work. The scans were taken through the 100, 110 and 001 planes.

Inelastic x-ray scattering measurements of graphite were taken by Mohr *et*

al. [60]

Figure 6.2: Phonon dispersion of graphite from inelastic x-ray scattering. Triangles and circles are inelastic x-ray data and the full squares are INS data. Solid lines are the force-constant calculations, the dashed line is a quadratic extrapolation of the data. The lines are denoted by their symmetry representation in space group notation. [60]

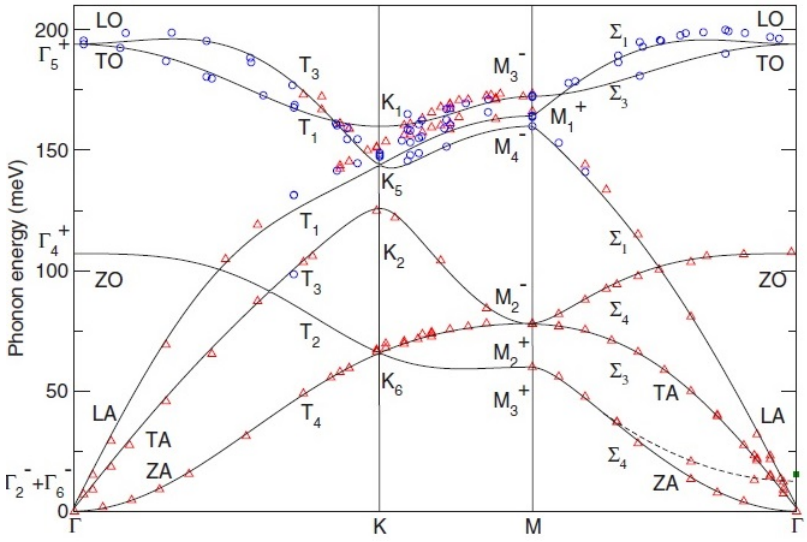

Figure 6.3: Phonon dispersion of graphite along the 002 direction. Open triangles are present IXS data and full squares are neutron scattering data. The lines are a guide to the eye. [60]

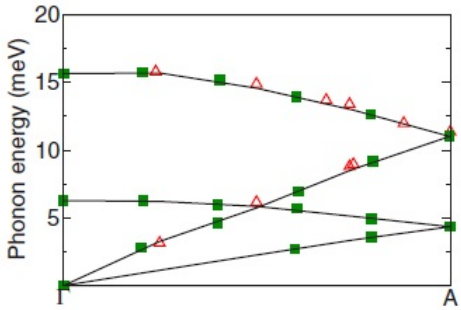

Comparing these measurements with the predicted curves gives us an idea of the validity of the models. Figure (6.4) shows the comparison of the 100 and 110 curves of both models with experiment. The figures clearly highlight some of the deficiencies of the models, neither fully matches the experimental data and though it seems that the axially symmetrical model does better over all, there are areas in which the Young and Kopple model gives a better match.

Figure 6.4: Comparison of graphite models with experimental measurements

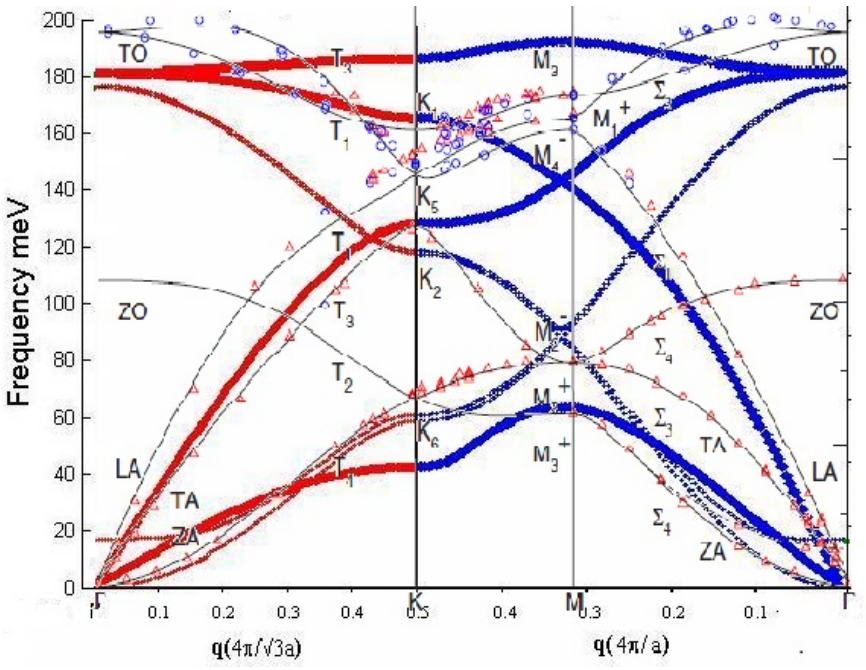

(a) Young and Kopple model compared to experiment

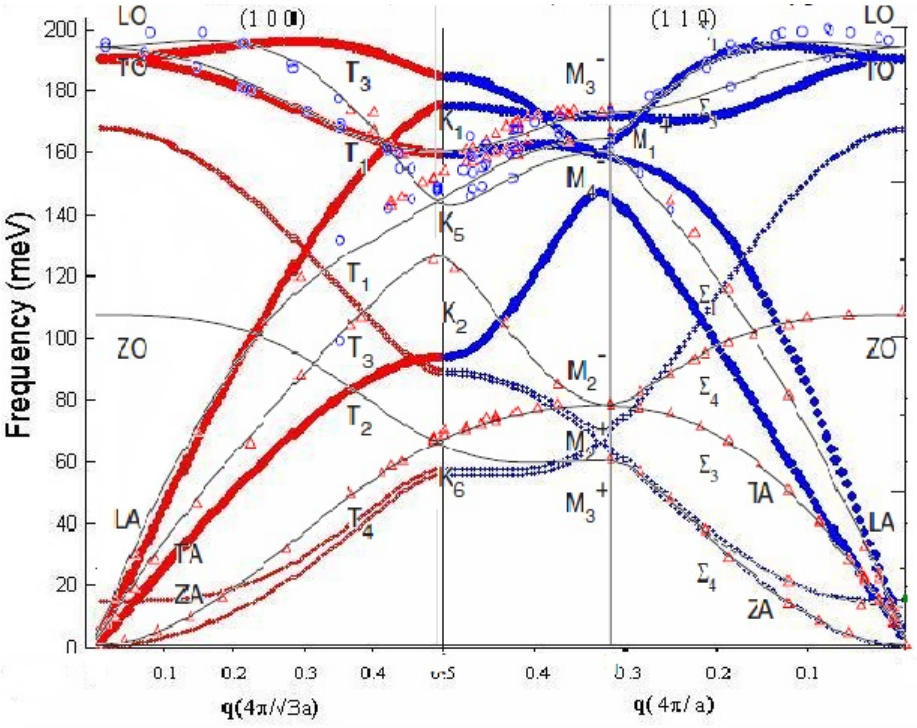

(b) Axially symmetrical model compared to experiment

The area of most interest for this work is the low energy 002 curve. The experimental data for this area was shown separately by Mohr and can also be

compared to the force constant models.

Figure 6.5: Experimental and calculated 002 phonon curves

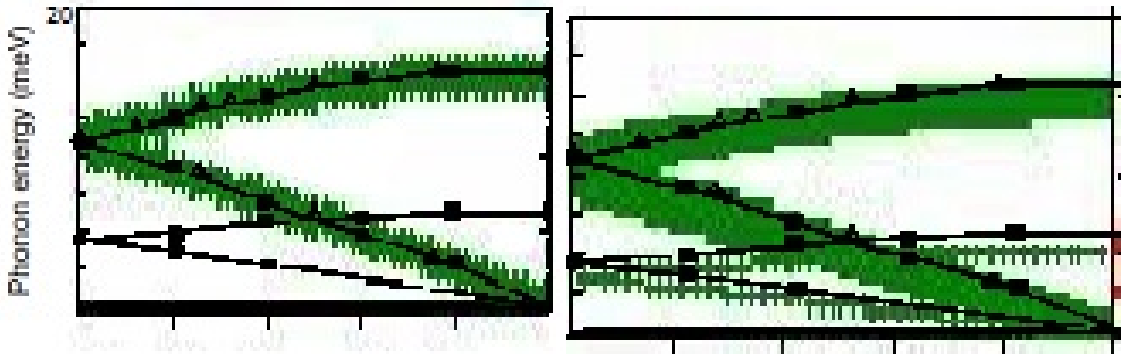

(a) Young and Kopple model 002 curve compared to experimental data.

(b) Axially symmetrical model 002 curve compared to experimental data.

Both of these models show good agreement with experiment in this area, with the axially symmetrical model showing the curve which crosses the axis at 5 meV as well as the one at 15 meV, and both fitting the data of the 15 meV curve. Due to the focus on this area we can be confident that our data will be well modelled with either force constant model, however we tend to use the axially symmetrical model due to the extra data and better fit of other curves.

Figure 6.6: Extended phonon dispersion curves predicted by Young and Kopple and axially symmetrical models

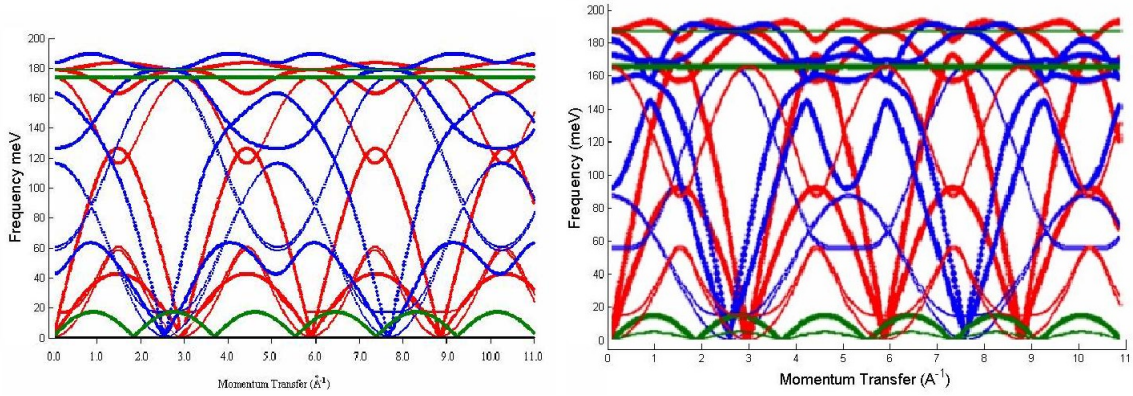

(a) Extended representation of Young and Kopple model 100(red) 110(blue) 001(green)[3]

(b) Extended representation of axially symmetrical model 100(red) 110(blue) 001(green)[3]

These calculations can also be presented in extended form. This presentation does not use the Brillouin zone to overlap equivalent points and is closer to the data as shown in poly-CINS experiments.

In figure (6.6) it can be seen that the scan through the 001 direction gives a pure sinusoidal acoustic dispersion curve which holds in the case of both models. At energies below 20 meV the 100 and 110 directions meet the origin between 2 and 4 $Å^{-1}$. The models disagree at energies above 40 meV particularly in the case of the 110 direction where there is a difference in the shape of the curves and the peak energies. In the case of the 100 direction the peak energies are around 40 meV lower in the Y&K case. For the purposes of this work the models are used interchangeably as we are focused only on low energies looking mainly at the vibrations of the 002 plane. The models do differ slightly, with Young and Kopple giving a 002 curve peak of 15.79 meV and the axially symmetrical model giving a peak of 15.96 meV. This difference is well within errors expected in experimental measurements.

These force constant models are used in Scatter[61] to create predicted poly CINS data. The full details and validation of this technique are explained in Roach[3]. Some details of the models are shown below.

6.1.2 Simulated Poly-CINS Graphite Measurements

Figure (6.7) shows a poly-CINS spectra, simulated by Scatter, of the perfect hexagonal graphite lattice. This spectra shows several important features of graphite scattering data, particularly the 002 curves which leave a window between 0 and 1.9 $Å^{-1}$ which can be used to identify non graphite material in the sample, and the presence of optical modes at around 200 meV.

Looking at a smaller range of data which was simulated using the axially symmetric model (6.8) the gap between 0 and 1.9 $Å^{-1}$ is clearer and other

Figure 6.7: Young and Koppel model poly-CINS simulation

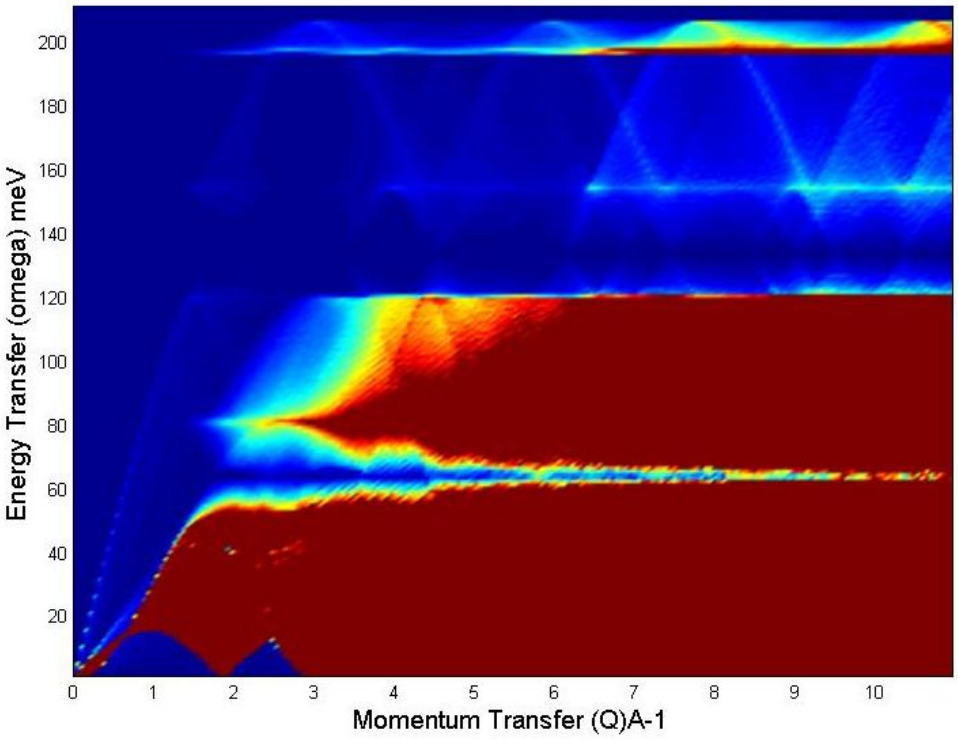

Figure 6.8: Axially symmetric Scatter data of low frequency phonons

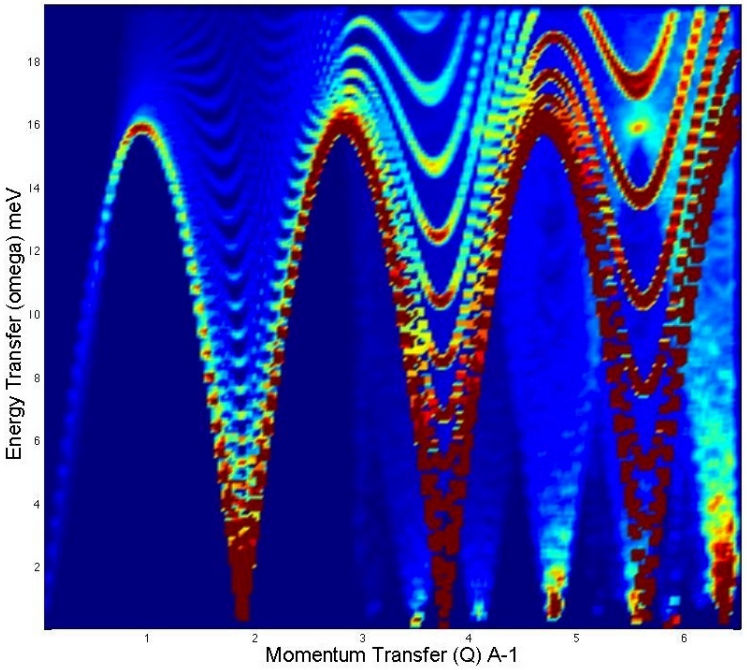

curves can be seen from 3 $Å^{-1}$.

These figures demonstrate that calculations can be performed over different areas of Q, ω. Calculation time is governed by the amount of points in Q, ω space calculated, the quantity of points and their distribution in a calculation is know as sampling. A high detail, wide Q, ω calculation has high sampling and takes a great deal of time. By focusing on the area of Q, ω which is of most interest the calculation time can be reduced. The figures at (6.9) show the same Q, ω area of graphite modelled using the axially symmetric model at different levels of detail.

Figure 6.9: Calculations of the 002 phonon curve of graphite using the axially symmetrical model at different levels of sampling

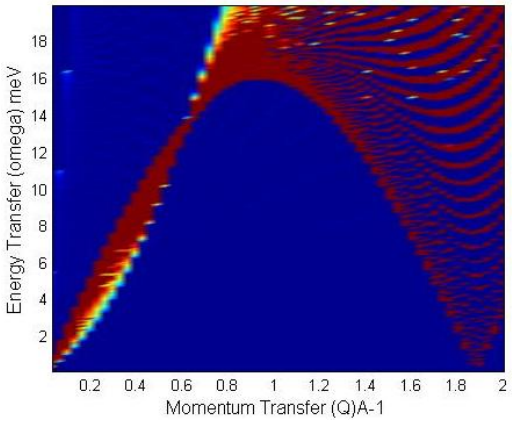

(a) The 002 curve with low sampling

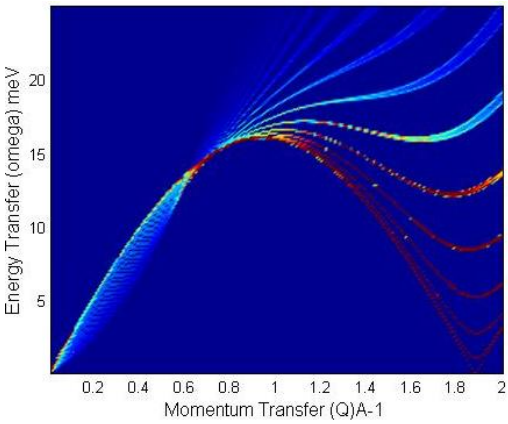

(b) The 002 curve with medium sampling

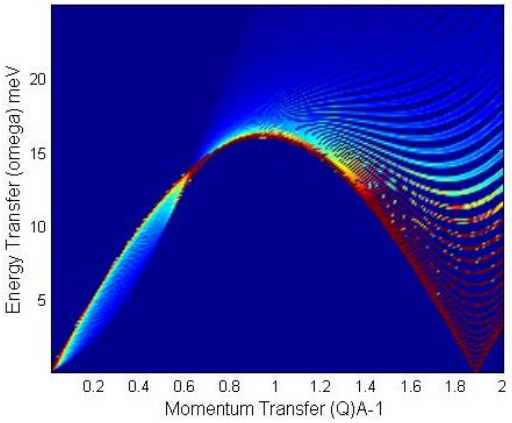

(c) The 002 curve with high sampling

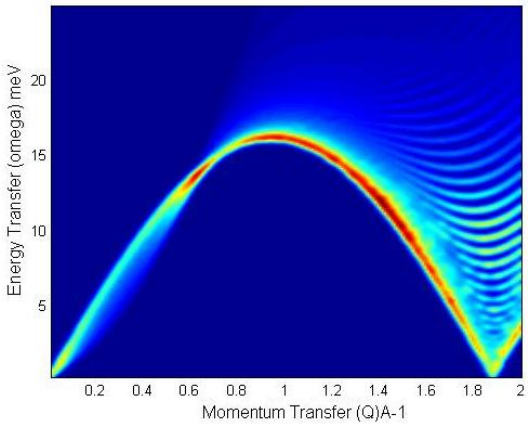

(d) The high sampling 002 curve with smoothing

Beginning with figure (6.9a) we show the 002 curve from 0 to 2 $Å^{-1}$. This demonstrates a calculation which covers more points than the calculation shown in figure (6.9b) but has more pixelation due to a coarse sampling. Figure (6.9c) demonstrates the same curve with the area in fine detail. Figure (6.9d) shows the effect of smoothing on the high detail curve. It has further removed some pixelation and reduced the difference in intensity of different parts of the spectrum.

These different calculations can be compared with an experimental measurement showing the same curve at a higher Q value in figure (6.10). This measurement shows slightly less coarseness than the (6.9a) calculation, but is more pixelated than the other calculations.

Figure 6.10: Section of the Branwell D IN5 spectrum

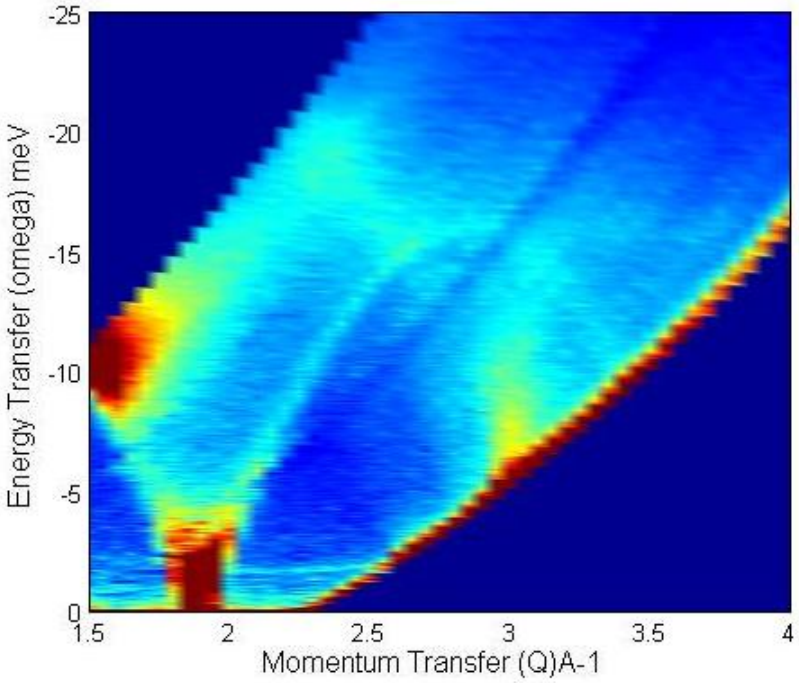

All of the calculations do show the same information, and are suitable for comparison with experiment at a general level. The effect of sampling on comparison with experimental data is explored further in a later section.

6.2 Experimental Graphite Measurements

Poly-CINS experiments were performed at the ILL facility on graphitic materials, including a natural graphite, an expanded graphite and carbon-nano fibres. Present were Dr D.Roach and Dr S.Keens.

Measurements were taken at a wavelength of 5 Å which should give a flux at sample of around 10^5 n/cm^2/s[62]. The IN5 has 12 ^{3}He detectors each comprised of 32 tubes.

Figure 6.11: IN5 spectrometer at the IIL[62]

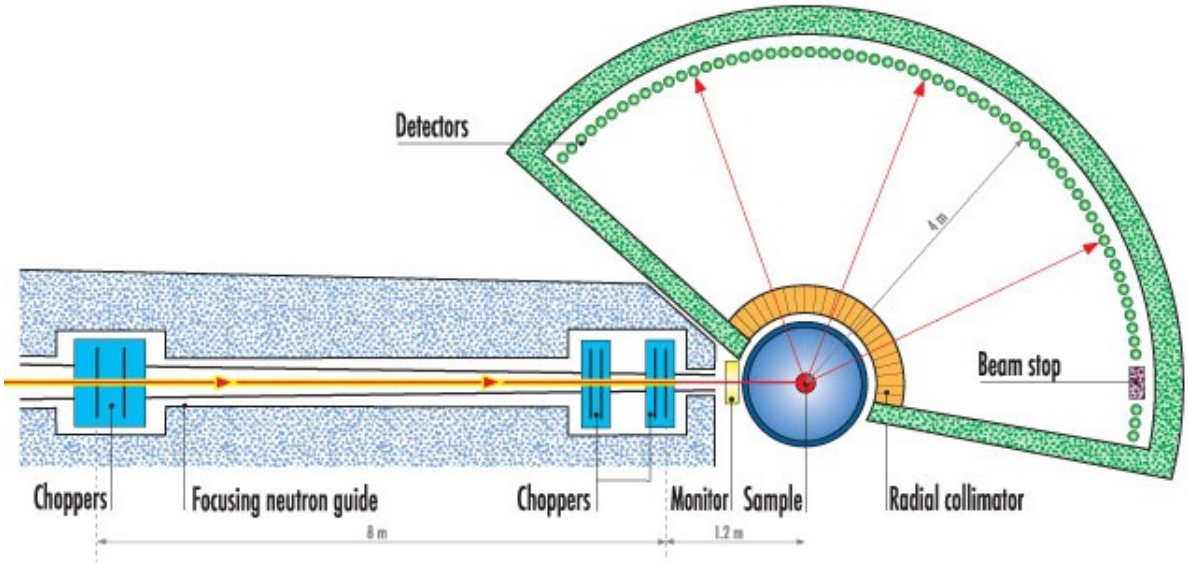

The data sets below were vanadium corrected and converted from TOF to $S(Q, E)$ using LAMP. The following analysis was performed using Neutronplot.

6.2.1 Branwell D

Figure (6.12) is the spectrum of Bran D graphite taken by the IN5 spectrometer at a temperature of 494 K for 15 minutes. This figure shows the data as presented by Neutronplot when first loaded by the user, displayed with a default

medium cut off as described in the Neutronplot section.

Figure 6.12: Bran D IN5 data as presented by default by Neutronplot

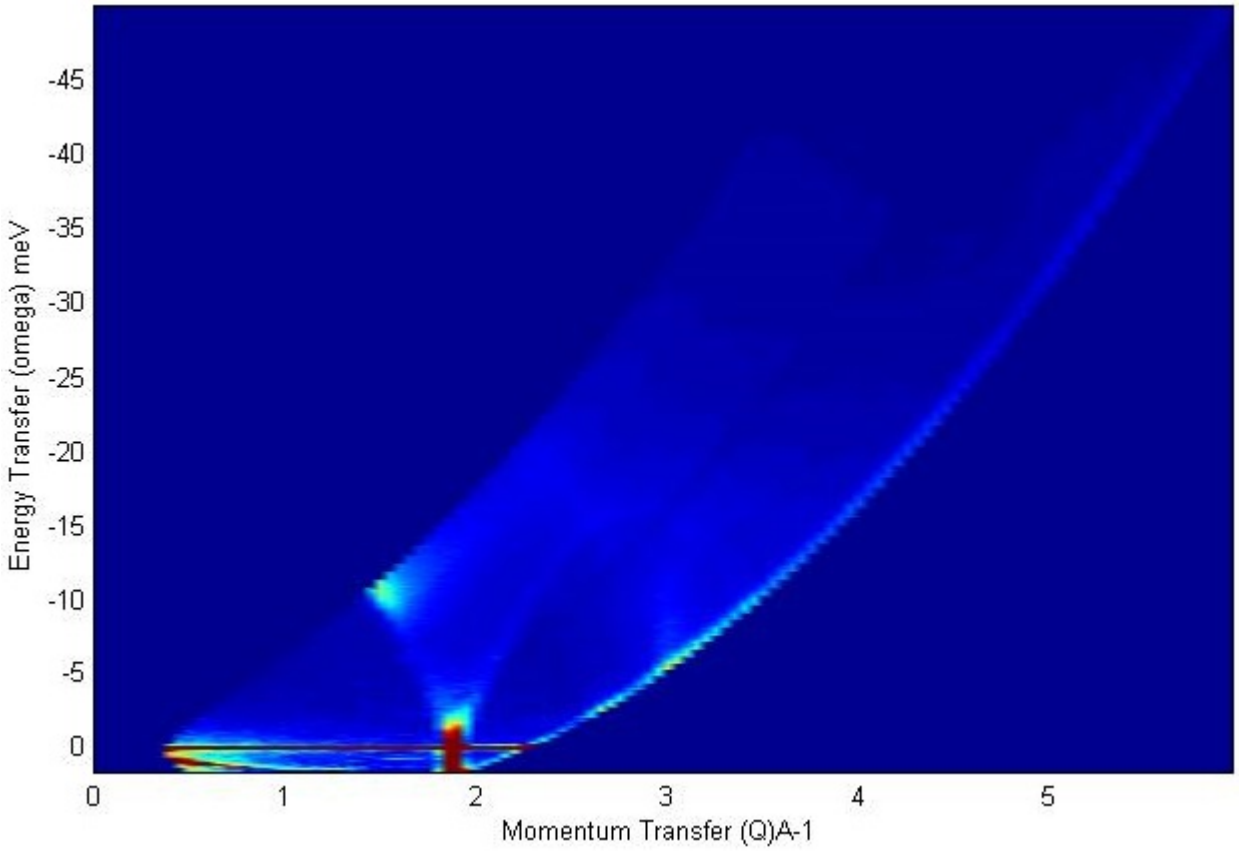

The data clearly shows the shape of the loci from the instrument. The majority of the measurement is from neutron energy loss, as IN5 is a direct geometry spectrometer. The data has not been smoothed by Neutronplot and is shown at a maximum energy transfer of 50 meV. The thick red line at zero energy transfer is the elastic line. The neutrons which landed at this part of the spectrum have neither lost nor gained energy but have still been diffracted by the material. The elastic line is the highest intensity poly-CINS data, as most of the neutrons will pass through the material without a change in energy. Elastic data intensity therefore needs to be reduced to make the lower intensity energy transfer data visible.

Increasing the cut off and therefore looking more closely at lower intensities

Figure 6.13: Bran D IN5 data focusing on lower intensity data

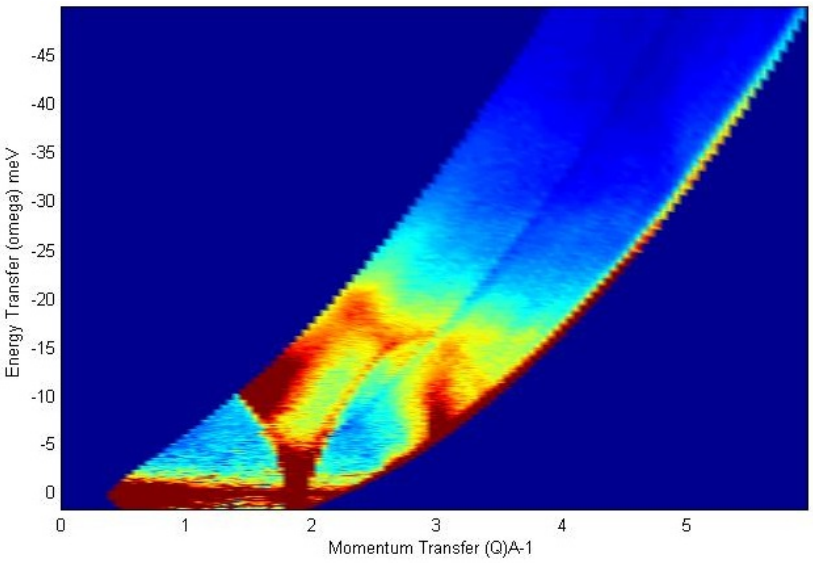

Figure 6.14: Bran D IN5 data at low intensity showing curves at 2.5 Å^{-1} and above

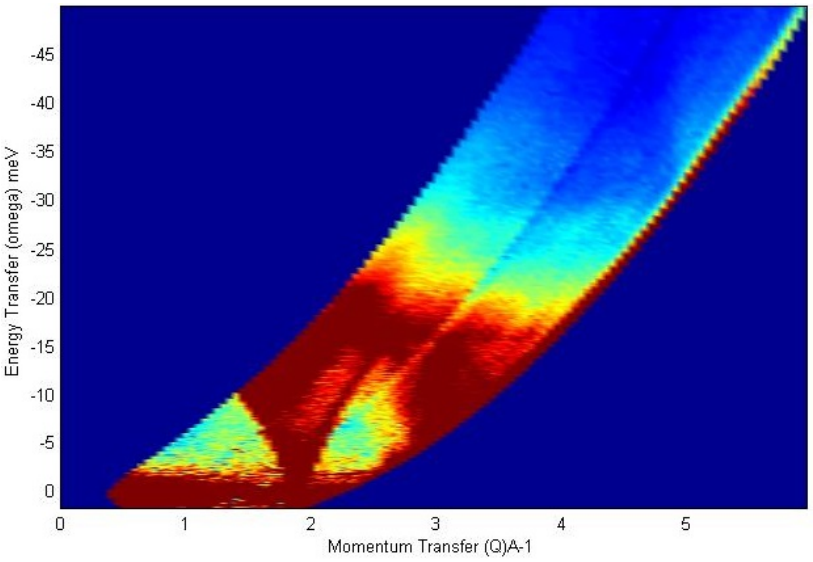

shows the 002 curve more clearly as shown in figure (6.13). Further increasing the cut off begins to highlight other phonon curves at higher Q.

In all the spectra the 002 curve is visible, starting at 1.9 Å^{-1} as are several higher curves with the 110 curve showing very faintly at around 2.75 Å^{-1} and the more visible 100 reflection coming in after 3 Å^{-1}. Detector deficiencies

leading to a loss in intensity are faintly visible cutting through the 002 curve. This loss is far more visible at lower intensities.

The figures showing the full spectrum do not show the neutron energy loss side clearly. Neutronplot allows the separation of neutron energy gain and loss thus the two sides can be compared. Figure (6.15) shows the energy loss side on its own. The line at 1.8 $Å^{-1}$ is part of the 002 dispersion curve.

Figure 6.15: Energy loss spectrum of Bran D graphite

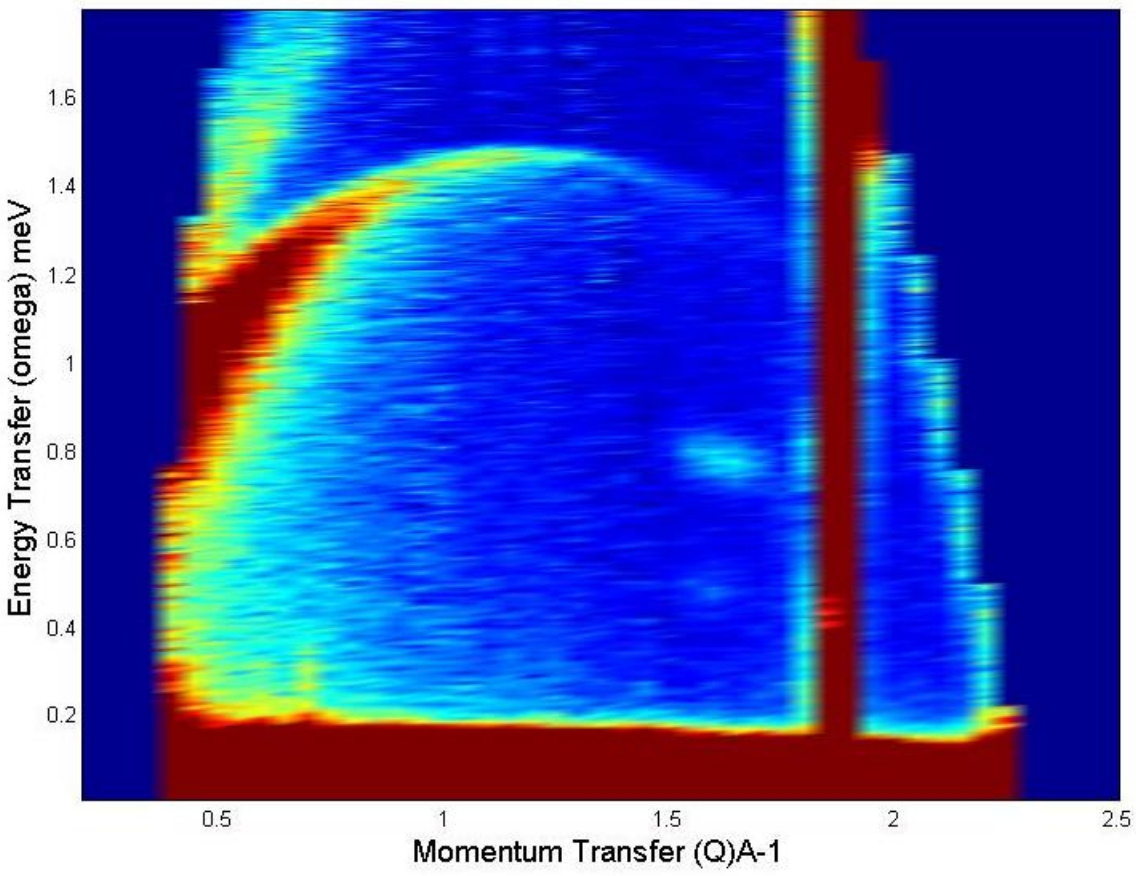

Figure (6.16) shows the two sides of the spectrum compared at the same energy transfer. These should show the same information other than differences in intensity due to detailed balance.

Figure 6.16: Energy loss and gain Bran D data at the same energy transfer

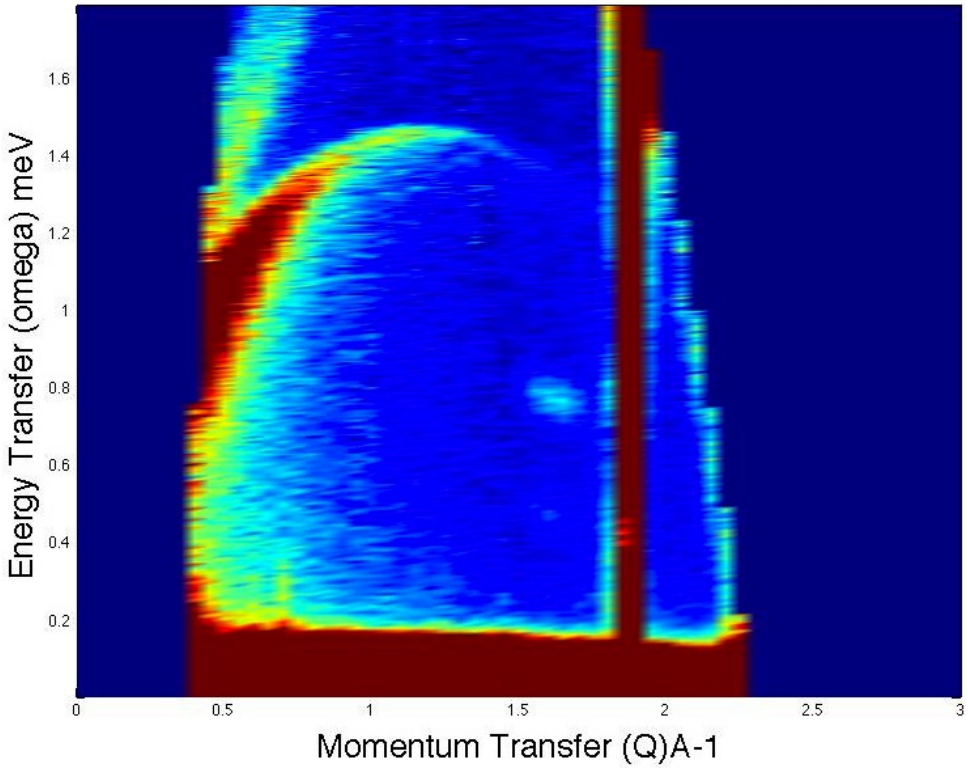

(a) Energy loss spectrum of Bran D graphite

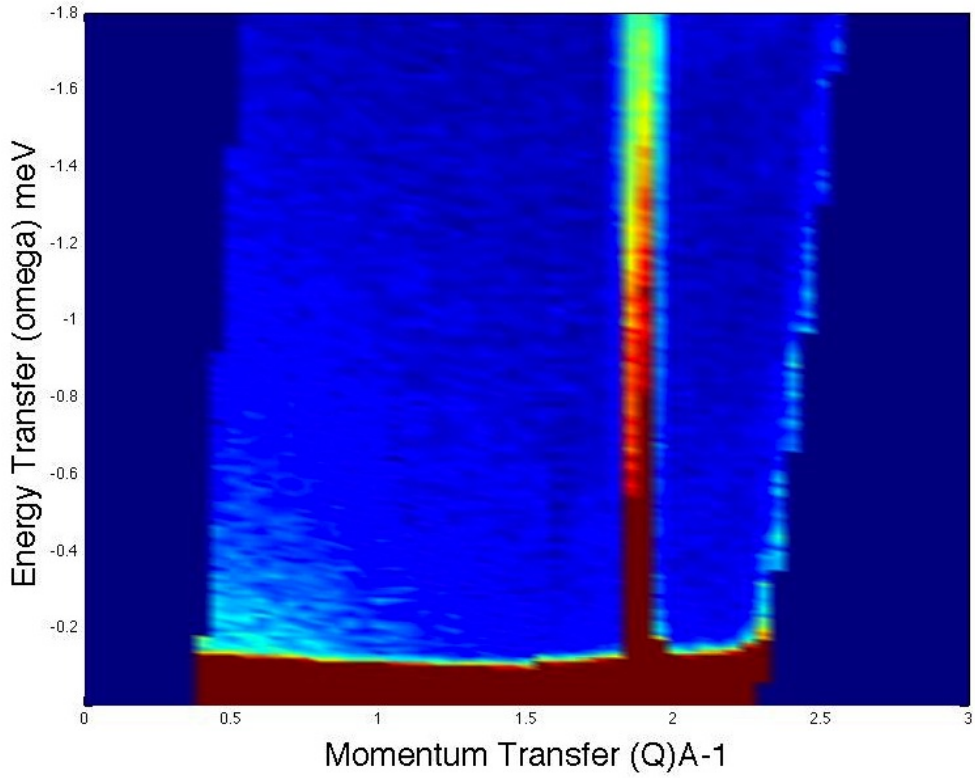

(b) Energy gain spectrum of Bran D graphite

However the energy loss spectrum shows a strange feature which shows up very clearly. If this feature is a real dynamic effect it should also be present on the energy gain side of the spectrum, albeit at a slightly lower intensity. It seems from the comparison that the feature is not present on the energy gain side of the spectra, however it is possible that it is just at a very low intensity. Cuts through the data allow a clearer inspection of the area containing the spectra.

Figure 6.17: Cut through IN5 Bran D data at $\pm$1.24 meV

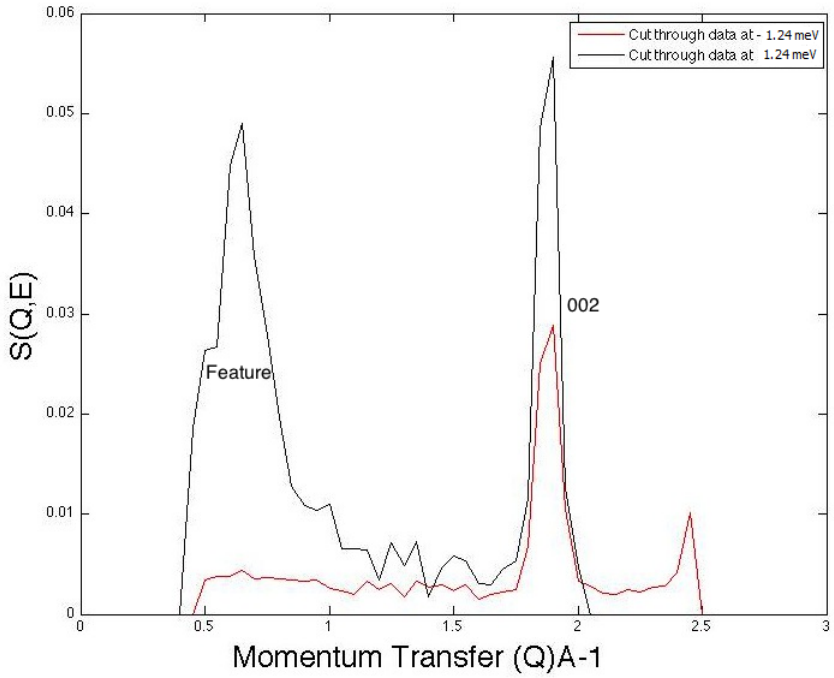

Cuts through the data at $\pm$1.24 meV show the intensities of the 002 curve and the feature on both sides of the elastic line. At this energy transfer the 002 curve has an intensity of 0.025 for energy gain and 0.056 for energy loss, thus loss is 2.2 times more intense at this energy transfer. The feature's intensity peaks at 0.049 so a peak would be expected at 0.022 on the energy gain graph, but this is not present. There is a peak at 0.0048 but this is a magnitude less than expected.

Several cuts through the data from ± 0.99 to ± 1.24 meV (6.18) were taken to check the result above. The 002 peaks increase in intensity at lower energy transfer.

Figure 6.18: Cuts through IN5 Bran D data at different energy transfers

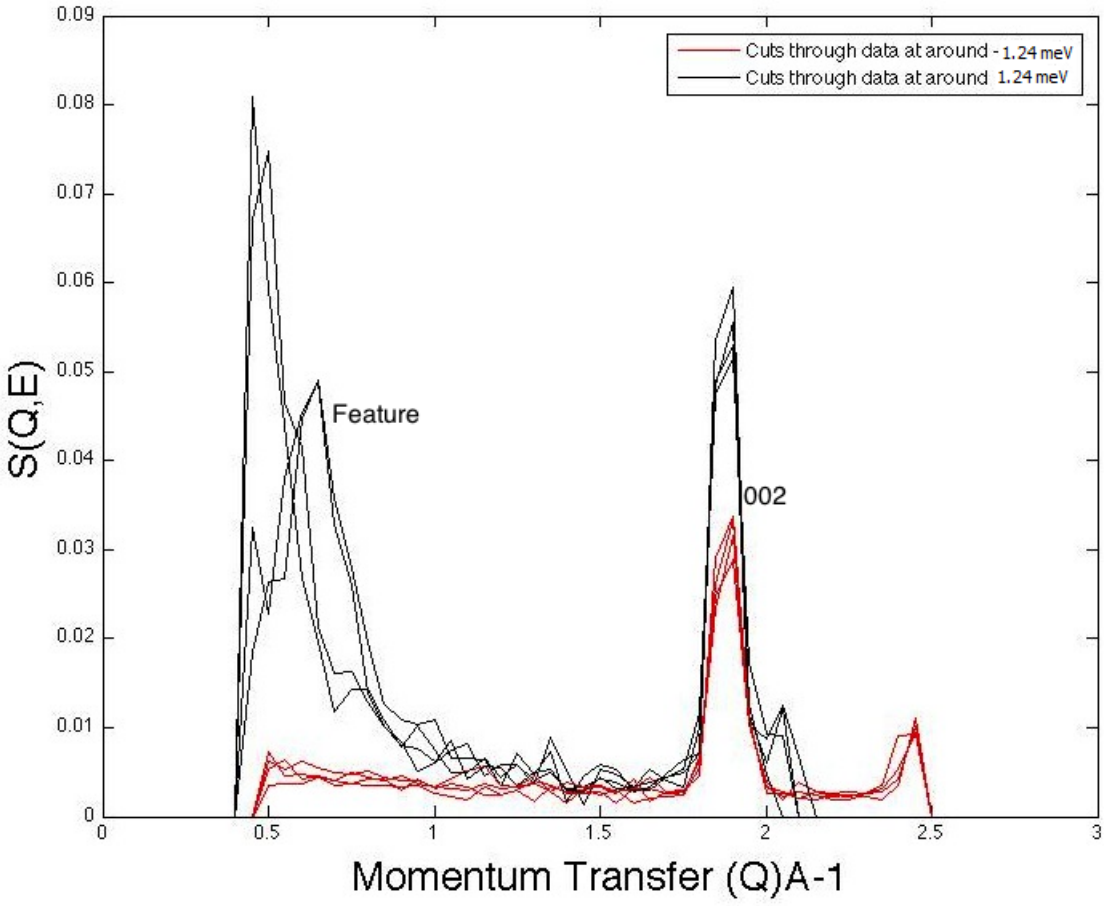

As the feature is not present on any of the cuts through the energy gain spectra the feature cannot be due to the properties of the sample and is a spurious set of data created by the conditions in the spectrometer.

Looking at the time-of-flight data, the feature is present at later time measurements and must have been caused by neutrons being delayed.

This delay was most likely caused by a sequence of elastic diffractions, the first in the sample and the second somewhere inside the detector array box, giving rise to a longer path length and therefore an apparent energy loss. IN5 at this

Figure 6.19: IN5 Bran D time-of-flight data

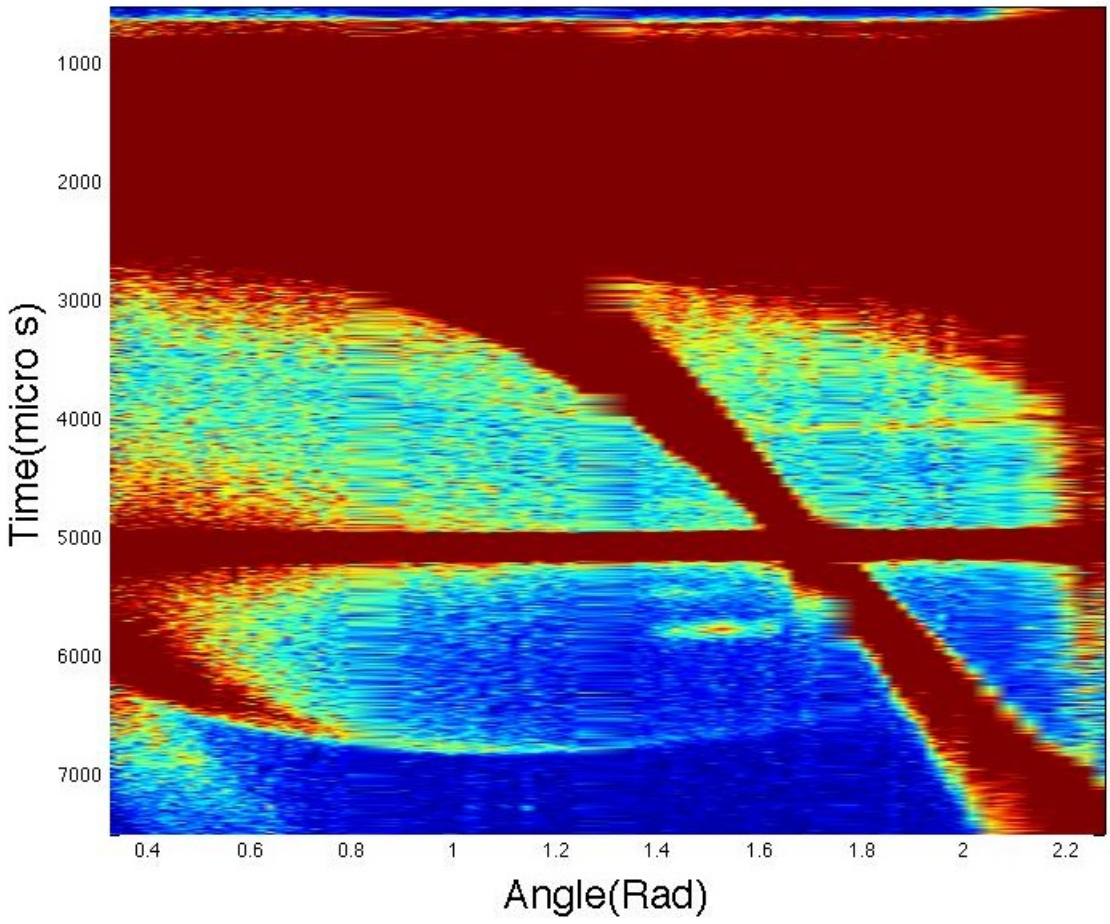

point was an old spectrometer and these measurements were some of the last taken before a full refitting and upgrade of the instrument.

6.2.2 Bran D 002 Curve

The energy gain side of the spectra also seems to show a difference in the curvature of the dispersion curves on either side of the $1.9A^{-1}$ peak. Scattering theory predicts these curves to be identical, as shown by Scatter data. Sine curves were fitted to the data with an amplitude of 16 meV and 14 meV respectively. It seems that the 14 meV curve fits the left hand side curve better and the 16 meV data gives a better fit to the right hand side curve, but the fit

is somewhat ambiguous.

Figure 6.20: Energy gain spectrum of Bran D with two sine curves fitted at 14 meV(black) and 16 meV(white)

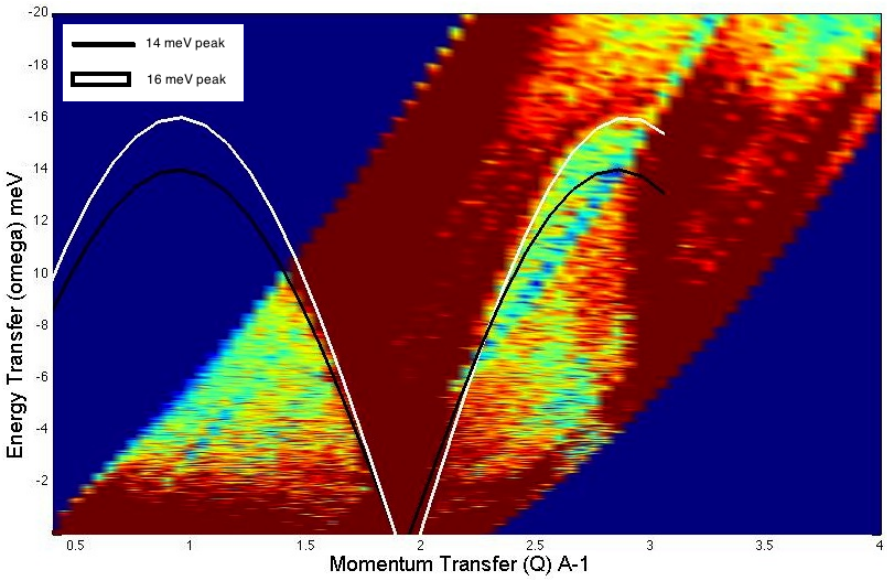

Using the Locus Options function a graph of Scatter data can be created which covers the same loci as the experimental data. Thus a direct comparison can be made.

Figure 6.21: Scatter data for graphite at the loci covered by the instrument

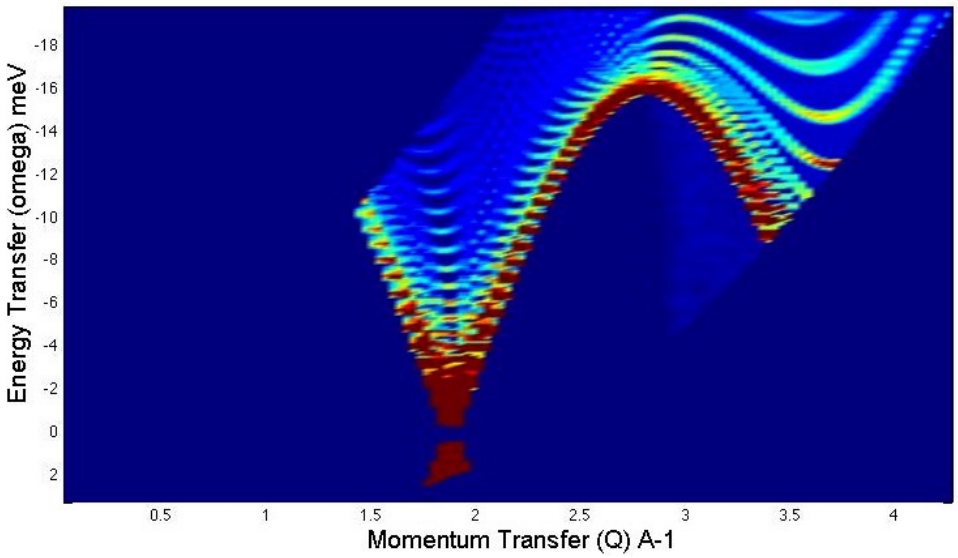

When the contours of the Scatter data (in black) are overlaid onto experimental data the ambiguity of the sine curve data is removed.

Figure 6.22: Contours of Scatter data, over Bran D data

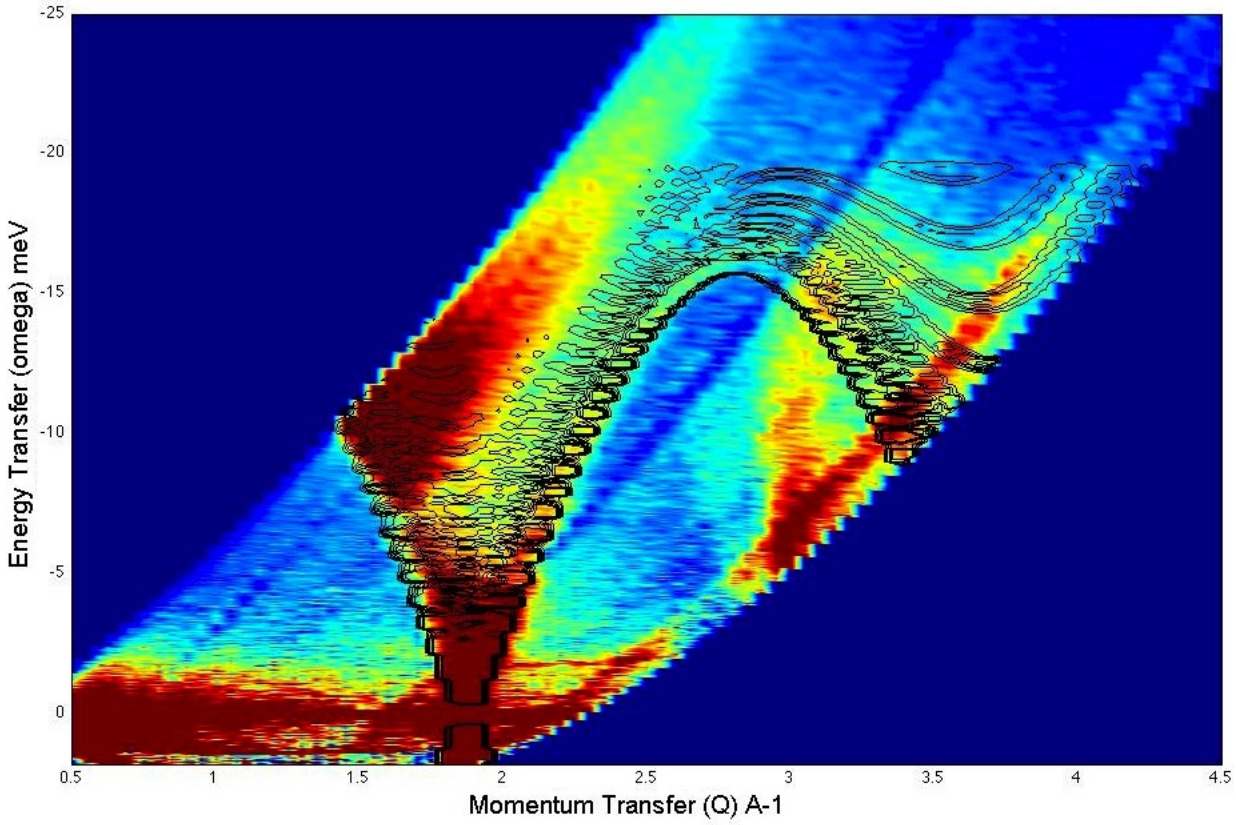

The scatter data shows clearly that the curves are different. However the left hand curve does seem to match the Scatter data at the top and bottom of the visible curve. Though it is possible that these differences are caused by defects in the material. The matching of the curve at areas with high intensity, as well as the existence of some level of intensity at all areas covered by the Scatter data, suggests that the curves are in fact the same as predicted. It seems that we are again having issues caused by the spectrometer.

6.2.3 Expanded Graphite

For the expanded graphite sample, measurements were taken at 497 K for 15 minutes.

Figure 6.23: Full spectrum of expanded graphite data showing a maximum energy transfer of 30 meV

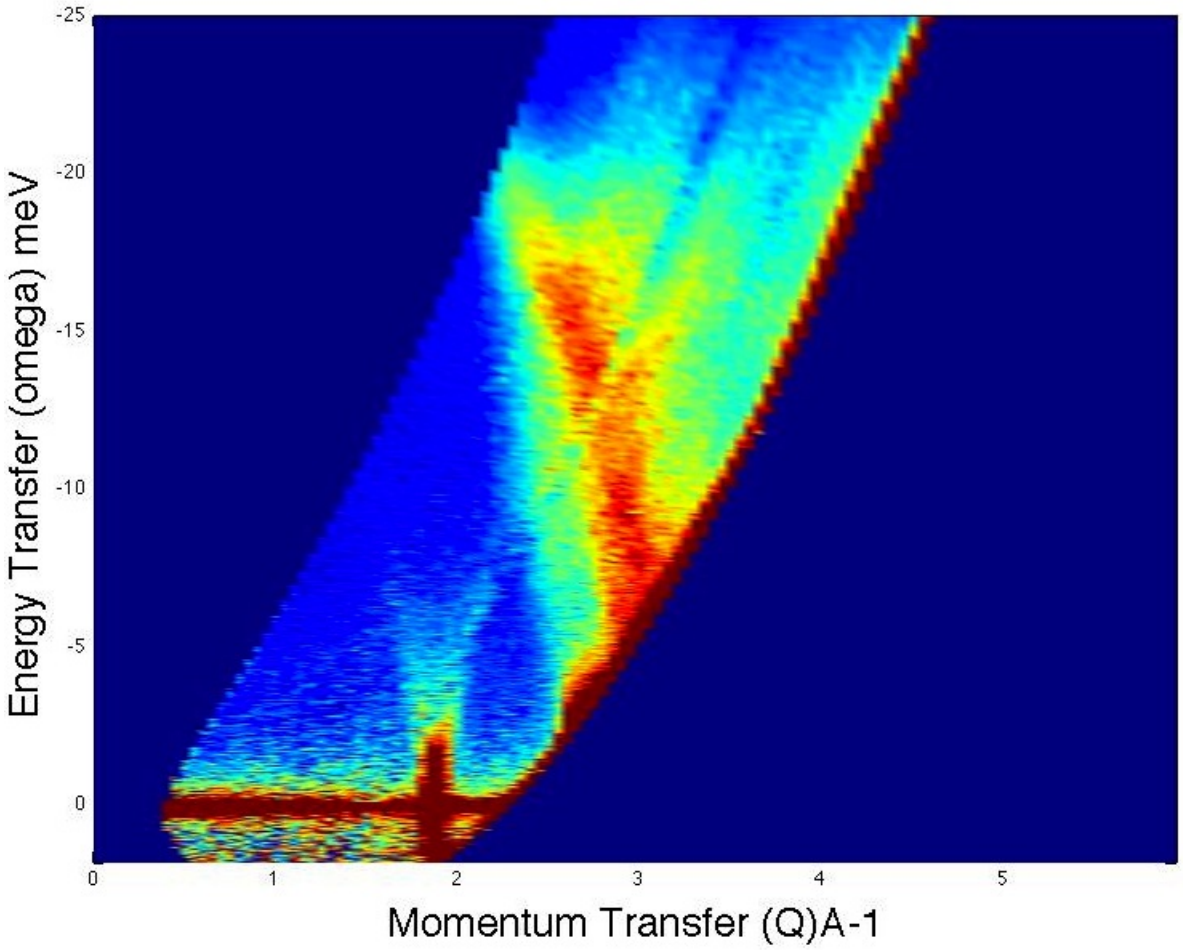

In the spectra of this sample the highest intensity has changed from the 002 curve to the higher Q dispersion curves. This fits the results seen in the XRD measurements where the relative intensity of the 002 peak was much reduced. It also has a greater amount of noise around the elastic line than the Bran D data, the detector deficiencies are still visible.

We can show Scatter data overlaid at several different cutoffs. The Scatter data

Figure 6.24: High intensity Scatter data over expanded graphite data

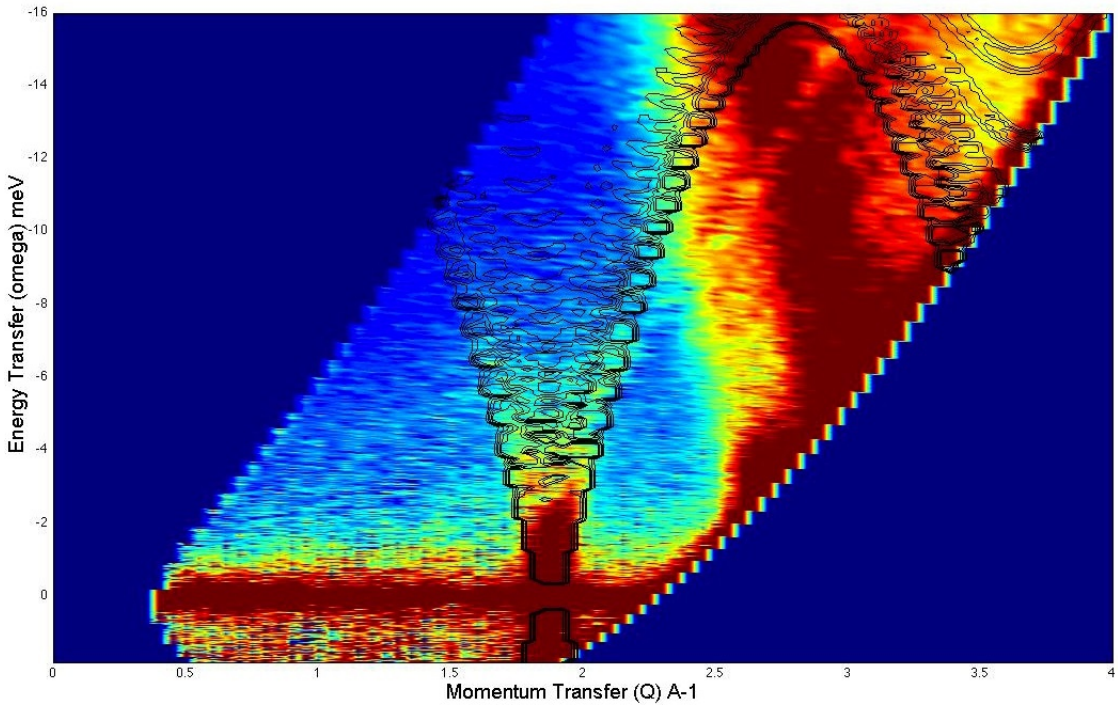

Figure 6.25: Theoretical and experimental graphite data directly compared

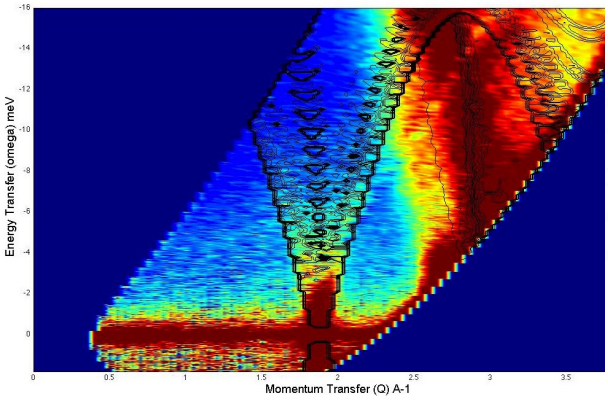

(a) Medium intensity Scatter data over expanded graphite data

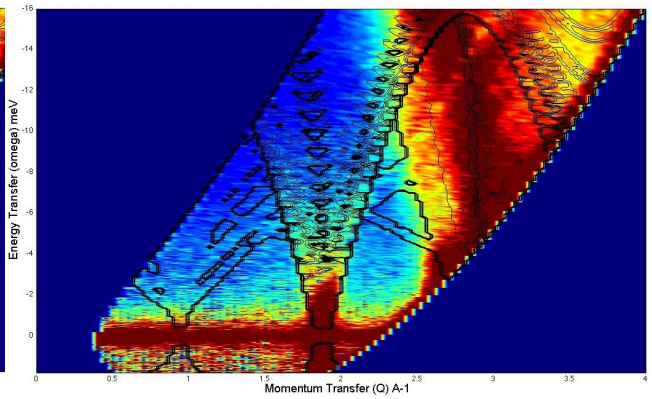

(b) Very low intensity Scatter data over expanded graphite data

seems to match well with the experimental data, with no visible broadening or shifting of curves. Using the cut off function we can see the low intensity scatter curves.

These figures show a progression of Scatter data intensities. The first figure shows the highest intensity Scatter data. The next figure has a lower cut off which shows more low intensity data. The final figure shows the Scatter data with all of the intensity values were set to one, so that all intensities are shown equally. At this level, some of the data is an artifact of the calculation but it also shows some data which fits well with the curve at 2.5 $Å^{-1}$.

This expanded graphite was then used to create the C60 GIC sample. The results of poly-CINS experiments on this material are shown in the next chapter.

6.3 Comparison of Calculated and Measured Data

Using the Line Graphs functionality of Neutronplot we can compare data in a less ambiguous way.

Figure 6.26: Lines through axially symmetric model graphite data

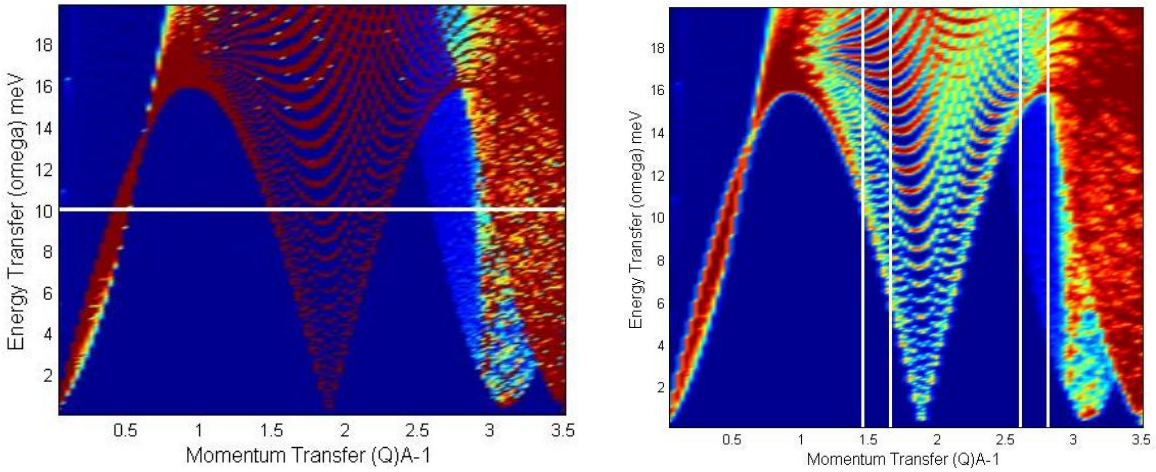

(a) Line through calculated graphite data at 10 meV

(b) Lines through calculated graphite data at constant Q

Figure (6.26) shows lines through modeled graphite data set. Line graphs have been produced at these areas for the Branwell D, exfoliated and Young and Kopple model data sets. The data sets were normalised to the most intense

data point.

Figure 6.27: Several graphite data sets at 10 meV

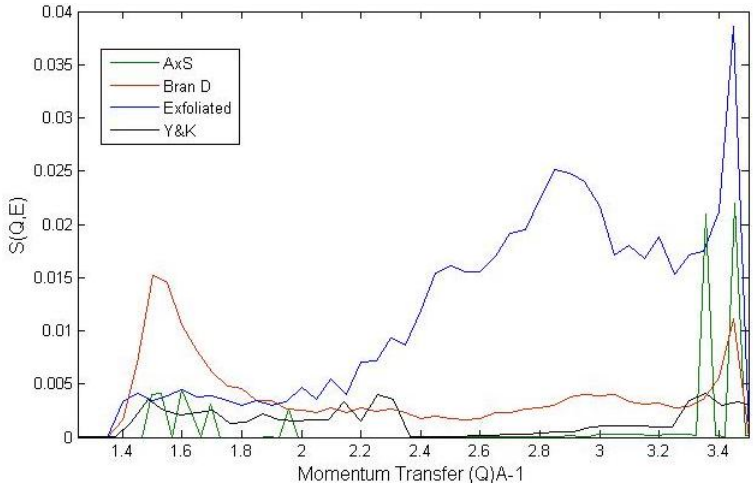

Figure 6.28: Cuts through graphite data sets at constant Q values

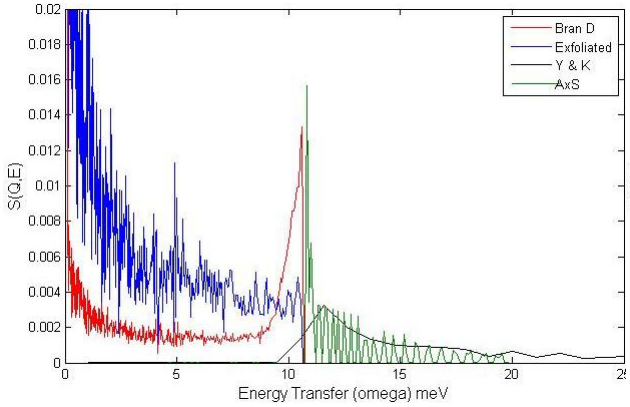

(a) Graphite data sets at 1.45 Å^{-1}

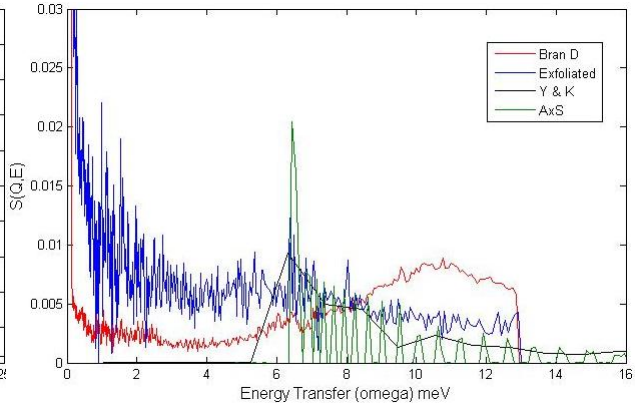

(b) Graphite data sets at 1.65 Å^{-1}

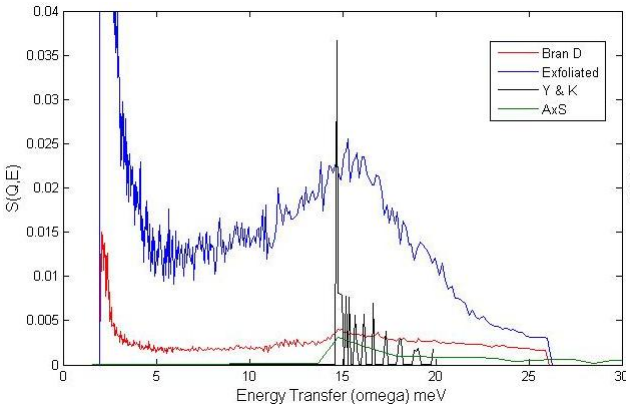

(c) Graphite data sets at 2.6 Å^{-1}

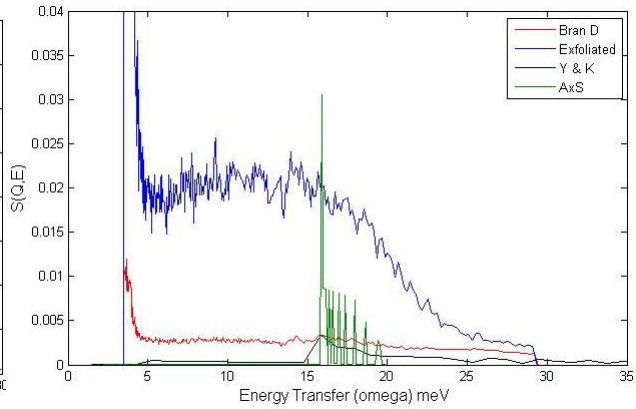

(d) Graphite data sets at 2.8 Å^{-1}

Figure (6.27) shows line graphs of calculated and measured graphite data sets taken at 10 meV. From figure (6.26a) peaks would be expected 0.5, 1.5, 2.3, 2.6, 3.0 and 3.4 $Å^{-1}$. The graphs shown in figure (6.27) do not show the peak at 0.5 due to the range covered by the experimental data. The other features are visible on the data sets but show different intensities to those predicted by the calculated data. As the calculated data sets are biased on a perfect graphite lattice they underestimate the intensity of the none 002 curves. Orientation effects could also be involved as with the diffraction measurements.

Lines were also taken through the data sets at Q values of 1.45, 1.65, 2.60 and 2.80 $Å^{-1}$. These values were chosen to match important areas in the Branwell D data such as the peak of the 002 curve at 2.80 $Å^{-1}$, other points on the curve and the beginning of other curves at 2.6 $Å^{-1}$.

Figure (6.30) shows the intensity expected from the 002 curve at the 1.45$Å^{-1}$ point. The experimental data sets do not cover an energy transfer over 11 meV at this point, so there is no data to compare with that shown for the calculated. The exfoliated and Branwell D graphites show differences in intensity, with the exfoliated graphite showing more intensity over all but not showing a clear peak at 10 meV. The calculated data sets predict the peak to be at a slightly higher energy transfer than that shown by Branwell D. In figure (6.31) The experimental and calcualted data sets agree with a peak at 6.5 meV, albeit at slightly different intensities, the Branwell D also shows a rise in intensity at around 11 meV which is also shown in its full $S(Q, E)$ spectrum. Figures (6.28c) and (6.28d) show clearly the difference in intensity of the exfoliated graphite to the other samples at these Q values. The positions of the peaks are largely in agreement, however the exfoliated sample does not show a clear peak at 16 meV in figure (6.28d).

The calculated data shows the issues with sampling, as discussed in an earlier

section, in these graphs. The experimental data covers the areas in question more thoroughly than the calculated data and is less jagged. Figure (6.29) shows the quality of the Young and Kopple data set at the areas used.

Figure 6.29: Young and Kopple model data at similar Q, E to experimental data

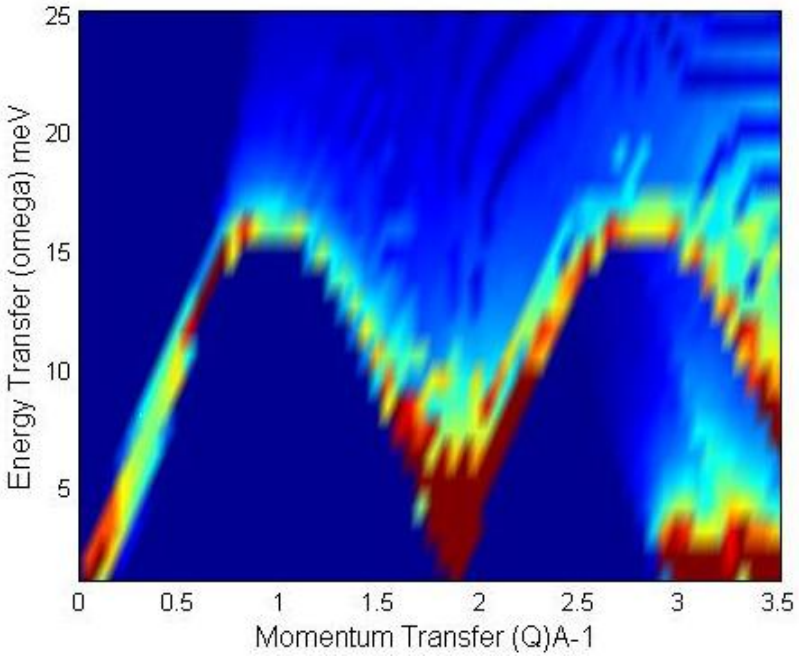

Although the data is quite rough the curve positions are still captured by these calculations and can be compared to experiment.

These cuts through the data can also be used to find other information about the properties of the materials. They are used to find elastic constants for the experimental data in the following section.

6.4 Elastic Constants

The neutron scattering measurements can be used to find information about forces in materials, such as the the compressibility in the z direction, known as the C_{33} constant. The phonon curve arising from the interaction between

the layers is clearly shown in the above measurements. Elastic constants are measured directly by finding the speed of sound through a single crystal of material. This is difficult to achieve with graphite samples so they are found using information from inelastic x-ray and neutron spectra. An inelastic x-ray measurement by Bosak *et al.*[63] gave a figure of 3.87×10^{11} dynes cm^{-2}.

C_{33} can be measured from this phonon curve. The equation which describes the phonon curves in graphite relates the frequency of the phonon v to a force constant K′

$$v = \pm\frac{1}{2\pi}\sqrt{\frac{2K'}{M}}sin(\pi q/2\tau_{002}) \tag{6.1}$$

where K′ is the force constant for stretching the bond between atoms in adjacent planes, M is the mass of the carbon atom, q is the wave vector and τ is a reciprocal lattice vector.

The relation between the compressibility in the z direction C_{33} and the force constant K′ is

$$C_{33} = \frac{K'\rho c^2}{8M} \tag{6.2}$$

substitution of equation (6.1) gives

$$C_{33} = \frac{4\pi^4\rho v_{max}^2}{\tau^2} \tag{6.3}$$

To obtain values for the 002 curve necessary for the C_{33} calculation cuts through the data were taken at intervals of 0.5 Å^{-1}.

In figure (6.30) there is a sharp rise in intensity at 6.082meV which is the edge of the phonon curve. The measurement for the point of the phonon curve is therefore taken at this point. Other graphs do not show this clear edge.

Figure (6.31) has a hump rather than an edge. For these cases a point at the highest point of the hump was used as it is the least ambiguous measurement

Figure 6.30: Cut through Bran D IN5 data at 2.15 Å^{-1}

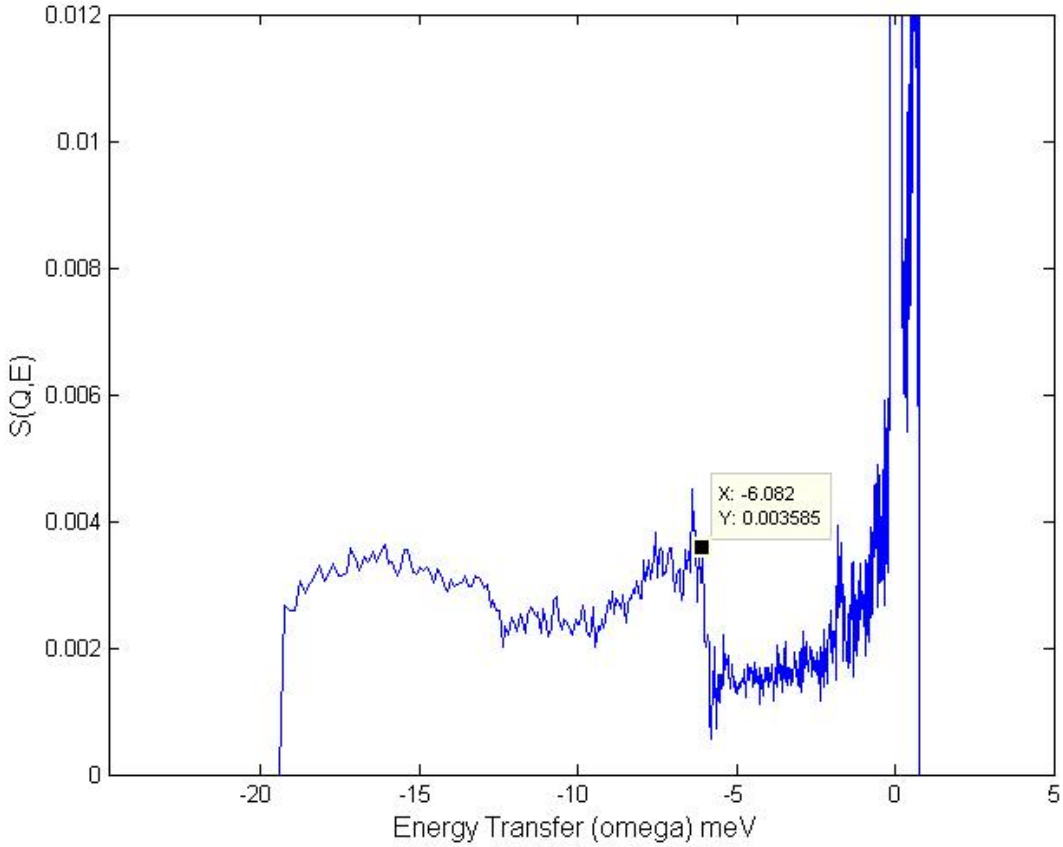

of where the phonon curve is at that Q value.

This approach does have issues in terms of the accuracy of the measurement, thus the error bars at these points are much larger. Taking measurements at many points around the curve should minimise the error in the C_{33} calculation. The Bran D sample gives the curve shown in figure (6.32).

The points taken from the cuts can be compared to the poly-CINS data. This shows clearly the where the measurements were more ambiguous, such as around 3 Å^{-1} where contributions from other phonons overlap with the 002 curve.

The points on the right hand of the curve were fitted to a sine curve using the

Figure 6.31: Cut through Bran D IN5 data at 2.3 $Å^{-1}$

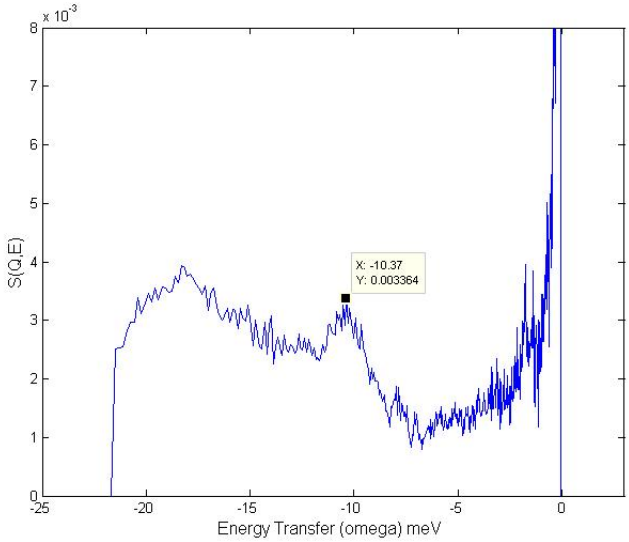

Figure 6.32: The 002 curve of BranD graphite taken from the IN5 measurement with error bars

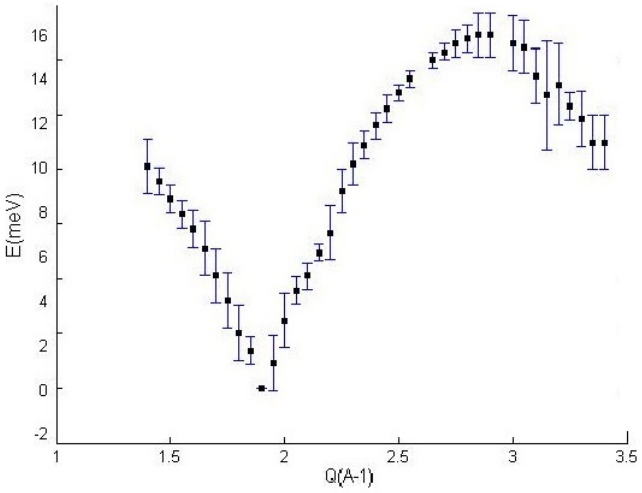

MATLAB curve fitting tool, $cftool$.

This fitting gave the curve $15.93 * \sin(1.616 * x + 3.226)$ with an error of ± 0.25 in the amplitude. This corresponds to a maximum energy of 16 meV$\pm$0.25 from which a V_{max} value for Bran D can be calculated. The exfoliated graphite sample does not give as clear a 002 phonon curve as the Bran D.

Figure 6.33: Data points taken from cuts on poly-CINS data

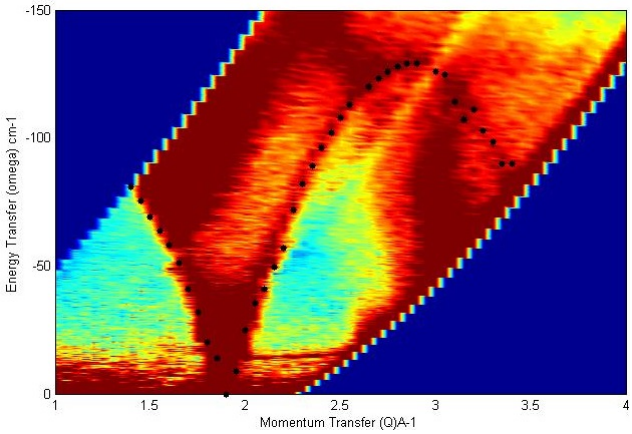

Figure 6.34: Curve fitted to 002 data points

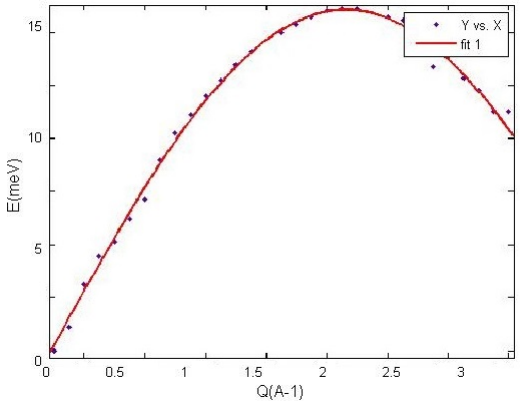

Figure 6.35: Fit to full Branwell D 002 curve

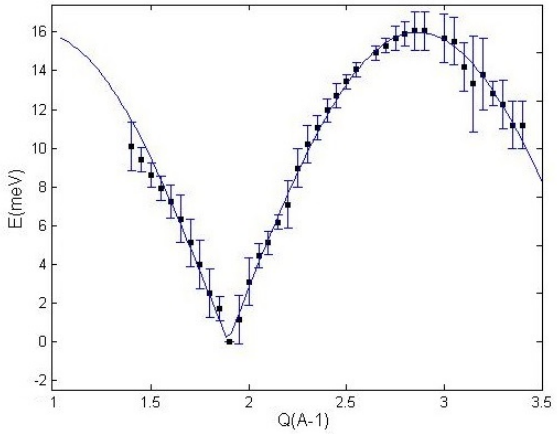

Figure 6.36: Exfoliated graphite IN5 measurement

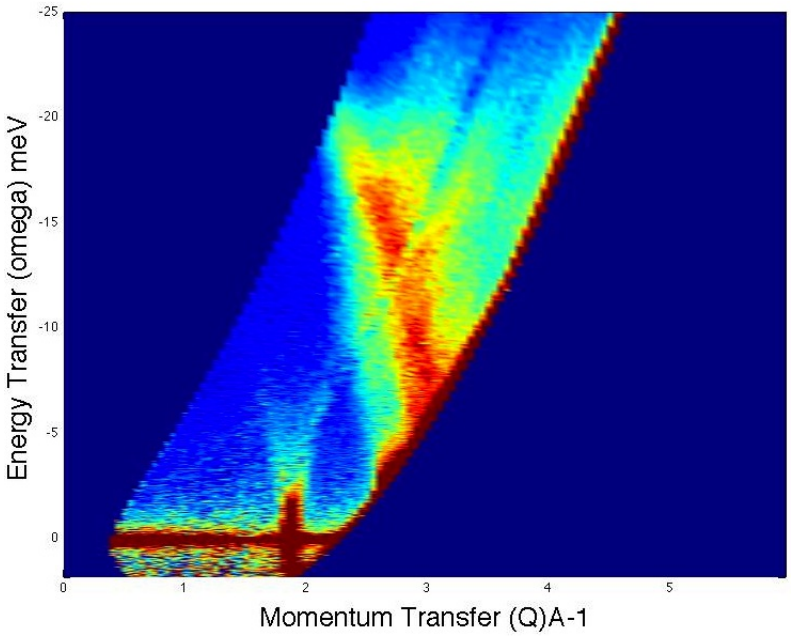

Cuts through the data were taken using the same method as for Bran D, however the intensity of the 002 curve is lost at around 2.4 Å^{-1} well before the peak position. The curve fitting method used above cannot be used in this case as it requires a peak estimate.

Figure 6.37: 002 curve points of exfoliated graphite taken from cuts

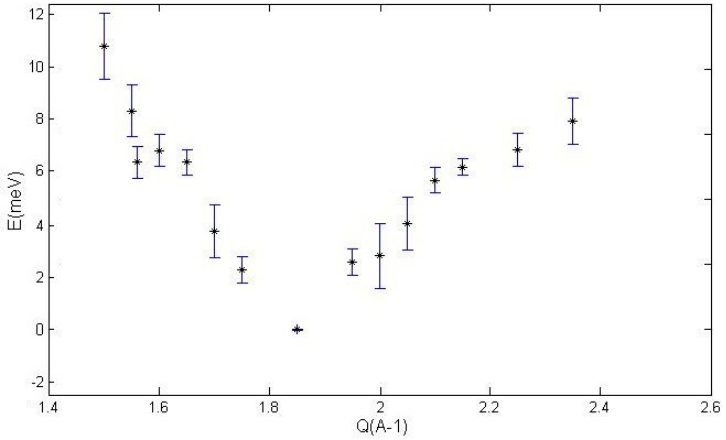

A theoretical graphite data set was overlaid to give a guide to the shape of the phonon curve and thus allow an estimate of the peak height to be made.

Figure 6.38: Scatter data over IN5 data for exfoliated graphite as a guide to the 002 curve

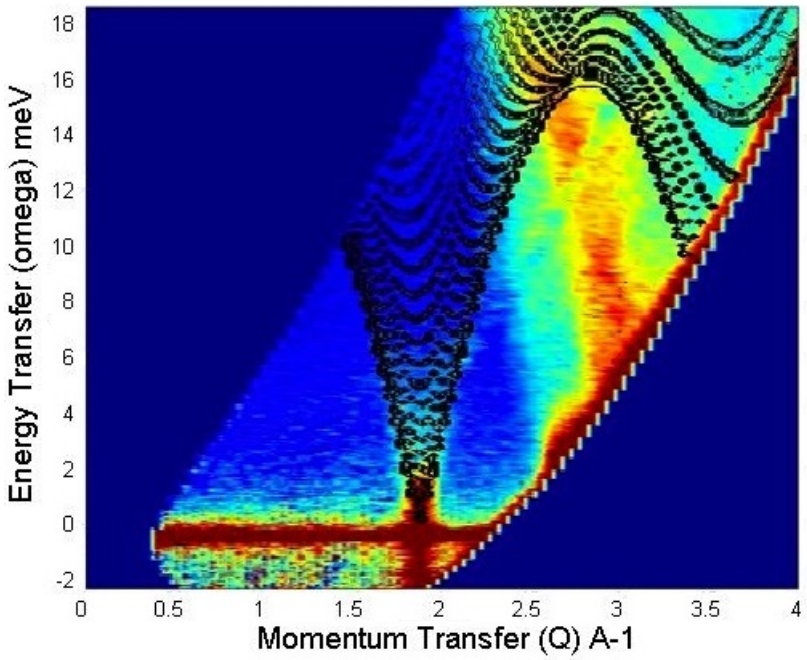

Based on the slight expansion of the curve it has been assumed that the peak of the curve would be slightly lower than that predicted by the theoretical data, thus a peak height of 15.37 meV was used for the calculation of the C_{33} value, however this assumption will give quite large errors.

Table 6.1: Comparison of the C_{33} values of different graphites

Graphite	V_{max} (meV)	τ_{002} (Å^{-1})	$C_{33}(\times 10^{11}$ dynes cm$^{-2})$	p	Temperature (K)
Bran D	16.00 ± 0.25	1.9	3.8787 ± 0.1	0.25	494
Exfoliated Bran B	15.37 ± 0.4	1.85	3.527 ± 0.2	0.524	497
Ax Scatter	15.96	1.9	3.6891	0	0
YandK Scatter	15.80	1.87	3.69	0	0
Ross[55]	14.00	1.87	2.94 ± 0.4	0.2	293
Ross[55]	13.50	1.819	2.808 ± 0.2	0.2	1273
Ross[55]	11.50	1.768	2.097 ± 0.2	0.2	2193
Dolling[64]	15.90	1.876	3.78	0	296
Roy[65]		1.853	3.42	0	480
Seldin[66]		1.876	3.65+-0.1	0	293

The C_{33} values obtained from the IN5 data seem to fit well with values from other sources. The Ross[55] data demonstrates that increasing temperature reduces the C_{33} values measured, though between authors there is a spread in

values due to different sample types. Increases in p value also decrease the C_{33} value which fits with the exfoliated graphite measurement though there is a large uncertainly in this value due to the disorder in this material creating a noisy phonon curve.

In this chapter we have shown an analysis of the dynamics of two different types of graphite. The analysis tools of Neutronplot were highlighted with the use of theoretical data overlays and line graphs through the experimental data. This has allowed us to come to a definitive answer to questions posed by the data. We proved that the strange feature shown on the energy loss spectra is not present on the energy gain side and thus cannot reflect a true behavior of the natural graphite sample. We were also able to directly compare theoretical and experimental poly-CINS data to demonstrate the difference in curve intensity for two sides of a 002 phonon curve of natural graphite and provide a possible explanation for this. This was followed by an investigation into an exfoliated graphite sample. This demonstrated that the loss in 002 intensity shown in diffraction measurements has an effect on the dynamics of the material, with the higher Q curves showing a much higher intensity, to the point of dominating the 002. The data was then used to find the C_{33} elastic constant for the graphites. With Neutronplot being used again to show regular lines through the data and for using theoretical data as a comparison to give an idea of the shape of the exfoliated curve. This gave results which fit well with patterns of the constant at different temperatures and for samples with different p values.

Chapter 7

Inelastic Scattering C60 Graphite Intercalate

Unlike graphite, which has been investigated and characterised over many years, C60 GIC is a novel material. There are no previous inelastic neutron scattering measurements of C60 GIC, though there has been investigation into the dynamics of the pure C60 lattice.

Poly-CINS measurements were performed on a C60 GIC sample, in the NEAT Facility at Helmholtz Zentrum Berlin (HZB) by D. Roach, M. Russina, N. Tsapatsaris and the author. These measurements can be interpreted using previous investigations into C60 together with the neutron diffraction measurements, giving us some insight into the behaviour of C60 in the graphite lattice. These measurements were taken over a period of two weeks, with each measurement having around three days in the beam. This is in contrast to the IN5 measurements which were typically taken in a few minutes. NEAT is said to have a flux at sample of 2×10^4 n/cm^2/s given an initial wavelength of 6 Å. This is an order of magnitude less than the figure quoted for the IN5. Both neutron scattering centres use a reactor to produce their neutrons.

The areas of forbidden scattering in graphite, which are below the 002 curves,

give a good window for the indication of other materials in the graphite sample. If features appear within them this gives a clear and unambiguous indication that there is something else, with a periodic nature, in the sample. As in the diffraction measurements it is expected that features from C60 will be present at Q values below that of the 002 graphite peak.

7.1 C60 Literature

There have been several investigations into the dynamics of the C60 lattice, with DFT and molecular dynamics calculations and inelastic neutron scattering measurements taken by different groups. Solid C60 can have an face centred cubic (FCC) or simple cubic (SC) lattice structure depending on the temperature of the material, the transition to SC takes place at around 250 K. It is also known that the molecules in the FCC lattice rotate quite freely, this rotation lessens at lower temperatures but is not believed to halt entirely[67]. We will discuss the dynamics of both the FCC and SC forms, as the C60 GIC sample was created at temperatures above 250 K but the inelastic neutron scattering measurements were taken at temperatures below 50 K.

Yu *et al.*[68] used molecular dynamic tight-binding calculations to predict the phonon dispersion and density of states for solid C60. The results below are for the simple cubic form. These dispersion curves shown in figure 7.1 show a clear gap between 7.6 and 30 meV, where the lower phonon curves arise from interactions between the molecules and the higher curves are interactions within the molecule. We are interested in the lower energy intermolecular vibrations, thus discussion will be focused on these modes. The modes at 2.3 and 3.7 meV are librational modes.

Yu also calculated density of states (DOS) for several ordered and disordered

systems show in figure 7.2. Starting with a system labelled (a) which has an an orientation angle Γ of 23.45° with respect to the 111 FCC axis, the standard ordered form for SC, going through to (d) a different ordered form which has an an orientation angle Γ of 70.54° with disordered intermediate forms at (b) and (c).

Figure 7.1: Calculated dispersion curves of C60 FCC lattice by Yu *et al.*[68]

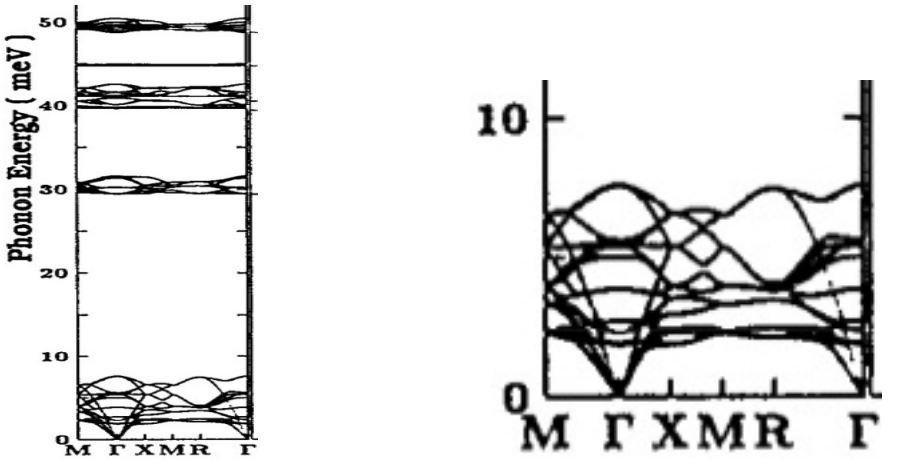

(a) Calculated dispersion curves of C60 SC lattice up to 50 meV

(b) Calculated dispersion curves of C60 SC lattice up to 10 meV

Figure 7.2: Calculated DOS for C60 lattices calculated by Yu *et al.*[68]

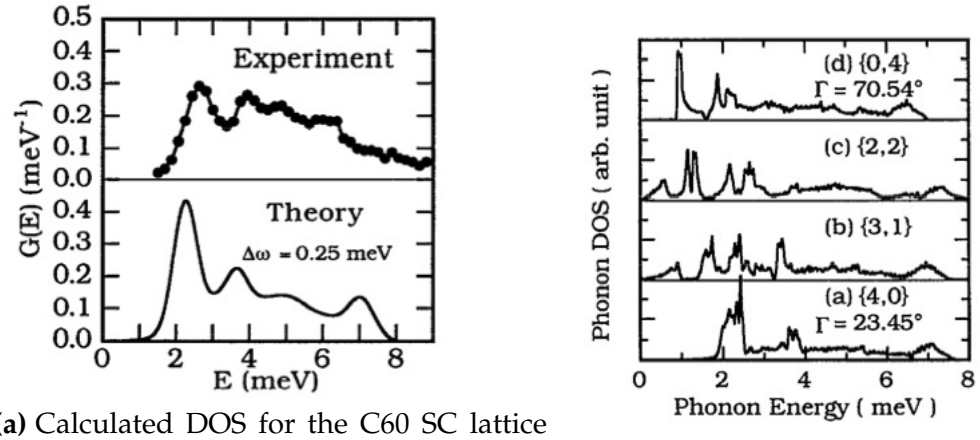

(a) Calculated DOS for the C60 SC lattice compared to neutron scattering measurement

(b) Calculated DOS for ordered and disordered C60, (a) is non disordered

Parker *et al.*[69] characterised the dynamics of the C60 lattice using neutron

scattering and CASTEP DTF calculations. They covered both the simple cubic and FCC forms. The intermolecular energies calculated by Parker peak at around 70cm which is around 8.7 meV, 1 meV higher than the value calculated by Yu, showing disagreement between molecular dynamics and density functional theory. Parker notes that the DFT calculations overestimate energies by 10cm^{-1} (1.24 meV) compared to experiment, thus the values from Yu are shown to be more accurate.

Figure 7.3: C60 lattice phonon dispersion curves calculated by Parker[69]

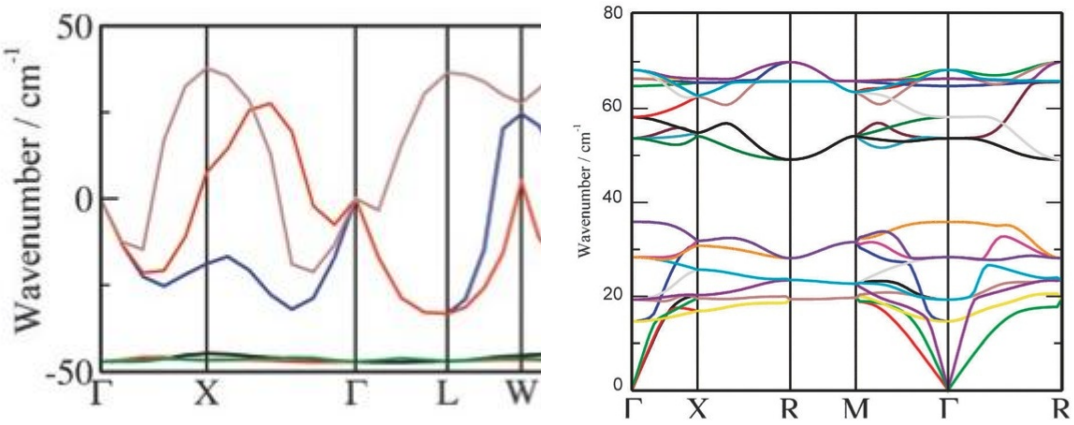

(a) Calculated phonon dispersion for FCC C60

(b) Calculated phonon dispersion for simple cubic C60

Figure 7.4: INS spectra of C60 measured by TOSCA (a) calculated by CASTEP (b)[69]

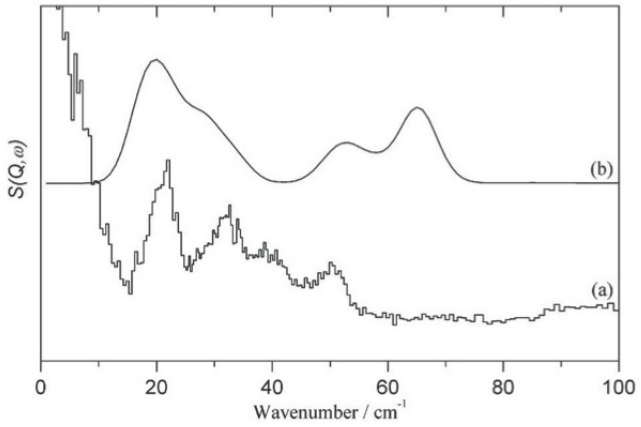

A inelastic neutron scattering measurement of a C60 lattice was taken on TOSCA. This was performed at a temperature of 17 K so the lattice in this case should be simple cubic. A CASTEP simulation was also performed and compared to the experimental result.

The experimental and calculated spectra do not match entirely and a peak is shown at higher energy in the calculation which is not shown in the experimental data.

Glebov *et al.*[67] used helium atom scattering (HAS) and lattice dynamics calculations to investigate C60 films in the 111 direction.

Figure 7.5: C60 HAS measurements taken by Glebov *et al.*[67]

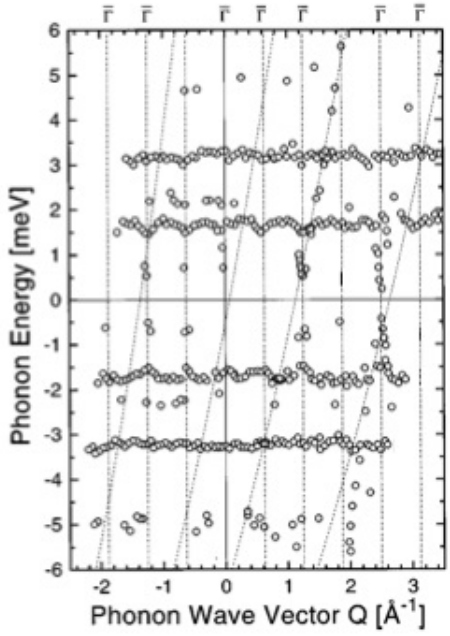

(a) Measured phonon dispersion from HAS for the 111 surface of C60, vertical lines indicate Brillouin zone centres

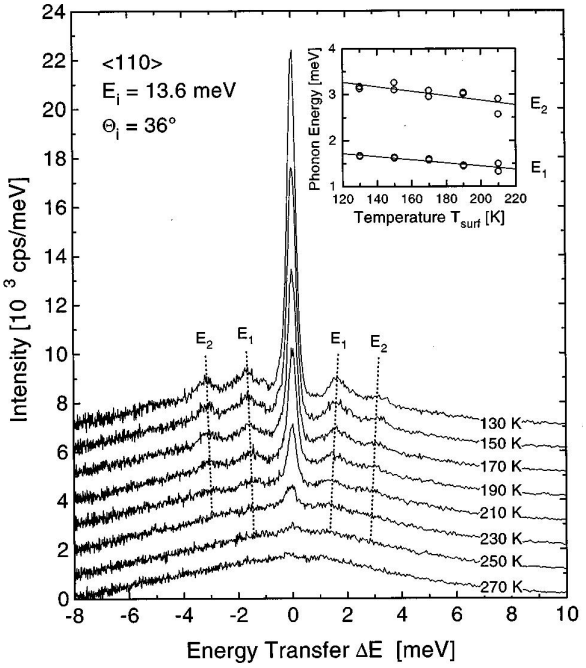

(b) C60 TOF spectra for different temperatures

The phonon data shows lines of intensity at 1.75, 3.25 and 5 meV, with curves dipping to 0 meV at 0, 1.2, 2 and 2.5 Å^{-1}. The data shown in figure (7.5b) shows the change of intensity for energy peaks with temperature. The peaks reduce

in energy and intensity as the temperature increases. Glebov *et al.* calculated phonon curves using lattice dynamics for intermolecular interactions, their results agree with those calculated by Yu *et al.* and peak around 7 meV.

7.2 NEAT Data

Figure 7.6: Poly-CINS measurement of the C60 GIC taken at 30 K with an initial wavelength of 2.1 Å

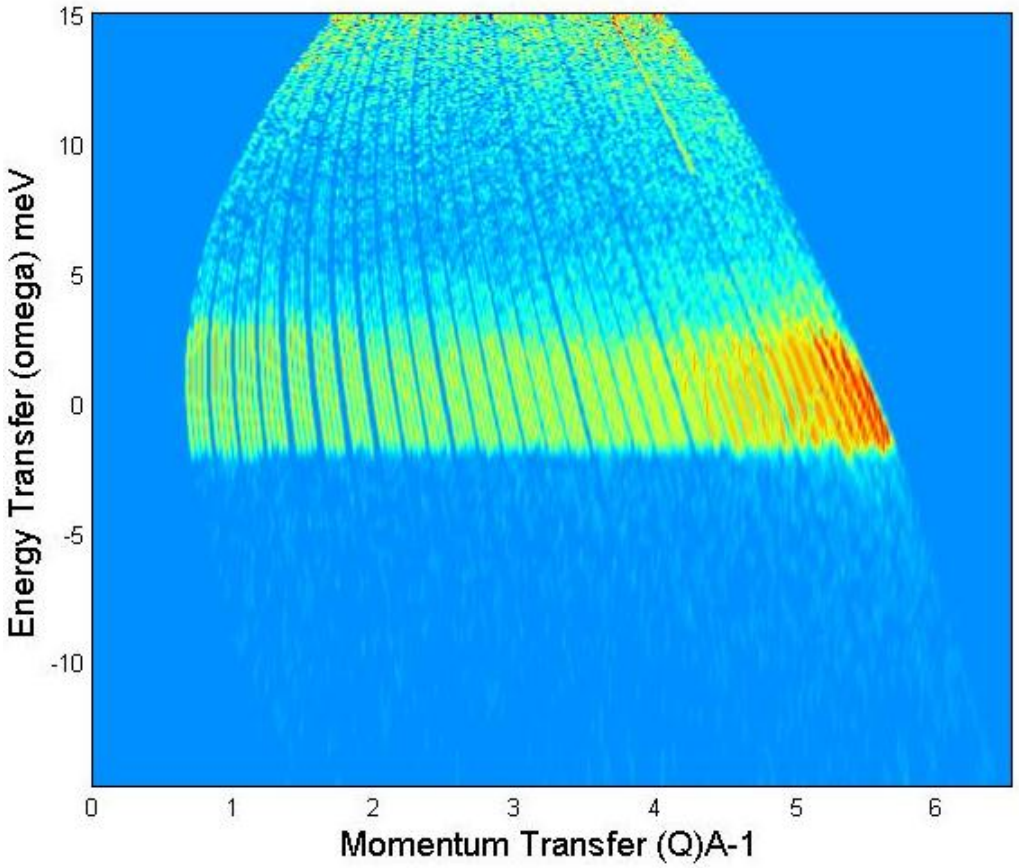

As mentioned above, for the C60 GIC sample the most interesting data was at the low energy transfer range which corresponds to low Q. Studying this range involved lowering the temperature of the sample and changing the chopper speeds, incurring a loss of flux. The sample was also very fine and light so there was not a good quantity of material in the beam. The combination of low

flux and the low density of sample makes analysis more difficult as the features become very hard to see, this is demonstrated in the figures below. Using Neutronplot we can analyse data obtained from NEAT. All of this data was converted from TOF to $S(Q, E)$ using the conversion routine in Neutronplot which is based on the equation $Q^2 = k^2 + k'^2 - 2kk' \cos\phi$.

Measurements of the C60 GIC were taken at several wavelengths in an attempt to see the low Q areas of most interest. We will first present an overview of the measurements taken to show the range of data obtained and the issues with it.

Figure 7.7: Poly-CINS measurement of the C60 GIC taken at 10 K with an initial wavelength of 4.8 Å

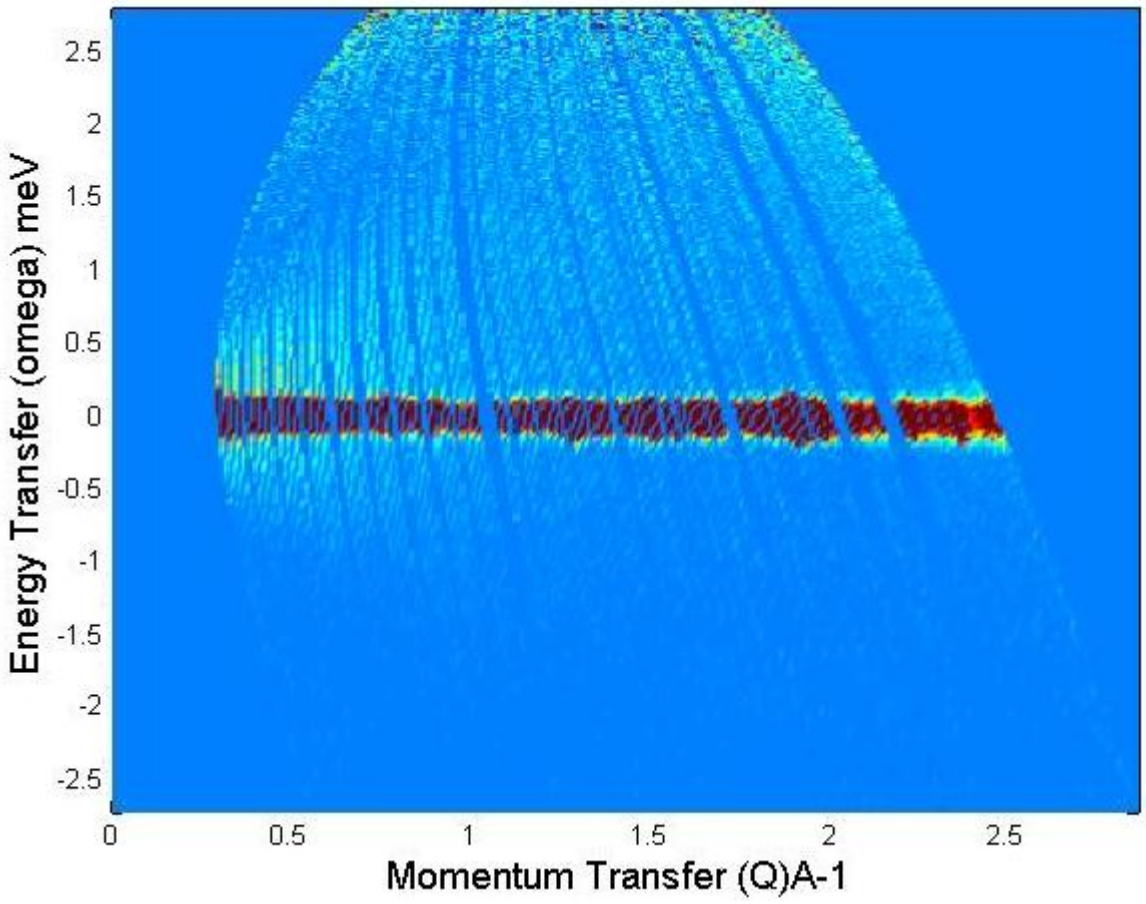

Figure (7.6) shows a measurement taken with an initial wavelength of 2.1 Å at 30 K. This has the widest Q range of the measurements but does not cover

Q lower than 1 $Å^{-1}$. This measurement has reasonably good statistics, no obvious phonon curves are present, but this is true for all the C60 GIC measurements.

The measurement with an initial wavelength of 4.8 Å at 10 K, figure (7.7) covers a Q range of 0.5 $Å^{-1}$ to 3 $Å^{-1}$. A vanadium run was also taken at 4.8 Å allowing this data to be vanadium corrected. The measurement also has reasonably good statistics.

Vanadium data can be used to normalise for detector efficiency and to remove any features caused by the instrument. It also provides the resolution function of the instrument. The resolution function can be used to decide whether features are real or an artifact of the resolution of the instrument.

Figure 7.8: Vanadium correction of data

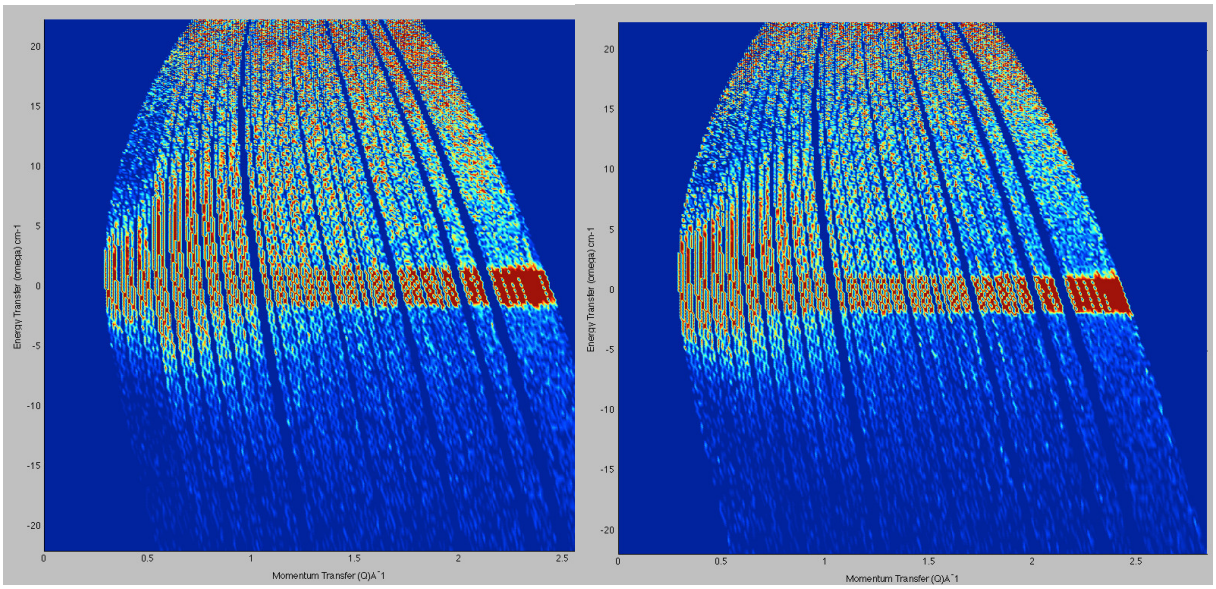

(a) Unaltered scan **(b)** Vanadium corrected scan

As shown in figure (7.9a) the measurement with an initial wavelength of 6.5 Å gives slightly more data at low Q but has poorer statistics and also has a detector fault which passes through the elastic line at 1.75 $Å^{-1}$, this has been removed in the figure. The measurement with an initial wavelength of 7.5 Å,

figure (7.9b), at 30 K covers a low Q range but has very poor statistics.

Figure 7.9: Poly-CINS measurement of C60 GIC at two wavelengths

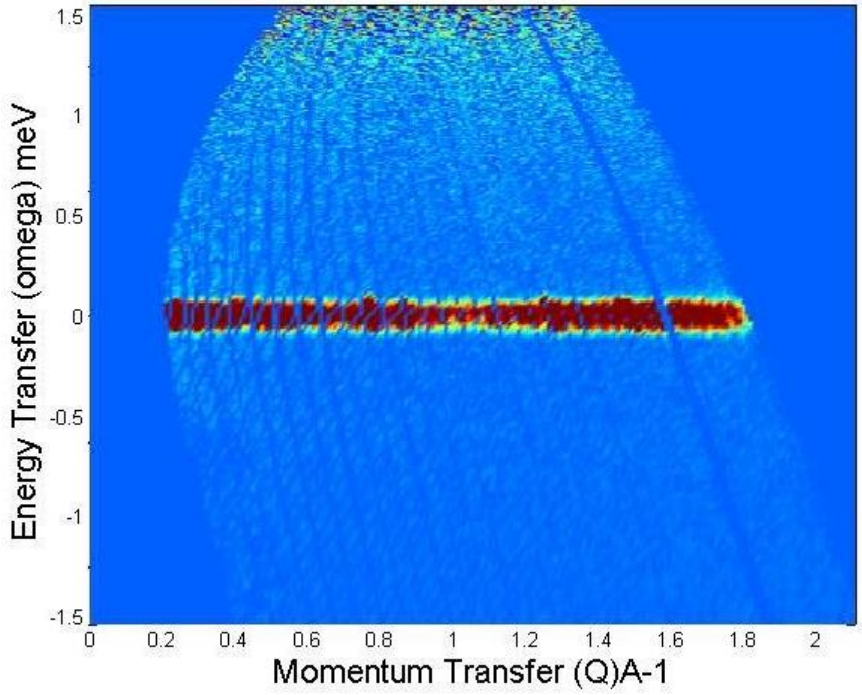

(a) Poly-CINS measurement of the C60 GIC taken at 30 K with an initial wavelength of 6.5 Å

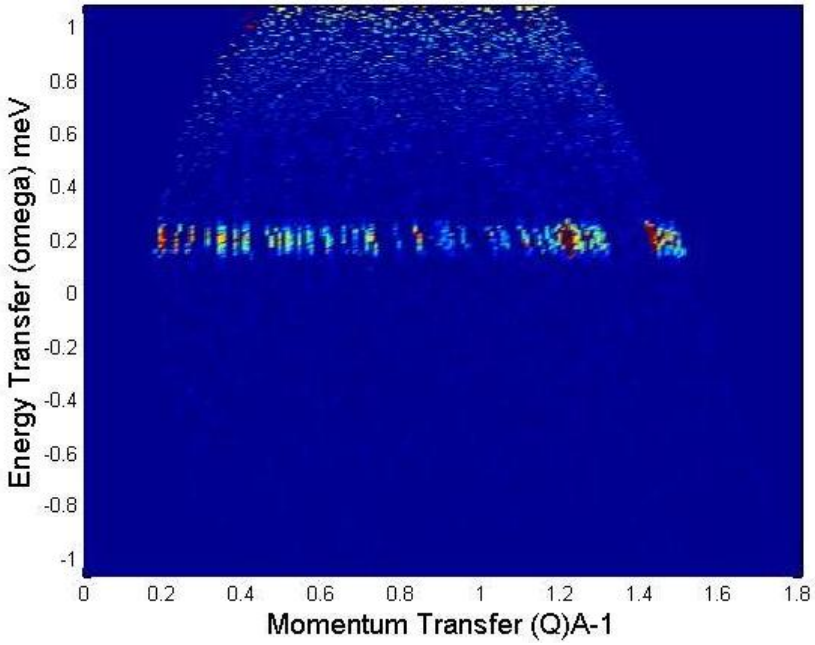

(b) Poly-CINS measurement of the C60 GIC taken at 30 K with an initial wavelength of 7.5 Å

We chose to focus our investigation on the measurements taken at 2.1 Å and

4.8 Å due to the ranges covered and the quality of the data. The structural data showed that the areas of interest for the intercalate are between 0.5 and 1.5 $Å^{-1}$, although this area is covered by the 6.5 Å and 7.5 Å data the quality is so low that there is no more information than that shown in the low Q section of the 4.8 Å measurement.

Figure 7.10: Resolution of the NEAT Poly-CINS data

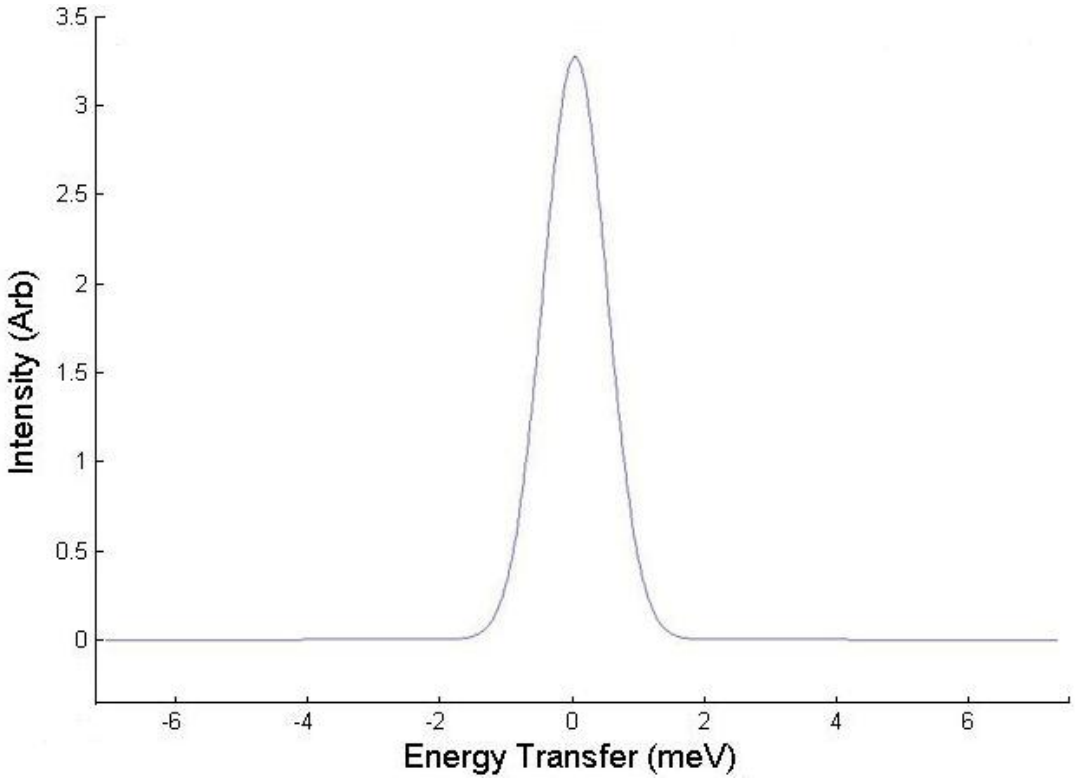

Due to concerns with the low statistics the resolution function of the instrument was calculated to ensure that data was not just an artifact of the instrument. The calculation used the vanadium data as a basis and a Gaussian distribution was assumed. As shown in figure (7.10) the data beyond the elastic line was found to be outside the resolution function.

7.2.1 Zero Energy Transfer PolyCINS data

Cuts were taken through the NEAT data at zero energy transfer for comparison with neutron diffraction data.

Figure 7.11: Comparison of NEAT and E9 data

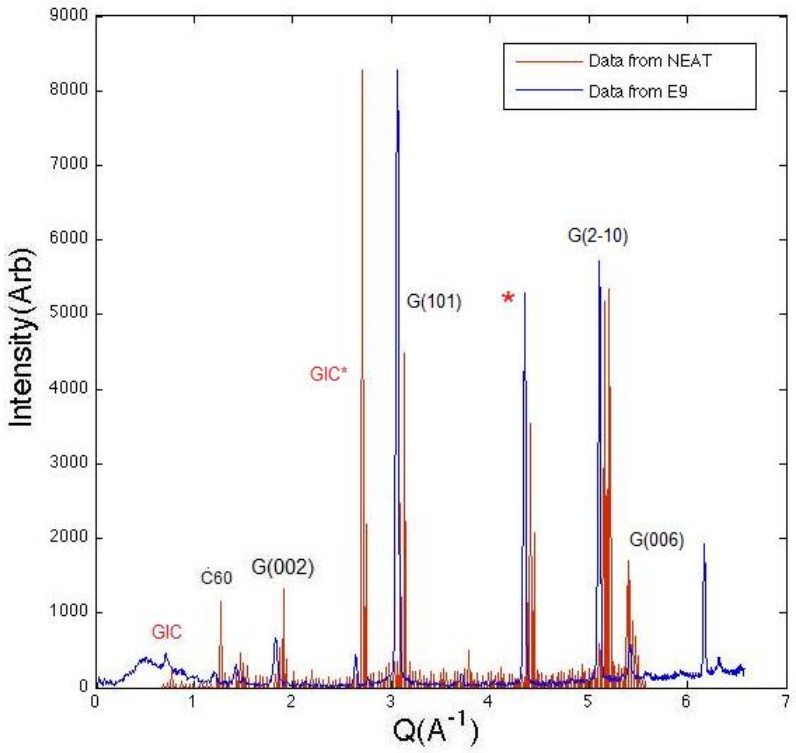

It can be seen that the peaks are shifted to the right by approximately 0.0689 $Å^{-1}$ and that the relative intensities vary from those in the diffraction data. The shift could be due to NEAT not being correctly calibrated, also the two measurements were taken at very different temperatures with the NEAT measurements being performed at around 270 K less than the diffraction. There are at least two peaks which are not attributable to typical C60 or graphite lattice structures, it is possible that these are intercalate peaks which were not modelled by the simple system used to prove the evidence of intercalation in the Structure chapter.

We can also compare the data at low Q.

Figure 7.12: Low Q comparison of NEAT and E9 data

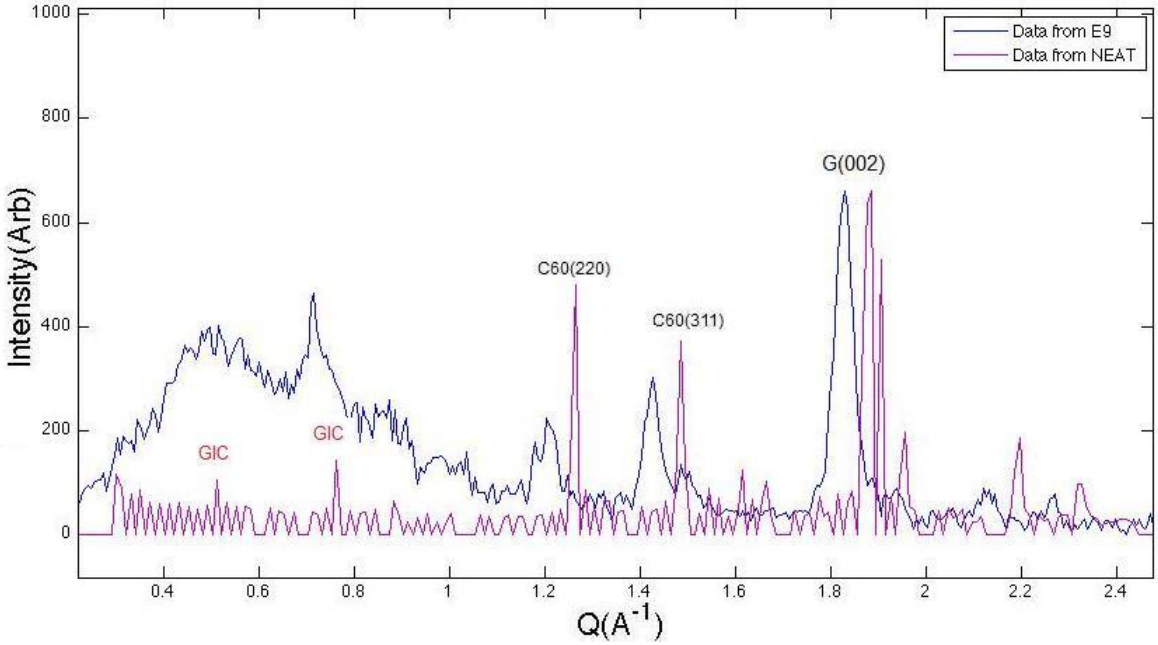

Again the peaks are shifted to the right and the intercalate peaks are visible at 0.55 Å and 0.78 Å. The C60 peaks are particularly intense in this measurement. The diffuse peaks around the intercalate are not visible but are shown in the full poly-CINS measurements as shown in later sections.

7.2.2 Graphite Contribution

Starting with the 2.1 Å data we will try to find evidence of information relating to the dynamics of the structures in the material. First we attempt to isolate the features arising from the graphite in the material.

The data obtained is confined to low energy transfer and is only present as small wings extending from the elastic line. Although we can be confident that the data is not just due to noise as it is beyond the resolution function we cannot see true phonon curves and thus the dynamic information which can

be obtained is limited.

Figure 7.13: C60 GIC at an initial wavelength of 2.1 Å

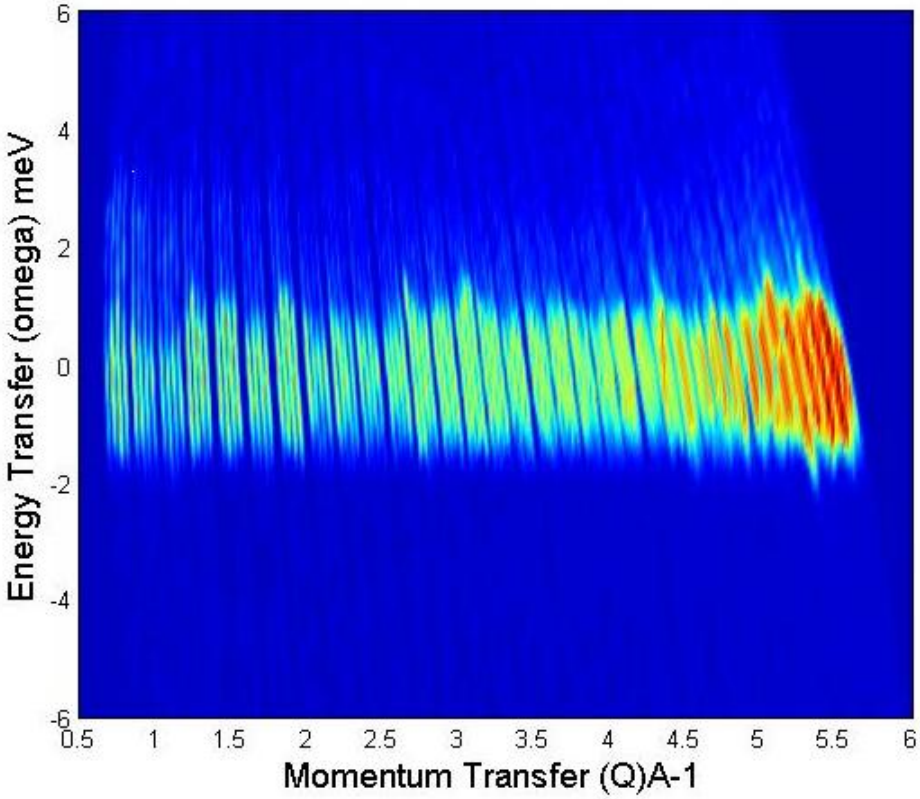

In figure (7.13) the 2.1 Å data has been smoothed and focused on the area of most interest. Several features can be seen, in the form of extensions from the elastic line, but it is not clear what structures these are associated with as we are missing features such as the obvious 002 curve typically found in graphitic materials.

Calculated graphite poly-CINS data can be compared to data from NEAT, thus showing which features belong to graphite. Figure (7.14) shows graphite data in black overlayed on to the NEAT data.

Possible features corresponding to those of graphite can be seen at 1.9 $Å^{-1}$, 3 $Å^{-1}$ and 3.4 $Å^{-1}$. Several features are not accounted for and those which occur in the region between the 002 curves are of most interest.

Figure 7.14: Comparison of model graphite data (black) with 2.1 Å data (colour)

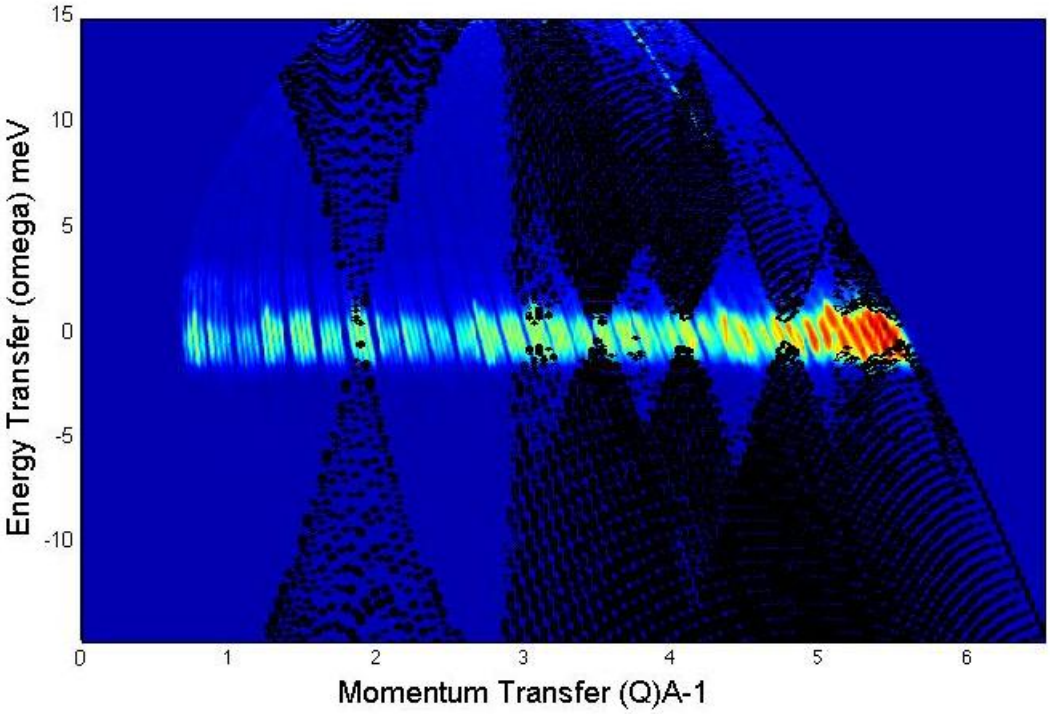

Figure 7.15: Line through 5 meV in 2.1 Å data compared with graphite calculation

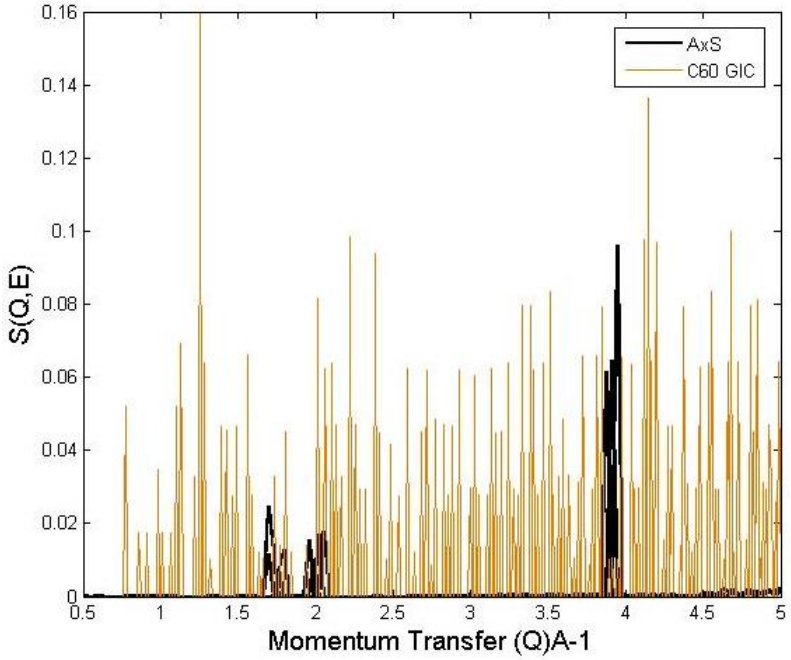

The technique of comparing line graphs as shown in the Dynamic Analysis of Graphite chapter does not yield good results for this data. Figure (7.15) shows the graphs at 5 meV for the C60 GIC compared to the axially symmetric model data. There are no obvious peaks in the data where they would be expected for graphite phonon curves it is possible the features are present but they are not clear.

Figure 7.16: Comparison of model graphite data (black) with 4.8 Å data (colour)

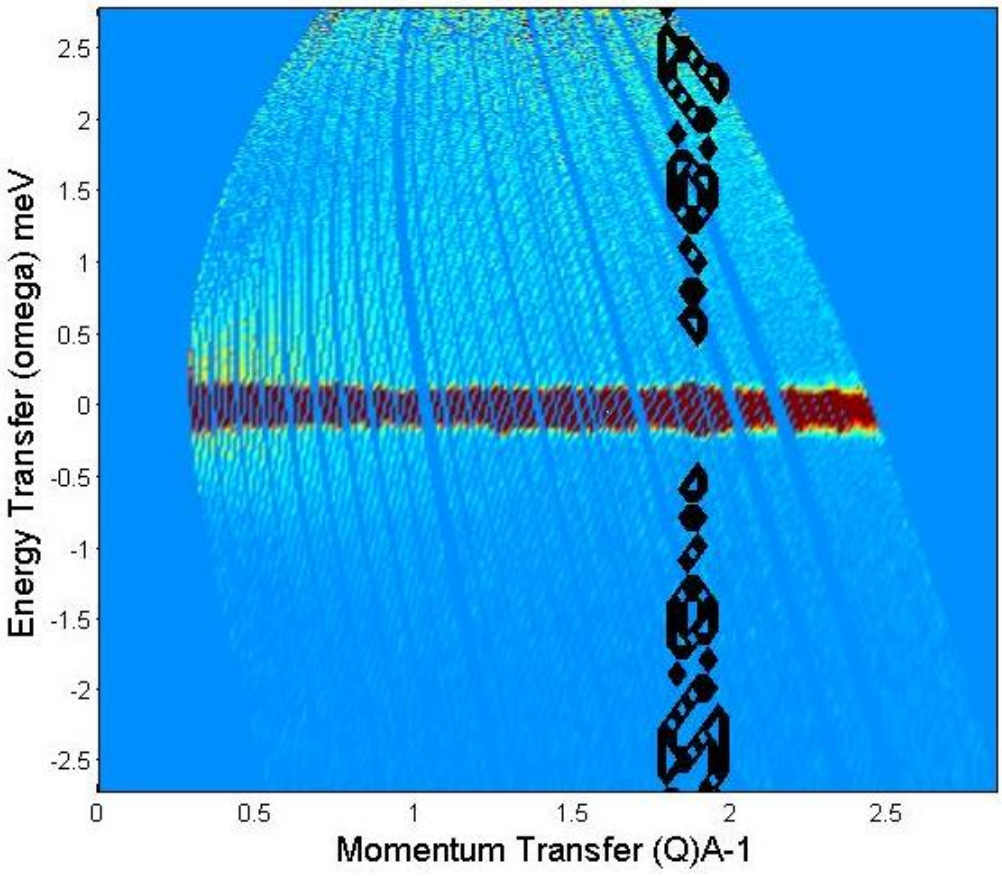

Overlaying the calculated data onto the 4.8 Å measurement as demonstrated in figure (7.16) shows that only a small part of the 002 curve is expected to be shown in this measurement. The comparison shows no evidence of the curve. There is a feature in the elastic line in the area expected but nothing obvious beyond this.

Figure (7.17) shows a comparison of the 4.8 Å data with the axially symmetric model at 1.5 meV. As with the 2.1 Å data any graphite features are far from obvious, this technique is clearly not suitable for this data.

Figure 7.17: Line through 1.5 meV in 4.8 Å data compared with graphite calculation

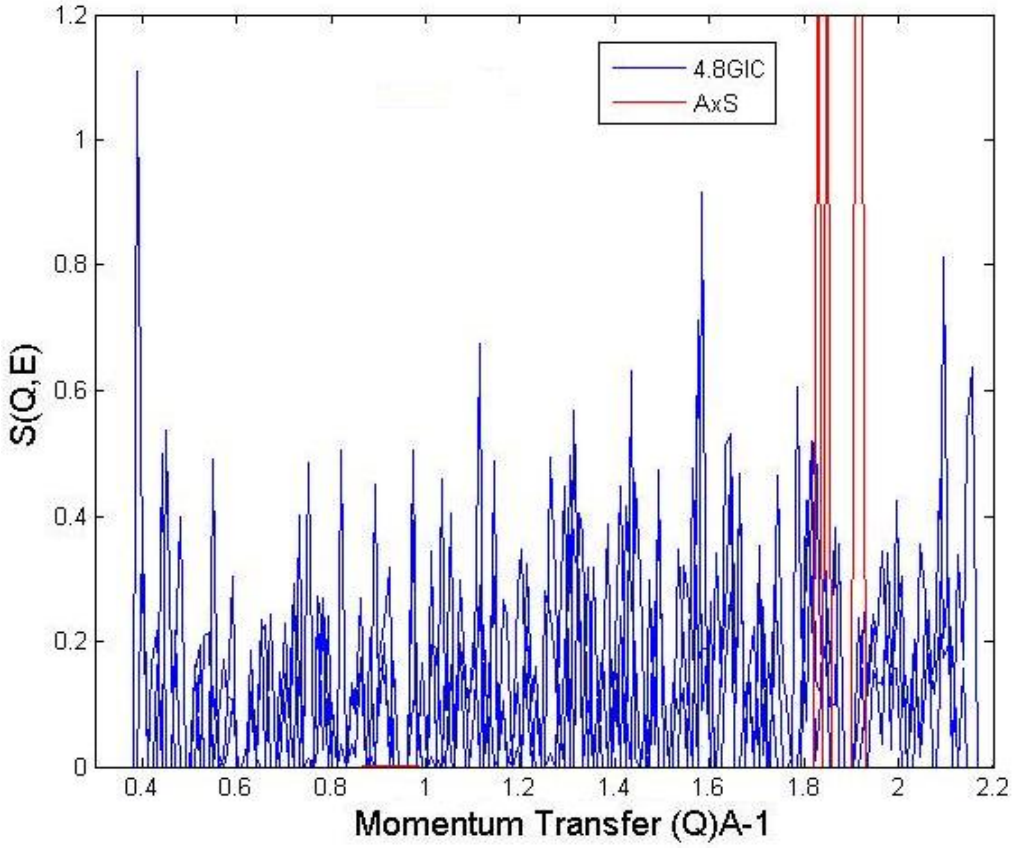

7.2.3 C60 Contribution

C60 phonons at low energy transfer have been shown by several groups in the literature review above to occur between 2.5 and 10 meV. Phonon curves are shown by Glebov *et al.*, in figure (7.5a), and cross the elastic line at around 0.6, 1.2 and 2.5 $Å^{-1}$.

Scattering can be seen in the forbidden area between the 002 graphite curves, this could correspond to the C60 phonon modes and interactions between the

C60 and the graphite. Intensity between 2.5 and 10 meV does not seem to be shown by the NEAT data. It is possible that the curves shown by Glebov *et al.* are present, there are features at 0.77, 1.242 and 2.644 $Å^{-1}$ but they are subtle and not conclusive.

Figure 7.18: NEAT data (colour) compared to model graphite data (black) and E9 diffraction data (white)

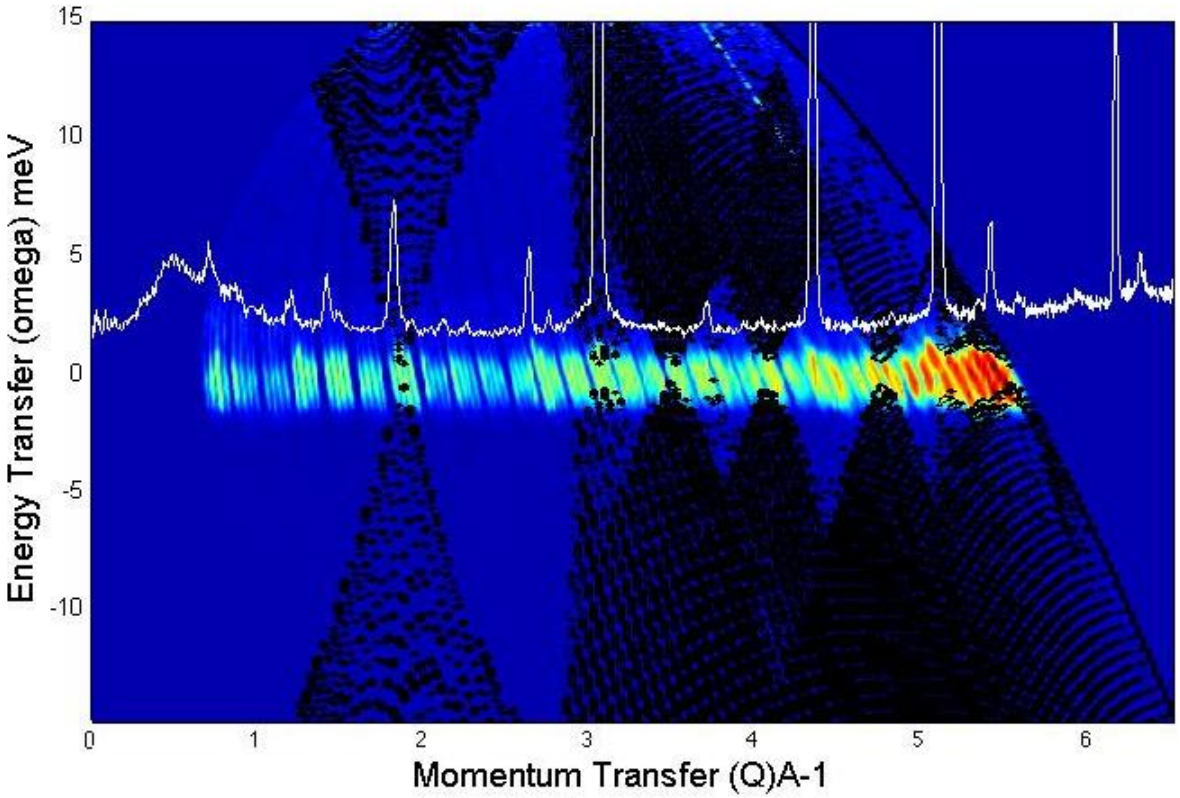

Comparison of the neutron diffraction data shows that the features not explained by the graphite phonons correspond with diffraction peaks. It is not clear if there is any dynamic information present in this data.

The measurement taken at 4.8 Å has a Q range which covers the C60 spectra and has been vanadium corrected. Looking at a lower intensity than the previous 4.8 Å figure, diffuse scattering between 0.5 $Å^{-1}$ to 1 $Å^{-1}$ is evident.

Figure 7.19: Diffuse Scattering in the C60 GIC

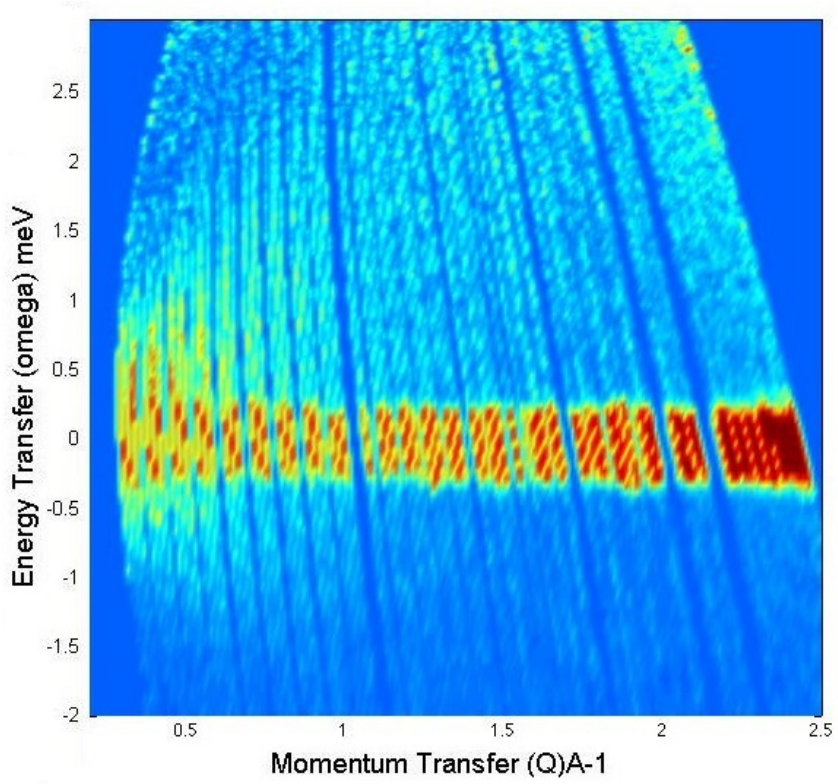

(a) Poly-CINS of C60 GIC taken at 4.8 Å showing diffuse scattering

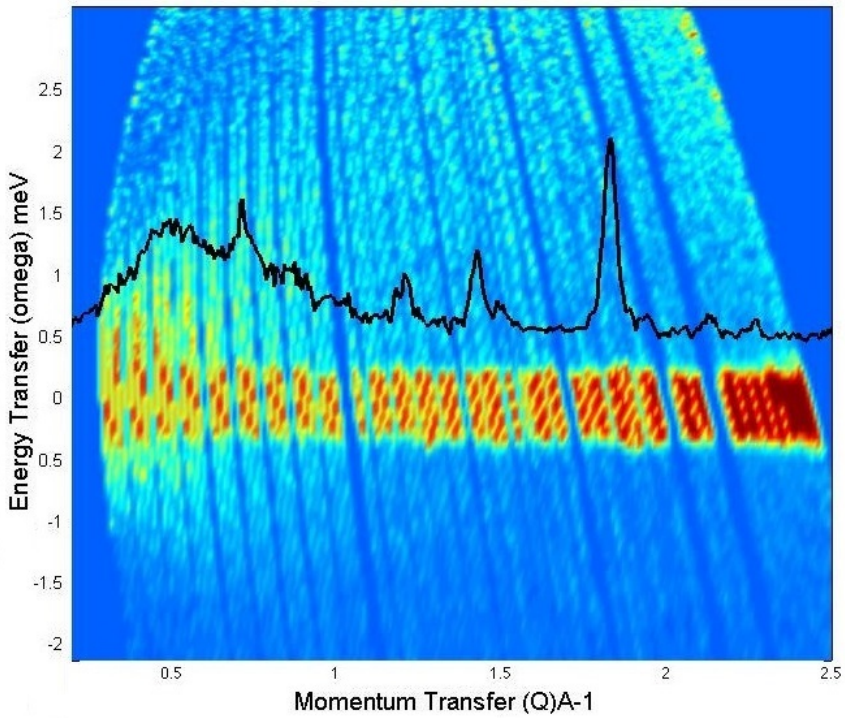

(b) Poly-CINS of C60 GIC taken at 4.8 Å with diffraction measurement overlaid

Comparison with the neutron diffraction shows that this corresponds with the hump present in the diffraction. Thus the disordered C60 demonstrated in the diffraction pattern is also showing an effect in the dynamics of the material.

7.2.4 Sum Over Q Data

As demonstrated by Yu[68] for the C60 lattice interactions between the molecules are separated from interactions within the molecule by a gap around 20 meV. The first internal interactions are present at 30 meV which is not covered by our data. The peak of the first graphite phonon, the 002 vibration, occurs at around 16 meV an energy transfer not covered by the NEAT measurements.

Summing over all Q should therefore give data that is only a result of interactions between C60 molecules. This summation allows features to be seen which are too weak to be visible in the $S(Q,\omega)$ scans or cuts through data.

Figure 7.20: Summation over all Q for C60 GIC NEAT measurement

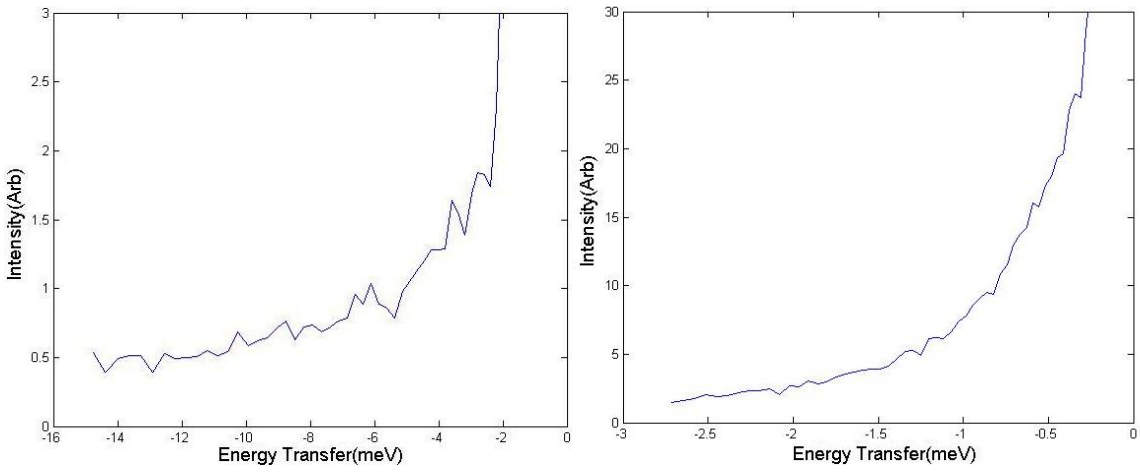

(a) Sum over Q for C60 GIC at 2.1 Å **(b)** Sum over Q for C60 GIC at 4.8 Å

We can see several clear peaks in intensity particularly in the 2.1 Å measurement. In order to ascertain if this is valid data and not just noise, the vanadium sample was also summed over Q to show the background. Figure (7.21) shows

a comparison between the vanadium and C60 GIC data, demonstrating the clear distance between the background and the C60 GIC data.

Figure 7.21: The sum over Q for C60 GIC compared to vanadium

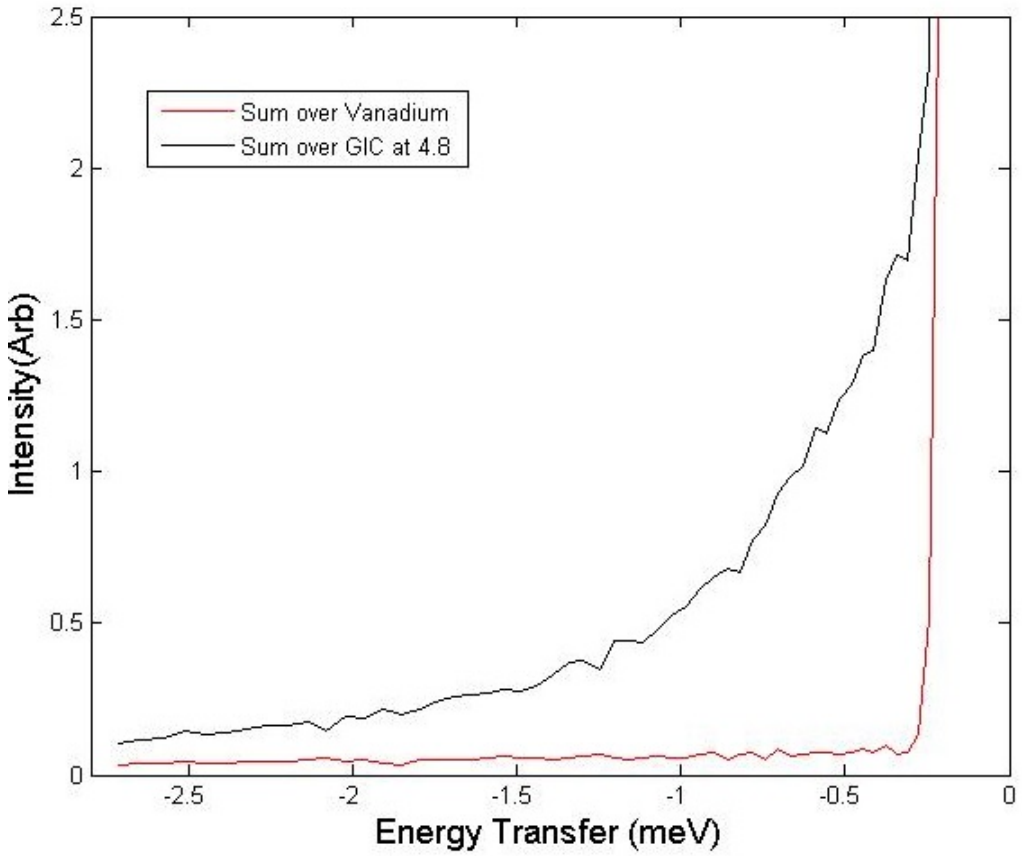

Now we are satisfied the data is valid we can compare these peaks with data from literature to ascertain which vibrations they correspond with and possibly to deduce the effect of the GIC on the sample's dynamics.

Due to the temperature at which the poly-CINS measurements were taken we cannot be sure if the C60 in the sample is in an FCC or SC lattice structure. The C60 GIC was created at high temperatures and thus is presumed to have solidified into an FCC lattice, however the low temperature of the measurement means that the C60 molecules could have shifted to an SC lattice depending on the amount of movement available to the molecules in the sample. We will therefore explore both possibilities.

FCC intensities are given by Parker[69] at 5.8 meV and 3.7 meV. Neumann[70] measured librational motion, using neutron scattering, at 2.0 meV for a measurement at 250 K, which moved to 2.8 meV at 20 K. Glebov *et al.*[67] showed that the libration modes at 1.75 and 3.25 meV shift to lower energies and reduce in intensity as temperature is increased, they also showed a mode at 5 meV.

SC modes are given by Parker at 2.7, 4.3 and 6.2 meV with a calculated peak at 8.7 meV. Yu[68] shows intensity in neutron scattering at 2.8, 3.8, 4.8 and 6.2 meV with calculated intensities at 2.5, 5 and 7 meV. Pintschovius *et al.*[71] used inelastic neutron scattering to find modes at 2.4, 3.6,and 4.6 meV. Horoyski *et al.*[72] used Raman spectroscopy at 77 K which gave peaks at 2.2, 2.6, 3.0 and 4.0 meV which were identified as libration modes with other peaks at 5.1, and 6.1 meV. These higher modes were also found by Horoyski *et al.*[73] using infrared spectrosopy at 5.0 and 6.8 meV at a temperature of 2 K. Also measured with infrared were peaks at 1.0, 1.6, 2.2, and 2.7 meV by Huant *et al.*[74] at 2 K.

Figure 7.22: Peaks in the sum over Q for NEAT data compared to energies from literature

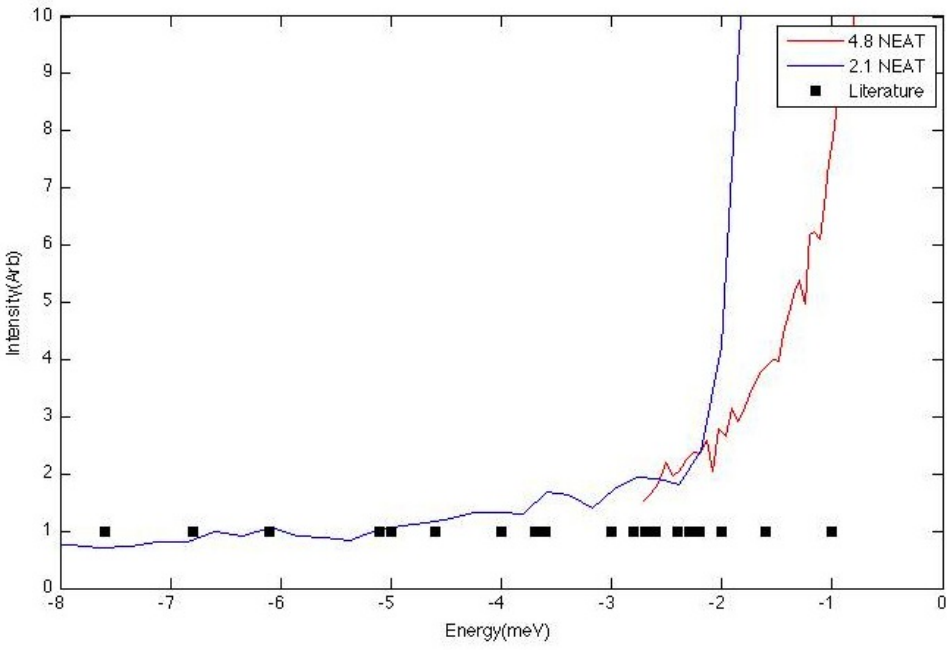

These values have been compared to the NEAT measurements in figure 7.22 and we can see that most of the peaks are accounted for.

NEAT (meV)	Other Work
0.7041	
0.8619	1.0[74]
1.205	
1.297	
1.539	1.6[74]
1.91	
2.023	2.0[70]*
2.14	2.2[74][73]
2.77	2.5[68], 2.6[73],2.7[74][69] 2.8[68][70]
3.594	3.5[69], 3.6[71],3.8[68]
4.236	4.3[69]
4.9	4.8[68], 5[68][73]
6.094	6.1[73], 6.2[69][68]
6.59	6.8[73]
7.109	7[68]
7.912	
8.753	8.7[69]
9.635	

Table 7.1: Peaks in NEAT data between 0.7 and 9.7 meV compared to literature values, FFC peaks are starred

The table 7.1 shows all the peaks from the NEAT data compared to the literature values. Those from FCC measurements are starred.

In this data the FCC values of 1.75, 3.25 and 5 meV from Glebov *et al.* are not present in the C60 GIC measurements and there are few matches to other FCC values such as those given by Parker *et al.*. The match to SC values is good with some missing or shifted values but the majority of peaks present. This suggests that the C60 is in the simple cubic form in the NEAT data.

The peaks for the C60 GIC tend to be lower than those for the pure simple cubic forms, suggesting that the C60 is more disordered as shown by the Glebov et al data which illustrates a reduction of energy value with increased temperature. The data also shows the peaks between 1 and 2 meV shown by Yu in their calculations of disordered C60.

We also have several peaks unaccounted for, particularly at low energy transfer which could be due to the intercalate. However it is not possible to specify if any effects arise from the interactions between the C60 and the graphite layers without a model for this system.

In summary we have shown that despite the low quality of data we have still been able to find some information about the sample, although it has not been possible to find any specific information about the intercalation of the C60 GIC. The information found in the poly-CINS and diffraction data shows that more investigation of this material would be justified. As we have shown, there are features which cannot be explained by graphite and C60 independently. Further poly-CINS experiments would be needed to find the best conditions for gaining information such as true phonon curves which would give real information about the dynamics of the material. It is not obvious if this would be easy to achieve with a better instrument as although the experiments with higher flux did give more information, the nature of the sample makes it difficult to put a lot of material in the neutron beam. As shown in the next section the instrument is capable of showing phonon curve information given a high enough quantity of scattering material.

7.2.5 Deuterium in C60 GIC

As the material was created for possible hydrogen storage applications an experiment was performed at NEAT which added D_2 gas to the C60 GIC under pressure. Deuterium is used in coherent scattering experiments instead of hydrogen as it has a coherent scattering cross-section similar to that of carbon. The deuterium and carbon coherent scattering cross-sections are 5.59 and 5.55 barns respectively. Hydrogen however has a low coherent cross-section of 1.76 barn and a very high incoherent cross-section of 79.9 barns, this incoherent

cross-section results in data loss for the other coherent scatterers in the system.

The experiments were performed at a pressure of 20 bar and with an initial wavelength of 4.8 Å as this wavelength provided the best data range in the previous experiments.

In the first experiment the gas was added when the system was at a temperature of 10 K. It was forgotten that D_2 solidifies at temperatures below 18 K thus this measurement shows dynamic information from solid D_2.

Figure 7.23: Poly-CINS measurement of C60 GIC and solid D_2

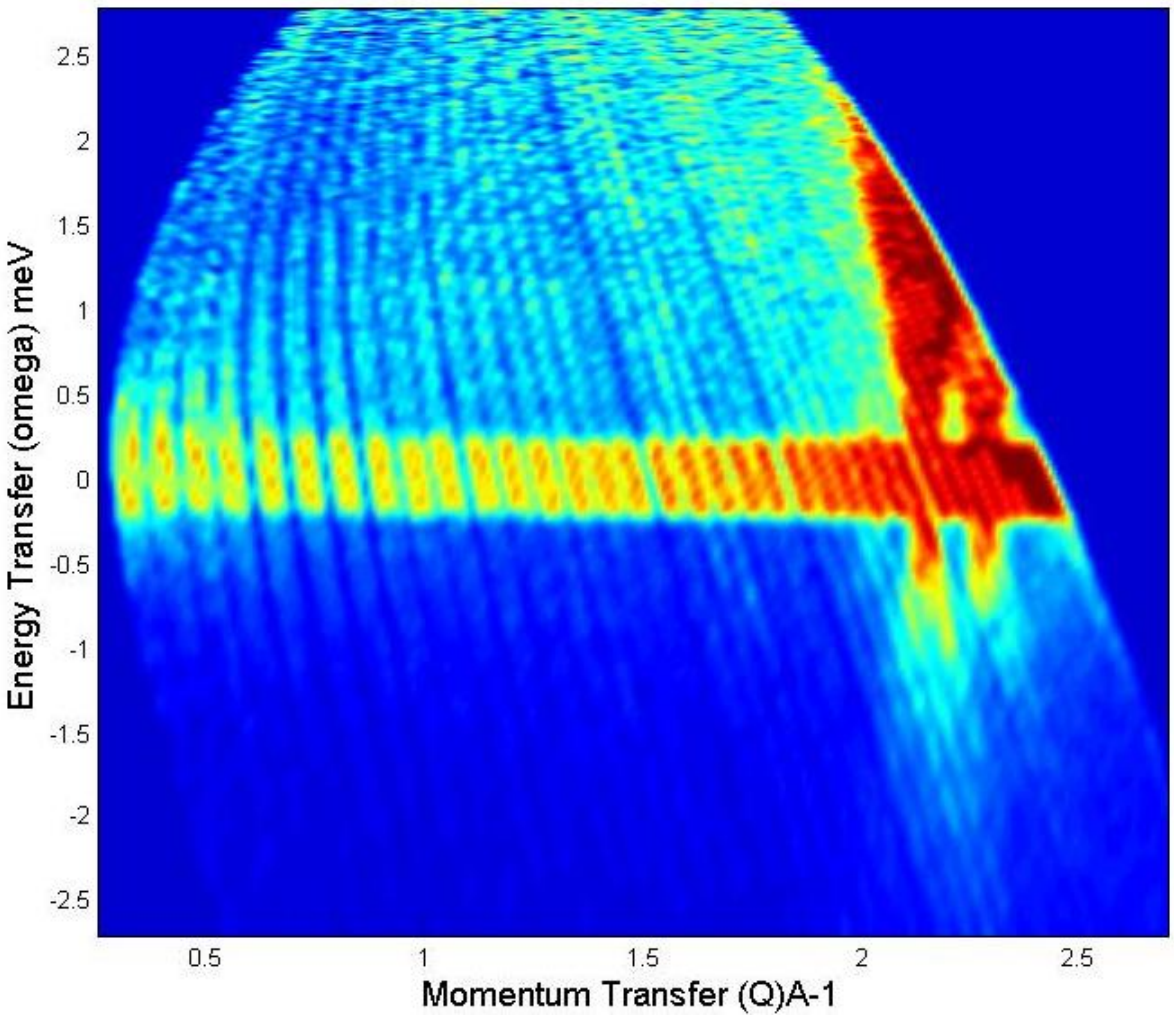

This data does demonstrate that clear intense phonon curves can be shown by

the NEAT spectrometer under the same conditions as the other measurements were taken, thus the lack of C60 GIC in the beam seems to be the main contributor to the low quality of the previous data. The curves beyond 2 $Å^{-1}$ fit with those expected from solid D_2 as measured by Nielsen[75] and others.

The temperature of the system was then raised to 34 K to allow the D_2 to return to its gaseous form. The poly-CINS spectra of this system is shown in figure (7.24).

Figure 7.24: Poly-CINS of C60 GIC with D_2 gas added

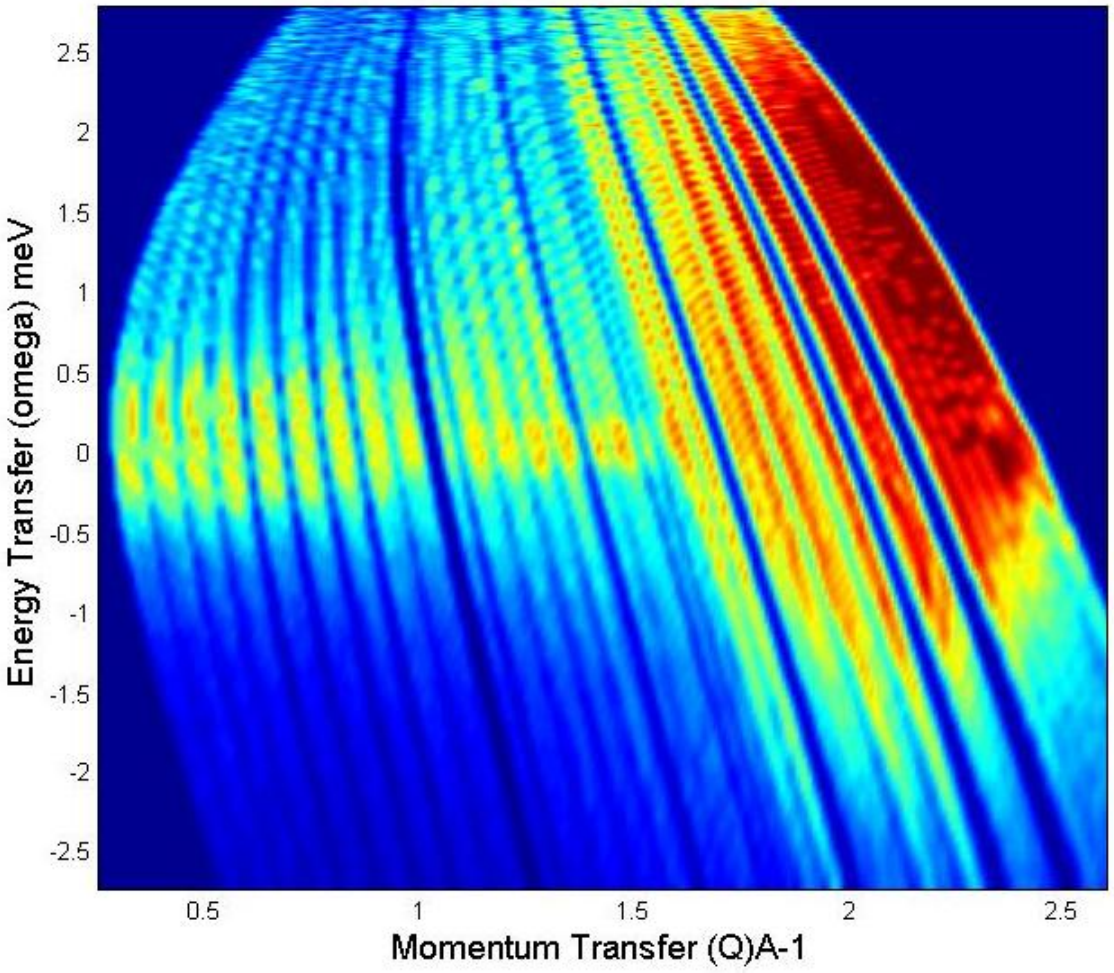

This shows strong diffuse scattering at Q values associated with D_2 gas. However it is unclear if the D_2 has travelled into the C60 GIC.

Comparison with the GIC measurement at the same wavelength, figure (7.25), shows how the system has changed with the addition of the gas.

Figure 7.25: Comparison of C60 GIC before and after the addition of D_2 gas

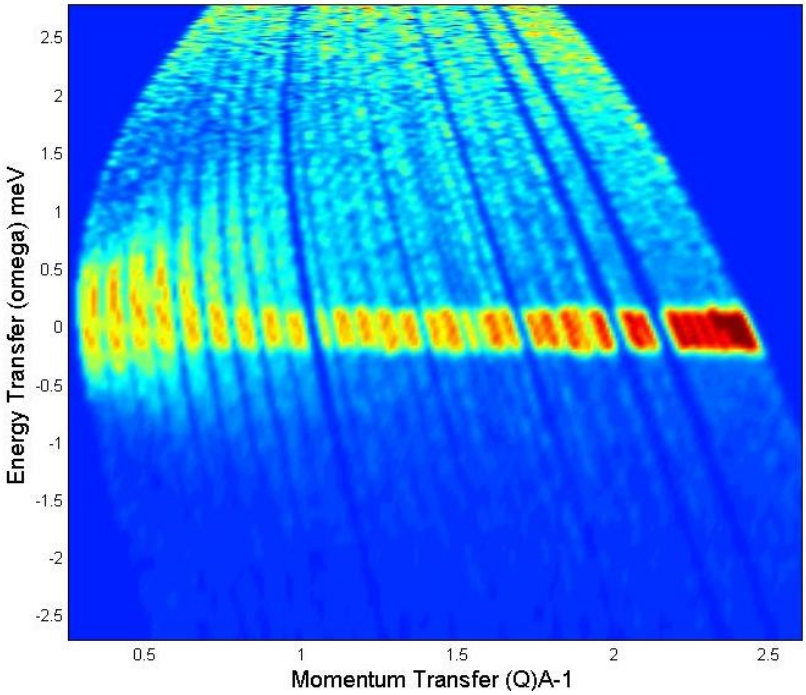

(a) Poly-CINS of C60 GIC taken at 4.8 Å

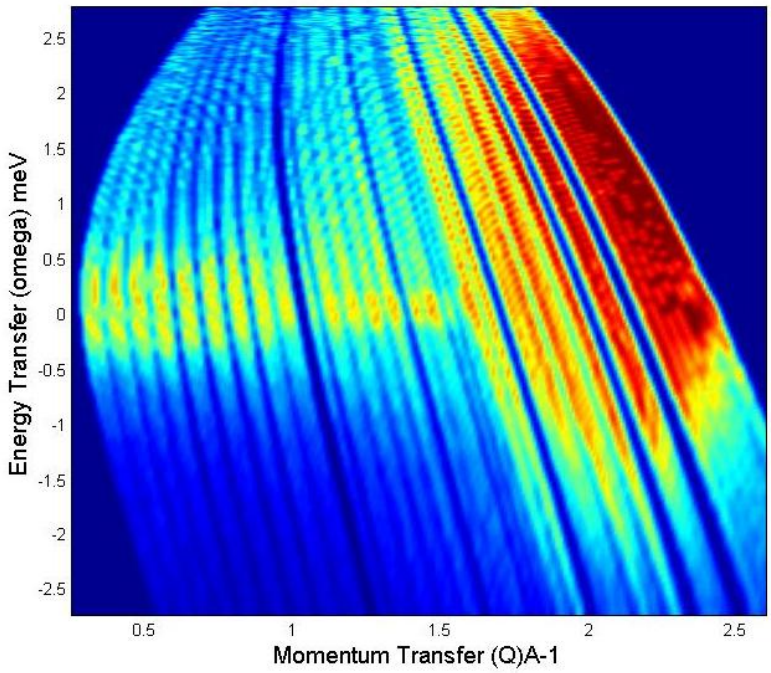

(b) Poly-CINS of C60 GIC with D_2 gas added

Figure 7.26: Comparison of C60 GIC before and after the addition of D_2 gas at full intensity

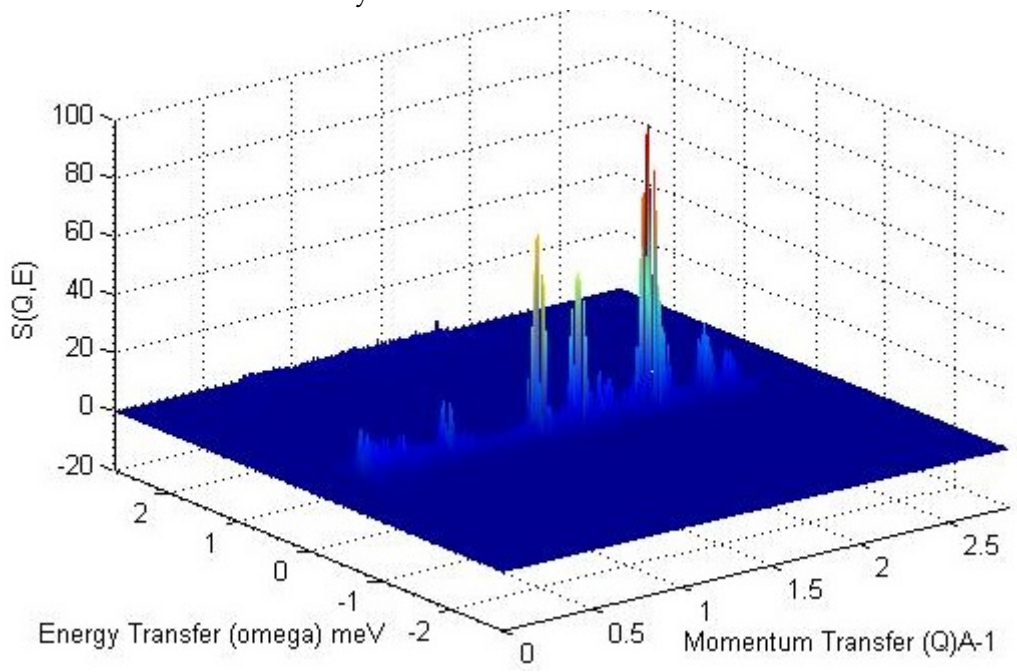

(a) Poly-CINS 3D plot of C60 GIC at full intensity

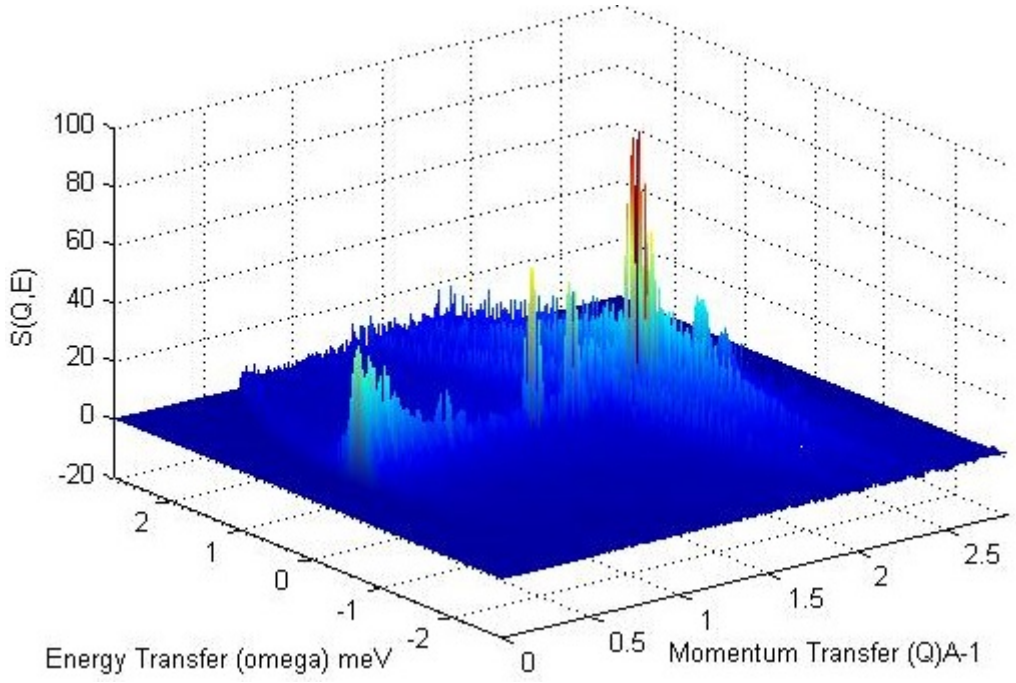

(b) Poly-CINS 3D plot of C60 GIC with D_2 gas added at full intensity

Figure (7.25) seems to show an increase in intensity between 1 and 1.5 $Å^{-1}$ but it is not entirely clear.

In figure (7.26) the two data sets have been normalised to the most intense elastic peak and are shown in full in a 3D plot.

These figures show an increase in intensities at low Q relative to the peak at 1.8 Å^{-1} which is the graphite 002 peak. This would seem to suggest that the D_2 has diffused through the material and has possibly accumulated around the intercalated areas. However more analysis is needed to definitively show the locations and movement of D_2 in the system.

It is also interesting that the graphite 002 peak dominates the elastic line despite the high intensity of the D_2 diffuse scattering. The elastic line for the sample with solid D_2 shows D_2 peaks with an intensity almost two orders of magnitude higher than the graphite 002 peak.

Figure 7.27: Poly-CINS measurement of C60 GIC and solid D_2 at full intensity

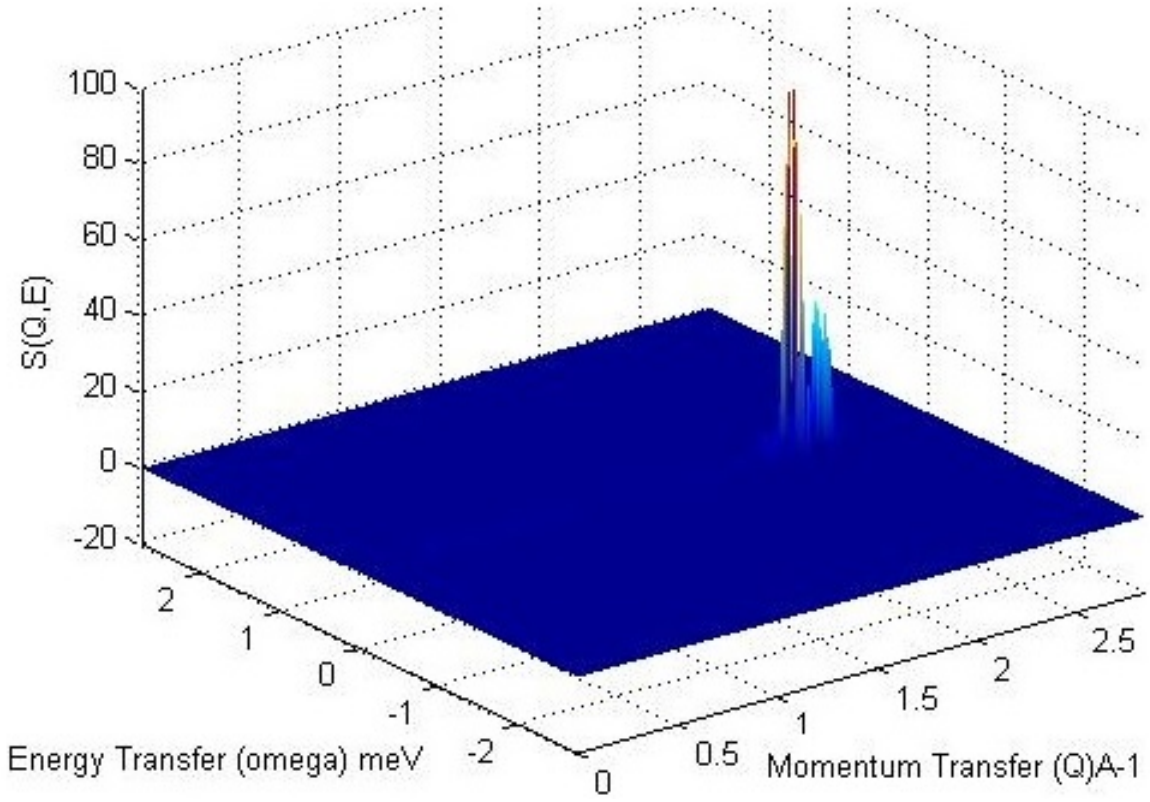

In figure (7.27) only D_2 peaks are visible, all other intensities are too low to see

if not highlighted by the removal of very high D_2 intensities.

In summary, the deuterium added data shows that it is possible to gain good poly-CINS data from the NEAT spectrometer, and that the main issue with the measurements are related to the nature of the C60 GIC sample. The data seems to show D_2 gas traveling through the GIC at a pressure of 20 bar but more investigations would be needed, at different temperatures and pressures to characterise the full behavior of D_2 or hydrogen gas in a C60 GIC material.

Chapter 8

Conclusions and Further Work

8.1 Conclusions

In this work we covered the creation and use of the neutron scattering visualisation and and analysis software Neutronplot. The creation of Neutronplot was necessary to allow the comparison of theoretical and experimental data. Without this software Scatter data would have to be transformed into input files for each analysis suite. Although this would be relatively easy to achieve, it would not allow the comparison capabilities of Neutronplot such as overlaying, and combining data sets. Neutronplot is also particularly user friendly, as a specific poly-CINS visualiser it performs several default actions to show the data in a clear form. Features such as the radio buttons moving to the next data set after loading and allowing points for line graphs to be chosen by a mouse click are unique.

Chapter four covered analysis of the structure of natural graphites. For natural graphite we found that the rhombohedral stacking in graphite tended to give a larger interlayer spacing than that of hexagonal and that at least one sample contained areas of different interlayer spacing. The exfoiliated graphite demonstrated the reduction in intensity of the 002 peak with the addition of

disorder to the system and the loss of visible rhombohedral peaks after exfoilation.

We also found that the sample created by Keens had C60 molecules intercalated in the graphite layers, giving a structure with dimensions similar to that found by Gupta *et al.*, with a large amount of disorder in plane spacing.

Poly-CINS measurements were used to investigate the dynamics of a natural graphite and an exfoilated graphite. We saw the natural graphite sample showed features which were a product of instrument error and were able to identify these by comparison of both sides of the energy transfer. It also showed differences in intensity from the predicted ideal graphite structure, this is likely to be due to defects in the material. The exfoilated sample showed a great difference in intensity from the theoretical and natural graphite data. With the phonon curves starting above 3Å showing higher intensity than the 002 curve.

The poly-CINS measurements of the C60 GIC proved challenging to interpret due to the poor statistics leading to a lack of clear phonon curves. We were able to find that the C60 in the structure showed similar dynamics to the the simple cubic form with alterations due to the disorder in the material. We also showed that the NEAT spectrometer was capable of showing dispersion information under the same conditions and that deuterium gas would percolate through the sample.

8.2 Further Work

There are many avenues for further investigation raised by this work. In the case of Neutronplot, it would be more accessible if it was written in a language such as C which can be easily complied to allow easy distribution and is more

commonly known. Ideally the functions specific to Neutronplot would be added to the current MANTID project, perhaps as an additional package for those interested in poly-CINS analysis.

In the case of the structural investigations more work needs to be undertaken to give a definitive answer to the subject of rhombohedral layer spacing in graphites, with diffraction measurements performed to investigate these peaks specifically. Ideally DFT or lattice dynamics calculations would be used to see if a different spacing is predicted, however DFT has difficulty in predicting the bonding between graphite layers.

The disordered nature of the C60 in the C60 GIC could be investigated further. The C60 sample used was not investigated prior to intercalation and it would be useful to perform diffraction analysis on this or a similar material to check if other fullerines or carbon based structures are present.

The investigation of the dynamics of graphite would be greatly improved with a model for the spectra expected from rhombohedral stacking to see what effect if any it has on the dynamics of graphite. A model of defected graphite, currently in development, would also be ideal for comparison with the natural and exfoilated samples. Experiments have also been performed investigating the effect of different orientations in the beam, this data could be used as comparison to this work to see how different phonon intensities are affected by both orientation and defects.

The dynamic properties of the C60 GIC could be better understood with the addition of models for the interactions between the C60 and the graphite and also by Scatter data for the C60 lattice and the GIC lattice. The model for diffraction proved essential in explaining peaks present in the neutron diffraction measurement and it is likely that Scatter data could give further insight into the poly-CINS data. This would be best done in conjunction with fur-

ther poly-CINS measurements with a higher neutron flux now that the areas of most interest have been identified. The analysis of the measurements of gaseous deuterium in the C60 GIC would benefit from more measurements taken under different conditions.

Appendices

Appendix A

Derivations

A.1 Box Normalisation

Starting with the result from Fermi's golden rule

$$\sum_{k'} \quad W_{k,\mu\to k'\mu'} = \frac{2\pi}{\hbar}\rho_{k'}|\langle \boldsymbol{k}'\mu'|V|\boldsymbol{k}\mu\rangle|^2 \tag{A.1}$$

we need to find an expression for $\rho_{k'}$

box normalisation imagines the quantum system in a large box, this fixes normalisation constants and means that the only neutrons states are those who de Broglie waves are periodic in the box. The wavevectors of these states forms a lattice in $\boldsymbol{k}$ space

The volume of the unit cell of this lattice is

$$v_{\boldsymbol{k}} = \frac{(2\pi)^3}{Y} \tag{A.2}$$

where Y is the volume of the box

neutron final energy is

$$E' = \frac{\hbar^2}{2m}\boldsymbol{k}'^2 \tag{A.3}$$

with

$$dE' = \frac{\hbar 2}{m}k'dk' \tag{A.4}$$

$\rho_{k'}dE$ is defined to be the number of states in $d\Omega$ with energy between E' and $E' + dE'$, this is equal to the number of wavector points in the element of volume $\boldsymbol{k}'^2 d\boldsymbol{k}' d\Omega$, giving

$$\rho_{k'}dE' = \frac{1}{v_k}\boldsymbol{k}'^2 d\boldsymbol{k}' d\Omega \tag{A.5}$$

substiution of the volume of the lattice gives

$$\rho_{k'} = \frac{Y}{(2\pi)^3}\boldsymbol{k}'\frac{m}{\hbar^2}d\Omega \tag{A.6}$$

the wavefunction of the neutron which is the plane wave $\exp(i\boldsymbol{k}.\boldsymbol{r})$ and there is one neutron in the box, thus the neutron density is $1/Y$ giving

$$\Psi_k = \frac{1}{\sqrt{Y}}\exp(i\boldsymbol{k}.\boldsymbol{r}) \tag{A.7}$$

thus the matrix element of the golden rule result is

$$\langle \boldsymbol{k}'\mu'|V|\boldsymbol{k}\mu\rangle = \int \Psi^*_{\boldsymbol{k}'}\chi^*_{\mu'}V\Psi_k\chi_\mu \; d\boldsymbol{R}\; d\boldsymbol{r} \tag{A.8}$$

$$= \frac{1}{Y}\int \exp(-i\boldsymbol{k}'.\boldsymbol{r})\chi^*_{\mu'}V\exp(i\boldsymbol{k}.\boldsymbol{r})\chi^*_\mu \; d\boldsymbol{R}\; d\boldsymbol{r} \tag{A.9}$$

We can also find the flux of the incident neutrons as it is the product of their density and velocity

$$\Phi = \frac{1}{V}\frac{\hbar}{m}\boldsymbol{k} \tag{A.10}$$

substitution of (A.1), (A.5), (A.9) and (A.10) into the differential cross section equation

$$\frac{d\sigma}{d\Omega}_{\mu\to\mu'} = \frac{1}{\Phi}\frac{1}{d\Omega}\sum_{k'} \quad W_{k,\mu\to k'\mu'} \tag{A.11}$$

gives

$$\left(\frac{d\sigma}{d\Omega}\right)_{\mu\to\mu'} = \frac{\boldsymbol{k}'}{\boldsymbol{k}}\left(\frac{m}{2\pi\hbar^2}\right)^2 |\langle \boldsymbol{k}'\mu'|V|\boldsymbol{k}\mu\rangle|^2 \tag{A.12}$$

References

[1] S G Keens. *Hydrogen storage in novel carbon materials*. PhD thesis, University of Salford, 2009.

[2] Agnieszka Kuc, Lyuben Zhechkov, Serguei Patchkovskii, Gotthard Seifert, and Thomas Heine. Hydrogen sieving and storage in fullerene intercalated graphite. *Nano letters*, 7(1):1–5, January 2007.

[3] Daniel Lee Roach. *Computational Investigations of Polycrystalline Systems Using Inelastic Neutron Scattering Techniques.* PhD thesis, School of Computing, Science & Engineering, 2006.

[4] R F Egerton. Electron energy-loss spectroscopy in the TEM. *Reports on Progress in Physics*, 72(1):16502, January 2009.

[5] A J Ramirez-Cuesta PCH Mitchell SF Parker and J Tomkinson. *Vibrational Spectroscopy with Neutrons*, volume 3 of *Series on Neutron Techniques and Applications*. World Scientific, 2005.

[6] D Richard, M Ferrand, and G J Kearley. Analysis and visualisation of neutron-scattering data. *Journal of Neutron Research*, 4(1):33–39, December 1996.

[7] T.Perring. Mslice. \url{http://mslice.isis.rl.ac.uk/Main_Page}.

[8] Main Page - LIBISIS. \url{http://www.libisis.org/Main_Page}.

[9] MATLAB and Simulink for Technical Computing. \url{http://www.mathworks.co.uk/}.

[10] G.E Bacon. The interlayer spacing of graphite. *ACTA CRYSTALLOGRAPHICACryst*, 4:558, 1951.

[11] W. JOHNSON and W. WATT. Structure of High Modulus Carbon Fibres. *Nature*, 215(5099):384–386, July 1967.

[12] Katrin Risch Henri Romanus Vinay Gupta Peter Scharff and Rene Muller. Synthesis of C60 intercalated graphite. *Solid State Communications*, 131(3-4):153–155, 2004. ISSN 0038-1098.

[13] R Satija, D L Jacobson, M Arif, and S A Werner. In situ neutron imaging technique for evaluation of water management systems in operating PEM fuel cells. *Journal of Power Sources*, 129(2):238–245, 2004.

[14] G.L.Squires. *Introduction to the Theory of Thermal Neutron Scattering*. Dover Publications, Inc, 1978.

[15] E Merzbacher. *Quantum Mechanics*. Wiley, 1970.

[16] Martin T.Dove. *Structure and Dynamics*. Oxford University Press, 2003.

[17] Charles Kittel. *Introduction to Solid State Physics*. John Wiley & Sons, Inc., New York, 8th edition, 2005.

[18] Klaus-Dieter Liss, Arno Bartels, Andreas Schreyer, and Helmut Clemens. High-Energy X-Rays: A tool for Advanced Bulk Investigations in Materials Science and Physics. *Textures and Microstructures*, 35(3-4): 219–252, 2003.

[19] B P Pandey and B Dayal. Lattice dynamics of silicon and diamond. *Journal of Physics C: Solid State Physics*, 6(20):2943, 1973.

[20] Léon Van Hove. Correlations in Space and Time and Born Approximation Scattering in Systems of Interacting Particles. *Physical Review*, 95(1):249–262, July 1954.

[21] B.N.Brockhouse. *Inelastic Scattering of Neutrons in Solids and Liquids*, 1: 113–151, 1961.

[22] Three-axis spectroscopy - Dynamics - Techniques for ... - Neutron research - The NMI3 information portal. URL `http://nmi3.eu/neutron-research/techniques-for-/dynamics/three-axis-spectroscopy.html`.

[23] Albert Jose Dainoux. *Neutron Data Booklet*. ILL Neutrons for Science, 2002.

[24] J Niderhaus, J Brenizer, and K Unlu. Thermal Neutron Time-of-Flight Spectroscopy at Penn State using a Single-Disk Chopper. In *PHYSOR 2004 -The Physics of Fuel Cycles and Ad vanced Nuclear Systems: Global Developments*, 2004.

[25] Module Chopper. URL `http://rencurel2006.essworkshop.org/packages/vitess-/vitess/WWW/chopper\_fermi\_str.html`.

[26] Helmholtz Zentrum Berlin. \url{http://www.helmholtz-berlin.de/zentrum/index_en.html}.

[27] ISIS - Instruments Instruments. http://www.isis.stfc.ac.uk/instruments/instruments2105.html.

[28] ORNL Neutron Sciences Instruments. URL `http://neutrons.ornl.gov/instruments/`.

[29] ILL :: Neutrons for science : Instruments & groups. http://www.ill.eu/instruments-support/instruments-groups/.

[30] O. Arnold, J. C. Bilheux, J. M. Borreguero, A. Buts, S. I. Campbell, L. Chapon, M. Doucet, N. Draper, R. Ferraz Leal, M. A. Gigg, V. E. Lynch, A. Markvardsen, D. J. Mikkelson, R. L. Mikkelson, R. Miller, K. Palmen, P. Parker, G. Passos, T. G. Perring, P. F. Peterson, S. Ren, M. A. Reuter, A. T. Savici, J. W. Taylor, R. J. Taylor, R. Tolchenov, W. Zhou, and J. Zikovsky. Mantid - Data Analysis and Visualization Package for Neutron Scattering and μSR Experiments. page 16, July 2014.

[31] William H Bragg and William L Bragg. *X rays and Crystal Structure*. 1915.

[32] P P Ewald. In *Sitzungsberichte, Munch*, 1914.

[33] J D Bernal. The Structure of Graphite. *Proceedings of the Royal Society of London.*, Vol. 106,(Series A, Containing Papers of a Mathematical and Physical Character):749–773, 1924.

[34] P. Touzain, N. Balasooriya, K. Bandaranayake, and C. Descolas-Gros. VEIN GRAPHITE FROM THE BOGALA AND KAHATAGAHA-KOLONGAHA MINES, SRI LANKA: A POSSIBLE ORIGIN. *The Canadian Mineralogist*, 48(6):1373–1384, January 2011.

[35] M Endo, Y.A Kim, T Takeda, S H Hong, T Matusita, T Hayashi, and M S Dresselhaus. Structural characterization of carbon nanofibers obtained by hydrocarbon pyrolysis. *Carbon*, 39(13):2003–2010, November 2001.

[36] W Betz, D Shollenberger, M Keeler, M Buchanan, L Sidisky, and K Patel. Graphitized Mesoporous Carbons | Sigma-Aldrich.

[37] Z Q Li and Y Zhou. Structural evolution of a graphite–diamond mixture during ball milling. *Physica B: Condensed Matter*, 405(3):1004–1010, February 2010.

[38] R E Franklin. The structure of graphitic carbons. *Acta Crystallographica*, 4 (3):253–261, May 1951.

[39] G Parthasarathy, B Sreedhar, and T R K Chetty. Spectroscopic and X-ray diffraction studies on fluid deposited rhombohedral graphite from the Eastern Ghats Mobile Belt, India. *Current science*, 90(7), 2006.

[40] T S Ong and H Yang. Effect of atmosphere on the mechanical milling of natural graphite. *Carbon*, 38(15):2077–2085, January 2000.

[41] Harold P. Klug and Leroy E Alexander. *X-Ray Diffraction Procedures: For Polycrystalline and Amorphous Materials*. Wiley, 1974.

[42] H. Lipson and A. R. Stokes. The Structure of Graphite. *Proceedings of the Royal Society A: Mathematical, Physical and Engineering Sciences*, 181(984): 101–105, September 1942.

[43] Yasushi Soneda and Hiroaki Hatori. FORMATION OF RHOMBOHEDRAL CRYSTALLITE IN PLATELET GRAPHITE. *Physical Review B*, pages 3–5, 2001.

[44] W Kohs, H J Santner, F Hofer, H Schröttner, J Doninger, I Barsukov, H Buqa, J H Albering, K.-C. Möller, J O Besenhard, and M Winter. A study on electrolyte interactions with graphite anodes exhibiting structures with various amounts of rhombohedral phase. *Journal of Power Sources*, 119-121:528–537, June 2003.

[45] EITARO MATUYAMA. Rate of Transformation of Rhombohedral Graphite at High Temperatures. *Nature*, 178(4548):1459–1460, December 1956.

[46] Yuejian Wang, Joseph E Panzik, Boris Kiefer, and Kanani K M Lee. Crystal structure of graphite under room-temperature compression and decompression. *Scientific reports*, 2:520, January 2012. ISSN 2045-2322.

[47] R. Nuske, A. Jurgilaitis, H. Enquist, M. Harb, Y. Fang, U. Hakanson, and J. Larsson. Transforming graphite to nanoscale diamonds by a femtosecond laser pulse. *Applied Physics Letters*, 100(4):043102, January 2012.

[48] H. W. Kroto, J. R. Heath, S. C. O'Brien, R. F. Curl, and R. E. Smalley. C60: Buckminsterfullerene. *Nature*, 318(6042):162–163, November 1985. ISSN 0028-0836.

[49] J B Howard, J T McKinnon, Y Makarovsky, A L Lafleur, and M E Johnson. Fullerenes C60 and C70 in flames. *Nature*, 352(6331):139–41, July 1991.

[50] Detection of C60 and C70 in a young planetary nebula. *Science (New York, N.Y.)*, 329(5996):1180–2, September 2010.

[51] Paul Heiney, John Fischer, Andrew McGhie, William Romanow, Arnold Denenstein, John McCauley Jr., Amos Smith, and David Cox. Orientational ordering transition in solid C_{60}. *Physical Review Letters*, 66(22):2911–2914, June 1991.

[52] Yufeng Zhao, Yong-Hyun Kim, A. C. Dillon, M. J. Heben, and S. B. Zhang. Hydrogen Storage in Novel Organometallic Buckyballs. *Physical Review Letters*, 94(15):155504, April 2005.

[53] Susumu Saito and Atsushi Oshiyama. Design of C60-graphite cointercalation compounds. *Physical Review B*, 49(24):17413–17419, June 1994.

[54] CaRIne Crystallography Software. URL
`http://carine.crystallography.pagespro-orange.fr/`.

[55] D K Ross. Inelastic neutron scattering from polycrystalline graphite at temperatures up to 1920 degrees C. *Journal of Physics C: Solid State Physics*, 6(24):3525–3535, December 1973.

[56] R. Nicklow, N. Wakabayashi, and H. Smith. Lattice Dynamics of Pyrolytic Graphite. *Physical Review B*, 5(12):4951–4962, June 1972.

[57] J Maultzsch, S Reich, C Thomsen, H Requardt, and P Ordejón. Phonon Dispersion in Graphite. *Physical Review Letters*, 92(7):75501, February 2004. ISSN 0031-9007.

[58] James A. Young and Juan U. Koppel. Phonon Spectrum of Graphite. *The Journal of Chemical Physics*, 42(1):357, January 1965.

[59] Akio Yoshimori and Yoshiharu Kitano. Theory of the Lattice Vibration of Graphite. *Journal of the Physical Society of Japan*, 11(4):352–361, April 1956.

[60] M. Mohr, J. Maultzsch, E. Dobardžić, S. Reich, I. Milošević, M. Damnjanović, A. Bosak, M. Krisch, and C. Thomsen. Phonon dispersion of graphite by inelastic x-ray scattering. *Phys. Rev. B*, 76: 035439, Jul 2007.

[61] D. L. Roach, J. D. Gale, and D. K. Ross. Scatter: A New Inelastic Neutron Scattering Simulation Subroutine for GULP. *Neutron News*, 18(3):21–23, 2007. ISSN 1044-8632. doi: 10.1080/10448630701492475.

[62] J Ollivier, M Plazanet, H Schober, and J C Cook. First results with the upgraded IN5 disk chopper cold time-of-flight spectrometer. 350: 173–177, 2004. doi: 10.1016/j.physb.2004.04.022.

[63] Alexey Bosak, Michael Krisch, Marcel Mohr, Janina Maultzsch, and Christian Thomsen. Elasticity of single-crystalline graphite: Inelastic x-ray scattering study. *Phys. Rev. B*, 75:153408, Apr 2007.

[64] G. Dolling and B. Brockhouse. Lattice Vibrations in Pyrolitic Graphite. *Physical Review*, 128(3):1120–1123, November 1962.

[65] A. P. Roy. Temperature Variation of the Frequency of Longitudinal Inter-Planar Oscillations in Pyrolitic Graphite. *Canadian Journal of Physics*, 49(2):277–279, January 1971.

[66] E S Seldin. In *Proc. of the Ninth Biennial Conference on Carbon, Chestnut Hill, Mass.*, pages 59–60. Defence Ceramic Information Centre), 1969.

[67] A Glebov, V Senz, and J P Toennies. Low-frequency phonon dynamics of the C 60 (111)surface. *Physical Review B*, 56(15):9874–9880, 1997.

[68] Jin Yu, Rajiv K Kalia, and Priya Vashishta. Phonon dispersion and density of states of solid C60. *Applied Physics Letters*, 63(23):3152, 1993.

[69] Stewart F Parker, Stephen M Bennington, Jon W Taylor, Henryk Herman, Ian Silverwood, Peter Albers, and Keith Refson. Complete assignment of the vibrational modes of C60 by inelastic neutron scattering spectroscopy and periodic-DFT. *Physical chemistry chemical physics : PCCP*, 13(17): 7789–804, May 2011.

[70] D. A. Neumann, J. R. D. Copley, W. A. Kamitakahara, J. J. Rush, R. L. Cappelletti, N. Coustel, J. E. Fischer, J. P. McCauley, A. B. Smith, K. M. Creegan, and D. M. Cox. Rotational dynamics and orientational melting of C60: A neutron scattering study. *The Journal of Chemical Physics*, 96 (11):8631, June 1992.

[71] L. Pintschovius, B. Renker, F. Gompf, R. Heid, S. Chaplot, M. Haluska, and H. Kuzmany. Inelastic neutron scattering study of the external vibrations in single crystal C60. *Physical Review Letters*, 69(18):2662–2665, November 1992. ISSN 0031-9007.

[72] P. Horoyski, M. Thewalt, and T. Anthony. Disorder, impurity, and isotope effects in the Raman-active libron spectrum of crystalline C60. *Physical Review B*, 52(10):R6951–R6954, September 1995.

[73] P. Horoyski and M. Thewalt. Optically detected librons and phonons in crystalline C60. *Physical Review B*, 48(15):11446–11449, October 1993.

[74] S. Huant, J. Robert, G. Chouteau, P. Bernier, C. Fabre, and A. Rassat. Lattice phonon modes in solid C60 studied by far-infrared spectroscopy. *Physical Review Letters*, 69(18):2666–2669, November 1992.

[75] M. Nielsen. Phonons in solid hydrogen and deuterium studied by inelastic coherent neutron scattering. *Phys. Rev. B*, 7:1626–1635, Feb 1973.